INTERPRETING HIGH RESOLUTION SUNYAEV ZEL'DOVICH EFFECT MEASUREMENTS WITH MUSTANG

Charles Romero
Fort Collins, CO

B.A., University of Colorado, 2009

M.S., University of Virginia, 2011

A Dissertation Presented to the Graduate
Faculty of the University of Virginia
in Candidacy for the Degree of
Doctor of Philosophy

Department of Astronomy

University of Virginia
August, 2015

Brian Mason

Craig Sarazin

Mark Whittle

Mike Skrutskie

Barry Condron

Acknowledgements

There are many people I must thank for inspiring and supporting my path towards a graduate degree in astronomy. Certainly somewhere in elementary school, between the science classes and fairs, my interest in science took formation. Thus, I wish to thanks all the science teachers and volunteers whom I have encountered who have taught me that science is cool, fun, interesting, and ever growing.

I thank my advisor, Brian Mason, for introducing me to the Sunyaev Zel'dovich effect and means of observing it. Brian has been an excellent advisor for me; he has pushed me when I needed motivation and given my space when I needed some time off.

To my collaborators, I am grateful for the collegiality and willingness to answer any questions (simple or otherwise) I may have had. To those at the astronomy department at the University of Virginia, I am thankful for the opportunities presented and the guidance offered.

Of course, my family: Henry, Paolo, and Marian Romero have encouraged me from the start (from my earliest interests in science) through graduate school and have been more supportive than I could have asked of them to be. This is especially true of my partner, Rachael Beaton. I thank Jack, Ginny, and Nora Beaton for providing stress relief and an ever optimistic outlook. I would also like to thank Rachael Beaton's family who have encouraged both of us on our paths in astronomy.

Abstract

We present pressure profiles of galaxy clusters determined from high resolution Sunyaev-Zel'dovich (SZ) effect observations in fourteen clusters, which span the redshift range $0.25 < z < 0.89$. We assume spherical geometry for our pressure profiles and compare to pressure profiles derived from X-ray analysis (ACCEPT catalog), which also assumes a spherical geometry.

A technique to jointly fit SZ data from the Bolocam and MUSTANG instruments is developed and implemented to determine cluster pressure profiles. Bolocam is a bolometer array on the Caltech Submillimeter Observatory (CSO) with a resolution of $58''$ and $8'$ field of view (FOV), and MUSTANG is a bolometer array on the 100-m Robert C. Byrd Green Bank Telescope (GBT) with a resolution of $9''$ and FOV of $42''$. Jointly, these two instruments allow a wide range of spatial scales to be constrained by solely SZ observations. Most notably, MUSTANG is one of a few SZ instruments with high resolution, and provides unique insight into the pressure in the core of galaxy clusters.

Our constraints on pressure profile parameters are consistent with those in previous studies, but on individual clusters we find discrepancies with pressure profiles from ACCEPT. We investigate potential sources of these discrepancies, especially in the context of cluster geometry, electron temperature of the intracluster medium, and substructure.

Additionally, efforts to prepare for the upcoming MUSTANG-2 are presented. In a desire to identify the preferred materials for the dewar window and radome, we investigate the transmission properties of several potential materials. We also model shocks in the plane of the sky to estimate the sensitivity necessary to observe shocks.

Table of contents

Chapter 1

Introduction

1.1 Historical Background

The tendencies for galaxies to cluster has long been known, before the nature of nebulae were known. The first detailed study of clusters of galaxies came in 1906 by Wolf, with notable advances aided by catalogs from Zwicky and Abell in the 1930s through 1950s. In 1970 and 1972 the Coma and Perseus clusters of galaxies were discovered to be X-ray luminous (Fritz et al. 1971; Gursky et al. 1971). By 1972, the Uhuru X-ray satellite confirmed that many other clusters of galaxies are strong X-ray emitters (Giacconi et al. 1972). See Sarazin (1988) for an excellent review of the history of X-ray observations clusters of galaxies.

The Sunyaev-Zel'dovich (SZ) effect is a spectral distortion in the Cosmic Microwave Background (CMB). It was predicted by Sunyaev & Zel'dovich (1970) not long after the discovery of the CMB by Penzias & Wilson (1965). Despite the earliest SZ searches occurring in 1976 (Gull & Northover 1976), and a steady progression of SZ observations with radiometers, generally in the Raleigh-Jeans tail of the CMB, it was not until Meyer et al. (1983) that the first bolometric SZ observation attempts

were made, and not until Holzapfel et al. (1997) that bolometer technology had progressed sufficiently for the first SZ detections at millimeter wavelengths. A major driving force in the first two decades of SZ observations was to determine the Hubble parameter, H_0, by directly measuring the distance of clusters of galaxies (Gunn 1978; Silk & White 1978; Birkinshaw 1979; Cavaliere et al. 1979). However, by 2006, the SZ effect and X-ray determination (e.g. Bonamente et al. 2006) of the Hubble parameter had not caught up to constraints via the distance ladder based on Cepheid variables (Madore et al. 1999; Freedman et al. 2001). With little advancement since 2006 (Bonamente et al. 2013), it is clear that the majority of the SZ field has taken up other pursuits.

It has been recognized that a great advantage of SZ observations of clusters of galaxies is that the intrinsic signal is redshift independent (e.g. Korolev et al. 1986; Birkinshaw 1999; Carlstrom et al. 2002). That is, unlike observations at any other wavelength, the SZ signal does not suffer from cosmological dimming. Thus, any studies that rely on the combination of SZ observations with another wavelength (especially X-rays) will, in principle, be limited by the sensitivity of observations from the other wavelength. In practice, X-ray observations have benefited greatly from *ROSAT*, *Chandra*, and *XMM-Newton* telescopes. SZ observations have seen several telescopes and instruments built in the past two decades, and there are roughly a dozen instruments that as of 2015 have access to millimeter observations and are designed, at least partially, to observe the SZ effect. Two major SZ survey instruments are ACT (Swetz et al. 2011) and SPTpol (Austermann et al. 2012); Planck (Planck Collaboration et al. 2011) also acts as a SZ survey instruments, but its low resolution ($\sim 4.5'$ at 350 GHz) lessens the extent to which it can detect new clusters of galaxies relative to the other two instruments. While not an SZ survey instrument,

the Yuan-Tseh Lee Array for Microwave Background Anisotropy (AMiBA Ho et al. 2009) is a dedicated CMB telescope able to do SZ studies as well. Several other instruments have been placed on non-CMB dedicated single-dish telescopes: Bolocam (Glenn et al. 1998), now replaced with MUSIC (Sayers et al. 2014) on the Caltech Submillimeter Observatory; APEX-SZ (Schwan et al. 2012) on the APEX telescope; GISMO (Staguhn et al. 2006), to be replaced with GISMO-2 (Staguhn et al. 2012), was placed on the IRAM-30m, which also hosts the New IRAM KID Arrays (NIKA) (Monfardini et al. 2010) instrument, which is to be upgraded to NIKA-2 (Monfardini et al. 2014). The AzTEC (Wilson et al. 2008) was originally commissioned on the James Clerk Maxwell Telescope (JCMT), but has moved to the Large Millimeter Telescope (LMT), and the MUltiplexing SQUID TES At Ninety Gigahertz (MUSTANG) instrument (Dicker et al. 2006, 2008) on the 100-m Green Bank Telescope (GBT), to be replaced by MUSTANG-2 (Dicker et al. 2014b). There are also three telescope interferometer arrays suited for SZ studies: the Australia Telescope Compact Array (Sinclair et al. 2001), the Arcminute MicroKelvin Imager (Kneissl et al. 2001), and CARMA (e.g. Plagge et al. 2013). CARMA is the combination of three separate arrays: the Sunyaev-Zel'dovich Array (SZA), the Owens Valley Radio Observatory (OVRO) array, and the Berkeley-Illinois-Maryland-Association (BIMA) array.

The features of recent SZ telescopes and instruments are summarized in Table 1.1. While there are likely many instruments that access the millimeter/submillimeter regime where the SZ effect is observable, those which are not intended to perform SZ observations (and thus may not be well suited to whole-cluster SZ observations) are not included.

Instrument	Telescope	Frequency (GHz)	Years in use	Resolution	FOV	Reference	Notes
			Single Dish Telescopes				
SCUBA	JCMT	350 (& 650)	1999-2009	$15'$	$2.'8$	Holland et al. (1999)	
SCUBA-2	JCMT	350	2010-present	$10'$	$6.'7$	Holland et al. (2013)	
SuZIE-II	CSO	145, 221, & 355	2002-2005	$1.'4$	$1.'4$	Benson et al. (2003)	Successor to SuZIE
Bolocam	CSO	140 & 260	2002-2012	$1'$	$8'$	Glenn et al. (1998)	
NOBA	Nobeyama	150	1993-2007	$13''$	$1.'9$	Kuno et al. (1993)	
MBAC	ACT	148, 215, & 277	2011-2013	$1.'3$	$24'$	Swetz et al. (2011)	Resolution from 215 GHz
ACTpol	ACT	150 & 220	2013-present	$1.'3$	1deg	Niemack et al. (2010)	
LABOCA	APEX	345	2007-present	$19''$	$11'$	Siringo et al. (2009)	
APEX-SZ	APEX	150	2007-present	$58''$	$22'$	Schwan et al. (2011)	
SPT-SZ	SPT	95, 150, and 220	2007-2011	$1.'6$	1deg	Carlstrom et al. (2009)	Survey instrument
GISMO	IRAM 30-m	150	2008-present	$17.''5$	$3.'7$	Staguhn et al. (2006)	
NIKA	IRAM 30-m	150 & 240	2009-2013	$12.''5$	$2'$	Monfardini et al. (2010)	
MUSTANG	GBT	90	2008-2014	$9''$	$42''$	Dicker et al. (2008)	
AzTEC	LMT	270	2011-present	$6''$		Wilson et al. (2008)	Previously on JCMT and APEX
			Arrays				
HEMT[2] & MMIC[3]	SZA	31 90	2005-2007	$18''$	$5'$	Muchovej et al. (2007)	Resolution from long baselines
HEMT & SIS[4]	OVRO	31, 90, & 250	-2007	$> 1''$	$1.'3$	Padin et al. (1991)	Max. Resolution ; 250 GHz
MMIC & SIS	BIMA	22, 90, & 220	1996-2007	$> 0.4''$	$2'$	Welch et al. (1996)	Max. Resolution ; 100 GHz
–	CARMA	25, 90, & 220	2007-2015	$> 0.1''$	$5'$	Woody et al. (2004)	SZA + OVRO + BIMA
AMiBA	AMiBA	90	2006-present	$2'$	$20'$	Ho et al. (2009)	
HEMT	AMI	15	2001-present	$>1.'5$	$21'$	Kneissl et al. (2001)	8 13m dishes and 10 3.7m dishes
HEMT	CBI	31	1995-2005	–	–	Udomprasert et al. (2004)	13 dishes
			Current and soon-to-come				
MUSIC	CSO	150 - 350	2012-present	$22''$	$14'$	Sayers et al. (2014)	Successor to Bolocam, 4 bands
SPTpol	SPT	90 & 150	2012-present	$1.'6$	1deg	Austermann et al. (2012)	Survey instrument
Planck	Planck	25 to 1000	2009-present	$4.'5$	$4.'5$[1]	Planck Collaboration et al. (2011)	Resolution given for 350 GHz
NIKA-2	IRAM 30-m	150 & 240	Planned 2015	$12.''5$	$6.'5$	Monfardini et al. (2014)	Uses KIDs
GISMO-2	IRAM 30-m	150 & 250	Planned	$12.''5$	$7.'4$	Staguhn et al. (2012)	
SPT-3g	SPT	95, 150, and 220	Planned 2016	$1'$	1deg	Benson et al. (2014)	Resolution given for 150 GHz
MUSTANG-2	GBT	90	2014-present	$9''$	$2.'5$	Dicker et al. (2014b)	Current implementation deemed "MUSTANG-1.5"

Table 1.1: SZ instruments and telescopes in use from 2000 on. Resolution is given as the full-width, half-maximum (FWHM) of each instrument, for the lowest frequency band. Field of view (FOV) should be understood as the diameter, or for instruments with a roughly square layout, as the length of a side. [1]Planck has a 1×8 detector layout for the 353 GHz detectors the sky is undersampled for a nominal FOV of 4 deg. [2] HEMT: High Electron Mobility Transistor. [3]MMIC: Monolithic Microwave Integrated Circuit. [4] SIS: Superconductor-Insulator-Superconductor (radiometer).

To utilize the advantage of redshift independence, SZ studies will inherently have to rely minimally on additional wavelength observations to accurately determine counts of clusters of galaxies as a function of redshift and mass (i.e. determine the mass function of clusters of galaxies). The redshift of a cluster cannot be garnered from SZ observations themselves; obtaining spectroscopic redshifts are time intensive, so photometric redshifts are typically the first means of constraining redshift (e.g. Reichardt et al. 2013; Sehgal et al. 2013). While X-ray follow up is still feasible, as SZ instruments continue to improve (e.g. SPT-3G and ACTpol Niemack et al. 2010; Benson et al. 2014), SZ surveys will need to become self-reliant for accurate mass determinations. As is, there is already significant progress in this arena predominantly from observable scaling relations (e.g. Plionis et al. 2008; Kravtsov & Borgani 2012). However, they note that a sensitive, high resolution SZ instruments would clearly be needed within the next 10 years (from 2008), and ideally it would have multifrequency capabilities (Birkinshaw & Lancaster 2008). The high resolution is necessary to resolve structure in clusters at a complementary resolution to what X-ray instruments will have. Of the instruments available, bolometer cameras on large single dish telescopes are the closest to reaching this ideal.

Many interferometric arrays can achieve a resolution of $\sim 10''$ or better. Taking CARMA as an example, it can achieve better than $10''$, or even $1''$, and its collecting area is that of roughly a single 40m dish, but it will still have worse sensitivity to surface brightness because it is not a filled aperture. Similarly, the Atacama Large Millimeter/submillimeter Array (ALMA Hills & Beasley 2008) has a total of 66 antennas (54 12-m antennae, and 12 7-m antennas) with the equivalent collecting area of a single 91-m dish. In addition to not being a filled aperture, ALMA will also have a limited maximum recoverable scale: for 100 GHz (Band 3) this is $25''$, and for

150 GHz (Band 4, which is nearly complete), this is 17″. Thus, despite high resolution (between 0.27″ and 7.5″, depending on configuration and observing frequency). Any SZ observations with ALMA would be fundamentally limited to a small portion of a cluster. By comparison, an ideal SZ telescope according to Birkinshaw & Lancaster (2008) would recover signal out to 10′. Therefore, while ALMA will provide incredible new observational capabilities in the millimeter/submillimeter regime, it is not well suited to whole-cluster SZ observations (it was not designed to be), and is not included in Table 1.1.

The Nobeyama Bolometer Array (NOBA Kuno et al. 1993) on the Nobeyama 45-m telescope was a pioneering high resolution instrument on a single dish. With a resolution of 13″, it was able to resolve an enhancement in the well studied cluster RXJ 1347 (Komatsu et al. 2001; Kitayama et al. 2004). While Submillimeter Common User Bolometer Array (SCUBA Holland et al. 1999), on the James Clerk Maxwell Telescope (JCMT) also observed the cluster, the 350 GHz data had a noise of 5.3 mJy/beam (FWHM = 15″), compared to the 1.6 mJy/beam noise achieved by NOBA. There have been a number of subsequent SZ instruments which have achieved comparable sensitivity and resolution. A few notable instruments are MUSTANG, NIKA, and AzTEC. MUSTANG (and its current successor MUSTANG-1.5) operates at 90 GHz on the GBT with a resolution of 9″, and was able to unambiguously confirm (Mason et al. 2010) the shock heating interpretation of RXJ 1347 (Kitayama et al. 2004). NIKA operates at 140 and 240 GHz on the IRAM-30m with resolution of 18.5″ and 12.5″, respectively, and AzTEC operates at 270 GHz on the LMT with a resolution of 6″.

It is in the context of the utility, and to a certain extent, necessity of a high resolution SZ instrument that my thesis takes shape. MUSTANG establishes a significant

progression towards this need and has shown the value of sensitive, high resolution SZ measurements (Mason et al. 2010; Korngut et al. 2011; Mroczkowski et al. 2012).

1.2 Scientific Background

Current motivations for studying galaxy clusters via the Sunyaev-Zel'dovich effect generally fall under two categories: cosmology or astrophysical processes, although astrophysical processes have been a recent addition with the advent of sub-arcminute resolution SZ instruments. Cosmological parameters affecting the growth of structure (e.g. Bahcall & Fan 1998) can be constrained by galaxy clusters, and are complimentary to constraints of those parameters from other methods, including measurements of the primary and other secondary anisotropies the cosmic microwave background (CMB), large scale structure (LSS), supernovae, baryon acoustic oscillations (BAOs), and strong and weak gravitational lensing. As surveys have detected more galaxy clusters in the optical (e.g. Koester et al. 2007), X-ray (e.g. Burenin et al. 2007), and with Sunyaev-Zel'dovich measurements (e.g. Sehgal et al. 2011; Bleem et al. 2015; Planck Collaboration et al. 2015), cosmological parameters derived from their counts have improved (e.g. Sehgal et al. 2011; Vikhlinin et al. 2009; Mantz et al. 2010; Böhringer et al. 2014), and are placing meaningful constraints on cosmological parameters, especially in conjunction with the other methods listed.

Because the SZ effect is not sensitive to redshift, it will play a crucial role in finding and observing galaxy clusters at high redshift, where galaxy cluster counts are highly sensitive to the underlying cosmology (Carlstrom et al. 2002). As seen in Figure 1.1, which assumes a wide field SZ survey instrument, the mass limit does not change much above $z \sim 0.5$. The slight improvement seen in Figure 1.1 with redshift is due to the angular size of clusters decreasing, thus enhancing surface brightness.

Furthermore, the signal will be well contained in the field of view of a wide field SZ survey instrument.

The thermal SZ (tSZ) effect, due inverse Compton scattering of CMB photons off of the hot thermal distribution of electrons in the ICM, is proportional to integrated pressure along the line of sight. The distortion is given by

$$\frac{\Delta I_{SZ,\nu}}{I_{CMB,\nu}} = g(x) \times y, \tag{1.1}$$

where $g(x) = \frac{x^4 e^x}{(e^x-1)^2}(x\frac{e^x+1}{e^x-1} - 4)[1 + \delta_{SZ}(x, T_e)]$, $x = h\nu/(k_B T)$, and the dimensionless parameter y is given by:

$$y = \frac{\sigma_T}{m_e c^2} \int n_e(\mathbf{r}) k_B T_e(\mathbf{r}) dl, \tag{1.2}$$

where σ_T is the Thomson scattering cross-section of the electron, m_e is the mass of the electron, n_e is the electron density, k_B is the Boltzmann constant, and T_e is the electron temperature. At frequencies below $\sim$ 220 GHz the tSZ appears as a decrement, and above that frequency, the tSZ appears as an increment. As the temperature of gas increases beyond $\sim$ 5keV, relativistic corrections (Itoh et al. 1998) need to be considered. Relativistic corrections will tend to move the null towards higher frequencies and decrease the amplitude of the distortion. While the distortion from the tSZ is small, typically less than 1 mK, it is greater than the distortion due to the kinetic SZ (kSZ) effect, which is a spectral distortion of the CMB due to the Doppler effect from the peculiar motion of the galaxy cluster. In this thesis, unspecified SZ signal is assumed to be dominated by the tSZ signal.

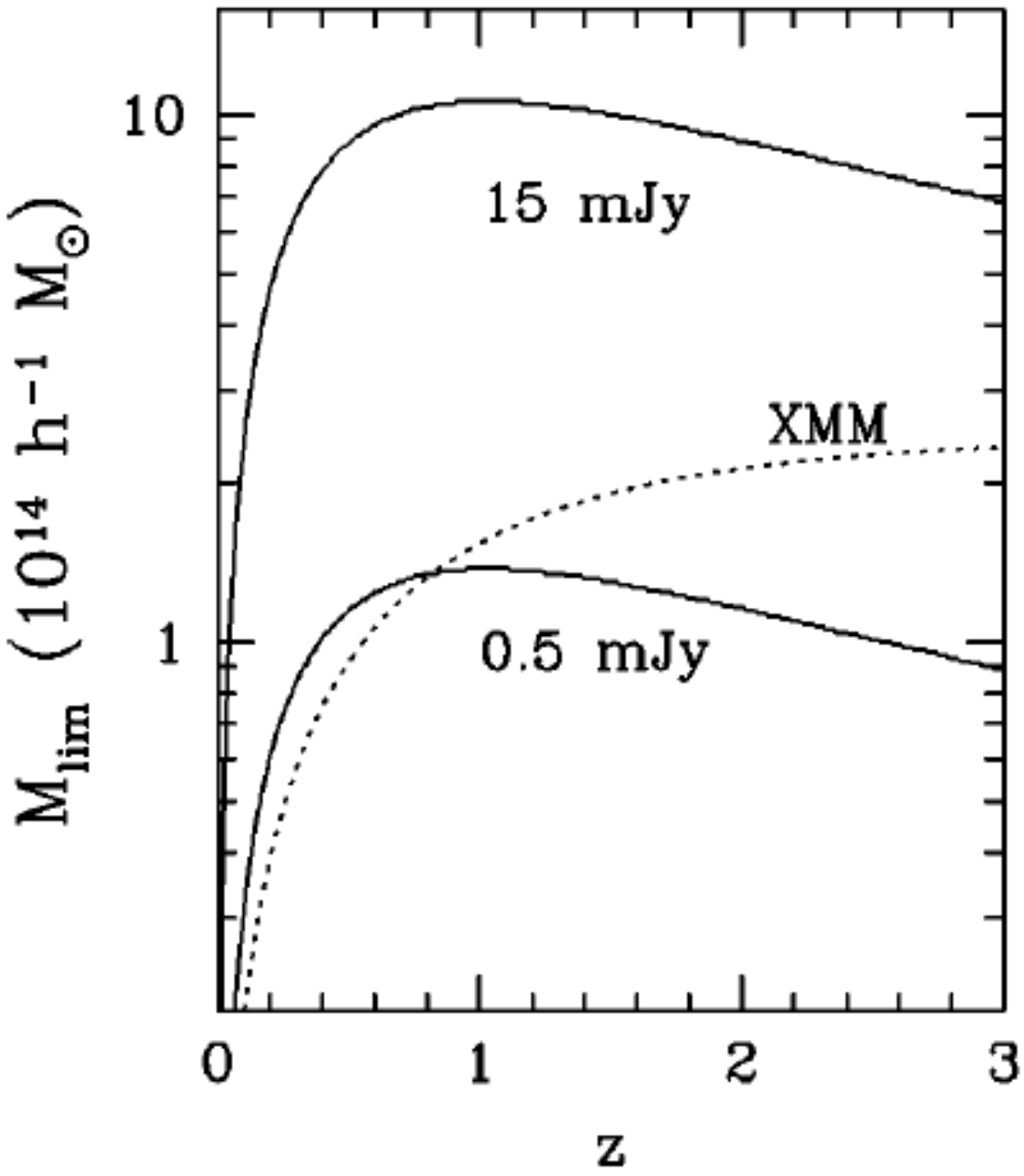

Fig. 1.1.— Copied from Carlstrom et al. (2002). The solid lines show the typical limits of a wide-field SZ survey at 30 GHz with two different survey sensitivities, with an approximate limit for XMM-Newton as the dotted line.

1.2.1 SZ Scaling Relations

There is a simple, intuitive connection between the tSZ signal and a cluster's mass: the tSZ signal is directly proportional to integrated pressure along the line of sight, and given hydrostatic equilibrium (HSE), the gradient of the pressure is proportional to the gradient of the gravitational potential, which is related to a cluster's mass. However, the assumption of HSE introduces systematic errors given the inevitable departure of clusters from HSE (e.g. Nagai et al. 2007). Thus, a more common approach is to use a scaling relation, relating an observable to the total cluster mass. For SZ studies, the observables of choice have been y_{max} or Y, where y_{max} is the maximum Compton y value in a map of a cluster, and integrated Compton Y is given by $Y \equiv \int_\Omega y d\Omega$, where Ω is the angular extent (solid angle) of the cluster. When the extent of the cluster can be determined, Y is preferable as it exhibits a tighter correlation with cluster mass than does y_{max} (e.g. Reid & Spergel 2006). An X-ray analog to Y can also be defined as: $Y_x = M_{gas}T_x$ where M_{gas} is the mass of gas within a given radius, and T_x is the temperature with that radius, but excluding the core of the cluster. The motivation for excluding the core are discussed below. This is not to say that the Y-M relation is without scatter; simulations show that Y will be briefly boosted in merging clusters (e.g. Wik et al. 2008) and internal physics such as AGN feedback (e.g. Battaglia et al. 2012). Battaglia et al. (2012) note that sorting clusters into subsamples based on ellipticities can reduce the scatter in the scaling relation, where this introduces a bias in the normalizations of a few percent.

Some recent observationally determined Y-M scaling relations of note come from the REXCESS X-ray sample (Arnaud et al. 2010), ACT [(Marriage et al. 2011), the Planck satellite (Planck Collaboration et al. 2011), and the Bolocam X-ray SZ (BOXSZ) sample (Czakon et al. 2014). The scaling relations can see several variations.

The total mass, M, is generally defined as the spherically enclosed mass at a particular radius, where common choices are R_{200}, R_{500}, or R_{2500}, which are defined as the radius at which the average enclosed mass density is 200, 500, and 2500 times the critical density of the universe at the redshift of the cluster, $\rho_c(z)$. The radii scale roughly such that $10R_{2500} \sim 3R_{500} \sim R_{200} \sim R_{vir}$ at $z = 0$, where R_{vir} is the virial radius for the cluster. If growth of structure proceeds in a linear manner then the growth can be shown to be self-similar (e.g. Press & Schechter 1974; Kaiser 1986) and the relations between the radii defined by density contrast (i.e. not R_{vir}) should remain constant over redshift, while the values themselves change. The utility of using characteristic radii to define quantities such as Y_{500} is that we should expect a simple, known, self-similar evolution with redshift, such that the scaling relation can be used across redshifts.

Unfortunately, the evolution of galaxy clusters is not necessarily linear (e.g. Kravtsov & Borgani 2012), where mergers are a profound case of the nonlinearity of their evolution. Despite this, models describing linear and mildly nonlinear can describe the evolution of fluctuations with sufficient accuracy (Borgani & Kravtsov 2011). Remarkably, the scaling relations of gas density, temperature, and pressure to total mass agree with self-similar scalings over the range $R_{2500} < r < R_{500}$ (Kravtsov & Borgani 2012). Moreover, the intrinsic scatter of gas density (Vikhlinin 2006; Croston et al. 2008; Maughan et al. 2012; Eckert et al. 2012), temperature (Vikhlinin 2006; Pratt et al. 2007; Leccardi & Molendi 2008), and pressure (Arnaud et al. 2010; Sun et al. 2011) are roughly 10%-40% in this region. Thus, the scaling relations defined on this region do reasonably well at constraining cluster masses (e.g. Arnaud et al. 2010; Andersson et al. 2011).

1.2.2 Substructure in the ICM

Much of the previous discussion of the mass-observable scaling relations focused on the gravitational process of galaxy formation. However, the scatter in ICM observable quantities, for a given mass is dominated by baryonic processes, especially the heating and cooling of the ICM. The dominant source of heating for gas comes from its accretion onto a galaxy cluster (Sarazin 1988), whether by infalling diffuse gas, or by mergers. Simulations (e.g. Pfrommer et al. 2006; Skillman et al. 2008; Vazza et al. 2009) find that much of the kinetic energy of infalling gas is processed through shocks. Specifically, much of the kinetic energy is processed through weak (Mach numbers $M \lesssim 3$) internal (occur within the virial radius) shocks (Skillman et al. 2008). By contrast, external shocks have much larger Mach numbers ($M > 30$). At large radii, the accretion is ongoing, equilibration timescales are long, and thus the pressure support is dominated by kinetic (i.e. non-thermal) pressure. This increase in kinetic support is associated with an increase in substructure (Battaglia et al. 2012), which would only be revealed by instruments with sufficient sensitivity and resolution.

The gas cools primarily from radiative cooling via bremsstrahlung, or free-free, radiation, which has emissivity given by $\Lambda_{ff} g_\nu n_e^2 T^{0.5}$ (Sarazin 1988), where Λ_{ff} is the cooling function, and g_ν is the Gaunt factor, and T is the temperature of the plasma (ICM). Thus, cooling timescales will be drastically shorter where the density is higher. In the cores of a substantial fraction of clusters, the cooling times are of order, or shorter, than the Hubble time, and without additional heating a cooling flow (e.g. Fabian 1994) will form, where gas should cool onto a central dominant (cD) galaxy. Such clusters are denoted as cool core clusters, and are generally relaxed clusters. In the absences of heating, this would require inflow of gas throughout the ICM, however soft X-ray spectroscopy does not support this case (Cavagnolo et al.

2009, and references therein), giving rise to the *cooling flow problem*.

The leading mechanism is thought to be AGN feedback, which causes so called X-ray cavities (e.g. McNamara & Nulsen 2007). AGN feedback is a promising mechanism for heating the ICM in cool core clusters as the total energy injected by AGN jets is comparable to the energy needed to offset the cooling flow as calculated by X-ray luminosity, and bring it into agreement with observed flows (McNamara & Nulsen 2007). Unfortunately, it's not clear how that energy can effectively be distributed throughout the core region (McNamara & Nulsen 2007). Phenomena associated with AGN feedback, such as ripples and sound waves (e.g. Fabian et al. 2006) and sloshing (e.g. ZuHone et al. 2010) could contribute heating and transport, but do not appear sufficient in themselves. Instabilities such as magnetothermal instability (MTI) (e.g. Balbus 2000), heat flux driven buoyancy instability (HBI) (Quataert 2008), and Richtmyer-Meshkov instability (RMI) (Friedman et al. 2012), which would result in turbulent transport of energy, are promising energy transport mechanisms.

Relaxed cluster physics

Determining a cluster's dynamical state is an essential step towards understanding the relevant physical processes within clusters. Dynamical states can be determined from SZ effect, optical, or X-ray observations, although they don't necessarily agree due to their differing dependencies (sensitivities) on physical quantities. For instance, several Cluster Lensing And Supernovae with Hubble (CLASH) clusters have been identified as relaxed from optical observations, but from X-ray observations are noted as potentially disturbed (Postman et al. 2012). To the same extent, recent observations of MACSJ0744.9+3927 reveal evidence for a shock in the SZ effect, which the X-ray observations did not readily reveal (Korngut et al. 2011). With the knowledge

of the SZ observations, the X-ray data are consistent with the shock seen in the SZ effect.

If we can assume a cluster is in hydrostatic equilibrium (HSE), i.e. the cluster is dynamically relaxed, and we can determine the pressure profile, we can calculate the total mass. Our fundamental equations are the equation of hydrostatic equilibrium, the continuity equation, and the ideal gas law, which holds as long as relativistic effects can be neglected. In the past, it was common to assume isothermal beta models (e.g. Reiprich & Böhringer 2002) for density distributions; where temperature profiles were not well constrained, this allowed for an easy way to calculate the mass of a cluster, while giving a reasonable description of the X-ray derived pressure profile. Recent works tend to use NFW profiles for the total density, which come from cosmological simulations of dark matter (Navarro et al. 1997), and a generalized NFW profile (e.g. Nagai et al. 2007; Arnaud et al. 2010) for a pressure profile as a function of scaled radius, $x = r/R_{500}$.

$$P(x) = \frac{P_0}{(c_{500}x)^{\gamma}[1 + (c_{500}x)^{\alpha}]^{(\beta-\gamma)/\alpha}} \tag{1.3}$$

Here, $c_{500} = r_s/R_{500}$, P_0 is a normalization, and r_s is the scaling radius for the NFW profile. A relatively new method (Mroczkowski 2011, 2012) for calculating the mass assumes an NFW profile for the total density, and that the $f_{gas}(r)$ is constant with radius. By invoking the virial theorem, he finds

$$\frac{(1+1/\mu_e)}{16\pi^2 G f_{gas}}[3\frac{m_e c^2}{\sigma_T}Y_{sph}(r) - 4\pi r^3 P_e(r)] = (\rho_0 R_s^2)^2[-\frac{R_s}{2(1+R_s/r)^2} + \int_0^r \frac{\ln(1+r'/R_s)}{(1+r'/R_s)^2}dr], \tag{1.4}$$

where $Y_{sph} \equiv \frac{\sigma_T}{m_e c^2}\int_0^r P_e(r')4\pi r'^2 dr'$, P_e is the electron pressure, R_s is the scaling radius found in the NFW profile, and ρ_0 is the normalization of the density in the NFW profile. For observationally well determined $Y_{sph}(r)$, one can fit for ρ_0 and R_s,

and with the NFW parameters solved for, one can find $M(r)$ for a galaxy cluster. Because the SZ effect directly measures the integrated electron pressure, it holds a significant advantage over X-ray observations which do not directly measure electron pressure.

A complicating matter is that the distribution of gas may not be uniform; that is, μ_e or μ will be functions of position (to first order, a function of radius) within a galaxy cluster. Currently these are taken to be uniform, despite the prediction that helium might sediment to the cluster core (Fabian & Pringle 1977; Gilfanov & Syunyaev 1984). There are currently investigations to detect helium sedimentation (Bulbul, private communication) with X-ray (Chandra) and SZ measurements (SZA and MUSTANG). One encouraging study finds suggestive evidence for helium sedimentation from the ultraviolet upturn in brightest cluster galaxies (BCGs) (Peng & Nagai 2009).

Determining pressure profiles of clusters provides insight into the regularity of relevant physical phenomena. That is, if the pressure profiles exhibit large cluster-to-cluster scatter at certain radial ranges, we can infer the physical processes at play in those ranges differ significantly. Such analyses have been done (e.g. Cavagnolo et al. 2009; Arnaud et al. 2010). An SZ study of ICM at all scales of interest will provide direct access to the pressure profiles. In particular, high resolution SZ studies of the ICM allow comparison to X-rays at scales of interest for understanding processes within the core, as well as outside the core where high resolution can detect substructure.

Merging cluster physics

There is evidence that the scatter in scaling relations is relatively independent of dynamical state and detailed cluster physics (e.g da Silva 2004; Nagai 2006; Wik et al. 2008). Nonetheless, because our calculations of mass often depend on the assumption of HSE, any departure from HSE should be taken into account. With hierarchical formation, galaxy clusters are continually growing, whether it be by filamentary accretion or cluster mergers.

Thus it is inevitable that mergers will need to be studied, seeing that they provide the opportunity to study exciting and sometimes unforeseen physics (e.g. cold fronts, c.f. Markevitch & Vikhlinin 2007). Likely the most famous case is the "Bullet Cluster", 1E 0657-56, which shows a classic bow shock (Markevitch et al. 2002) and the separate locations of baryonic and dark matter (Markevitch et al. 2004). X-ray data on the gas allowed Markevitch et al. (2002) to calculate the Mach number (2-3) and shock velocity (3000 - 4000 km s^{-1}) using Rankine-Hugoniot jump conditions [see Landau & Lifshitz (1959) for a review]. These conditions are assume thermal equilibrium within the pre and post shock plasma (e.g. $T_{ions} = T_e$), which may not necessarily hold. It is of interest then to try to determine any departure from equipartition, and compare the expected heating in the case of non-equipartition (e.g. Markevitch & Vikhlinin 2007; Wong et al. 2010). This has been calculated in at least two cases where the geometry has been favorable: in 1E 0657-56 and Abell 2146, where collisional heating was slightly preferred in Abell 2146 Russell et al. (2012), and instant equilibration was favored in 1E 0657-56 (Markevitch & Vikhlinin 2007).

Recent SZ observations have also detected the kSZ signal over an ensemble of clusters (Hand et al. 2012) and in a single cluster (Sayers et al. 2013). The kSZ detection in a single cluster undergoing a triple merger, is found towards one of the subclus-

ters traveling at a velocity of roughly 3000 km/s and was observed with Bolocam, a bolometer array on the Caltech Submillimeter Observatory (CSO). Bolocam is able to observe at 140 GHz and 268 GHz, with resolution of 58″ and 31″ respectively and a field of view (FOV) of 8′ (Glenn et al. 2002). While multi band SZ observations are required to disentangle the tSZ signal from the kSZ signal, MUSTANG showed a distinct (separate) decrement coincident with the subcluster with large radial motion (Mroczkowski et al. 2012), which is consistent with the scenario suggested in Mroczkowski et al. (2012); Sayers et al. (2013).

1.3 Scope of my Thesis

1.3.1 What MUSTANG has to contribute

The MUltiplexed SQUID/TES Array at Ninety Gigahertz (MUSTANG) is an 8x8 continuum bolometer array at the Gregorian focus of the 100m Green Bank Telescope (GBT). Its angular resolution at 90 GHz is 9" (FWHM) with an instantaneous field of view (FOV) of 42", with a mapping speed equivalent to mapping a 3' x 3' region to an RMS noise of 0.4 mJy in an hour (Dicker et al. 2008). MUSTANG's sensitivity and angular resolution make it ideal for high resolution SZ studies, although it can be used to study synchrotron and thermal emission as well. SZ observations with MUSTANG are done by scanning over the sky; a variety of scan patterns have been employed, but scanning in a Lissajous daisy has been the preferred pattern.

Observations of galaxy clusters to date with MUSTANG have been promising (Korngut et al. 2011; Mason et al. 2010; Mroczkowski et al. 2012). Due to the fact that SZ observations with a single dish are differencing measurements, a limiting aspect of MUSTANG is the FOV leads to a spatial transfer function that drops

dramatically at scales larger than the FOV (Korngut et al. 2011; Mason et al. 2010). Nonetheless, its ability to resolve substructure has allowed MUSTANG to detect shocks in MACSJ0744 and RXJ1347 and asymmetries in Abell 1835 and CLJ1226 (Korngut et al. 2011; Mason et al. 2010).

To reiterate, MUSTANG excels at observing substructure in galaxy clusters. Thus, it will be a great tool for any cluster we observe that has a shock in it. It may also be able to detect AGN cavities. For determination of pressure profiles, it will be able to constrain the inner profile well, but will not be able to constrain the outer profile.

1.3.2 Thesis Overview

Well constrained pressure profiles in clusters will advance precision cosmology and our understanding of physical processes in the ICM. To determine pressure profiles, we jointly fit MUSTANG and Bolocam data, thus covering angular scales between 9" and 8′, which covers roughly out to R_{500}. The joint fitting procedure was developed and provides robust results constraining the pressure profile of galaxy clusters.

Chapter 2 discusses how SZ observations are made, including how the receivers work, and what processing must be done to the data to determine the astronomical signal of interest. Chapter 3 highlights my investigations into transmission properties of potential window and radome materials for the successor to MUSTANG. Chapters 4 discusses the joint fitting procedure, determination of pressure profiles for a sample of galaxy clusters, and Chapter 5 investigates quantitative constraints on cluster geometry, ICM temperature, and helium sedimentation with the inclusion of X-ray data. In Chapter 6, I discuss shocks as seen in the SZ and how we can model them, especially if they are in the plane of the sky.

Chapter 2

SZ Observations

Abstract

The manner in which galaxy clusters are observed via the SZ effect impacts the quality of data. We discuss the development of instruments (bolometers in particular) and SZ observational techniques, especially with regard to Bolocam and MUSTANG. In order to understand our observations fully, we need to know the beam for MUSTANG accurately. We determine this beam, its variations, finding that a one-dimensional double Gaussian fits the beam profile well. We also investigate potential factors of MUSTANG data quality, and find that the flagging data is a primary factor in the noise in the final MUSTANG maps.

2.1 Introduction

As indicated in the condensed historical background in Section 1.1, the progression of SZ observations was largely due to detector technology development. This development has also changed the manner in which SZ observations are conducted, especially

for single dish telescopes.

To start, we have the intensity or rather, change in intensity, in the astronomical signal from Equation 1.1. The total intensity [W·sr^{-1}·m^{-2}·Hz^{-1}] to be received by a telescope is then:

$$I_{r,\nu} = (I_{\nu,CMB} + \Delta I_{\nu,SZ})(e^{-\tau_\nu}) + S_\nu(1 - e^{-\tau_\nu}), \tag{2.1}$$

where S_ν is the source function for the Earth's atmosphere, which can roughly be taken as a blackbody function (B_ν) at ~ 300 K. At the best telescope sites, we might expect to achieve $\tau_\nu \sim 0.03$ at 90 GHz (see Appendix Appendix B.1 for more information), which would cause the atmospheric signal to have a brightness temperature of 9 K, which is not much greater than the CMB signal itself. However, the SZ signal is roughly a factor of Compton y smaller than the CMB signal (see Equation 1.1), and a typical value for the peak Compton y for massive clusters is 10^{-5}. At 90 GHz $g(x) \sim 3$, such that $y = 10^{-5}$ will translate to a surface brightness temperature (decrement) of 9×10^{-5} K. Thus, the atmospheric and CMB signals must be removed very precisely to recover the SZ signal.

SZ observations of galaxy clusters are further complicated by contaminants such as radio or sub-millimeter galaxies. Radio galaxies emit via synchrotron and thus are fainter at higher frequencies. Fortunately, at the peak of the SZ decrement (roughly 150 GHz), radio sources are not particularly luminous and are not seen to be a large source of contamination (e.g. Sehgal et al. 2011). Sub-millimeter galaxies are dusty, star forming galaxies at high redshift (most are within the redshift range $1 < z < 3$, but have the potential to be at even larger redshifts), and have an increased chance of being detected when observing galaxy clusters due to gravitational lensing. If the spectrum is reasonably well known, then observations at 220 GHz (at the null in the

tSZ) can be used to subtract the expected contamination at other frequencies (e.g. Lueker et al. 2010).

Another potential source of contamination is more prevalent at larger scales: the primary anisotropy of the CMB itself (e.g. Udomprasert et al. 2004). However, this is not expected to contribute on scales less than a few arcminutes (e.g. Hu & White 1997). Moreover, at smaller scales, the CMB primary anisotropy will only diminish: the tSZ signal dominates over the primary CMB at $\ell \geq 3000$, or scales $\lesssim 3.5'$ (e.g. Birkinshaw 1999). This does depend on the observing frequency, and only recently are we starting to empirically constrain the SZ power spectrum with ACT and SPT. The latest numbers (e.g. George et al. 2015) show that $\ell = 3000$ is still appropriate for this transition at least at 90 GHz. At 150 GHz, the SZ power spectrum dominates over the primary CMB closer to $\ell = 4000$. Yet one more consideration is that the Cosmic Infrared Background (CIB), which is dominated by dusty star forming galaxies (DSFGs), has an order of magnitude *less* power than the SZ power at 90 GHz, but is roughly an order of magnitude *greater* than the SZ power spectrum at 150 GHz. Of course, the CIB would manifest itself with positive distortions, so it is clearly not mistaken for an SZ signal where the SZ signal is a decrement relative to the CMB. Fortunately, by targeting known massive clusters, the tSZ signal we observe is well above the statistical SZ background over the entire sky, which is dominated by much less massive clusters.

Thus as far as contaminants are concerned, the CMB is not a concern for high resolution SZ studies. Other (non-CMB) contaminants may still be a concern, but they can readily and confidently be identified by high resolution, multi-wavelength SZ observations, allowing for accurate determination of the tSZ. Moreover, separation of the kSZ allows for investigations into galaxy cluster formation and galaxy evolution

(via observations of DSFGs).

2.2 Observing with a Single Dish

With single dish observations, the basic strategy is to observe the galaxy cluster and then observe a nearby region that does not include the galaxy cluster. The strategy will allow the primary CMB and atmospheric signal to be subtracted. Provided that the off-source region is fairly close to the galaxy cluster, then the atmospheric signal should be effectively the same.

There are three basic strategies for removing extra signals: (1) position switching (PS), (2) beam switching (BS), and (3) on-the-fly (OTF) observing, which is sometimes referred to as driven scan. PS simply points the telescope on and off target. BS either moves the sub/secondary reflector of a telescope, or differences signal between two feeds (which observe different directions on the sky). Finally, OTF mapping can either be a driven scan (with a particular telescope trajectory) or drift scan, such that the signal is read out at a rapid rate: at least fast enough to recover astronomical signal on scales which they are expected to change. The Nyquist criterion states that the sampling rate must be at least twice that at which you expect the signal to change. We can write the sampling rate, τ_{samp}, as $\tau_{samp} = \theta/(2v_{scan})$ where θ is the angular extent of smallest expected astronomical signal, and v_{scan} is the scan speed (e.g. arcmin s^{-1}). Both τ_{samp} and v_{scan} can be tuned at the outset, with limitations from electronics and telescope slew speed. Most observers only have control over the scan speed.

In any of these cases, observing an off-source location that is offset in azimuth is a standard choice as this should keep the atmospheric opacity and ground spillover roughly constant. Over the course of a night, the offset beam sweeps out arcs (in

right ascension and declination). In the driven scan case, an off-source location is not always observed, especially if the receiver has multiple feeds or detectors. That is, some of the detectors will either be viewing an off-source location, or sufficiently off source location that its received signal can be used to subtract atmospheric and CMB signal. If the atmospheric signal is sufficiently dominant, then some averaging of the detectors can be used for subtracting the atmospheric signal.

2.3 Instruments

2.3.1 Bolometer primer

A bolometer allows the power of incident radiation to be measured via a change in its electrical resistance due to the radiation heating the bolometer. The first bolometer was developed by Langley (1881), where a Wheatstone bridge was used to determine the resistance of one thermal varying resistor, composed of two strips of metal, where one strip is exposed to radiation. A major utility of the bolometer is that the responsivity dependence on temperature can be large and well studied for many materials.

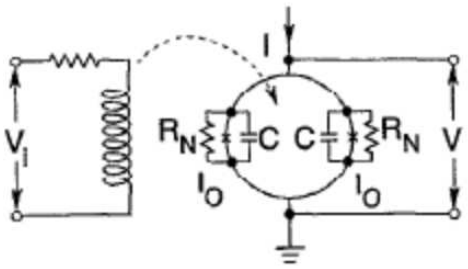

Fig. 2.1.— From Richards (1994), a circuit diagram of a SQUID. The SQUID is a loop with two Josephson junctions which are each shunted by a resistor and capacitor. The capacitor represents the self capacitance of the junction.

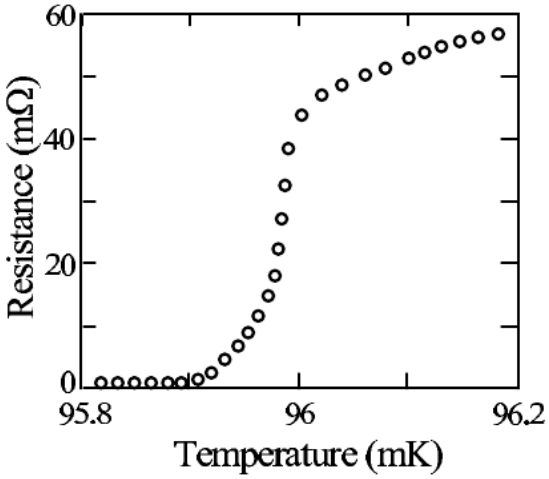

Fig. 2.2.— From Irwin & Hilton (2005); resistivity vs. temperature for a Mo/Cu proximity bilayer TES. The transition close to 96 mK would, where the slope is steepest would be desirable for measuring small changes in temperature (i.e. received radiation.)

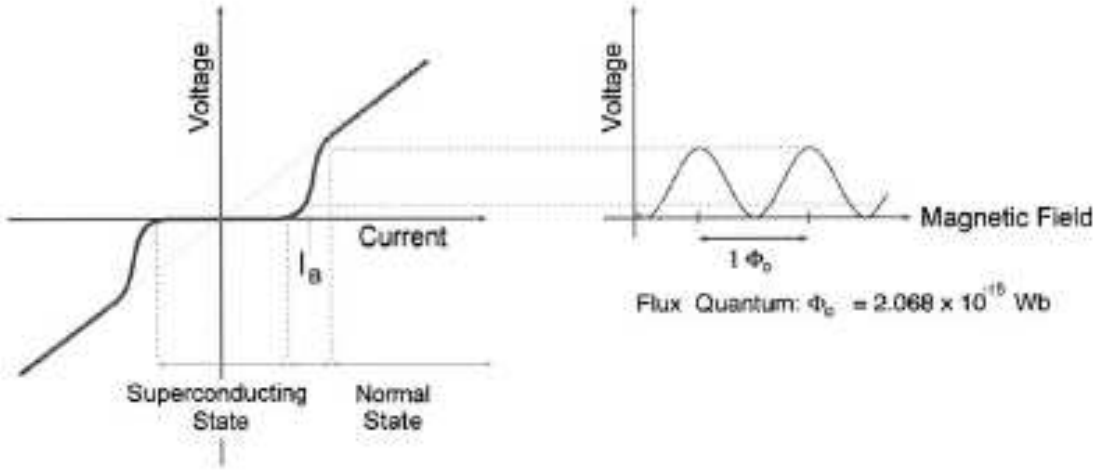

Fig. 2.3.— From Fagaly (2006), just as the TES has a sharp transition (Figure 2.2) with resistance and temperature, so too the SQUID (left) has a sharp transition with voltage and current. It is thus desirable to bias the SQUID to I_B, roughly in the middle of the steep transition. The corresponding relation between magnetic flux through the SQUID and voltage is shown on the right.

Today there are many means of measuring incident radiation, and bolometers have recently become the preferred detectors for infrared and millimeter/submillimeter observations in some situations. A significant advance in bolometer sensitivity came with the advent of the transition edge sensor (TES), where the bolometer is held at the superconducting transition temperature, T_C, which has a steep change in resistivity with change in temperature as shown in Figure 2.2. Additionally, by reaching superconducting temperatures, this allows the use of Superconducting QUantum Interference Devices (SQUIDs, see Figure 2.1) as amplifiers, which often have T_C at or above the operating temperature of most bolometers. A bolometer typically consists of two distinct components, one that absorbs the incident radiation, and a temperature sensing element (such as, here, a TES). As Figure 2.5 shows, these need not be spatially coincident as long as the thermal coupling being the absorbing material and TES is strong.

Signal From One Detector

For a TES, the change in electrical resistance is the effect of our incident radiation. Thus, we may either seek to observe a change in voltage, if we have a constant (bias) current, or vice versa (observe a change in current given a fixed voltage). Given that $P = I^2R$ or $P = V^2/R$, we see that for a fixed current, if the resistance of the TES increase, the power dissipation increases, which would lead to an increase in the temperature of the TES and thus a thermal runaway. We may avoid this by biasing the TES with a constant voltage, which then decreases the power dissipation with increasing resistance, and thus will be thermally stable (given no other complications).

To measure the current, which we are fundamentally concerned with, it is common to add an inductor in series with the TES and couple the inductor to the SQUID.

Given that the steep linear regime for a SQUID is narrow, it is crucial to keep the current within the transition region (Figure 2.3, left hand side). Therefore, the bias current, I_B is set slightly above the critical current, I_0, where below I_0, no voltage difference is observed. However, SQUIDs are dependent on the the magnetic flux through the loop, Φ, owing to the requirement that trapped flux be quantized in units of $\Phi_0 = h/2e = 2.07 \times 10^{-15}$ Wb. The V-Φ response is shown in Figure 2.3, on the right hand side, for a current-biased SQUID. Again, keeping with the game of finding the steepest slopes, the flux through the SQUID should be biased ("locked") at $\Phi_0/4 + n\Phi_0/2$, where n is an integer. These steps then allow for a maximal change in voltage readout per change in TES signal. Yet one more concern may be evident. If the signal from the TES is strong enough ($\Delta\Phi \gtrsim \Phi_0/4$), then our voltage readout will no longer be linear with our signal. To solve this, a feedback signal may be sent to a feedback coil (i.e. inductor, just like that from the TES). Generally, this signal is created from electronics outside the cryogenic (superconducting) region.

Another consideration with maximizing the signal recovered is the readout rate. One must consider the timescale on which the observed signal is expected to change, and the rate at which the bolometer dissipates heat. The former is determined by the beam size and slew speed of the telescope, while the latter (thermal time constant) is determined by the bolometer's heat capacity divided by the thermal conductivity. The bolometer will actually have a faster response rate than the thermal time constant because the a change in the temperature of the TES results in a strong negative feedback in dissipated electrical power through the TES. It is crucial to sample the data much faster than the electrothermal time constant, which for MUSTANG is $\sim$ 0.5ms, or 2 kHz. To be sure that all signals are measured, the sampling rate is greater than the Nyquist sampling rate (twice the rate of interest); specifically, a

readout rate of 5.5 kHz is used (primarily for use with the feedback loop). This is faster than the astronomical signal will change, so data is coadded down to 500 Hz to be saved to disc.

Multiplexing with SQUIDs

At this point, the signal for a single detector (one TES, coupled to one SQUID) would be ready to be passed to warmer electronics. However, any wire flowing from the cryogenic region to the warmer electronics will also allow conduction of heat into the cryogenic region. Thus, to maintain an array of superconducting detectors, one wants to send multiple signals along a single wire, i.e. multiplex the signal. There are two modes of multiplexing: time domain multiplexing (TDM) and frequency domain multiplexing (FDM). A time domain multiplexer sequentially reads (combines) the signal from the N detectors along the wire. N is generally limited by the readout rate of the multiplexer chip itself. MUSTANG uses TDM and has eight detectors (and one dark channel) on each multiplexer chip, and eight multiplexing chips and has a second stage of SQUID amplifiers (Figure 2.4). Each multiplexing chip could read up to 32 detectors. Pushing beyond 32 detectors along a chip with TDM becomes quite challenging with TDM, but FDM in principle will allow many more detectors along a wire.

The alternative approach, FDM relies on assigning each detector a resonant frequency. Such a frequency is established by effectively making an RLC (resistor-inductor-capacitor) circuit. To implement FDM, each SQUID must be used to change the resonant frequency for its associated bolometer. To do this, a radio frequency (rf) SQUID is used. An rf SQUID differs in that it only has one Josephson junction, and in the case of MUSTANG-1.5 (discussed more in Section 2.3.4), it has an inductor so

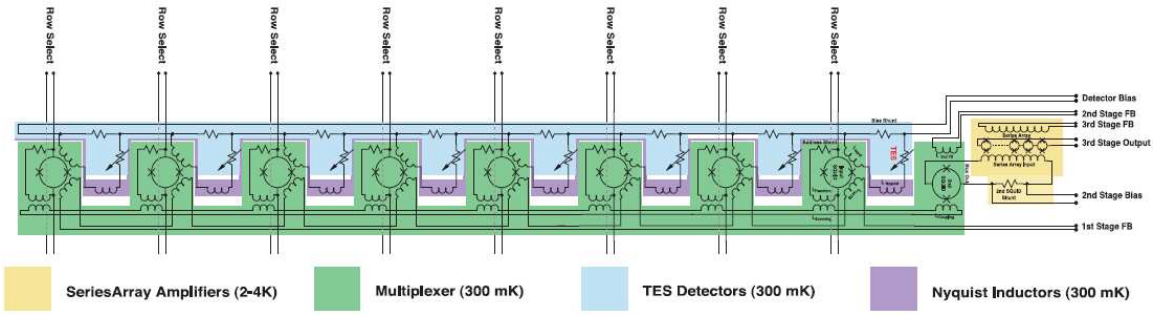

Fig. 2.4.— MUSTANG SQUID multiplexing schematic; from MUSTANG documentation: Dominic Benford.

that it may couple to the microwave resonators for each bolometer readout, as shown in Figure 2.5. Each TES and SQUID pair is coupled to a microwave resonator with a different resonant frequency (per readout wire). The signal from the TES and SQUID pair may then be measured as a slight shift in resonant amplitude and/or phase.

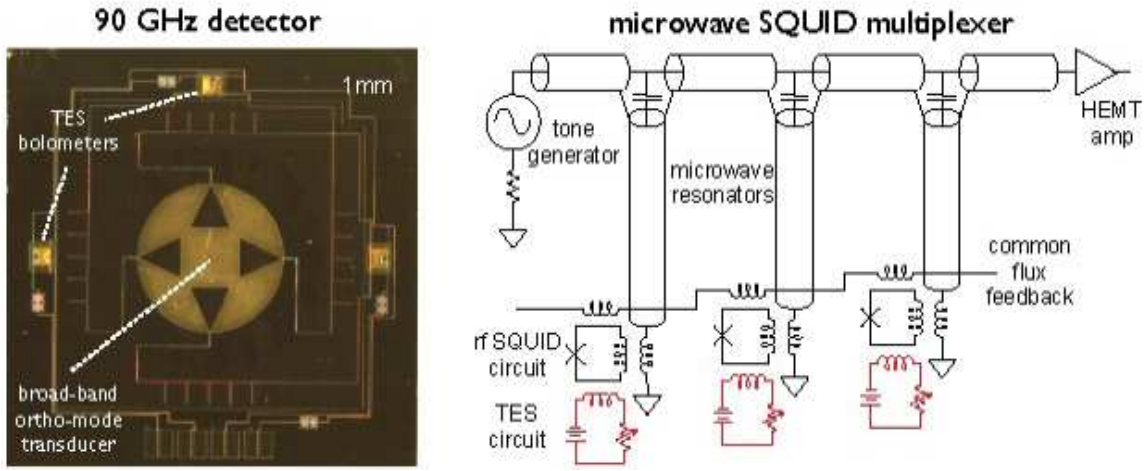

Fig. 2.5.— From Dicker et al. (2014a). The orthomode transducers (OMTs) absorb the incident radiation and transfer thermal energy to the TESs. The OMTs allow for dual polarization measurements, and the coupling with the radiation is strengthened by placing the OMTs a quarter wavelength from a backshort.

2.3.2 CSO and Bolocam

The Caltech Submillimeter Observatory (CSO) is a 10.4 m diameter telescope on top of Mauna Kea in Hawaii. It is located at 4140 m in altitude, and has an active surface adjustment that allows the CSO to achieve 13 μm RMS in surface accuracy. With a median zenith precipitable water vapor (PWV) of 2 mm, the CSO is able to observe at frequencies up to 860 GHz (350 μm)[1]. Bolocam can observe at two frequencies: 140 GHz and 260 GHz, depending on the bandpass (filter) chosen. The 140 GHz channel has been used more than 260 GHz. At 140 GHz Bolocam has a resolution of $58''$. Bolocam has a circular FOV with a diameter of $8'$.

The Bolocam instrument (Glenn et al. 1998; Haig et al. 2004) is a 144 element bolometer array, with 119 working elements. Each bolometer consists of a micromesh absorber coupled to a TES, and is AC voltage biased with a square wave at $\sim$ 400 Hz. The bolometers operate at roughly 300 mK, and are connected to JFET amplifiers (see Figure 2.6) at a 1.2K stage before the signal is passed to the 4.2K and finally 120 K stages. The signal is not multiplexed, so that means that there are many wires (288) between the cryogenic stages, and care had to be taken to reduce thermal loading.

Bolocam Observations and Reduction

The observing strategy adopted by Bolocam is that of a driven scan. In particular, they use a Lissajous pattern designed to provide radially symmetric coverage. A pattern amplitude of $4'$ is used, resulting in a circular coverage out to a radius of roughly $12'$where half of the peak weight (coverage) occurs at a radius of $5'$. The Bolocam maps used in this analysis are $14' \times 14'$.

[1]http://cso.caltech.edu/wiki/cso/telescope/telescope

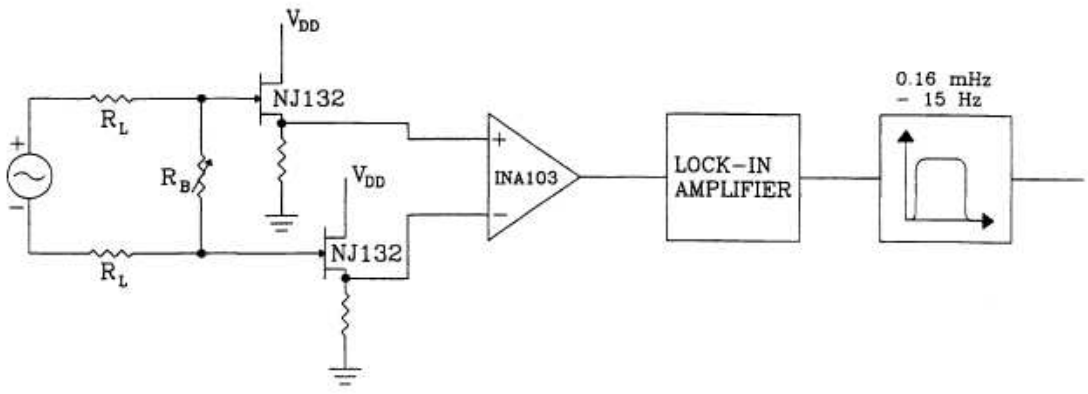

Fig. 2.6.— From Glenn et al. (1998). The JFET NJ132 was a common low-noise amplifier when Bolocam was built, as was INA 103.

The Bolocam data are the same as those used in Czakon et al. (2014) and Sayers et al. (2013); the details of the reduction are given therein, along with Sayers et al. (2011). Bolocam has observed all the clusters used in our pressure profile analysis (Section 4). Two clusters with representative noise performance are Abell 1835 and MACS 0647. Abell 1835 was observed for 14.0 hours resulting in a noise of 16.2 μK_{CMB}-arcminute, and MACS 0647 was observed for 11.4 hours resulting in a noise of 22.0 μK_{CMB}-arcminute, where $K_{CMB} \equiv \frac{T(K)}{T_{CMB}(K)}$. The full sample is tabulated in Table 4.3. Overall, the reduction and calibration is quite similar to that used for MUSTANG, and Bolocam achieves a 5% calibration accuracy and 5″ radial pointing accuracy (1σ).

2.3.3 GBT and MUSTANG

The NRAO Robert C. Byrd Green Bank Telescope (GBT) is a 100 meter radio telescope located in Green Bank, West Virgina. Receivers on the telescope allow for observations between 290 MHz and 92 GHz and an active surface designed to give a surface accuracy of 200 μm RMS across the entire surface, where each panel should

have a surface accuracy of 68 μm (Jewell & Prestage 2004). The surface accuracy has steadily crept towards this limit (Dicker et al. 2008): Nikolic et al. (2007) report an RMS of 390 μm, while improvements by 2009 (Hunter et al. 2011) yielded a surface accuracy of 240 μm.

Both conventional holographic and out-of-focus holographic techniques have been employed to improve the surface accuracy of the GBT. Conventional holography is performed in the Ku-band, making use of the Ku satellite downlink, and has allowed for the development of surface corrections due to gravitational stresses of the telescope. The out-of-focus (OOF) holographic technique described in Nikolic et al. (2007) is designed to measure and correct for thermal gradients in the surface.

The elevation of the Green Bank site is 2800′, or 853 m. While West Virginia is not as arid as many other telescope sites, it does see good weather for observing at high frequencies. In particular, the mode of the precipitable water vapor (PWV) is between 5 and 6 mm during high frequency season (October 1 through May 1)[2].

The MUltiplexing SQUID TES Array at Ninety Gigahertz (MUSTANG Dicker et al. 2006, 2008), is a 64 pixel array of Transition Edge Sensor (TES) bolometers arranged in an 8×8 array located at the Gregorian focus on the 100 m GBT. Operating at 90 GHz (81–99 GHz), MUSTANG has an angular resolution of 9″ and pixel spacing of $0.63 f\lambda$ resulting in a FOV of 42″. MUSTANG is the highest frequency receiver currently on the GBT. The array consists of eight by eight Transition Edge Sensor (TES) bolometers. SQUIDS are used to multiplex the readout. The multiplexing is achieved by time-division: there are 8 channels that read out 8 detectors each, and the detectors along each channel are read out sequentially. These 8 channels, at the first stage, are then summed into one readout line which carries the signal from the cryogenic (superconducting) temperatures of the detector package to room tem-

[2]http://www.gb.nrao.edu/mustang/wx.shtml

perature electronics. The Superconducting Quantum Interference Devices (SQUIDs) are used as amplifiers. Because SQUIDS are interferometers, they have a periodic response, which is often modified by a feedback loop to keep the SQUID at a fixed bias point, which effectively linearizes the response.

Observing with MUSTANG

The bulk of the clusters in my thesis sample, and a significant fraction of the galaxy clusters observed by MUSTANG, are from the Cluster Lensing And Supernova with Hubble (CLASH) sample (Postman et al. 2012). The sample contains 25 massive galaxy clusters that are X-ray and lensing selected. The CLASH sample is further discussed in Section 4.2.4.

Observations consisted of scanning on pointing centers covering the central region of each galaxy cluster. A variety of scan durations ranging between 90 and 300 seconds were employed. Over the seasons of observations, we found that scans lasting 200 to 220 seconds provided the best yields, and accordingly we began to favor scans of this length (see Section 2.4.6). Abell 1835 and early CLASH clusters were observed in the winter/spring of 2009 and 2010 with one central pointing as described in Korngut et al. (2011). For later CLASH clusters (observed 2011-2013), we adopted an observing strategy that consisted of one central pointing, and six off-center pointings, spaced hexagonally such that each was $1'$ from the center, and $1'$ away from the two nearest pointings (Figure 2.7). Using the offset pointings with a Lissajous daisy scan pattern provides more uniform coverage within the central arcminute of our maps than using only one central pointing with Lissajous daisy scans. For each pointing center, the Lissajous daisy has a $3'$ radius. The coverage (weight) drops to 50% of its peak value at a radius of $1.3'$.

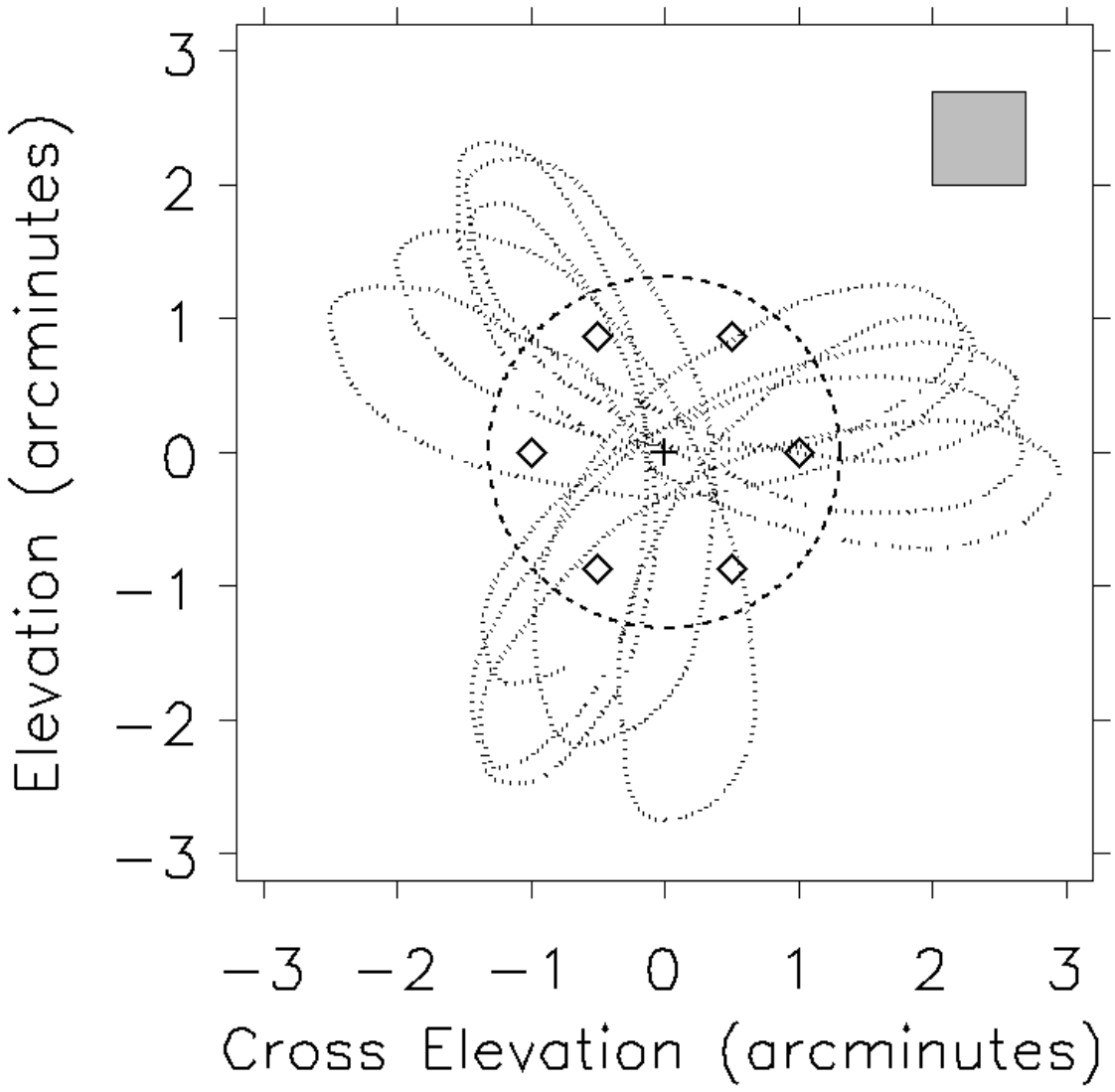

Fig. 2.7.— Dotted line: an example GBT trajectory for a 140 second scan with a Lissajous daisy scan pattern. Three 140 second scans result in complete coverage of a circle with 3′ radius. The plus sign indicates the pointing center used for this daisy scan. The diamonds indicate six offset pointings, used on observations of MACS 0647. The FOV of MUSTANG is shown by the shaded box. The dashed circle encloses 50% of the peak weight over the ensemble of scans for a given cluster.

An absolute flux calibrator (often a planet, see Section 2.4.1) is observed at least once per night. At the start of each night of observing and before observing our

flux calibrators, medium-scale, mostly thermal imperfections in the GBT surface are measured and corrected using out-of-focus (OOF) holographic technique (Nikolic et al. 2007). Interspersed with scans on clusters, we observe nearby compact quasars as secondary calibrators. Secondary calibrators are observed roughly once every 30 minutes, and allow us to track the pointing, beam profile, and gain changes of the telescope. If the the beam ellipticity or gain degrade by more than 10%, another OOF measurement is performed.

2.3.4 MUSTANG-1.5

The successor to MUSTANG, MUSTANG-2 will be a 223 dual-polarization feedhorn array. Each bolometer will be feedhorn coupled and will be packed in a hexagonal pattern with spacing of roughly 2 f-λ at 90 GHz. The instantaneous FOV will be 6 arcminutes, with an increase of sensitivity by roughly a factor of 10.

Collaborators from the University of Pennsylvania, National Institute for Standards of Technology (NIST), Jet Propulsion Laboratory (JPL), and Green Bank are involved in the production of the instrument as currently funded (termed MUSTANG-1.5), which is MUSTANG-2, with 64 (dual polarization) feedhorns. Most of what is being developed for MUSTANG-1.5 will be able to accommodate the full array of 223 detectors. In Chapter 3, we investigate the transmission properties of potential window and radome materials for MUSTANG-2.

MUSTANG-1.5 saw first light in spring 2015. Performance was not as good as expected, but a multiplexer was found to be a primary culprit. The team is working to have MUSTANG-2 as sensitive as expected and complete the array (add the remaining detectors) for the winter of 2015-2016.

2.4 Data Reduction and Procedures

2.4.1 Calibration of data

Absolute flux calibrations are based on the planets Mars, Uranus, Neptune, Saturn, or nebulae. At least one of these flux calibrators was observed at least once per night. Planets are the preferred targets, as they can be calibrated directly to WMAP observations (Weiland et al. 2011), with assumed temperatures of 120 K, 142 K, and 135 K for Uranus, Neptune, and Saturn respectively. Mars' temperature is calculated from Wright (2007), and a correction factor of 0.953 is supplied in Weiland et al. (2011). Betelgeuse can be cross calibrated to these planets and nebulae, and may be used as an absolute calibration itself when no planets or nebulae were observed in a given night. We estimate our calibration is accurate to a 10% RMS uncertainty.

Secondary calibrators are observed roughly every half hour and serve to correct telescope pointing offsets, as well as monitor observing conditions (e.g. beam shape, telescope efficiency). Scans on secondary calibrators precede or follow "Cal and Blank" scans which fire a calibration lamp, chopped with a 0.5 Hz square wave pattern, followed by a blank exposure, which is used to monitor detector responsivity. We calibrate these secondary calibrators from the primary one for that night. Despite streamlining the calibration where possible, there is still the need for manual rejection and ensuring proper application of calibration. The MUSTANG radial pointing accuracy (1σ) is found to be $2''$.

2.4.2 Data Reduction

Processing of MUSTANG data is performed using a custom IDL pipeline. Raw data is recorded as time ordered data (TOD) from each of the 64 detectors. An outline of

the data processing for each scan on a galaxy cluster is given below.

(1) We define a pixel mask from the nearest preceding calibration lamp (CAL) scan; unresponsive detectors are masked out. The CAL scan provides us with unique gains to be applied to each of the responsive detectors.

(2) A common mode template is calculated as the arithmetic mean of the TOD across detectors. The pulse tube used to cool the array produces a coherent 1.411 Hz signal across all detectors. A sinusoid and nearby frequencies are used as a template to fit this signal. The common mode template, pulse tube template, and a polynomial of order N are then simultaneously fit to each detector and then subtracted. The polynomial order is given by $N = t_{scan}/(t_{poly} * 1.25)$, where t_{scan} is the scan duration, $t_{poly} = FOV/\bar{v}$, and $\bar{v}$ is the mean scan speed. This limits the polynomial to filtering scales greater than the FOV, preserving features within the FOV. Subtracting the common mode is powerful at removing atmospheric emission, but has the downside of removing astronomical signals much larger than the instrument FOV. For Abell 1835 ($z = 0.25$), $42''$ corresponds to 166 kpc; for MACS 0647 ($z = 0.59$), $42''$ corresponds to 285 kpc.

(3) After the common mode and polynomial subtraction, each scan undergoes further data quality checks: spike (glitch) rejection, skewness, and Allan variance. We expect our data at this point to contain fairly white (Gaussian) noise, and these quality checks will flag deviations from white noise. Spikes are flagged such that the remaining TOD is still used, while detectors that fail skewness and Allan variance checks are masked for that scan.

(4) Individual detector weights are calculated as $1/\sigma_i^2$, where σ_i is the RMS of the non-flagged TOD for that detector.

(5) Maps are produced by gridding the TOD in $1''$ pixels in Right Ascension

(R.A.) and Declination (Dec). A weight map is produced in addition to the signal map. Unsmoothed signal-to-noise (SNR) maps are produced by dividing the signal map by the inverse square root of the weight map. For smoothed SNR maps, the signal and variance maps are smoothed, and the SNR map is then calculated as the signal map divided by the square root of the variance map.

2.4.3 Noise Maps

Because we are in the small signal limit, we need to understand our noise very well in both the time domain and map (spatial) domain. In the map domain, we can produce noise maps by sending our TOD through the above reduction process and either data-flipping, i.e. reversing, the TOD per scan in the time domain, or by gain-flipping: flipping the sign of the gain between scans. The former works by no longer allowing the signal to be coherently matched to location on the sky, while the latter works by effectively cancelling any signal observed. Thorough analysis has shown better behavior in the gain-flipped maps. For instance, if we make an unsmoothed SNR map from the gain-flipped TOD, we find a mean of 0 with a standard deviation of 1. In both the gain- and time-flipped noise maps (not smoothed), we find that pixel weights (which form a weight map) accurately reflect the RMS of pixel values within a weight bin, and the pixel values follow a Gaussian distribution. However, when determining the RMS noise in our maps, we smooth our flipped noise maps by a $10''$ FWHM Gaussian kernel. While the weight map can be smoothed with the same kernel, the smoothed pixel weights will be biased high by a factor of roughly 2.5 (i.e. imply a pixel RMS value 1.6 times lower than what is found). We correct for this bias by making smoothed SNR maps.

Smoothed SNR maps produced from either of the flipped TOD methods produce

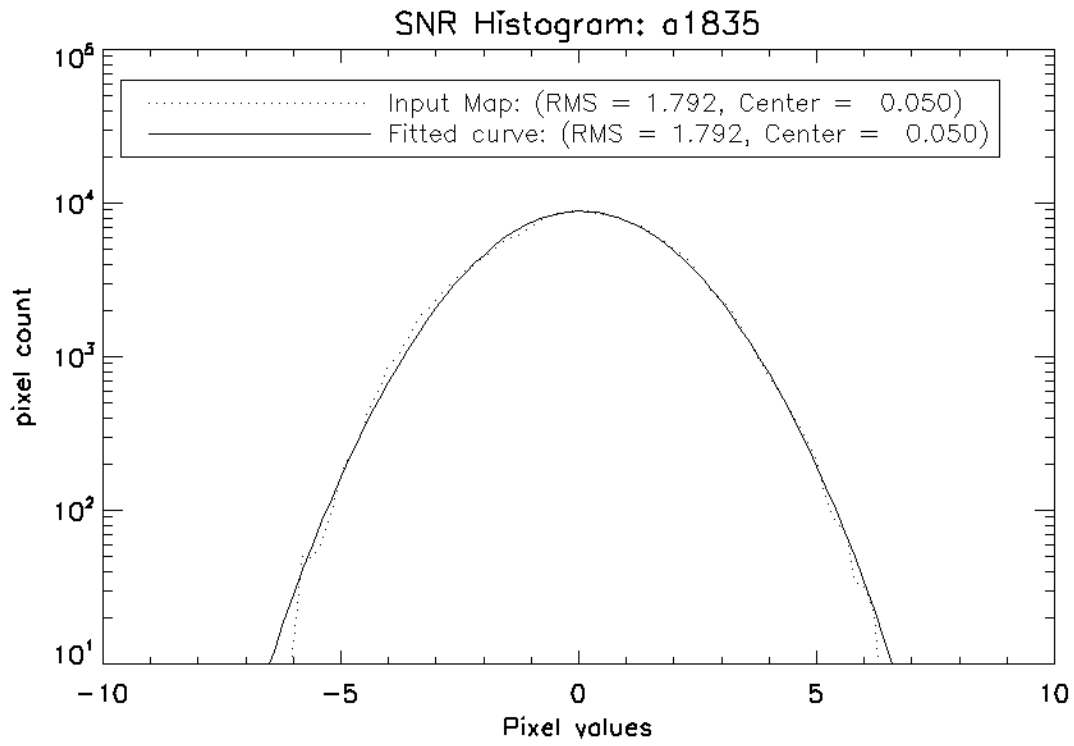

Fig. 2.8.— A histogram of the pixels in an SNR map of Abell 1835. The SNR map was smoothed by a 10″ FWHM Gaussian kernel.

standard deviations greater than 1, as seen in Figure 2.8; the advantage of the gain-flipped smoothed SNR maps is that their means are 0, whereas the time-flipped SNR maps have means that are offset from 0. The standard deviation of our smoothed noise SNR maps (σ_{SNR}) tending towards values greater than 1 indicates our smoothing procedure will bias the weights of each pixel; thus, we use σ_{SNR} to correct our true (not noise) SNR maps. For our canonical smoothing kernel (10″FWHM), $\sigma_{SNR} \sim 1.6$; we then divide the true SNR map by the calculated factor for each cluster. As the model fitting presented in this work makes use of only the non-smoothed maps, this correction factor is only used for visualizing smoothed SNR maps.

2.4.4 Simulating Observations

Given a model map (Section 4) smoothed to the MUSTANG's resolution (convolved with the MUSTANG beam, see Section 2.4.5), we can simulate observations of that model. The means of simulating observations have been through a few iterations, but all incorporate the same filtering to which the raw data are subjected. A model map is filtered by converting the model map into model TOD, using the true TOD from the galaxy cluster being simulated as a template, principally for telescope pointing trajectory. The model TOD is then processed using the same custom IDL pipeline used to reduce the data to create the filtered MUSTANG model map.

Initially, simulations were performed by effectively re-reducing the data, flipping the data (as in Section 2.4.3 for noise maps), and adding the model signal, attenuated by the atmospheric opacity and gain corrected. In this manner, the simulated observations are truly simulated: they have the noise of actual observations, as well as the signal of interest. However, we are generally more interested in identifying the nature of the observed (filtered) signal. Thus, we seek to subtract out the noise. Because we have generated our noise separate from the model, this can be accomplished by simply subtracting the noise map from our simulated observation map. For a purely linear filter, this will be exact; however, our earliest means of data reduction employed a common mode calculated as the median across detectors (hereafter median common mode), which did not provide adequate filtered signal (noise-subtracted) maps.

A median common mode had been adopted because of its ability to reject outlier detectors, and thus provide a more robust determination of the common mode. Conversely, a common mode calculated as the arithmetic mean across detectors (hereafter linear common mode) is more subject to deviations from outliers, but will provide a means to produce a noiseless filtered maps. An attempt to obtain the advantages

of both these calculations is to calculate the arithmetic mean of a trimmed selection (hereafter CM trim) of detectors, where typically two or three of the highest and lowest detectors are excluded from the calculation of the common mode. A limited comparison of the the filtering choices is presented in Figure 2.9. No median common mode filtering is shown for model filtering as we had well established it would not be suitable. We do, however, compare the linear common mode filtering of the data to the median common mode filtering of the data.

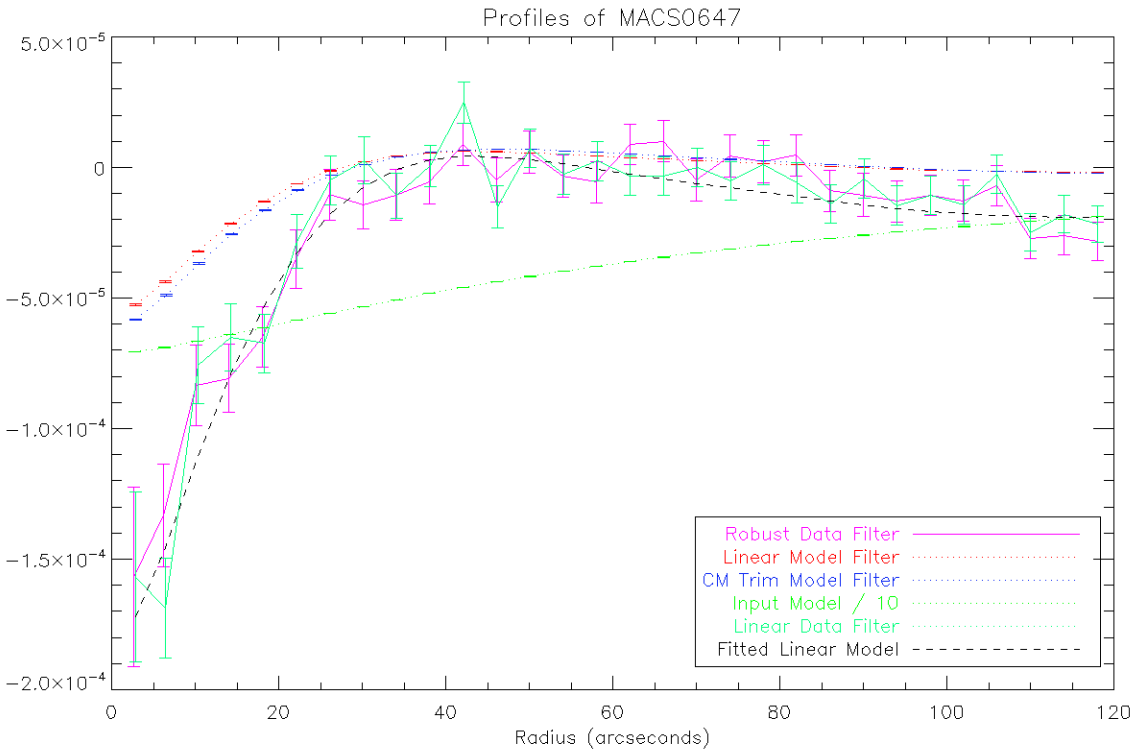

Fig. 2.9.— Robust Data Filter indicates a median common mode filter has been applied to the MUSTANG data. Linear Model Filter indicates a linear common mode filter has been applied to the model (and noise has been subtracted). CM Trim Model Filter indicates a CM Trim filter has been applied to the model (and noise has been subtracted). The Input Model is the MUSTANG beam-convolved model map, and has been scaled down by a factor of 10 to plot in the same region. Linear Data Filter indicates a linear common mode filter has been applied to the MUSTANG data. The fitted linear model allows the linear model filter curve and a constant (dc level) to be fit to the data. The units on the ordinate axis are Jy/beam.

While the CM trim offers a reasonable filter, it is evident that it is still not a linear process, and does not provide a substantial advantage over the linear common mode filtering. Young et al. (2014) establishes the linear common mode filtering as the standard for both our data and our models.

With the linear common mode filtering established, we sought to improve the time cost of filtering models. The simulation time is easily cut in half by not including the noise in the filtering process, which initially was still based on reduction code which would read in raw data to find the appropriate telescope trajectories.

A better approach was realized by using the data structure, entitled QV, in which the final calibrated data are stored rather than reprocessing the data from scratch for each simulation instance. This form of filtering (QV filtering) is able to make use of the weight vectors of the true data, which is gain calibrated, and replace the filtered data vector with the filtered model vector. To calculate the filtered model vector, first the unfiltered model vector must be created by using the telescope trajectory information in the QV. This already applies step (1) in Section 2.4.2. Then, the filtering (steps (2)-(3) in Section 2.4.2) is performed on the model array. Step (4) is not necessary, as it is already done, and then the array must simply be gridded onto a map (step (5)). In its nascent form, filtering via this method took on order 20 to 30 minutes, which was an improvement upon the two to four hours with the reduction code. With some code optimization, the QV filtering was reduced to ~ 10 minutes.

Further improvements were necessary to allow this filtering approach to be feasible for filtering hundreds of models, as would be required for determination of the pressure profiles of clusters (Section 4). To improve by a factor of 10, an obvious avenue is to reduce the amount of simulated data we filter by a factor of 10. That is, rather than use the full QV (long QV), we may shorten the QV (short QV) by a factor of 10. Given

that filtering is dependent on the scan trajectory and speed, we want to be sure that the fraction of QV that we retain is representative of the full dataset. Fortunately, the scan patterns (and speeds) were limited across the full dataset. In particular, by the end of our observing campaign, we had established (see Section 2.4.6) a standard scan pattern which became our workhorse. The end result is that we simply needed to ensure that the weight map from the short QV has the same shape (profile) as our long QV weight map. See the appendix, Section Appendix C for further discussion on the weight maps. As Figure 2.10 shows, the filtered models are very similar between the long QV and short QV, where the short QV model does have more "noise". However, this scatter is roughly an order of magnitude less than the pixel noise in the data, and is therefore negligible. The final time to filter a simulation is typically a minute, with shorter runtimes ($\sim$ 30 seconds) when iterating models over the same QV.

MUSTANG-1.5 simulations

In preparing for MUSTANG-1.5 (Section 2.3.4), we wanted to simulate the filtered signal and noise. Simulating the filtered signal can simply be achieved by modifying the detector positions in the full reduction pipeline (from raw data). Once a QV structure has been created for the MUSTANG-1.5 layout, simulations can proceed via the QV filtering as presented in the previous section. Figure 2.11 shows the improvement in recovered signal, both in amplitude and radial extent. The simulations assumed 32 detectors for a MUSTANG-1.5 layout.

Noise for MUSTANG-1.5 is simulated from the full reduction pipeline, where the raw MUSTANG data is used, but the gain is multiplied by 3.5 to account for the expected improvement in detector sensitivity. Thus, the noise investigation attempts

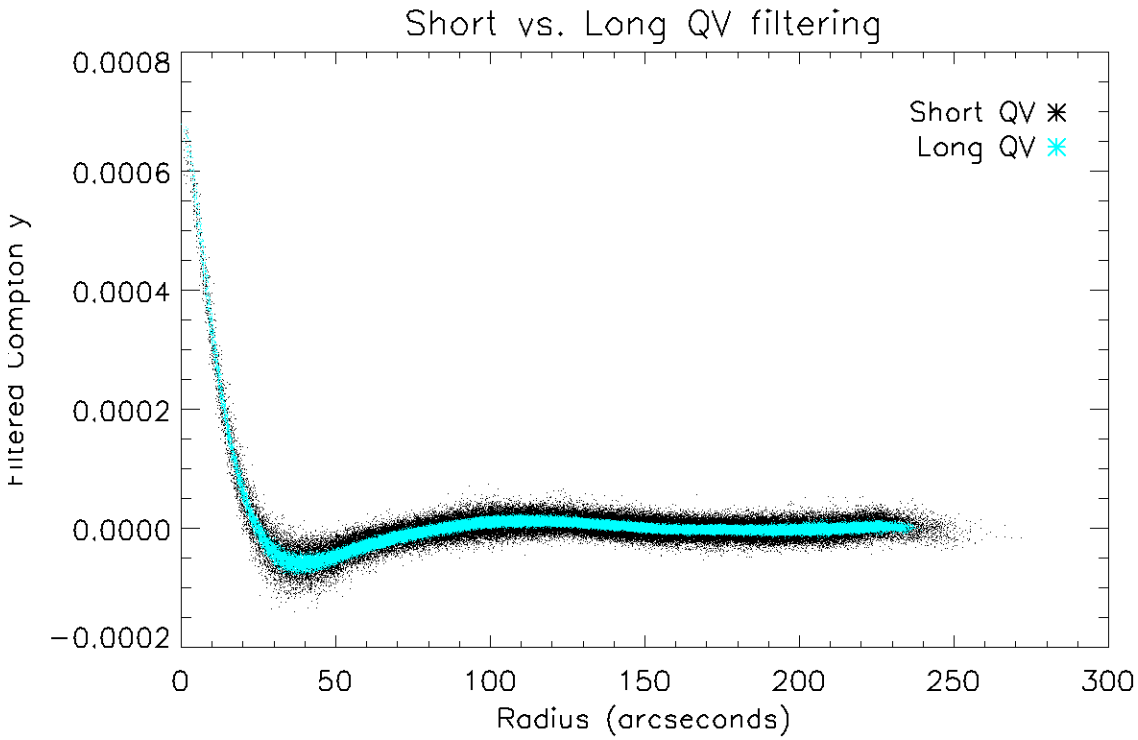

Fig. 2.10.— A fitted model to MACS 0647 (see Section 4). The scatter in the short QV is $\lesssim 3\%$ of the peak Compton y. In absolute terms, this translates to roughly 2×10^{-5} in Compton y. Typical pixel noise in maps is 15×10^{-5}.

to find how the redistribution of weight affects the noise in the maps, especially if we are to adopt scan patterns other than the standard Lissajous Daisy (Section 2.3.3). While this investigation was limited to scan patterns previously employed, the results were indicative that the Lissajous Daisy would still serve SZ observation best.

2.4.5 Characterizing the MUSTANG beam

The accuracy of simulated observations of clusters models depends heavily on the accuracy of the assumed MUSTANG beam shape, as the sky model must be convolved with the MUSTANG beam before it is passed through our filtering pipeline. It is therefore critical that we know the MUSTANG beam precisely in order to determine

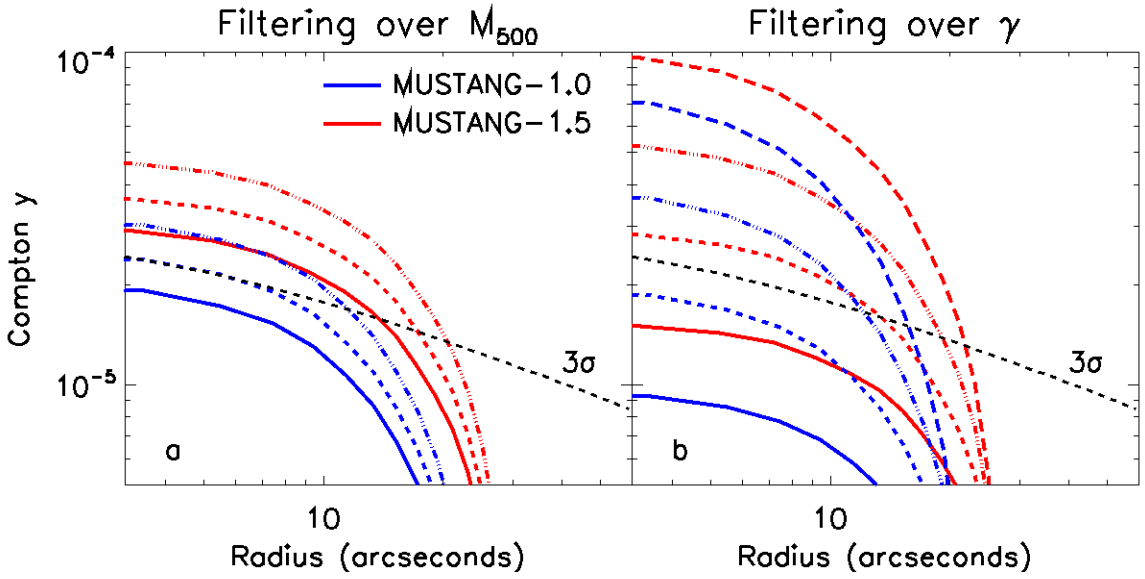

Fig. 2.11.— Panel **a** shows the (simulated) filtered A10 Compton y profiles for $M_{500} = [6.0e14, 8.0e14, 1.1e15]M_{\odot}$. Panel **b** shows the filtered Compton y profiles for $\gamma = [0.1, 0.3, 0.5, 0.7]$ (otherwise A10 parameters) for $M_{500} = 6.0e14M_{\odot}$. 3σ line shows azimuthally averaged significance for 1 hour of integration with MUSTANG-1.5. (Assumed redshift is $z = 0.591$). Unbeknown to most developers of MUSTANG-1.5, it was very aptly named: the filtered signal shows a factor of 1.5 increase!

properties of clusters we have observed.

While compact sources are comparably less of a problem at 90 GHz than at other frequencies, they cannot be ignored. For lower resolution instruments, such as Bolocam, the SZ decrement is generally much stronger than the beam-diluted compact source emission, and may not cause much concern. Still, if a compact source is known, then a subtraction is generally attempted based on extrapolating a typical spectral index. However, for MUSTANG, its high resolution and sensitivity means it will not dilute many compact sources and will therefore detect these sources above the SZ decrement. To recover the underlying SZ signal, it is therefore necessary to remove these compact sources. In order to do so, the instrument's beam must be precisely known, and effective compact source removal provides another check on our

assumed beam shape.

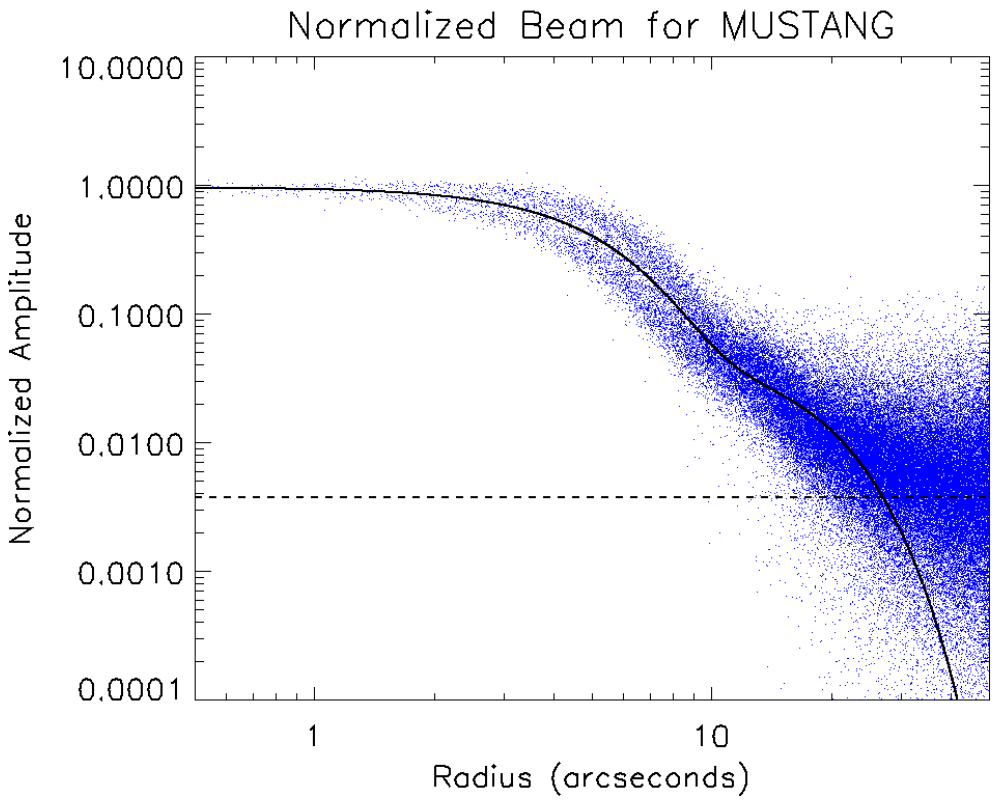

Fig. 2.12.— The solid line shows the fitted radial beam profile of MUSTANG. Fitting a double Gaussian, the primary beam has a FWHM of 8.7″, with normalization, B_1, of 0.94. The secondary beam has a FWHM of 28.4″ with a normalization B_2, of 0.06. The dashed line shows the weighted RMS of normalized pixels beyond 27″; it intersects the fitted line at 27″.

To accurately determine the beam, we compile observations of bright point sources (typically brighter than 1 Jy), which are observed for 60 to 90 seconds every half hour on a given night, over the seasons of observations. We focus on those observed in sessions where CLASH clusters were observed. Each scan on the secondary calibrator is then mapped using a much more gentle filtering routine. This very gentle filtering provides a map of the intrinsic beam. The IDL routine used to make maps of the calibrators is MULTIMAKEMAP, which was largely written by Brian Mason and

Simon Dicker. In this analysis, the data are gain calibrated, flagged, and then low-pass filtered by subtracting a high-order polynomial. The default polynomial timescale of 10 seconds has been used in the filtering of the data for this sample. Importantly, MULTIMAKEMAP allows one to choose a radius of interest (within which, the point source is expected to dominate) of which the corresponding TOD integrations will be excluded from the polynomial fitting. The radius of interest also sets an upper limited on the polynomial order, thus keeping the filtering gentle. The fitted polynomial is then subtracted from the entire TOD.

Once the map of a point source is made, a two-dimensional Gaussian is fit to the map. The sample of point sources is further trimmed to have only those whose flux density is greater than 0.5 Jy, with maximum wind speed is less than 5 m/s during the scan, and the geometric mean of the Gaussian widths (FWHM) along both axes is less than $11''$. Given that we OOF again when the beam deteriorates by roughly 10% as mentioned in Section 2.3.3, a $11''$ cut is conservative in allowing wider beams than we typically accept continue observing with. The final sample size from this selection criteria is 787.

For reference, if the sample used $12''$ instead of $11''$, and no wind speed criterion, the sample size would be 862. This does not necessarily correlate to the quality of science data, as many of these scans with broad beams maybe be performed consecutively to confirm poor beam shape, and to assess the improvement of autoOOFs.

With the trimmed sample, each map is normalized to unity based on the fitted peak of the point source. Using the centroid found from the two dimensional Gaussian fit, an azimuthal profile is taken of the normalized map. A profile with the weights of each pixel is also recorded. Once all values and weights are stacked, an azimuthally

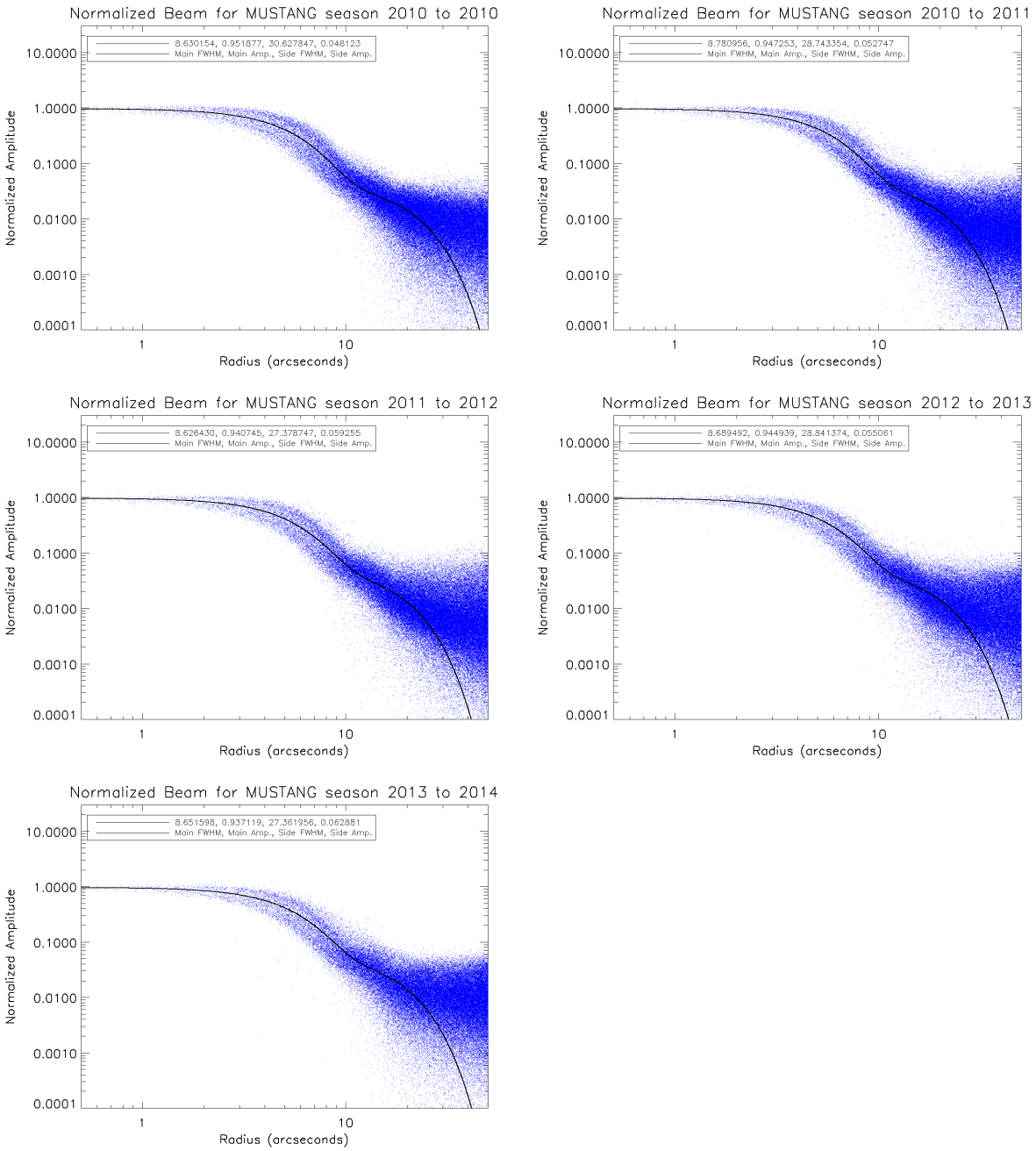

Fig. 2.13.— As Figure 2.12, but showing the beams over various seasons of MUSTANG data.

symmetric (one-dimensional) double Gaussian,

$$B(r) = B_1 e^{-\frac{r^2}{2\sigma_1^2}} + B_2 e^{-\frac{r^2}{2\sigma_2^2}}, \tag{2.2}$$

is fit using a Levenberg-Marquardt least squares minimization in IDL (MPFIT, Markwardt 2009). Here, B_1 is the normalization of the primary beam, and B_2 is the normalization of the secondary (error) beam. The fitted parameters over all 862 scans are $B_1 = 0.94^{+0.02}_{-0.03}$, $\sigma_1 = 3.69^{+0.23\prime\prime}_{-0.14}$, $B_2 = 0.06^{+0.03}_{-0.02}$, $\sigma_2 = 12.0^{+3.3\prime\prime}_{-2.8}$. This corresponds to a primary beam with FWHM of $8.69^{+0.53\prime\prime}_{-0.34}$ and a secondary (error) beam with FWHM of $28.4^{+7.8\prime\prime}_{-6.5}$. The secondary beam is qualitatively consistent with the expected near-sidelobes on the GBT given the MUSTANG illumination pattern and medium-scale aperture phase errors not fully corrected by the OOF procedure in Section 2.3.3.

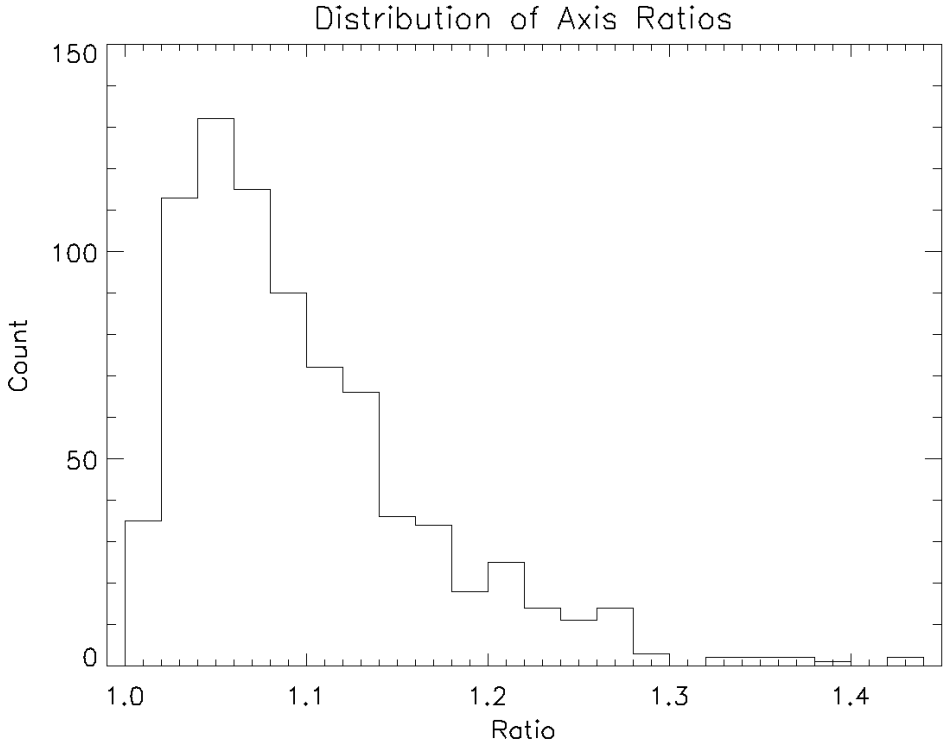

Fig. 2.14.— A histogram of the ratio of the major axis to minor axis for the entire sample (862 maps), and plotted the histogram. This is consistent with each axis having FWHM Gaussian distributions centered about $9.0''$ and $\sigma = 0.75''$, which is used as a loose proxy to the distribution of the fitted widths of the two-dimensional Gaussians.

There is some indication of bimodality in this data, especially within the main beam. The only discernible cause for this bimodality, which is extremely weak, is tendency for the beam to be slightly elliptical (see Figure 2.14).

The bimodality in the beam profiles can be replicated by taking azimuthal profiles of elliptical Gaussians. That is, from the fitted two-dimensional Gaussians that are fitted to the maps, the model beams can be mapped and the same analysis with one-dimensional double Gaussian can be performed on the model beams, which reveals the same bimodality as seen in the azimuthal profiles of the data. Figure 2.14 shows the distribution of axis ratios fitted to the data. The distribution for fitted widths, denoted as "widtha" and "widthb" are $9.07^{+0.90}_{-0.55}{}''$ and $9.05^{+1.06}_{-0.51}{}''$. This should be taken as confirmation that the fitting code does not preferentially fit one variable as the major axis, relative to the other. This distribution has been loosely approximated as $9.0^{+0.75}_{-0.75}{}''$ can reproduce a distribution consistent with the axis ratios reported in Figure 2.14.

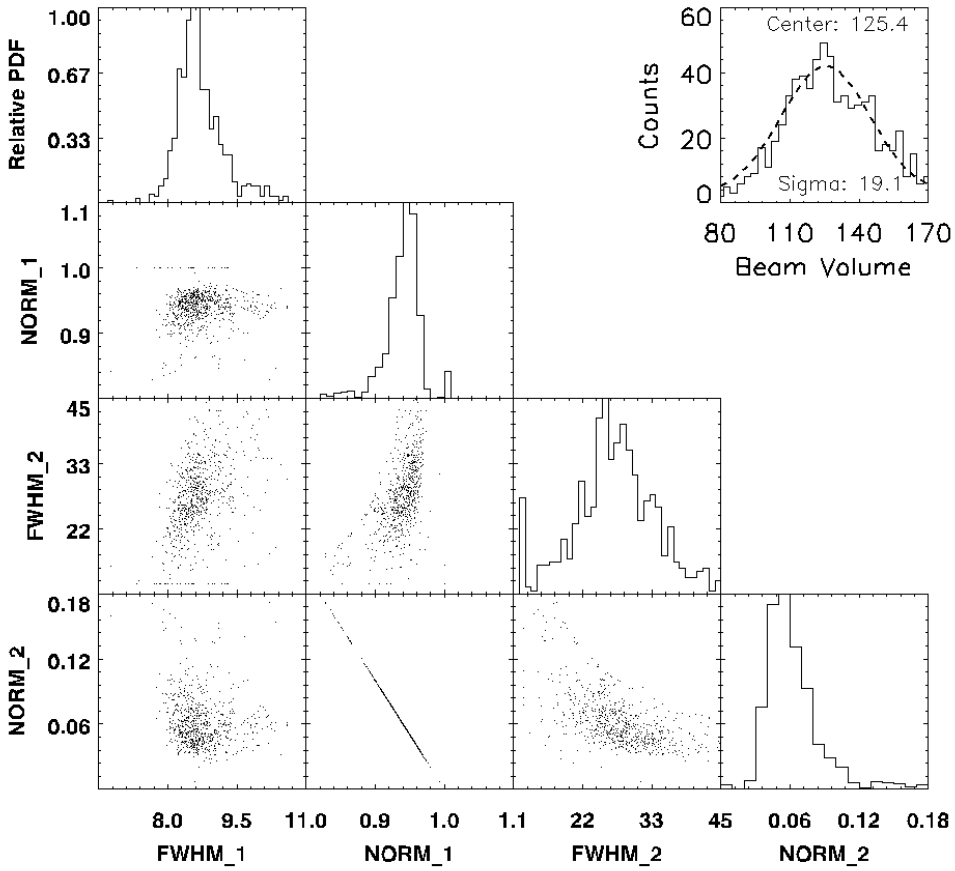

Fig. 2.15.— Here, the one-dimensional double Gaussians have been fit to each individual map in the sample, and the distribution of parameters have been plotted. FWHM_1 corresponds to the FWHM of the main beam, and NORM_1 corresponds to the fractional amplitude of the main beam. Those with "_2" correspond to the error beam. The total amplitude is constrained to be 1. In the upper right is a histogram for the total area (or beam volume) in square arcseconds. "Center" denotes the center for the fitted Gaussian (to the distribution of areas).

2.4.6 MUSTANG Data Quality

From Section 2.4.5, scatter in the fitted parameters of the beam shape is clear and quantifiable. The simple case of evolution over seasons of data has already been investigated. However, the scatter in parameters may not be purely random, and may be correlated with factors such as weather, scan strategy, telescope elevation, and potentially other factors. To examine any dependencies the beam may have, it's important to distinguish between those related to the observations themselves, and those in the reduction process.

Using a subset of hand-selected sources, an early investigation, in the summer of 2011, looked at dependencies of the beam on a variety of variables. The criteria focused more on observing logs and timestream quality than resultant beam-fitted parameters. The sources selected are given in Table 2.1. Most sources were above 1 Jansky, but 1459+7140, at 0.5 Jy, was included in the sample.

Source	Project
2253+1608	TPAR_20101013
1159+2914	AGBT09C_020_01
0721+7120	AGBT11A_009_03
0423-0120	AGBT09C_035_01
0646+4451	AGBT09C_059_06
1459+7140	AGBT09C_059_09

Table 2.1: Sources and projects used to investigate beam dependencies.

For modelling purposes, we are interested to know the volume contained in the main beam and error beam. In particular, we are interested in the fractional beam volume (and thus signal) that we receive outside of our main beam, where the extent of our main beam, r_0, is defined by $B_1 e^{\frac{-r_0^2}{2\sigma_1^2}} = B_2 e^{\frac{-r_0^2}{2\sigma_2^2}}$. That is, where the main beam and error beam have the same response. We can write the volumes of the beams internal to r_0 as $V_0 = 2\pi \int_0^{r_0} B_1 e^{\frac{-r^2}{2\sigma_1^2}} r dr$ and $V_1 = 2\pi \int_0^{r_0} B_2 e^{\frac{-r^2}{2\sigma_2^2}} r dr$, and the volumes of the

beams external to r_0 as $V_2 = 2\pi \int_{r_0}^{\infty} B_1 e^{\frac{-r^2}{2\sigma_1^2}} r dr$ and $V_3 = 2\pi \int_{r_0}^{\infty} B_2 e^{\frac{-r^2}{2\sigma_2^2}} r dr$. Then, we can compare how much received signal is due to our error beam (Equation 2.3), and of more concern, how much of it is coming from outside our main beam (Equation 2.4), as it then relates to how much signal we receive from off-target sources. Figure 2.16 shows the calculated values for f and f'.

$$f = \frac{V_3 + V_1}{V_0 + V_1 + V_2 + V_3} \tag{2.3}$$

$$f' = \frac{V_3}{V_0 + V_1 + V_2 + V_3} \tag{2.4}$$

We search for correlations between the beam shape and the following variables: telescope elevation, air temperature, hours after sunset, and hours after last OOF. Telescope elevation is a concern because the pulse tube (used in cooling the receiver) is known to perform poorly when the telescope is below 30° elevation. While the telescope dish does deform as a function of elevation, work by Fred Schwab and others at NRAO has been able to account for these deformations. Air temperature should only be a concern if ice were to form along the optical path. Hours after sunset is investigated because we know the structure of the GBT deforms under solar heating and can take time to equilibrate. Observations generally start no sooner than three hours after sunset. Finally, we know that even after we have adjusted the surface of the telescope from the OOF, the beam can degrade, thus we investigate the time after OOF as well.

The majority of the targets in our sample of 14 were observed for $\sim$ 12 hours, yet the time variations alone are not enough to account for the differences among the reported noise for each cluster. The beam shape appears to not be well correlated

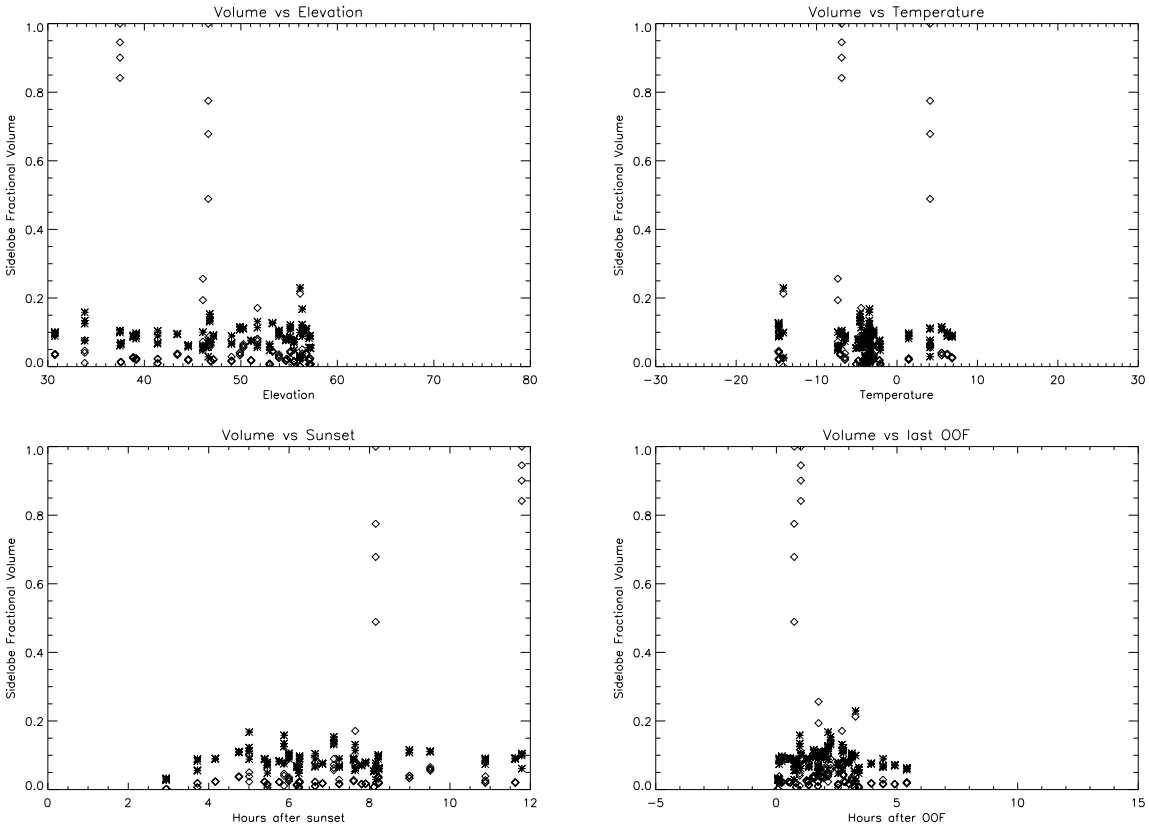

Fig. 2.16.— Fractional volumes from all scans, as a function of observation parameters. Diamonds are f, asterisks are f' as defined in Equations 2.3 and 2.4 respectively.

with any variable we examined. Thus, to unveil governing factors in data quality we correlate the noise in the final maps (of clusters of galaxies) with the same variables. In particular, we focused on a set of six clusters (MACS J0329, MACS J0429, MACS J0647, MACS J1115, MACS J1149, and MACS J1206) observed in project AGBT11B_001, which were largely observed with the same observing strategy.

While the telescope gain, another measure of the telescope beam, will clearly affect the data quality, the general independence of beam shape on other variables found above suggest that this is not the leading culprit. Given that the reduction pipeline is identical for the six clusters of concern (they are not processed with different

filtering options), the two initial variables we consider are the instrument's gain and the fraction of data that we flag. The telescope's gain is quantified in Janskys per Cal (i.e. calibration lamp), where the calibration lamp is taken to be equivalent to a 38.5 Jy source, as viewed by MUSTANG. Not surprisingly, both of these variables correlate well with the noise in our maps, and importantly, they do seem to account for the variations in noise, as seen in Figure 2.17. Crucially, the lower right plot shows the noise in the (smoothed) cluster maps compared to what we expect, "From QV" (Section 2.4.4), given the gains and flagged fraction for each scan.

Given the general independence that beam shape had on other variables, it is surprising to see the variations we do in gain. Setting this aside, I investigated correlations between flagged data fraction and other variables. A more prominent connection exists between flagged data and scan lengths, which may be addressed with improved software (flagging functionality). In particular, the lengthy 418 second scans show a considerable flagged fraction. If features lasting 5 seconds can be enough to flag a detector and occur, on average, at some predictable interval, then it is (a) not surprising that more data is flagged in a longer scan, and (b) notable that a large chunk of otherwise good data is also thrown out. However, the fact that the 139 second scans also show some tendency towards substantial flagged data fraction reveals that this is not the complete story.

Over the Full Sample

While the data quality analysis in the previous section helped us solidify a standard scan pattern and observing strategy, we want to assess the noise properties in the sample of clusters we are analyzing. Figure 2.18 shows the noise properties for each of the fourteen clusters in our sample to determine pressure profiles (see Section 4). We

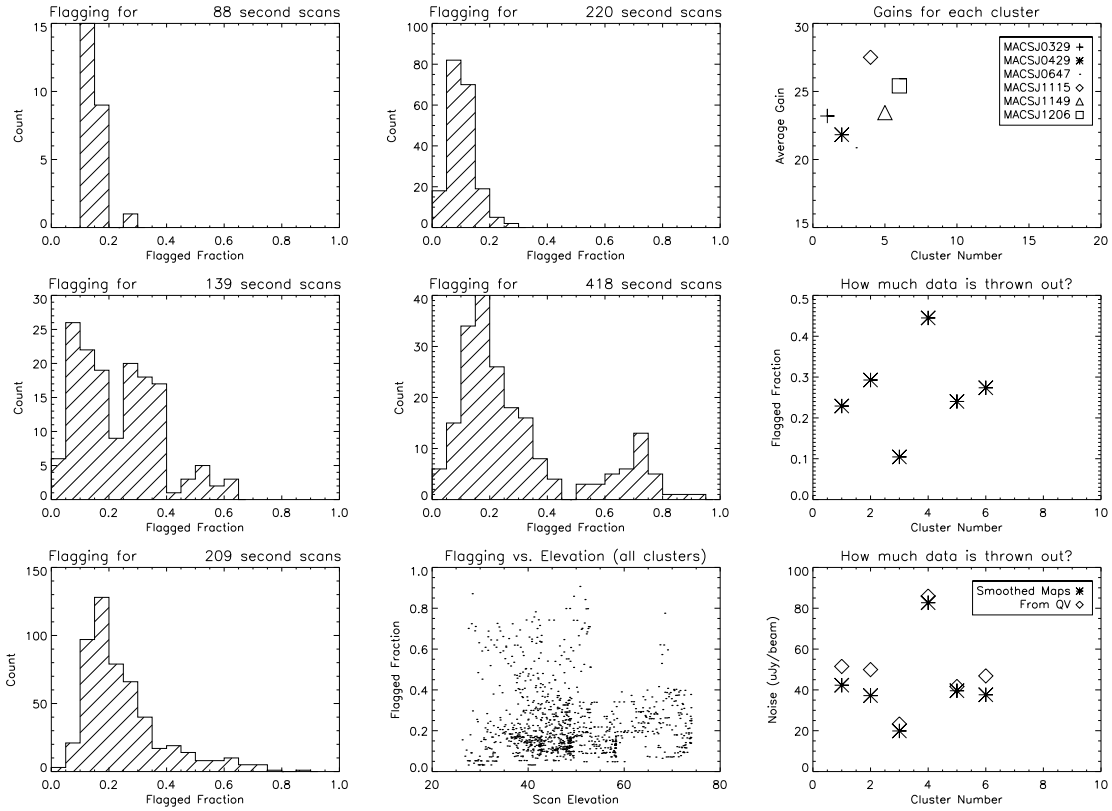

Fig. 2.17.— The first five plots (top-to-bottom, then right) show how much data is flagged for a given scan length. The sixth plot shows that there is no clear link between flagging and elevation. The remaining three plots show the variations in gain, flagged fraction, and expected noise in each cluster. QV is the data structure from which maps may be gridded (refer back to Section 2.4.4).

include averaged values of the gain (Jy/cal), telescope elevation, and flagged fraction of data, as we expect these to correlate with the final noise. Of course, the total integration time (Table 4.3) is also critical to noise determinations; thus, we include a plot of mapping speeds for the clusters. The expected mapping speed was 400 μJy/beam in an hour in a $3' \times 3'$ region, assuming uniform coverage, $2''$ pixelization, and no smoothing. The values plotted used σ_1, the noise over the central arcminute of a cluster map ($1''$ pixel gridding, $10''$ FWHM smoothing), w_1, the total weight in the central arcminute, w_{tot}, the total weight in the map, and t_{integ}, the total integration

time on the cluster. Thus, the map sensitivity ratio (MSR) for a $3' \times 3'$ region in an hour is calculated as:

$$\mathrm{MSR} = \frac{\sigma_1 \pi}{9} \left(\frac{w_1}{w_{tot}} t_{integ}\right)^{-1/2}. \tag{2.5}$$

The major discrepancy with the predicted value is due to the choice of smoothing.

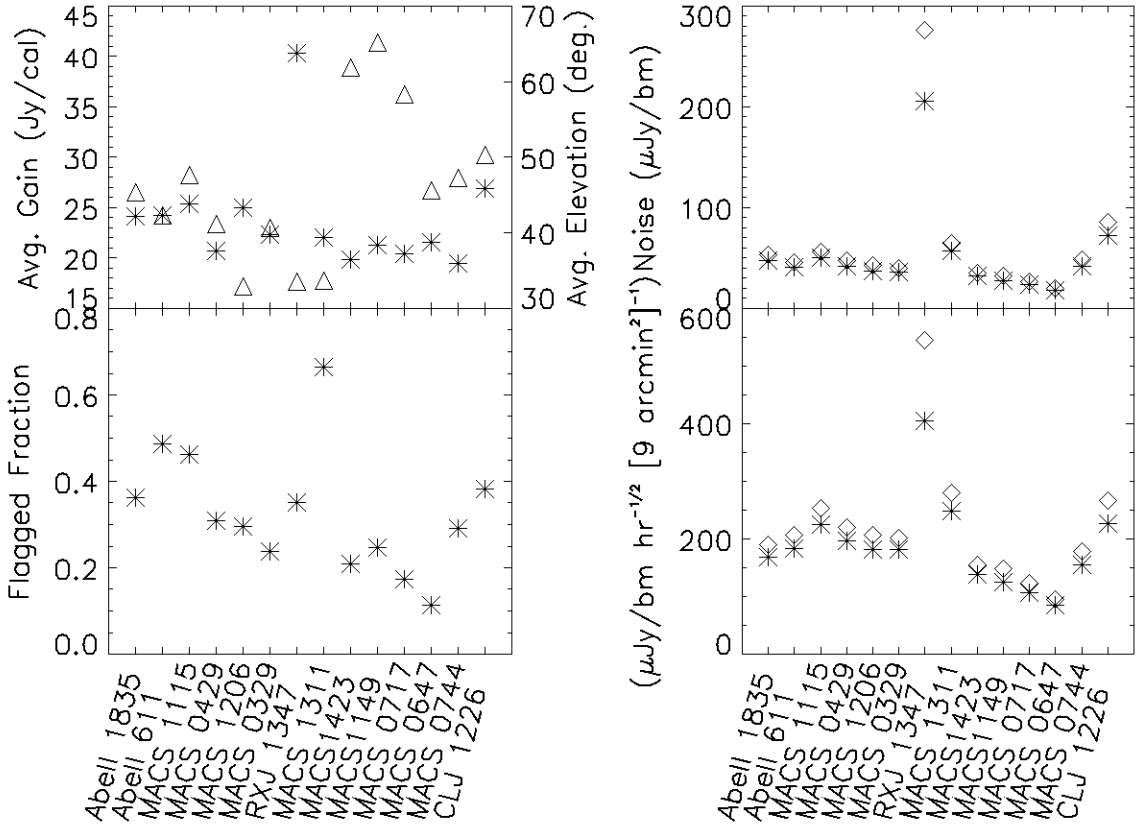

Fig. 2.18.— The upper left panel shows average gain (asterisk) and elevation (triangle) per cluster. The lower left panel shows the total flagged fraction per cluster. The right panels show the noise quantities as measured in for the central arcminute of a cluster map ($1''$ pixel gridding, $10''$ FWHM smoothing) as diamonds, and the associated estimate from the timestreams are asterisks.

We may also check the potential correlations between noise and observational parameters on a scan-by-scan basis. In Figure 2.19 we do not see any strong correlations except for elevation vs. hours after sunset, where we are tracking an object through-

out a run. We may take a more focused view on instrument gain versus elevation, Figure 2.20, as this is one of primary concern and we have some reason to expect some correlation. To further draw out any correlations, I have binned the data by elevation, and have fit a fourth order polynomial. The low gains at moderate elevations is not too surprising given that the pulse tube is known to not work well when the telescope is below 30°, thus letting the detector array warm up. Thus, for any observations that may have started out close to 30°, the array might yet have to cool down and stabilize later in the run, once the target has risen to a higher altitude. However, the increase in gain towards yet higher elevations is somewhat surprising.

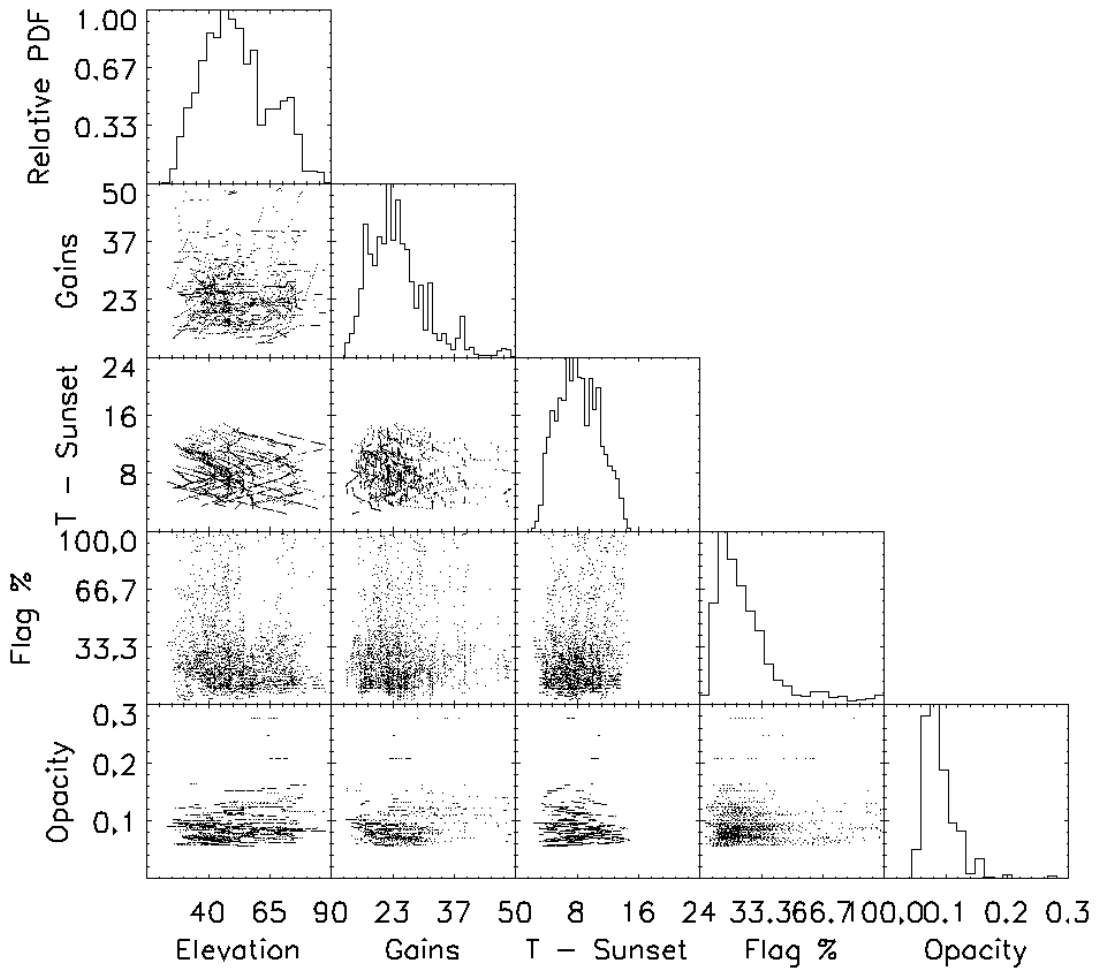

Fig. 2.19.— A comparison of potential dependent and independent variables. The variables are largely independent, except elevation vs. time after sunset, which would naturally reflect the tracking of an object.

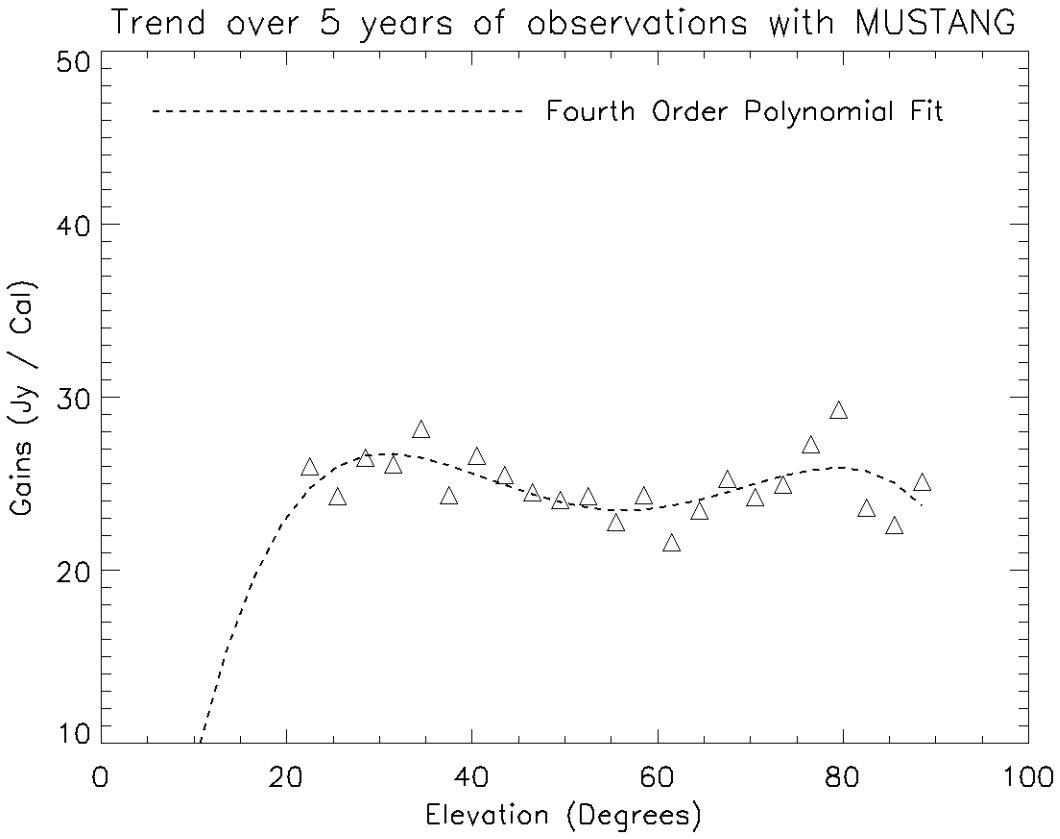

Fig. 2.20.— A plot of inverse gain vs. elevation, and binning the gains in elevation bins of 3°. That is, lower Jy/Cal values equate to lower noise and better performance. A fourth order polynomial has been fit to the points without constraints for elevations below 30° or above 80°. The error on these points (in Jy/Cal) is between 5 and 10.

Chapter 3

MUSTANG-2 window and radome

Abstract

We perform measurements at the Jansky Lab in Green Bank, West Virginia to quantify the transmission properties of candidate window and radome materials. These measurements are made by placing a sample of each material in front of a radiometric receiver, in our case a receiver that operates around 4 mm. Loads (microwave absorbers) at known temperatures (a hot and cold temperature) are then placed behind each sample, and the received power is recorded. Variations of this measurement allow us to determine the total transmission, reflection, and absorption of light. We perform these measurements for two window samples and four radome samples, and with some systematic corrections, we can comfortably select a radome material for MUSTANG-2.

3.1 Introduction

The window and radome are two parts on most receivers at radio wavelengths, which light must pass through before arriving at the detectors. This is generally the case because many receivers are installed in vacuum dewars so that they may be cooled, thus lowering the receiver noise. Noise is a property of power received and within the receiver (detectors). For simple radiometers at low frequencies, this is often expressed as a noise temperature, T_N, with the relation $T_N \equiv \frac{P_\nu}{k_B}$, where P_ν is the noise power per unit frequency. This relation comes from the use of the Rayleigh-Jeans approximation to black-body emission, but it is commonly applied independently of the actual emission mechanism(s) at work.

In this manner, the system noise is generally reported as a system temperature:

$$T_{sys} = T_{CMB} + T_{source} + T_{atm} + T_{spillover} + T_{rcvr} + T_{add} \tag{3.1}$$

where T_{CMB} is the temperature of the CMB, T_{source} is the temperature of the astronomical source being observed, T_{atm} is the equivalent temperature of the atmospheric emission being observed in the telescope beam, $T_{spillover}$ is the equivalent temperature of the excess emission (beyond the reflector, typically from the ground) received, T_{rcvr} is the inherent noise within the receiver, and T_{add} is a term to cover any additional sources of noise.

With many systems, it was, and can still be, the receiver which contributes most significantly to the system temperature. This is the motivation for cooling many receivers. As discussed in Section 1.1, bolometer arrays offered a major progression in SZ studies. These detectors offered increased sensitivity at millimeter frequencies over heterodyne technology.

The window is used to provide a relatively transparent barrier between the vacuum and cooled stage in the dewar. The radome is used to shield the receiver from water or ice entering, while also being (relatively) transparent. The window and radome affect observations in two potential ways: (1) they reduce the strength of the astronomical signal, and (2) they add noise to the system via thermal emission. The astronomical signal is attenuated by the reflection and absorption of the materials, while the additional noise would come from emission from the material. Just as Equation 2.1 applies to the absorption and emission from the atmosphere, the same can be applied to the window and radome materials. The key distinction here is that reflected light is not characterized by an optical depth, τ, but it does contribute to diminished signal received (i.e. diminished optical efficiency).

Given the concern of millimeter-wave transmission, especially absorption and emission, we seek to quantify the transmission properties of our candidate materials (Section 3.3.1). The typical setup is to place a sample of each material in front of a radiometric receiver and take separate measurements of the power received when (1) a cold load (i.e. microwave absorber) is behind the sample, and (2) a hot load is behind the sample. The loads are of a known, stable temperature, often the cold load is that of liquid nitrogen (77 K), and the hot load is room temperature ($\sim$ 288 K).

3.2 Approach

Attempting to determine the transmission properties of materials via these radiometric measurements may produce varied results. There are three common culprits which may introduce discrepancies in results:

1. the receiver emits thermal noise which is partially reflected back into the receiver by the sample,

2. the local oscillator (LO) emits power and is reflected back into the receive by the sample, and

3. the receiver gain and noise temperature may change with the insertion of a sample.

Particular to our measurements, we also consider the potential for extraneous light (light outside the main beam of the receiver) being reflected into the receiver. Additionally, we consider variations in the sample temperature as another source of discrepancies.

3.2.1 Notation

In investigating the transmission properties of potential window and radome materials for use with MUSTANG-2, the key concerns are quantifying the transmission properties of the materials, and if possible, distinguishing between the reflection and absorption losses. The transmission, $\mathbb{T}$, is restricted to the range $0 \leq \mathbb{T} \leq 1$, and the loss is defined as $L = \mathbb{T}^{-1}$, and are thus restricted to $L \geq 1$. While loss is commonly used, the subsequent analysis uses transmission.

The following conventions are used: R is the reflectivity, i.e. the fraction of intensity reflected at the surface, and D is the dissipation within the material. For transmission, I adopt the following notations: $1 - R = \mathbb{T}_{surface}$, $1 - D = \mathbb{T}_{material}$, and $\mathbb{T}_{tot} = \mathbb{T}_{surface} * \mathbb{T}_{material}$. For clarity, the loss terms which may be seen in other literature is related as: $L_R = \mathbb{T}^{-1}_{surface}$, $L_D = \mathbb{T}^{-1}_{material}$, and $L_I = L_R * L_D$, where L_R is the reflection loss, L_D is the dissipative loss, and L_I is the insertion loss.

3.2.2 Calculation of Transmissions

There are four standard measurements of receiver power that will allow us to calculate the total transmission (insertion loss). The measurement are done with (1) a hot load, no sample, (2) a cold load, no sample, (3) a hot load, hot sample laid flat, and (4) a cold load, hot sample laid flat. The rough setup(s) are illustrated in Figure 3.1, taken from Tony Kerr's write-up[1]. By recording the power read out of the receiver for these four setups, we can calculate the receiver temperature, the receiver gain, and the total transmission, $\mathbb{T}_{tot}$.

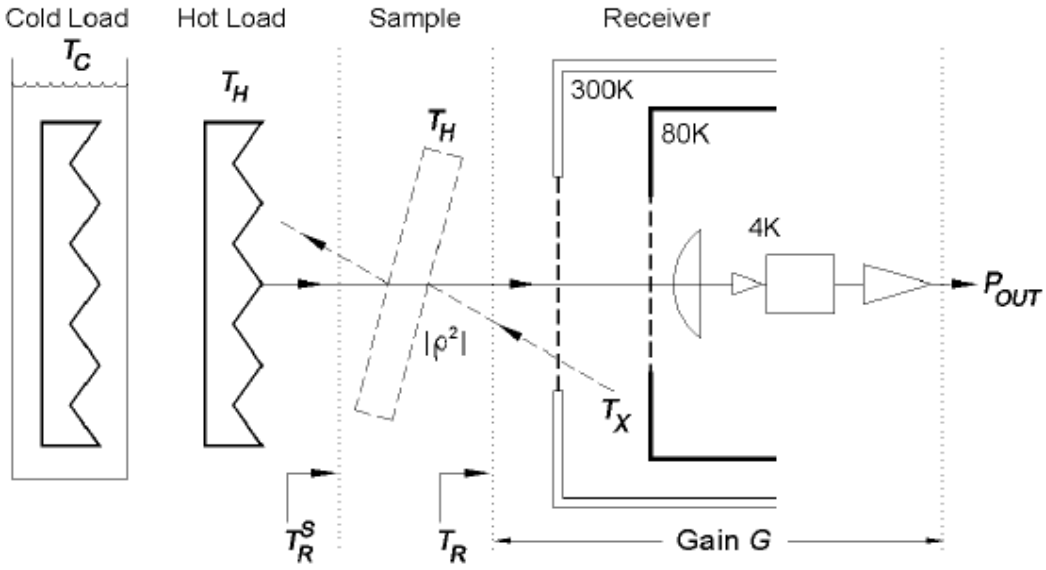

Fig. 3.1.— From Tony Kerr's write-up; this diagram shows how the apparatus to measure total transmission of a material (sample). When measuring, only one load is placed in front of the receiver at a time. A sample can be inserted or left out.

The four measurements listed above result in the following, respective, powers

[1] `http://www.cv.nrao.edu/~akerr/WindowMeasDraft1.pdf`

being read out by the receiver:

$$P_H = k_B GB(T_H + T_R) \tag{3.2}$$

$$P_C = k_B GB(T_C + T_R) \tag{3.3}$$

$$P_H^S = k_B GB(T_H \mathbb{T}_{surface} \mathbb{T}_{material} + T_H \mathbb{T}_{surface}(1 - \mathbb{T}_{material}) + T_X(1 - \mathbb{T}_{surface}) + T_R) \tag{3.4}$$

$$P_C^s = k_B GB(T_C \mathbb{T}_{surface} \mathbb{T}_{material} + T_H \mathbb{T}_{surface}(1 - \mathbb{T}_{material}) + T_X(1 - \mathbb{T}_{surface}) + T_R) \tag{3.5}$$

where k_B is the Boltzmann constant, G is the gain, B is the bandwidth, T_R is the receiver temperature, T_X is temperature of stray light reflected into the receiver, T_H is "hot" temperature, which is the temperature of the room, and T_C is the cold temperature. The sample is kept at room temperature, and so any emission from it is proportional to T_H. The cold temperature is taken as the temperature of liquid nitrogen, which is effectively the temperature at which it boils, i.e. 77 K.

From the above equations we can solve for GB, T_R, and $\mathbb{T}_{tot}$, if we assume we know T_C and T_H:

$$GB = \frac{P_H - P_C}{k_B(T_H - T_C)} \tag{3.6}$$

$$T_R = P_H \frac{T_H - T_C}{P_H - P_C} \tag{3.7}$$

$$\mathbb{T}_{tot} = \frac{P_H^s - P_C^s}{P_H - P_C} \tag{3.8}$$

Assigning the uncertainties σ_{P_H}, σ_{P_C}, σ_{T_H}, σ_{T_C} to their respective measured or assumed values, and assuming the uncertainties are independent, we calculate the un-

certainties in derived quantities as:

$$\sigma_{GB}^2 = \frac{\sigma_{P_H}^2 + \sigma_{P_C}^2 + GB^2(\sigma_{T_H}^2 + \sigma_{T_C}^2)}{k_B^2(T_H - T_C)^2}, \tag{3.9}$$

$$\sigma_{T_R}^2 = \frac{4P_C^2\sigma_{T_H}^2 + 4P_H^2\sigma_{T_C}^2 + T_R^2(\sigma_{P_H}^2 + \sigma_{P_C}^2)}{(P_H - P_C)^2}, \text{and} \tag{3.10}$$

$$\sigma_{\mathbb{T}_{tot}}^2 = \frac{\sigma_{P_H^S}^2 + \sigma_{P_C^S}^2 + \mathbb{T}_{tot}^2(\sigma_{P_H}^2 + \sigma_{P_C}^2)}{(P_H - P_C)^2}. \tag{3.11}$$

It's worth noting that the greater the temperature differences, $T_H - T_C$, the greater the power difference, $P_H - P_C$ will be, and thus the error in total transmission will be reduced. The desire for the large, and stable temperature difference motivates the choice of our hot and cold temperatures (room temperature and liquid nitrogen's temperature).

Because we are still interested in separating $\mathbb{T}_{surface}$ and $\mathbb{T}_{material}$, measurements of receiver power in additional setups will be required. Mathematically, there are two ways to solve for $\mathbb{T}_{surface}$: either varying the temperature in the second term (the temperature of the sample) or third term (the temperature of stray light) Equations 3.4 and 3.4.

Unfortunately, adjusting the sample temperature is not feasible (see Section 3.3). However, changing T_X, the reflected temperature of stray light off the sample and into the receiver, is feasible. While Figure 3.1 shows the sample slightly tilted to avoid standing waves between the receiver and sample, the sample may be tilted further, such that the object corresponding to T_X could be something outside of the receiver. If the samples are tilted to 45° relative to the receiver, such that T_X is the temperature of an object directly below the receiver window, in which case T_X can be T_C or T_H.

By adopting this setup, we can take the measurements:

$$P^S_{H,X_C} = kGB(T_H\mathbb{T}_{surface} * \mathbb{T}_{material} + T_H\mathbb{T}_{surface} * (1 - \mathbb{T}_{material}) + T_C(1 - \mathbb{T}_{surface}) + T_R) \tag{3.12}$$

$$P^s_{H,X_H} = kGB(T_H\mathbb{T}_{surface} * \mathbb{T}_{material} + T_H\mathbb{T}_{surface} * (1 - \mathbb{T}_{material}) + T_H(1 - \mathbb{T}_{surface}) + T_R) \tag{3.13}$$

Then we can solve for $\mathbb{T}_{surface}$:

$$\mathbb{T}^H_{surface} = 1 - \frac{P^s_{H,X_H} - P^S_{H,X_C}}{P_H - P_C} \tag{3.14}$$

$$\sigma^2_{\mathbb{T}_{surface}} = \frac{\sqrt{\sigma^2_{P^s_{H,X_H}} + \sigma^2_{P^S_{H,X_C}} + \mathbb{T}^2_{surface}(\sigma^2_{P_H} + \sigma^2_{P_C})}}{(P_H - P_C)} \tag{3.15}$$

With two more measurements:

$$P^S_{C,X_H} = kGB(T_C\mathbb{T}_{surface}\mathbb{T}_{material} + T_H\mathbb{T}_{surface}(1 - \mathbb{T}_{material}) + T_H(1 - \mathbb{T}_{surface}) + T_R)\text{and} \tag{3.16}$$

$$P^s_{C,X_C} = kGB(T_C\mathbb{T}_{surface}\mathbb{T}_{material} + T_H\mathbb{T}_{surface}(1 - \mathbb{T}_{material}) + T_C(1 - \mathbb{T}_{surface}) + T_R), \tag{3.17}$$

we can recover $\mathbb{T}_{tot}$ in two more ways:

$$\mathbb{T}^C_{tot} = \frac{P^s_{C,X_C} - P^S_{H,X_C}}{kGB(T_C - T_H)}, \text{and} \tag{3.18}$$

$$\mathbb{T}^H_{tot} = \frac{P^s_{C,X_H} - P^S_{H,X_H}}{kGB(T_C - T_H)}. \tag{3.19}$$

Here, the superscript on the transmission denotes the constant load temperature in a calculation. That is, for the total transmission, the secondary load is constant for

a given calculation of $\mathbb{T}_{tot}$. Similarly, for surface transmission, the primary load is constant for a given calculation of $\mathbb{T}_{surface}$, and the superscript will denote which load (hot or cold) was used.

We now have at least one way to derive each of the transmission quantities of interest. To keep track of reported quantities and the equation used to derive them, the results for each window and radome material tested will be reported in the format of Table 3.1.

Quantity	Method 1	Method 2	Method 3
$\mathbb{T}_{tot}$	$\frac{P^s_{C,X_C} - P^S_{H,X_C}}{P_C - P_H)}$	$\frac{P^s_{C,X_H} - P^S_{H,X_H}}{P_C - P_H)}$	$\frac{P^s_H - P^s_C}{P_H - P_C}$
$\mathbb{T}_{surface}$	$1 - \frac{P^s_{H,X_H} - P^S_{H,X_C}}{P_H - P_C}$	$1 - \frac{P^s_{C,X_H} - P^S_{C,X_C}}{P_H - P_C}$	
$\mathbb{T}_{material}$	$\mathbb{T}_{tot}/\mathbb{T}_{surface}$		

Table 3.1: Equations used to infer transmission values. $\mathbb{T}_{material}$ can in principle be calculated six different ways. However, the default calculation is to use the average of $\mathbb{T}_{tot}$ from methods 1 and 2, with the average of $\mathbb{T}_{surface}$ from methods 1 and 2.

3.3 Measurement Setup

We use the 3 mm test dewar in the Jansky Laboratory at the National Radio Astronomy Observatory in Green Bank, West Virginia. The test dewar can be seen in Figure 3.2, especially the top panels, where the cylindrical protrusion is where light enters the receiver (there are samples in front of this protrusion in both panels). The dewar is cryogenically cooled with the tubes adjacent to the cylindrical protrusion. The setup was designed to reduce the variations due to power emitted by the receiver as well as gain or receiver temperature fluctuations. An electronic diagram of the receiver is shown in Figure 3.3.

Measurements are controlled with LabView that was custom written by Steve White. Measurements are taken from 68 GHz to 92 GHz in 1 GHz steps for both

hot and cold load runs, where the range and stepsize can be set by the user. This frequency range (68 GHz to 92 GHz) is the full range for which performance of the receiver was deemed suitable. To run through this frequency range for one load takes about 5 seconds when done with 1 GHz steps. The LabView code records (1) the frequency of a measurement, (2) the received power for each load, and (3) the system temperature.

Fig. 3.2.— Here we have the measurement setup with the 3 mm receiver. The top panels show two different samples in front of the receiver, as in Figure 3.1. The lower panels show a waveguide exiting the dewar and entering the Vector Network Analyzer (VNA), where the signal can be mixed with a local oscillator (LO). This setup limits the power emitted from the receiver.

In addition to controlling for variations in the receiver, we must limit the variations in the materials (both samples and loads) being measured. That is, we must precisely and consistently place the samples and loads in the same position for a given measurement. The placement of the loads and sample are shown in Figure 3.4. The 3 mm test dewar receiver has a FWHM of 5°. Neglecting any sidelobes, this is small

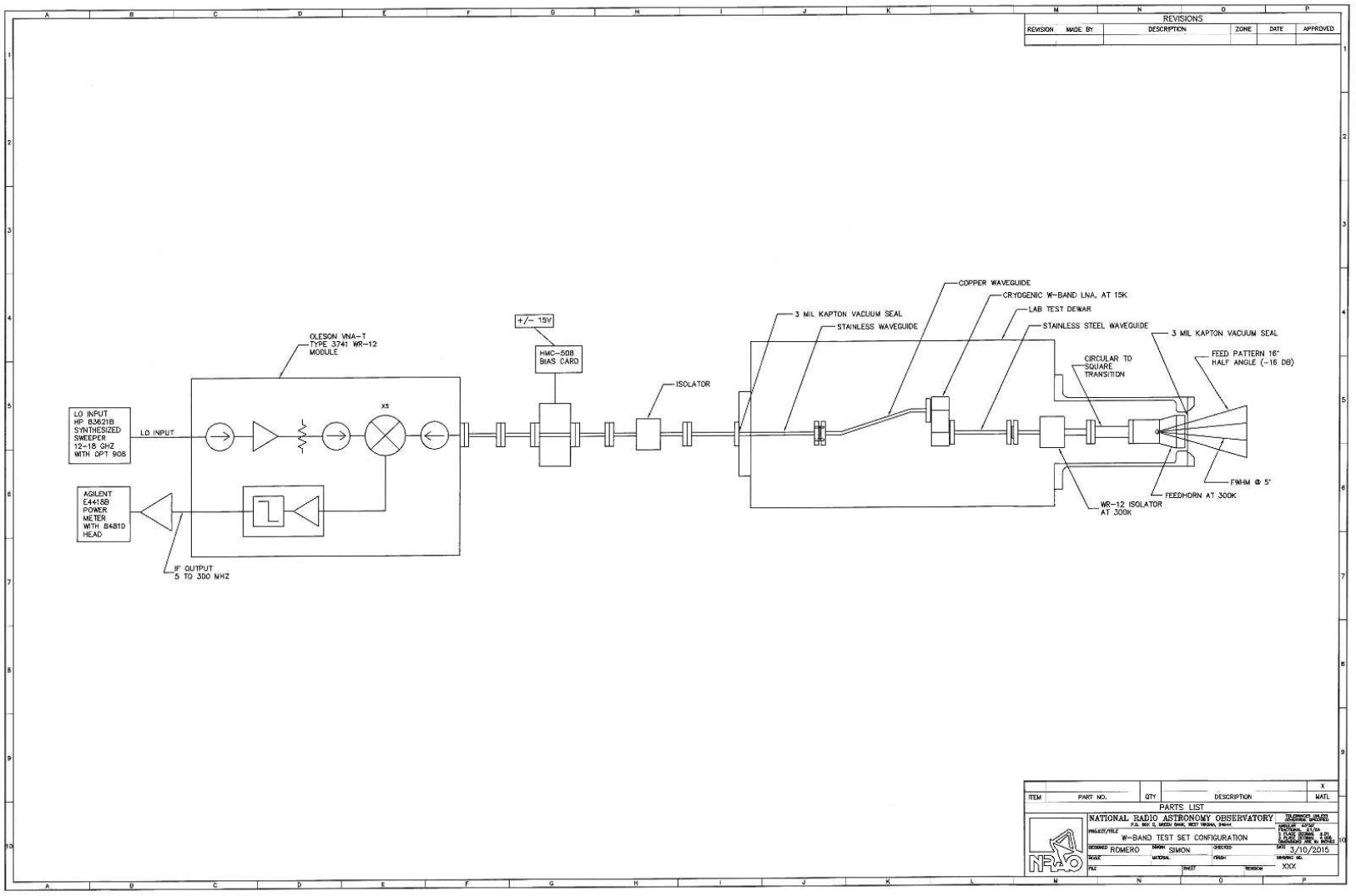

Fig. 3.3.— Courtesy of Bob Simon, the circuit diagram for the 3 mm test dewar used in window and radome tests.

enough that the reflections of the tilted (45°) sample will (a) clear the table (seen in Figures 3.2 and 3.4) on which the receiver rests, and (b) the secondary load will fully cover the beam.

Measurements with a cold primary load are a potential source of variation due to condensing water vapor. The cold primary load is kept in a bath of liquid nitrogen until measurements are ready to be taken. The cold goal is to keep the time out of the bath as short as possible, so that the primary load is heated by the air as minimally as possible.

The loads are cones 6 inches in diameter (at the base) with and 90° opening angle (i.e. its height is 3 inches). The cone is made of copper, with a plastic tube attached to the top to be used as a handle. The inside of the cone is then affixed with the microwave absorber. The copper reflects any non-absorbed signal back into the absorber. Moreover, the use of copper allows the absorber to keep its shape and temperature for the duration of a measurement.

3.3.1 Samples

In total we had six samples to test: two windows, and four radomes. The two windows were high density polyethylene (HDPE), where one had expanded teflon affixed to both sides of the material, and is termed the "matched" window, while the other window is then termed the "unmatched" window. The expanded teflon acts as an intermediate step in refractive index, thus reducing the reflected light. The radome materials tested were: Zitex G110, Eccofoam PP2 (1/8" thick), Goretex 3T20, and Goretex RA7906.

The window pieces are both $4'' \times 4'' \times 1/2''$. The radome sizes varied based on what was available in the lab, and samples were not permitted to be trimmed as they

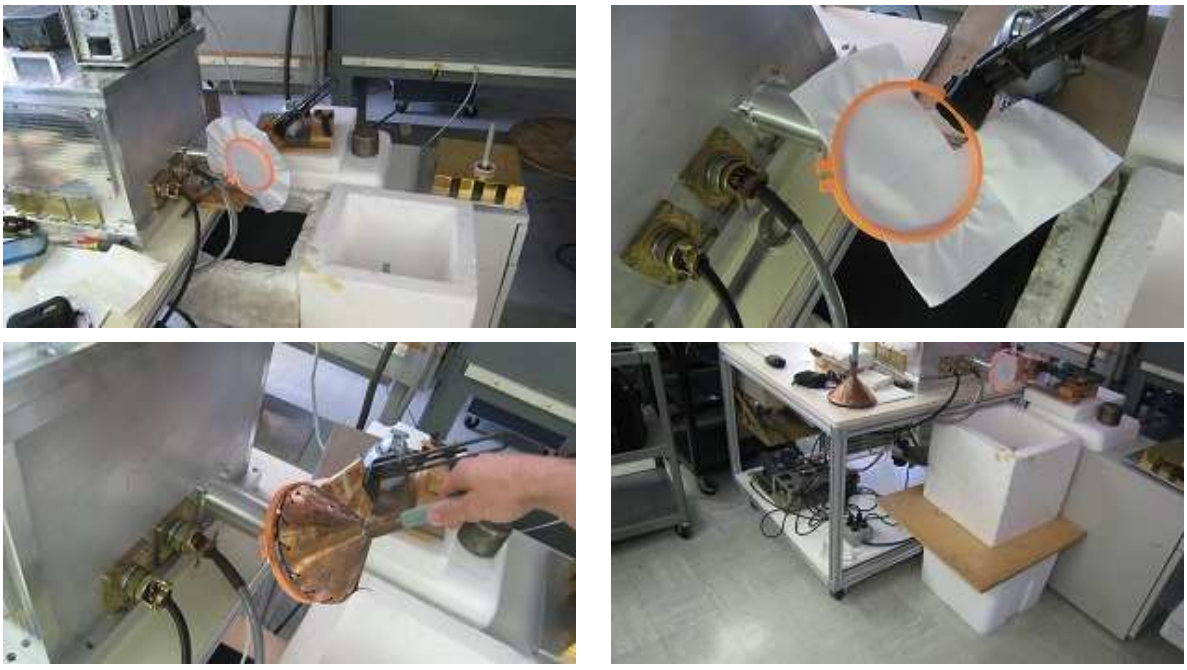

Fig. 3.4.— Upper left: Goretex 3T20 in position with hot secondary load. Upper right: Same, but with Zitex G110 Lower left: A hot primary load with no sample. Lower right: Goretex RA 7906, vertical, with a secondary load below it.

were the property of NRAO, and not of the MUSTANG team. Nonetheless, each sample had enough material to cover the receiver beam when measured vertically. In the 45° case, it is plausible that some of the samples, primarily that of Goretex RA7906 may not have fully covered the beam.

3.4 Trials

Measurements were conducted at Green Bank multiple times on June 6, 2014 and June 18, 2014. The results from June 6, 2014 established a baseline and led to refined measurement techniques used in the second visit (June 18, 2014.) In particular, this concerns the placement of the primary load when measuring the sample at a 45° angle. The preferred placement of the primary load is flush with the sample, such

that the base of the cone is also at a 45° angle. (Prior measurements kept the primary load such that the base of the cone would be vertical, which would be consistent with the placement when the sample was nearly vertical.) We discuss the reasoning for the preference in Section 3.5.

For each of the windows, to estimate the statistical errors, 10 measurements for each of the following: P^s_{C,X_C}, P^s_{H,X_C}, P^s_{C,X_H}, and P^s_{H,X_H} were taken. There are also 11 measurements of P_H and P_C (hot and cold loads with no sample). Sampling errors are then determined as the standard deviation for each of these measurements (at each frequency), to obtain $\sigma_{P^s_{C,X_C}}$, $\sigma_{P^s_{H,X_C}}$, $\sigma_{P^s_{C,X_H}}$, $\sigma_{P^s_{H,X_H}}$, σ_{P_H}, and σ_{P_C} (again, at each frequency).

Critically, no Eccofoam PP2 samples were visited on the second visit. In the second visit, the sample and load placements were carefully chosen and held constant. The radome materials were held in an embroidery ring, but the Eccofoam was too bulky to be held in the ring without risk of damage. No means to hold the Eccofoam PP2 sample tight and at a 45° presented itself.

3.5 Measurement Refinement

3.5.1 Preliminary Results

From the first trip, we are able to calculate $\mathbb{T}_{tot}$, $\mathbb{T}_{surface}$, and $\mathbb{T}_{material}$. All $\mathbb{T}_{tot}$ and $\mathbb{T}_{surface}$ values are physically plausible; however, some values of $\mathbb{T}_{material}$ are found to be greater than 1. This arises when $\mathbb{T}_{surface} < \mathbb{T}_{tot}$. Given that we have 3 methods to calculate $\mathbb{T}_{tot}$, and 2 to calculate $\mathbb{T}_{surface}$, the unphysical values of $\mathbb{T}_{material}$ arise when mismatched values of $\mathbb{T}_{tot}$ and $\mathbb{T}_{surface}$ are used.

The first, clear case, is the large discrepancy between $\mathbb{T}_{tot}$ in method 3 versus its

Time	09:18	09:20-09:40	09:41	09:43-10:09	10:10	10:12-10:34	10:35	10:37-11:17	11:18	11:20-11:55	11:57
Sample	none	All	none	All	none	All	none	Windows	none	Windows	none
Setup	–	Flat	–	45°; X_H	–	45°; X_C	–	45°; X_C	–	45°; X_H	–
Trials	1	2 each	2	2 each	2	2 each	2	8 each	2	8 each	2

Table 3.2: Trials performed during the first visit (June 6, 2014.) The temperature of a secondary load is denoted as X_H for hot and X_C for cold. No secondary load was placed for the "Flat" setup.

Time	13:20	13:40	13:54	14:39	15:00	15:22	15:35
Sample	none	RA7906	none	Goretex 3T20	none	Windows	G110 & RA7906
Setup	OI,VC,MR ; X_H	OI,10°,25°,45°; X_H	45°; X_H	45°; X_H	45°; X_H	45°; X_H	45°; X_H
Trials	6	5	2	10	8	2 each	2 & 1
Time	16:24	16:38	16:47				
Sample	G110, RA7906, and 3T20	none	Windows				
Setup	45°; X_C	45°; X_C	45°; X_C				
Trials	2 each	3	2 each				

Table 3.3: Trials from the second trip (June 18, 2014); tabulated by time and secondary load. OI, VC, and MR denote distances of the primary load to the sample: "one inch", "very close", and "mid range" respectively. If not specified, VC is assumed. For 45° this is puts the primary load as close to the sample without touching as is possible, as seen in Figure 3.4, bottom-left panel. No Eccofoam PP2 samples were measured at 45°.

values in method 1 or 2. We attribute this to standing waves between the receiver and the sample. This may have be alleviated with a more pronounced tilt of the sample for measurements used in method 3.

We also find that methods 1 and 2 are systematically offset from each other. Specifically, $\mathbb{T}^H_{tot} \leq \mathbb{T}^C_{tot}$, and $\mathbb{T}^H_{surface} \geq \mathbb{T}^C_{surface}$. One potential issue is leakage, where light not emitted from our absorbers enters the receiver, which we investigate in Section 3.5.2. However, as we'll find, this does not explain the systematic offset for a given transmission. We consider variations in sample temperature due to proximity to the cold load, but this would impart a signature in the data based on the time each measurement takes (5 seconds). That is, as it steps through frequencies, if the sample were being cooled, we would see this when comparing $P^s_{C,X}$ to $P^s_{H,X}$, which we do not.

Quantity	Method 1	σ_1	Method 2	σ_2	Method 3	σ_3	Material
$\mathbb{T}_{tot}$	0.78	0.007	0.77	0.003	0.96	0.01	Unmatched Window
$\mathbb{T}_{surface}$	0.85	0.004	0.85	0.006			
$\mathbb{T}_{material}$	0.92	0.006					
$\mathbb{T}_{tot}$	0.87	0.003	0.90	0.004	0.98	0.01	Matched Window
$\mathbb{T}_{surface}$	0.95	0.003	0.97	0.004			
$\mathbb{T}_{material}$	0.92	0.003					

Table 3.4: Initial results for transmission properties of the window samples. Uncertainties are calculated from the statistical error found across the 10 sets of measurements.

3.5.2 Accounting for Leakage

Our initial results likely suggest that there is leakage into our receiver. That is, power from loads other than the intended primary or secondary loads are entering into the receiver.

We thus want to find the fractional power that is being observed at various loca-

Quantity	Method 1	σ_1	Method 2	σ_2	Method 3	σ_3	Material
$\mathbb{T}_{tot}$	0.90	–	0.90	–	1.00	–	Eccofoam PP2
$\mathbb{T}_{surface}$	1.03	–	1.03	–			
$\mathbb{T}_{material}$	< 0.90	–					
$\mathbb{T}_{tot}$	0.91	–	0.90	–	0.99	–	Zitex G110
$\mathbb{T}_{surface}$	1.02	–	1.02	–			
$\mathbb{T}_{material}$	< 0.90	–					
$\mathbb{T}_{tot}$	0.74	–	0.71	–	0.95	–	Goretex 3T20
$\mathbb{T}_{surface}$	1.00	–	0.96	–			
$\mathbb{T}_{material}$	0.74	–					
$\mathbb{T}_{tot}$	0.80	–	0.72	–	0.99	–	Goretex RA7906
$\mathbb{T}_{surface}$	1.01	–	0.92	–			
$\mathbb{T}_{material}$	0.79	–					

Table 3.5: Initial results for transmission properties of the radome samples. No uncertainties are reported because we did not take a sufficient number of measurements to calculate a standard deviation. It is reasonable to assume the statistical uncertainties are roughly those reported for the window samples.

tions: (1) from the primary load, (2) from a secondary load, and (3) spillover from the room, when no sample is placed in front of any of the loads. We denote the fractions by α', β', and γ' respectively and have the restriction that $1 = \alpha' + \beta' + \gamma'$. Adopting $g = k_B GB$, we write:

$$P_{H,H} = g(T_R + \alpha' T_H + \beta' T_H + \gamma' T_H), \tag{3.20}$$

$$P_{C,H} = g(T_R + \alpha' T_C + \beta' T_H + \gamma' T_H), \tag{3.21}$$

$$P_{H,C} = g(T_R + \alpha' T_H + \beta' T_C + \gamma' T_H), and \tag{3.22}$$

$$P_{C,C} = g(T_R + \alpha' T_C + \beta' T_C + \gamma' T_H). \tag{3.23}$$

Here, the first and second subscripts denote the temperature of the primary load and secondary loads, respectively. The notation used in P^s_{C,X_C}, for instance, is not used because there is no sample to give the ^{s}, and thus there is no reflection of a surface of T_X by a sample.

For measurements made where the primary load was held horizontally, we find $\alpha' = 0.932$, $\beta' = 0.077$, $\gamma' = -0.009$. Clearly, $\gamma' < 0$ is unphysical, but it is consistent with 0 given that the uncertainty in each α', β', and γ' is roughly 0.03. However, the measurements with a 45° sample then also have the primary load at 45°, and these are the measurements with which we are more concerned. We then denote a no sample measurement made with the primary load in this diagonal position as $P^d_{C,H}$. Investigating the case where the only cold load is the primary load, we write the received power as:

$$P_{C,H} = g(T_R + \alpha' T_C + (\beta' + \gamma')T_H) \text{and} \tag{3.24}$$

$$P^d_{C,H} = g(T_R + \alpha'(\lambda T_C + \omega T_H) + (\beta' + \gamma')T_H). \tag{3.25}$$

Here, λ is the fraction angular extent that the diagonal primary load occupies relative to the horizontal primary load. Conversely, ω is the fraction of the angular extent that was occupied by the horizontal primary load, but is vacated when the primary load is placed diagonally. Constraining $1 = \omega + \lambda$, we find $\lambda = 0.96$ (and $\omega = 0.04$) and modify our previous definitions of α', β', and γ', such that $\alpha = \alpha'\lambda = 0.89$, $\beta = \beta' = 0.08$, $\gamma = \gamma' + \alpha'\omega = 0.03$. That is to say, the sample (and diagonal primary load) will account for 89% of radiation entering the receiver, the (unreflected) secondary load accounts for 8%, and the remaining 3% of is due to stray light in the room.

Refined Calculations

We then have the following equations for the power received for the 45° cases (with samples).

$$P^{s'}_{H,X_C} = g(\alpha[T_H\mathbb{T}_{surface}\mathbb{T}_{material} + T_H\mathbb{T}_{surface} * (1-\mathbb{T}_{material})] + T_C(1-\mathbb{T}_{surface}) + T_R + \beta T_C + \gamma T_H)$$

$$P^{s'}_{C,X_C} = g(\alpha[T_C\mathbb{T}_{surface}\mathbb{T}_{material} + T_H\mathbb{T}_{surface}(1-\mathbb{T}_{material})] + T_C(1-\mathbb{T}_{surface}) + T_R + \beta T_C + \gamma T_H)$$

$$P^{s'}_{H,X_H} = g(\alpha[T_H\mathbb{T}_{surface}\mathbb{T}_{material} + T_H\mathbb{T}_{surface}(1-\mathbb{T}_{material})] + T_H(1-\mathbb{T}_{surface}) + T_R + \beta T_H + \gamma T_H)$$

$$P^{s'}_{C,X_H} = g(\alpha T_C[\mathbb{T}_{surface}\mathbb{T}_{material} + T_H\mathbb{T}_{surface}(1-\mathbb{T}_{material})] + T_H(1-\mathbb{T}_{surface}) + T_R + \beta T_H + \gamma T_H)$$

and the following equations for the power received for the diagonal (45°) loads with no samples:

$$P^{d'}_{H,C} = g(T_R + \alpha T_H + \beta T_C + \gamma T_H) = \alpha P_H + g([1-\alpha]T_R + \beta T_C + \gamma T_H) \quad (3.26)$$

$$P^{d'}_{C,C} = g(T_R + \alpha T_C + \beta T_C + \gamma T_H) = \alpha P_C + g([1-\alpha]T_R + \beta T_C + \gamma T_H) \quad (3.27)$$

$$P^{d'}_{H,H} = g(T_R + \alpha T_H + \beta T_H + \gamma T_H) = \alpha P_H + g([1-\alpha]T_R + \beta T_H + \gamma T_H) \quad (3.28)$$

$$P^{d'}_{C,H} = g(T_R + \alpha T_C + \beta T_H + \gamma T_H) = \alpha P_C + g([1-\alpha]T_R + \beta T_H + \gamma T_H) \quad (3.29)$$

Furthermore, we can cast these equations in terms of the initial equations:

$$P^{s'}_{H,X_C} = \alpha P^{s}_{H,X_C} + g([1-\alpha]T_R + \beta T_C + \gamma T_H)$$

$$P^{s'}_{C,X_C} = \alpha P^{s}_{C,X_C} + g([1-\alpha]T_R + \beta T_C + \gamma T_H)$$

$$P^{s'}_{H,X_H} = \alpha P^{s}_{H,X_H} + g([1-\alpha]T_R + \beta T_H + \gamma T_H)$$

$$P^{s'}_{C,X_H} = \alpha P^{s}_{C,X_H} + g([1-\alpha]T_R + \beta T_H + \gamma T_H)$$

We can now re-solve for the transmission values with the more accurate equations:

$$\mathbb{T}_{tot}^{C'} = \frac{P_{H,X_C}^{s'} - P_{H,X_C}^{s'}}{P_{H,C}^{d'} - P_{C,C}^{d'}} \text{or} \tag{3.30}$$

$$\mathbb{T}_{tot}^{C'} = \frac{P_{H,X_C}^{s'} - P_{H,X_C}^{s'}}{P_{H,H}^{d'} - P_{C,H}^{d'}} \text{and then} \tag{3.31}$$

$$\mathbb{T}_{tot}^{H'} = \frac{P_{H,X_H}^{s'} - P_{H,X_H}^{s'}}{P_{H,C}^{d'} - P_{C,C}^{d'}} \text{or} \tag{3.32}$$

$$\mathbb{T}_{tot}^{H'} = \frac{P_{H,X_H}^{s'} - P_{H,X_H}^{s'}}{P_{H,H}^{d'} - P_{C,H}^{d'}} \tag{3.33}$$

Where the superscript in $\mathbb{T}_{tot}^{H'}$ denotes the value of the secondary when the sample is inserted. However, in the interest of limiting changing variables, Equations 3.30 and 3.33 are preferred.

We are now in a position to assess how the desired transmission quantities, denoted with a prime ($'$), and based on the 45° sample measurements, compare to previously calculated quantities. A transmission quantity with ^{mis} in the superscript will denote that a mismatch of load placement has occurred between the sample and no-sample measurements. In particular, the initial results for the 45° samples used no-sample measurements where the primary loads were placed horizontally, and much closer to the receiver than their placement with the sample. Finally, if neither $'$ or ^{mis} is present, then we take this to mean that the sample and no-sample measurements differ in only the presence of the sample. The relation to the mismatched cases is given as an approximation because, despite the notion that the load fully covers the receiver beam, the same analysis to determine any leakage from the horizontal load position has not been performed.

This resolves the issue that some values of $\mathbb{T}_{surface}$ were very close, or greater than, 1, as reported in Table 3.5. For reference, an assumed mismatched $\mathbb{T}_{surface}$ of

1.0, the correct value, $\mathbb{T}'_{surface}$, would be 0.91.

There are still some nuances to consider. Most notably, the radome samples were secured in an embroidery ring of diameter 6″, which is exactly matched to the diameter of the primary hot and cold loads. A likely inconsequential imperfection is the embroidery ring itself being visible to the receiver; the worrisome systematic is that the radome always had some excess material outside of the embroidery ring. Goretex RA7906 should have had the largest of this (the whole sheet was a circle with a diameter of perhaps 20″, while the Goretex 3T20 was a circle of something just over 12″ diameter. Finally, the Zitex G110 was an odd piece that was roughly a $9'' \times 9''$ square, with a $4.5'' \times 4.5''$ square missing from a corner. This means that there was inherently some radome "missing" inside the embroidery ring (but it was pretty well filled). In our variable lexicon, α will not change. Where γ is the fraction of the beam that is seeing the room (at T_H), more of the beam is now seeing the radome which is roughly reflecting the beam into the cold load. Thus, we have: $\beta \leq \beta^s \leq \beta + \gamma$, where β^s is the effective β with a radome sample inserted (due to excess material). Of course, $0 \leq \gamma^s \leq \gamma$. However, we do not expect this to be significant and do not attempt to constrain γ^s or β^s here.

$\mathbb{T}^{C'}_{tot} = \mathbb{T}^{C}_{tot}$	$\mathbb{T}^{C'}_{tot} \approx \frac{\mathbb{T}^{C,mis}_{tot}}{\alpha}$	$\mathbb{T}^{C'}_{surface} = \mathbb{T}^{C}_{surface} + \frac{\beta}{\alpha}$	$\mathbb{T}^{C'}_{surface} \approx \frac{\mathbb{T}^{C,mis}_{surface} - 2\beta - \gamma}{\alpha}$
$\mathbb{T}^{H'}_{tot} = \mathbb{T}^{H}_{tot}$	$\mathbb{T}^{H'}_{tot} \approx \frac{\mathbb{T}^{H,mis}_{tot}}{\alpha}$	$\mathbb{T}^{H'}_{surface} = \mathbb{T}^{H}_{surface} + \frac{\beta}{\alpha}$	$\mathbb{T}^{H'}_{surface} \approx \frac{\mathbb{T}^{H,mis}_{surface} - 2\beta - \gamma}{\alpha}$

Table 3.6: A table of transmission corrections. The desired quantities have a $'$ and are on the left of any equality. Transmission quantities with ^{mis} denote the no-sample power measurements were performed in a mismatched manner to the sample power measurements. No superscript means the power measurements were performed correctly, but a correction still needs to be applied.

3.5.3 Final Results

The measurements on the second trip (Table 3.3) were taken with care to consistently place both samples and loads. A few different positions were measured to reaffirm the hypothesis that the horizontal sample would create standing waves. We therefore discard method 3 for measuring $\mathbb{T}_{tot}$. In calculating our values, we then prefer the diagonal sample and primary load, which we then correct for leakage.

For the results listed below, where errors are reported, those values have been calculated via a weighted average, and the reported uncertainty is given as $\frac{1}{\sqrt{\sum w_i}}$, where the weights are given as $w_i = \frac{1}{\sigma_i^2}$. In doing this average, the assumption is that the transmission should be (roughly) constant across the frequency range. This is seen. For example, for the matched window, $\mathbb{T}_{material}$ ranges from 0.905 to 0.930, where the error bars are roughly 0.015. Thus, there are variations at the 2σ level across the frequencies. All reported uncertainties are statistical.

3.6 Discussion

We see that the offsets $\mathbb{T}^H_{tot} \leq \mathbb{T}^C_{tot}$ and $\mathbb{T}^H_{surface} \geq \mathbb{T}^C_{surface}$ persist. This is as yet unresolved and highlights that our statistical uncertainties severely underestimate the uncertainties in our measurements. Despite the identified inconsistencies, our data are generally consistent. The properties of the windows are in relative agreement, especially $\mathbb{T}_{material}$, which should be the same between the two window samples. Moreover, $\mathbb{T}_{material}$ appears quite consistent across methods for both window and radome samples. Finally, our derived values are generally consistent with other values in the literature and other tests done by the MUSTANG team.

We see that Zitex G110 has very favorable absorption properties. While Eccofoam

Quantity	Method 1	σ_1	Method 2	σ_2	Material
$\mathbb{T}_{tot}$	0.79	0.007	0.83	0.003	Unmatched Window
$\mathbb{T}_{surface}$	0.86	0.004	0.88	0.006	
$\mathbb{T}_{material}$	0.91	0.006	0.94		
$\mathbb{T}_{tot}$	0.91	0.003	0.94	0.004	Matched Window
$\mathbb{T}_{surface}$	0.95	0.003	0.97	0.004	
$\mathbb{T}_{material}$	0.96	0.003	0.96	0.004	

Table 3.7: Final results, leakage-corrected, for the window samples. Uncertainties are calculated from the statistical error found across the 10 sets of measurements.

Quantity	Method 1	σ_1	Method 2	σ_2	Material
$\mathbb{T}_{tot}$	0.95	–	0.98	–	Zitex G110
$\mathbb{T}_{surface}$	0.98	–	1.01	–	
$\mathbb{T}_{material}$	0.97	–	0.97	–	
$\mathbb{T}_{tot}$	0.77	–	0.86	–	Goretex 3T20
$\mathbb{T}_{surface}$	0.84	–	0.93	–	
$\mathbb{T}_{material}$	0.91	–	0.92	–	
$\mathbb{T}_{tot}$	0.83	–	0.89	–	Goretex RA7906
$\mathbb{T}_{surface}$	0.96	–	1.01	–	
$\mathbb{T}_{material}$	0.87	–	0.88	–	

Table 3.8: Final results, leakage-corrected, for the radome samples. As before, no uncertainties are reported because we did not take a sufficient number of measurements to calculate a standard deviation. It is reasonable to assume the statistical uncertainties are roughly those reported for the window samples. No Eccofoam PP2 measurements were taken for the second visit.

PP2 was not measured in the second run of trials, its properties in the first trials were similar to Zitex G110, and we expect that had we measured it again, we would again find consistent values with Zitex G110. Thus, with acceptable absorption properties, either Zitex G110 or Eccofoam PP2 were candidate materials for use on MUSTANG-1.5 (and subsequently MUSTANG-2). The MUSTANG team decided to use Eccofoam PP2 largely in part because of this study and Eccofoam PP2 is designed to be a radome material, so is suspected to be sturdier than Zitex G110.

Chapter 4

Pressure Profile Analysis

Abstract

Determining pressure profiles of clusters is particularly valuable for a sizable and universally representative sample (see Section 1.2). Specifically, assessing the scatter in pressure profiles within different radial regimes provides insight to the relevant physical processes and regularity within those regimes (Section 1.2.2). While the SZ effect is revealing in itself, we choose a sample of clusters which has a wealth of multiwavelength observations so that the interpretation of pressure profiles may be explored, even beyond this current work.

This chapter will first introduce some widely used models for the pressure profile of clusters (Section 4.1), then will discuss how we can fit those models to our data (Section 4.2), and the results from fitting to our data (Section 4.3). A brief comparison with X-ray data is discussed in Section 4.3.16, while in-depth analyses and interpretations of the fitted pressure profiles in comparison to X-ray derived values are found in Chapter 5.

4.1 Pressure Profiles Models

4.1.1 Introduction

As stated in Section 1.2.2, determining pressure profiles of galaxy clusters provides insights into the relevance and frequency of physical processes within the clusters. A variety of profiles has been used over the years; the isothermal beta model (Cavaliere & Fusco-Femiano 1978) has been one of the most commonly used models (Sarazin 1988; Reiprich & Böhringer 2002; Birkinshaw & Lancaster 2008). The gas mass density in the isothermal beta model is of the form:

$$\rho_g(r) = \rho_{g,0}\left(1 + \frac{r^2}{r_c^2}\right)^{-\frac{3}{2}\beta} \tag{4.1}$$

where $\rho_{g,0}$ is the central gas mass density, r_c is the core radius, and β is a free parameter with typical values between 0.65 and 0.75 (Jones & Forman 1984; Birkinshaw & Lancaster 2008). It should be noted that $\beta < 1$ results in an infinite mass cluster if integrated to infinity, but some deviation occurs fairly far into the cluster outskirts. For a gas of uniform metallicity (the standard assumption), and recalling Equation 1.2, the isothermal beta model yields:

$$y(\theta) = y_0\left(1 + \frac{\theta^2}{\theta_c^2}\right)^{\frac{1}{2}-\frac{3}{2}\beta}. \tag{4.2}$$

The isothermal beta model was developed by relating the thermal energy of the ICM to the specific kinetic energy of galaxies. Furthermore, hydrostatic equilibrium of the ICM under spherical symmetry:

$$\frac{dP}{dr} = -\rho g, \tag{4.3}$$

and an equation of state are assumed. In Equation 4.3, P is the (gas) pressure, ρ is the total density, and g is the gravitational acceleration. This model is in contrast to a King model (King 1966), which starts from the virial theorem to find possible density distributions (initially developed for star clusters). Both the King model and isothermal beta model were able to fit the data for the Coma cluster (Cavaliere & Fusco-Femiano 1978), but the advantage that the isothermal beta model is analytically integrable provides a compelling reason for its use, especially when either model is sufficient for fitting the data.

With the advent of numerical cosmological simulations of dark matter halos, Navarro, Frenk, and White (NFW, Navarro et al. 1996) found the density profile of the cold dark matter (CDM) was well described by:

$$\rho = \frac{\rho_0}{(r/r_s)(1 + r/r_s)^2}, \tag{4.4}$$

where r_s is a scale radius, and ρ_0 is a normalization for the profile (hereafter NFW profile). This CDM profile has been generalized in order to describe the pressure profile of the ICM. Such generalizations are plausible because the dark matter constitutes over 80% of the matter in clusters of galaxies (Allen et al. 2004; Ettori et al. 2009; Vikhlinin et al. 2009). One profile generalization from Bulbul et al. (2010) (hereafter B10) takes the form:

$$\rho_{tot} = \frac{\rho_0}{(r/r_s)(1 + r/r_s)^\beta}. \tag{4.5}$$

This formulation allows the total enclosed mass to be calculated analytically, and thus allows the right hand side of Equation 4.3 to be calculated. With the additional assumptions of a polytropic equation of state ($P = k\rho^\gamma$) and HSE, the B10 pressure

profile can be determined analytically as well as:

$$P(r) = P_0 \left(\frac{1}{(\beta - 2)} \frac{(1 + r/r_s)^{\beta-2} - 1}{(r/r_s)(1 + r/r_s)^{\beta-2}} \right)^{n+1}, \tag{4.6}$$

where P is the electron pressure and n is the polytropic index ($\gamma = n + 1$).

Yet another generalization of the NFW profile is proposed in Nagai et al. (2007), hereafter gNFW:

$$\tilde{P}_e = \frac{P_0}{(C_{500}X)^\gamma [1 + (C_{500}X)^\alpha]^{(\beta-\gamma)/\alpha}} \tag{4.7}$$

where $X = r/r_{500}$, and C_{500} is the fitted concentration parameter; one can also write $(C_{500}X)$ as (r/r_s), where $r_s = r_{500}/C_{500}$. The radius r_{500} is defined as the radius in which the enclosed mass density is 500 times the critical density of the universe, ρ_{crit}, at the redshift of the cluster. $\tilde{P}$ is the electron pressure in units of the characteristic pressure P_{500}. P_{500} is defined as $P_{500} = n_{g,500} k_B T_{500}$, where $n_{g,500} = 500 f_b \rho_{crit}/(\mu m_p)$, f_b is the cosmological baryon fraction ($f_b = \Omega_b/\Omega_m$, μ is mean molecular weight, and m_p is the mass of the proton. T_{500} is defined by invoking the Virial theorem, such that:

$$k_B T_{500} = \frac{G M_{500} \mu m_p}{2 r_{500}}. \tag{4.8}$$

For self-similar evolution (Kaiser 1986; Voit 2005), T_{500} and P_{500} can be expressed as (Nagai et al. 2007):

$$T_{500} = 11.05\,\mathrm{keV} \left(\frac{M_{500}}{10^{15} h^{-1} M_\odot} \right)^{2/3} E(z)^{2/3} \text{ and} \tag{4.9}$$

$$P_{500} = 1.45 \times 10^{-11} \mathrm{erg\ cm^{-3}} \left(\frac{M_{500}}{10^{15} h^{-1} M_\odot} \right)^{2/3} E(z)^{2/3}. \tag{4.10}$$

$$\tag{4.11}$$

While the B10 profile allows for distinct electron density and temperature profiles, therefore allowing easier application to both X-ray and SZ observations, it has not garnered as much traction as the gNFW profile (Mroczkowski et al. 2009; Arnaud et al. 2010; Planck Collaboration et al. 2013; Sayers et al. 2013). Due to its relative popularity, and therefore potential for comparison, we choose to adopt the gNFW pressure profile when modeling the bulk ICM.

4.2 Joint Fitting

In attempting to constrain pressure profiles, we want to cover a large radial range, and seek to cover out to at least r_{500}, which is made reference to in the gNFW pressure profile we adopt in our modeling (Equation 4.7). This reference is in part because $C_{500} \sim 1$ in past results (cf. Nagai et al. 2007; Mroczkowski et al. 2009; Arnaud et al. 2010; Planck Collaboration et al. 2013; Sayers et al. 2013), so $r_s \sim r_{500}$, but also the relative importance of quantities measured at, or out to, r_{500}, as discussed in Section 1.2.1, especially those used in scaling relations. A typical massive cluster has 1 Mpc$< r_{500} <$ 2 Mpc. The angular extent will depend on the redshift, but for $0.2 < z < 0.9$, this corresponds roughly to $2' < \theta_{500} < 6'$. Thus, we seek to jointly fit MUSTANG and Bolocam data, whose resolutions are $9''$ and $58''$ respectively and whose FOVs are $42''$ and $8'$respectively.

Jointly fitting MUSTANG and Bolocam data is also favorable as they are both SZ instruments, observing at fairly close frequencies, so they should be observing the same processes. More critically, they both observe and record data (Section 2.2) in the same manner, which make the two data sets very compatible for joint fitting. Both instruments record their data as time-ordered data (TOD), also called timestreams, and so it is conceivable to attempt to jointly fit the two data sets in the time domain.

In fact, this was attempted and is discussed in Appendix G, but we were unsatisfied with the performance of this approach.

Instead, we adopted a means to jointly fit the data in the map domain, as we had already made progress to fitting models to MUSTANG maps. Rather than attempt to deproject our SZ data, we choose to a forward modelling approach and fit our models after filtering sky maps (Section 2.4.4). Inherent in this approach is the assumption that our (total) model is a linear combination of individual model components, where the individual components of concern are: (1) a bulk cluster pressure profile, (2) a mean level, (3) a point source (if any), and (4) a residual component (if any). This linear combination can be written as:

$$\vec{d}_m = \mathbf{A}\vec{a}_m, \tag{4.12}$$

where d_m is the total model, each column in $\mathbf{A}$ is a model component, and $\vec{a}_m$ is an array of amplitudes of the components. Thus, $\mathbf{A}$ is a $M \times N$ matrix, where N is the number of data points in our data array, $\vec{d}$, and M is the number of model components used. The construction of $\vec{d}$ is is chosen to exclude pixels with low coverage; principally we select the inner radial arcminute of the MUSTANG maps, and a $14' \times 14'$box for Bolocam data. $\vec{d}_m$ is constructed for the exact same pixel selection, where the astrometry and pixelization is ensured to be the same across maps. Since this is done in map space, and our data, $\vec{d}$ have been filtered, we must filter our model components in the same manner, as discussed in Section 2.4.4. Thus, the model components referred to in this section should be understood to be the *filtered* model components. For each cluster, a bulk pressure component is always included.

To produce a sky model, we integrate the 3D gNFW pressure profile, which is

taken to be spherical, along the line of sight to produce a Compton y profile, given as

$$y(R) = \frac{P_{500}\sigma_T}{m_e c^2} \int_{-\infty}^{\infty} \tilde{P}(R,l)dl, \tag{4.13}$$

where $r^2 = R^2 + l^2$, R is the projected radius, and l is the distance from the center of the cluster along the line of sight. In practice, $(\pm)5R_{500}$ is used instead of $(\pm)\infty$, where we have verified that integration out to $(\pm)20R_{500}$ amounts to less than a 1% variation in $y(R)$ values. Once integrated, $y(R)$ is gridded as $y(\theta)$ and is realized as maps for MUSTANG and Bolocam (pixels of $1''$ and $20''$ on a side, respectively) using the *Archive of Chandra Cluster Entropy Profile Tables* (ACCEPT, Cavagnolo et al. (2009)) centroid for the cluster. From here, we produce two model maps: one for Bolocam and one for MUSTANG. In each case, we convolve the Compton y map by the appropriate beam shape. For Bolocam we use a Gaussian with FWHM = $58''$, and for MUSTANG we use the double Gaussian as determined in Section 2.4.5

We can then use the χ^2 statistic as our goodness of fit,

$$\chi^2 = (\vec{d} - \vec{d_m})^T \mathbf{N}^{-1} (\vec{d} - \vec{d_m}), \tag{4.14}$$

and find that the minimum χ^2 is achieved when:

$$\vec{a}_m = (\mathbf{A}^T \mathbf{N}^{-1} \mathbf{A})^{-1} \mathbf{A}^T \mathbf{N}^{-1} \vec{d}. \tag{4.15}$$

Here, $\mathbf{N}$ is the covariance matrix, which is formally defined as:

$$\mathbf{N}_{ij} = < d_i d_j > - < d_i >< d_j > \tag{4.16}$$

Here, d_i is the pixel value in a noise realization map, and the average is taken for a

given pixel of several noise realization maps (see Section 4.2.1).

To fit models jointly to MUSTANG and Bolocam data, we simply append the MUSTANG data array to the Bolocam data array, and do the same for the model arrays as:

$$\vec{d} = [\vec{d}_{Bolocam}, \vec{d}_{MUSTANG}] \tag{4.17}$$

$$\vec{d}_m = [\vec{d}_{m,Bolocam}, \vec{d}_{m,MUSTANG}], \tag{4.18}$$

then solving this set of equations would be a linear problem. We add a calibration offset term, k to allow for offsets in calibration between MUSTANG and Bolocam data. We leave Equation 4.17 as such because we expect there may be a calibration offset between instruments. We quantify the calibration uncertainties and thus put a prior on it. Solving Equation 4.15 is no longer a problem of linearly independent variables. Thus, we use a Levenberg-Marquardt least squares minimization routine, MPFIT (Markwardt 2009), to quickly solve for $\vec{a}_m$ and obtain a pseudo-χ^2: $\tilde{\chi}^2$. To calculate $\tilde{\chi}^2$, we use the same formulation as above, but redefine

$$\vec{d}_{cal} = [\vec{d}_{Bolocam}, \vec{d}_{MUSTANG}, 1.0]$$
$$\vec{d}_{m,cal} = [\vec{d}_{m,Bolocam}, k * \vec{d}_{m,MUSTANG}, k] = \mathbf{A}_{new}\vec{a}_{m,cal}$$

where $\vec{a}_{m,cal} = [\vec{a}_m, k]$, and expand $\mathbf{N}$ to $\mathbf{N}_{cal}$, which allows for the extra fitted value:

$$\mathbf{N}_{cal} = \begin{pmatrix} \mathbf{N} & \vec{0} \\ \vec{0} & \sigma_{cal}^2 \end{pmatrix}, \tag{4.19}$$

where σ_{cal} is the relative calibration uncertainty. We adopt a calibration uncertainty of 11.2%, the quadrature sum of the relative calibration accuracies of Bolocam and

MUSTANG cited in Section 2.3. Thus, our final goodness of fit is given by:

$$\tilde{\chi}^2 = (\vec{d}_{cal} - \vec{d}_{m,cal})^T \mathbf{N}_{cal}^{-1} (\vec{d}_{cal} - \vec{d}_{m,cal}). \tag{4.20}$$

4.2.1 Noise Considerations

In practice, we take $\mathbf{N}_{ij}$ to be a diagonal matrix for MUSTANG and Bolocam, with $\mathbf{N}_{ij} = \delta_{ij}/w_i$, where δ_{ij} is the Kronecker delta, and w_i is the weight for pixel i. MUSTANG's detector noise is dominated by phonon noise; thus with the common mode (which is dominated by atmospheric noise) subtracted, we expect the map pixel noise to be uncorrelated. Figure 4.1 confirms that the diagonal matrix is a good approximation for MUSTANG when gridded with $1''$ pixels. We note that the correlation matrix depends on pixelization, and that some correlation becomes evident as pixel size increases. There does not appear to be a noticeable trend with correlation as a function of map pixel separation, and the standard deviation of off-diagonal terms, over the full 11000×11000 correlation matrix, is 0.031.

While $\Delta\chi^2$ may be used for determining confidence intervals on fitted parameters, as in Figure 4.2, we wish to attempt to account for correlated noise in our pixels (a non-diagonal covariance matrix), especially in the Bolocam maps. To do this, we follow Sayers et al. (2011) and calculate the 68.5% (1σ) confidence interval of the best fits over 1000 noise realizations added to model clusters. The noise realizations for Bolocam are precomputed from previous work (Sayers et al. 2013), where the TODs are jack-knifed. Noise realizations for MUSTANG are computed by random number generation with Gaussian distribution for each pixel, with $\sigma_i = \sqrt{1/w_i}$, based on the same weight used to calculate the noise matrix. This also helps address the point that our calibration offset, k, is not an independent parameter, and the results

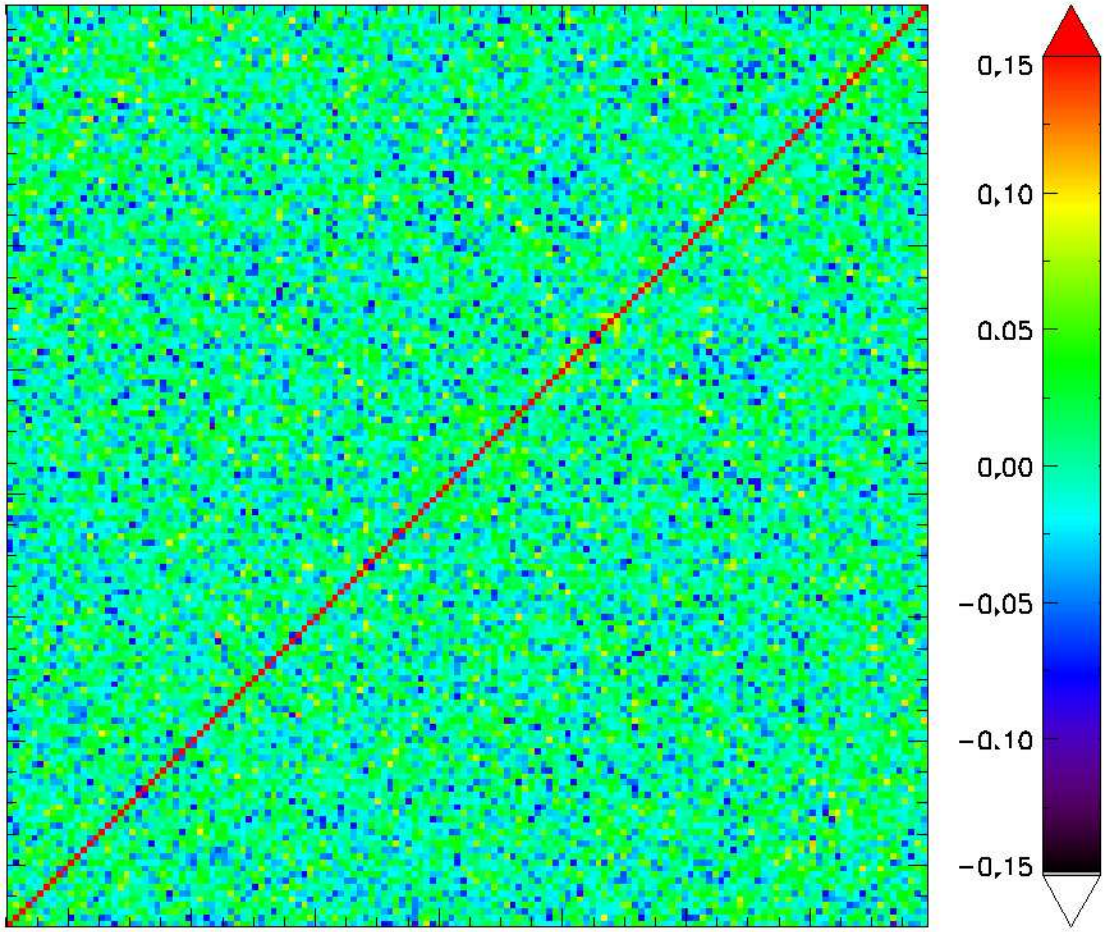

Fig. 4.1.— A cropped portion of the correlation matrix produced from 1000 jackknives of our data for the central arcminute of a MUSTANG map, with 1″ pixelization. For clarity, the image here shows the central 150 × 150 elements of the correlation matrix; this central region is representative of the full matrix for the region, which is 11000 × 11000 elements.

of these fits for an example cluster, Abell 1835, is shown in Figure 4.10. These fits are tabulated and used to rescale the $\Delta\chi^2$ confidence intervals as seen in Figure 4.2. The rescaling of the confidence intervals is primarily due to the non-diagonality of the noise in the Bolocam covariance matrix.

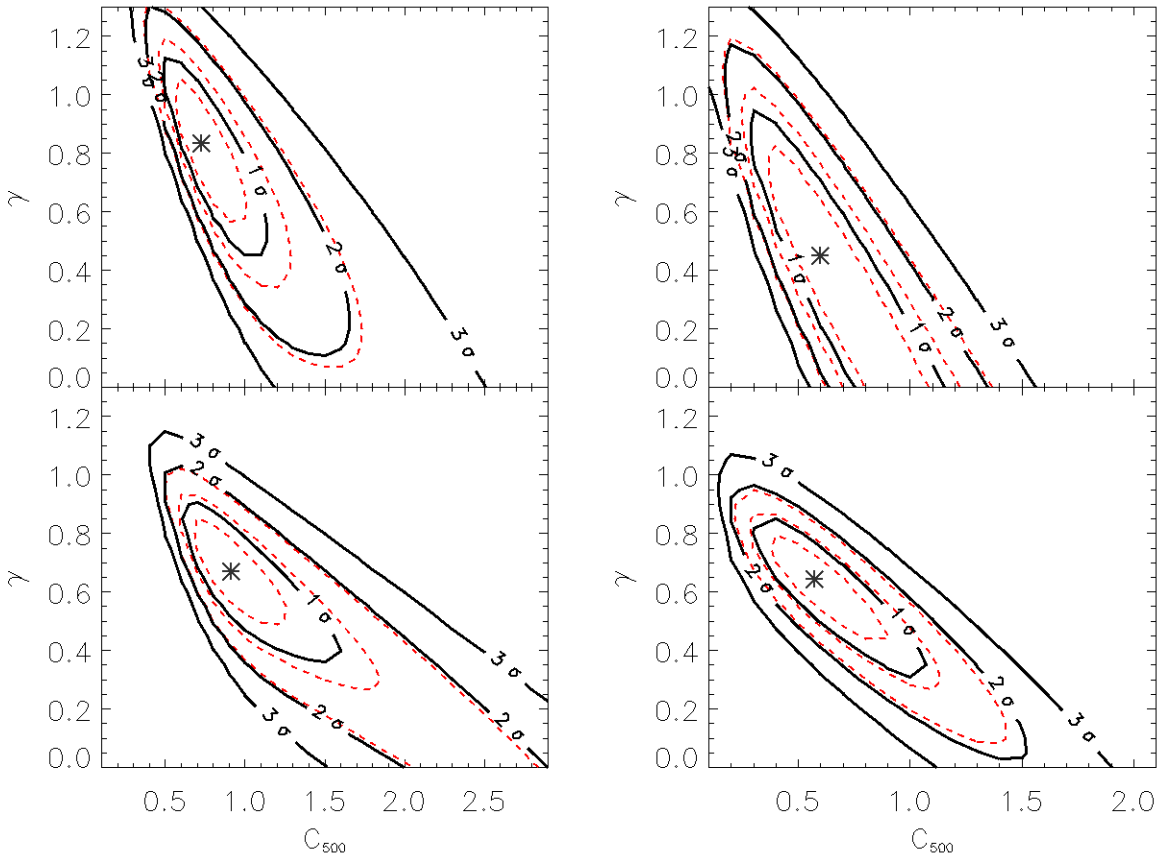

Fig. 4.2.— Confidence intervals for Abell 1835 (left) and MACS 0647 (right). Top panels show the confidence intervals for Bolocam only fits. Bottom panels show the confidence intervals for the joint fit. Dashed lines show confidence intervals based on $\Delta\chi^2$. Solid lines are confidence intervals rescaled based on the bootstrap MC results. The asterisks denote the best fit.

4.2.2 Point Source Model maps

While we clearly detect point sources in Abell 1835, MACS 1115, MACS 0429, MACS 1206, RXJ1347, MACS 1423, and MACS 0717 in the MUSTANG maps. A point source is identified by NIKA (Adam et al. 2015) in CLJ1226. For the Bolocam image, the point sources in Abell 1835, MACS 0429, RXJ1347, and MACS 1423 has been subtracted based on an extrapolation of a power law fit to the 1.4 GHz NVSS (Condon et al. 1998) and 30 GHz SZA (Mroczkowski et al. 2009) measurements (Sayers et al.

2012). The flux densities for the point sources fitted are shown in Table 4.1.

For MUSTANG, where a point source is detected at high significance in our galaxy cluster map, we take the following approach:

1. For each cluster, the same process for beam fitting as in Section 2.4.5 is applied to only those secondary calibrators which were observed during the same sessions as that particular cluster.

2. The above fitted profile is then evaluated as a map, with the centroid and total amplitude as determined by the 2D Gaussian fit to the cluster data map, and shape as determined by the 1D fit.

3. The point source map is filtered in the same manner in which the cluster model map is filtered, and the resultant image is used as our point source component in model fitting, with the normalization as a free parameter in the fit.

4.2.3 Residual Model maps

Some clusters may clearly have a component other than the bulk ICM or point source to consider. Given that we rarely have clear extended emission in our maps, these residual components are clearly an excess SZ decrement. Where the primary science goal is to model the bulk ICM, we need not develop a detailed model of the residual component. Thus, a simple means to consistently model residual components is to fit a two dimensional Gaussian to the component. It is worth noting that any residual components seen in the MUSTANG maps are small (of order $15''$ at the largest).

All residual components considered here were modeled from MUSTANG maps, and were subsequently smoothed to Bolocam resolution. Smoothing to Bolocam is taken to be sufficient. It is not unreasonable to assume that the residual is due

to substructure, or a relatively small feature, as MUSTANG filters out large scale signal (Section 2.4.2). Thus, these residual components may be treated as compact components for Bolocam, and thus, to first order, we need not worry about filtering the Bolocam model.

To create the third component, we must first select the feature we wish to fit. This is done with a MUSTANG signal-to-noise (SNR) map, the creation of which is discussed in Section 2.4.2. The typical SNR maps produced used a smoothing kernel of $10''$ (with $1''$ pixelization). All pixels below -3σ pertaining to the feature are selected, and a two dimensional Gaussian is fit to these pixels. This Gaussian is then fit to the unsmoothed MUSTANG data map, where only its amplitude is allowed to vary. The final residual models are saved in units of Compton y.

4.2.4 Sample

The Cluster Lensing And Supernova survey with Hubble (CLASH) is a 524-orbit multi-cycle treasury program. One of its main goals is to "measure the profiles and substructures of dark matter in galaxy clusters with unprecedented precision and resolution" (Postman et al. 2012). The CLASH sample has 25 massive galaxy clusters, 20 of which are selected from X-ray data (from Chandra X-ray Observatory), and 5 based on exceptional lensing strength. These clusters have the following properties: $0.187 < z < 0.890$, $5.5 < kT_e$ (keV)< 15.5, and $6.7 < L_{bol}/10^{44}$ (erg s^{-1}) < 90.8. Thus, these clusters are large enough that we should expect to observe them with MUSTANG with a reasonable amount of time on the sky (on average, <25 hours per cluster).

While these clusters are not a complete sample, many already have SZ effect observations from the Sunyaev-Zel'dovich Array (SZA), AMiBA, or Bolocam, making

them well studied, and deserving of high resolution SZ effect measurements. The overwhelming wealth of information (observations) on these clusters will allow us to constrain pressure and mass profiles of clusters as well as the impact of substructure. Additionally, we will be able to assess discrepancies between X-ray derived properties, shown in Table 4.2 and compare to SZ derived properties.

Table 4.1. Point source flux densities

Cluster	R.A. (J2000)	Dec (J2000)	S_{90} (mJy)	S_{140} (mJy)
Abell 1835	14:01:02.07	+2:52:47.52	1.37 ± 0.08	0.7 ± 0.2
MACS 1115	11:15:51.82	+1:29:56.82	1.04 ± 0.11	–
MACS 0429	04:29:35.97	-2:53:04.74	7.67 ± 0.84	6.0 ± 1.8
MACS 1206	12:06:12.11	-8:48:00.85	0.75 ± 0.08	–
RXJ1347	13:47:30.61	-11:45:09.48	7.40 ± 0.58	4.0 ± 1.2
MACS 1423	14:23:47.71	+24:04:43.66	1.36 ± 0.13	0.7 ± 0.2
MACS 0717	07:17:37.03	+37:44:24.00	2.08 ± 0.25	–
CLJ1226	12:27:00.01	+33:32:42.00	0.36 ± 0.11	–

Note. — S_{90} is the best fit flux density to MUSTANG, and S_{140} is the assumed flux density in the Bolocam maps (at 140 GHz). The location of the point source is reported from the fitted centroid to the MUSTANG data. The conversion for S_{140} values from mJy to the equivalent uK$_{CMB}$ is ~ 30.

Cluster	z	M_{500} ($M_\odot$)	P_{500} (keV/cm^3)	R_{500} (kpc)	T_x^1 (keV)	T_x^2 (keV)	T_{mg} (keV)	Dynamical state	Δr_0 ($''$)
Abell 1835	0.253	1.2E+15	0.00594	1490	9.0	10.0	8.17	CC	6.8
Abell 611	0.288	7.4E+14	0.00445	1240	6.8	–	6.55	–	18.7
MACS1115	0.355	8.6E+14	0.00545	1280	9.2	9.14	6.47	CC	34.8
MACS0429	0.399	5.8E+14	0.00448	1100	8.3	8.55	4.32	CC	18.7
MACS1206	0.439	1.9E+15	0.01059	1610	10.7	11.4	8.81	–	6.9
MACS0329	0.450	7.9E+14	0.00596	1190	6.3	5.85	5.05	CC & D	14.8
RXJ1347	0.451	2.2E+15	0.01171	1670	10.8	13.6	7.99	CC	9.6
MACS1311	0.494	3.9E+14	0.00399	930	6.0	6.36	4.70	CC	27.7
MACS1423	0.543	6.6E+14	0.00612	1090	6.9	6.81	4.14	CC	19.8
MACS1149	0.544	1.9E+15	0.01228	1530	8.5	8.76	7.29	D	6.0
MACS0717	0.546	2.5E+15	0.01490	1690	11.8	10.6	7.70	D	32.4
MACS0647	0.591	1.1E+15	0.00923	1260	11.5	12.6	9.97	–	6.9
MACS0744	0.698	1.3E+15	0.01199	1260	8.1	8.90	7.34	D	4.9
CLJ1226	0.888	7.8E+14	0.01184	1000	12.0	11.7	8.39	–	15.3
Abell 383	0.187	4.7E+14	0.00285	1110	5.4	5.47	–	CC	–
Abell 209	0.206	1.3E+15	0.00564	1530	8.2	8.69	–	–	–
Abell 1423	0.213	8.7E+14	0.00445	1350	5.8	6.61	–	–	–
Abell 2261	0.224	1.4E+15	0.00632	1590	6.1	8.09	–	CC	–
RXJ2129	0.234	7.7E+14	0.00423	1280	6.3	7.78	–	CC	–
MS 2137	0.313	4.7E+14	0.00342	1060	4.7	–	–	CC	–
RXC J2248	0.348	2.2E+15	0.01014	1760	10.9	11.5	–	–	–
MACS1931	0.352	9.9E+14	0.00595	1340	7.5	7.92	–	CC	–
MACS1532	0.362	9.5E+14	0.00589	1310	6.8	6.47	–	CC	–
MACS1720	0.387	6.3E+14	0.00465	1140	7.9	6.50	–	CC	–
MACS0416	0.397	9.1E+14	0.00625	1270	8.2	8.14	–	–	–
MACS2129	0.570	1.1E+15	0.00903	1250	8.6	8.11	–	D	–

Table 4.2: CLASH cluster properties, as tabulated by Mantz et al. (2010): T_X^1 is calculated from a single spectrum over $0.15R_{500} < r < R_{500}$ for each cluster. T_X^2 is from Morandi et al. (2015), and is calculated over $0.15R_{500} < r < 0.75R_{500}$. T_{mg} is a fitted gas mass weighted temperature, determined by fitting the ACCEPT (Cavagnolo et al. 2009) temperature profiles to the profile found in Vikhlinin (2006). The bolded clusters are the 14 clusters in our sample. Δr_0 denotes the offset between the ACCEPT and Bolocam centroids.

Of the 25 clusters in the CLASH sample, four are too far south to be observed with MUSTANG from Green Bank, WV. Of the remaining 21, we were only able to observe fourteen given the available good weather and their limited visibility. Abell 209 was observed, but was relatively noisy and showed no trace of any detection. Thus, our final sample includes thirteen CLASH clusters and Abell 1835, which shown in bold in Table 4.2. These clusters were also observed with Bolocam, and have been analyzed in Sayers et al. (2012, 2013); Czakon et al. (2014). The centroid differences between ACCEPT and Bolocam are also listed in Table 4.2. The total integration times of MUSTANG and Bolocam observations of our sample is listed in Table 4.3. The clusters were observed with MUSTANG over the projects AGBT08A_056, AGBT09A_052, AGBT09C_059, AGBT10A_056, AGBT10C_017, AGBT10C_026, AGBT10C_042, AGBT10C_031, AGBT11A_009, and AGBT11B_001.

Cluster	z	R.A. (J2000)	Decl. (J2000)	$T_{obs,Bolo}$ (hours)	Noise$_{Bolo}$ μK_{CMB}-amin	$T_{obs,MUSTANG}$ (hours)	Noise$_{MUSTANG}$ μJy/beam
Abell 1835	0.253	14:01:01.9	+02:52:40	14.0	16.2	8.6	53.4
Abell 611	0.288	08:00:56.8	+36:03:26	18.7	25.0	12.0	46.2
MACS1115	0.355	11:15:51.9	+01:29:55	15.7	22.8	10.0	56.4
MACS0429	0.399	04:29:36.0	-02:53:06	17.0	24.1	11.6	47.2
MACS1206	0.439	12:06:12.3	-08:48:06	11.3	24.9	13.3	42.5
MACS0329	0.450	03:29:41.5	-02:11:46	10.3	22.5	13.1	39.9
RXJ1347	0.451	13:47:30.8	-11:45:09	15.5	19.7	1.9	276.
MACS1311	0.494	13:11:01.7	-03:10:40	14.2	22.5	10.6	64.5
MACS1423	0.543	14:23:47.9	+24:04:43	21.7	22.3	11.2	35.7
MACS1149	0.544	11:49:35.4	+22:24:04	17.7	24.0	13.9	32.7
MACS0717	0.546	07:17:32.1	+37:45:21	12.5	29.4	14.6	27.1
MACS0647	0.591	06:47:49.7	+70:14:56	11.7	22.0	16.4	20.3
MACS0744	0.698	07:44:52.3	+39:27:27	16.3	20.6	7.6	48.5
CLJ1226	0.888	12:26:57.9	+33:32:49	11.8	22.9	4.9	85.6

Table 4.3: Bolocam and MUSTANG observational properties. Noise$_{MUSTANG}$ is calculated on maps with 10″ smoothing, in the central arcminute. T_{obs} are the integration times (on source) for the given instruments.

Figures 4.3 and 4.4 show the MUSTANG data maps with contours of significant features in MUSTANG and Bolocam overlaid, and arbitrary contours from X-ray surface brightness maps. The maps are $4'$ on a side and are centered on the ACCEPT centroid (red asterisks). Optical and lensing maps are provided in Appendix F and are just over $4'$ on a side.

Several of the clusters show significant features (significance accounts for decreasing weight at larger radii) in the MUSTANG maps, e.g. in MACS 1115, MACS 0329, Abell 611, and MACS 1149. MACS 1115 is the most compelling with a 5σ peak that is with a few arcseconds of two foreground galaxies at $z = 0.15$ and $z = 0.17$. MACS 0329 is also compelling with some hints from weak lensing that there is a NW-SE elongation of the cluster, and there may be a subcluster towards the NW. Abell 611 shows some evidence for disturbance, but the feature in the center of the map does not have a clear interpretation (we do not believe it to be a shock). Finally, MACS 1149 has a 3σ feature to the east of the center, but this too does not have a clear interpretation, even though MACS 1149 has significant merger activity (e.g. Mann & Ebeling 2012).

4.2.5 Parameter Space Searched

Given that the spatial coverage from MUSTANG and Bolocam is well suited to constraining the inner pressure profile, we choose to allow the gNFW parameters γ, C_{500}, and P_0 to vary. To reduce degeneracies, we fix α and β. For Abell 1835 and MACS 0647, we choose our fixed parameters from four established sets of gNFW parameters: those found in Nagai et al. (2007, hereafter N07), Arnaud et al. (2010, hereafter A10), Planck Collaboration et al. (2013, hereafter P12), and Sayers et al. (2013, hereafter S13); these are summarized in Table 4.4. We construct a model map for each set of

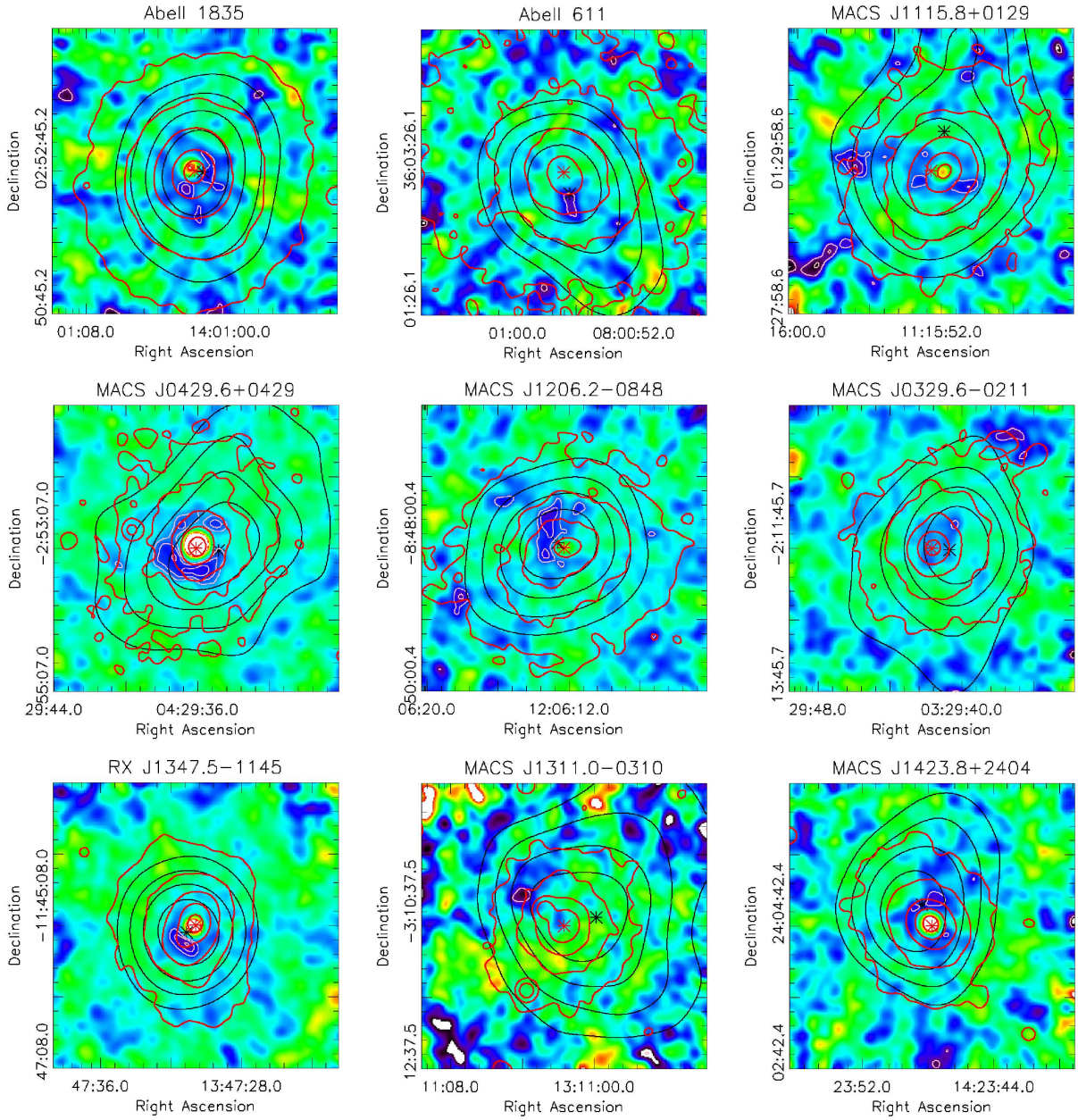

Fig. 4.3.— MUSTANG maps of 9 of the 14 clusters in our sample. Pale contours are MUSTANG contours; black contours are Bolocam. Both start at 3σ decrement, with 1σ intervals. Red contours are X-ray surface brightness contours at arbitrary levels. The red asterisk is the ACCEPT centroid; the black asterisk is the Bolocam centroid.

α, β, γ, and C_{500}, and assume a starting value for P_0, which is then determined in our fits. Since α and β are fixed, each cluster is initially searched over $0 < \gamma < 1$ in

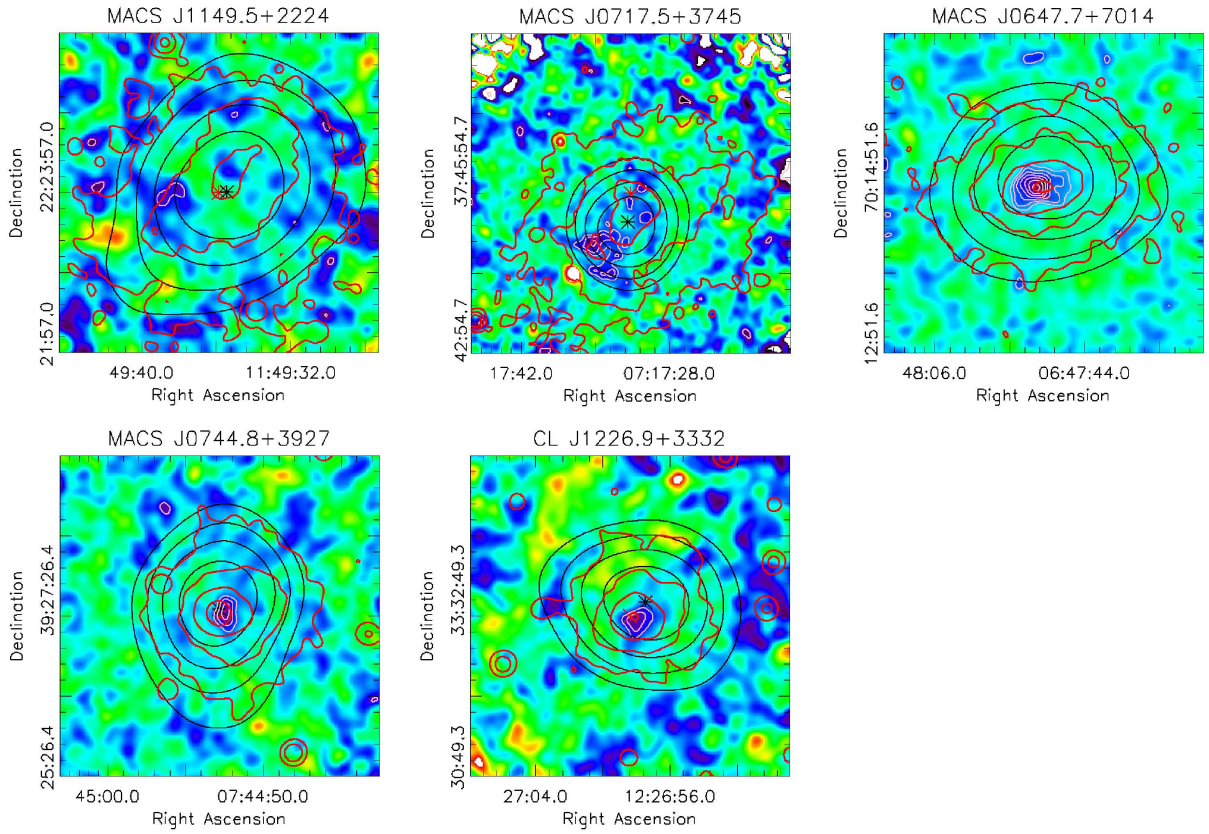

Fig. 4.4.— MUSTANG maps of the remaining 5 clusters in our sample. Pale contours are MUSTANG contours; black contours are Bolocam. Both start at 3σ decrement, with 1σ intervals. Red contours are X-ray surface brightness contours at arbitrary levels. The red asterisk is the ACCEPT centroid; the black asterisk is the Bolocam centroid.

steps of $\delta\gamma = 0.1$, and over $0.1 < C_{500} < 2.1$ in steps of $\delta C_{500} = 0.1$. These ranges are refined after the first pass, and generally $\delta\gamma$ is reduced to 0.05. To create models in finer steps than $\delta\gamma$ and δC_{500}, we interpolate filtered model maps from nearest neighbors from the grid of original filtered models.

Figures 4.5 and 4.6 show that the joint fit pressure profiles for a given cluster (either MACS 0647 or Abell 1835) are very similar despite being fixed at different values of α and β. Thus, for the remainder of the clusters in our sample, we focus only on the A10 values of α and β.

Given that MUSTANG is sensitive to substructure, we fix the MUSTANG cluster model centroid to the position of the ACCEPT centroid. If the MUSTANG centroid is allowed to vary, we find that the fit can significantly be influenced by the cluster substructure. As a result, such fits generally do not accurately represent the bulk cluster component that we seek to model. However, Bolocam maps are dominated by the bulk SZ signal from the cluster, and have a radial pointing accuracy (1σ) of $5''$. Thus we add to our parameter space by allowing the Bolocam pointing to vary up to a total range of $10''$ in R.A. and Dec, in steps of $2''$ for each direction, relative to the ACCEPT centroid with a Gaussian prior of radial offset: $\sigma_{cen} = 5''$.

Point source components are included for Abell 1835, MACS 1115, MACS 0429, MACS 1206, RXJ 1347, MACS 1423, MACS 0717, and CLJ 1226. Residual components are fitted for MACS 1206, RXJ 1347, and MACS 0744. The residual components are all modeled as prescribed in Section 4.2.3, despite the interpretation that the residual component in MACS 1206 is likely a subcluster (Young et al. 2014), and the residual components in RXJ 1347 and MACS 0744 are shocks (Mason et al. 2010; Korngut et al. 2011). For both point sources and residuals, the number of pixels at a given significance is compared to the expected count for a Gaussian distribution.

Table 4.4. Parameters of gNFW models considered

Model	Derivation	C_{500}	α	β	γ	P_0
N07	Numerical Simulations	1.80	1.30	4.30	0.71	3.3
A10	X-ray	1.18	1.05	5.49	0.31	8.41
P12	Planck SZ	1.81	1.33	4.13	0.31	6.41
S13	Bolocam SZ	1.18	0.86	3.67	0.67	4.29

Note. — We considered these four sets of models and fix α and β for each.

Our choice of modelling point source and residual components is generally consistent with criteria based on the pixel count above a signal-to-noise of $(\pm)4$ greatly exceeding the expected count and the component being within the central arcminute. We exclude the residual component for Abell 611 because the bulk cluster model appears to account for much of the decrement. For MACS 1115, the residual component is outside the central arcminute and does not affect our fits. Known point sources (from other observations, especially close to 90 GHz, and within our sensitivity) are also modeled, where the primary case of this is in CLJ 1226. The choice to model residual components is less well defined, as we also take into account the ability for the bulk ICM or point source to contribute to the observed decrement (cf. Section 2.4.4).

The resultant pressure profiles from fits over this parameter space for Abell 1835 and MACS 0647 are shown in Figures 4.5 and 4.6 respectively. We find that the pressure profiles are all in very good agreement with one another and that the differences in χ^2 values between these fits is not significant, as reported in Tables 4.6 and 4.7. Thus, for fits to other clusters, we limit our α and β in the gNFW parametrization to those values used in A10.

We also investigated the potential impact from the uncertainty in the point source subtraction. For a given cluster, we follow the steps in Section 4.2.2, and we then produce bracketing point source uncertainty models which adopt the 1σ values (typically around $0.5''$) for the width of the main beam, as reported in Section 2.4.5, and fit the remaining components. The fitting procedure is then rerun twice: once with each of these models. Neither the fitted gNFW parameters nor the confidence intervals change. However, across the three point source models (two uncertainty and best-fit point source models), the minimum χ^2 does change in the expected manner: it is greater for both of the uncertainty models than the best fit point source model. Thus,

Table 4.5. Parameters of Residual Components from MUSTANG

Cluster	RA (J2000)	Dec (J2000)	Peak y (Modeled)	FWHM$_A$ ($''$)	FWHM$_B$ ($''$)	θ (deg.)	Peak y (Fitted)
Abell 611	8:00:56.20	36:03:00.08	0.000084	20.7	35.3	160	–
MACS 1115	11:15:56.66	1:30:02.82	0.00014	17.8	28.8	138	–
MACS 1206	12:06:12.91	-8:47:33.48	0.000076	23.5	23.5	-115	0.000035
RXJ1347	13:47:31.06	-11:45:18.38	0.00042	12.2	30.1	-52	0.00052
MACS 0744	7:44:52.22	39:27:28.71	0.00011	17.0	23.5	1	0.000090

Note. — Residual components modeled with a two dimensional Gaussian with associated. θ is measured CCW (going east) from due north.

Table 4.6. Best fit gNFW parameters for Abell 1835

Model	C_{500}	α	β	γ	P_0	k	χ^2
N07	$1.44^{+0.71}_{-0.22}$	1.30	4.30	$0.74^{+0.15}_{-0.13}$	$3.43^{+1.41}_{-1.78}$	1.18	12837
A10	$0.83^{+0.35}_{-0.15}$	1.05	5.49	$0.75^{+0.14}_{-0.17}$	$2.54^{+1.25}_{-1.37}$	1.15	12835
P12	$1.45^{+0.35}_{-0.28}$	1.33	4.13	$0.84^{+0.18}_{-0.12}$	$2.80^{+1.54}_{-1.15}$	1.14	12838
S13	$2.29^{+1.30}_{-0.52}$	0.86	3.67	$0.36^{+0.33}_{-0.21}$	$19.3^{+9.75}_{-6.16}$	1.19	12831

Note. — γ, P_0, C_{500}, and k, the calibration offset, were varied. The degrees of freedom were 12880.

Table 4.7. Best fit gNFW parameters for MACS 0647

Model	C_{500}	α	β	γ	P_0	k	χ^2
N07	$0.93^{+0.31}_{-0.36}$	1.30	4.30	$0.70^{+0.10}_{-0.17}$	$2.10^{+0.93}_{-1.17}$	1.14	12845
A10	$0.60^{+0.25}_{-0.22}$	1.05	5.49	$0.61^{+0.12}_{-0.15}$	$2.24^{+2.03}_{-1.20}$	1.14	12844
P12	$1.03^{+0.32}_{-0.40}$	1.33	4.13	$0.70^{+0.10}_{-0.17}$	$2.25^{+1.04}_{-1.32}$	1.14	12845
S13	$1.19^{+0.54}_{-0.64}$	0.86	3.67	$0.38^{+0.20}_{-0.25}$	$8.18^{+4.68}_{-1.13}$	1.14	12843

Note. — γ, P_0, and C_{500} were varied. The degrees of freedom were 12914.

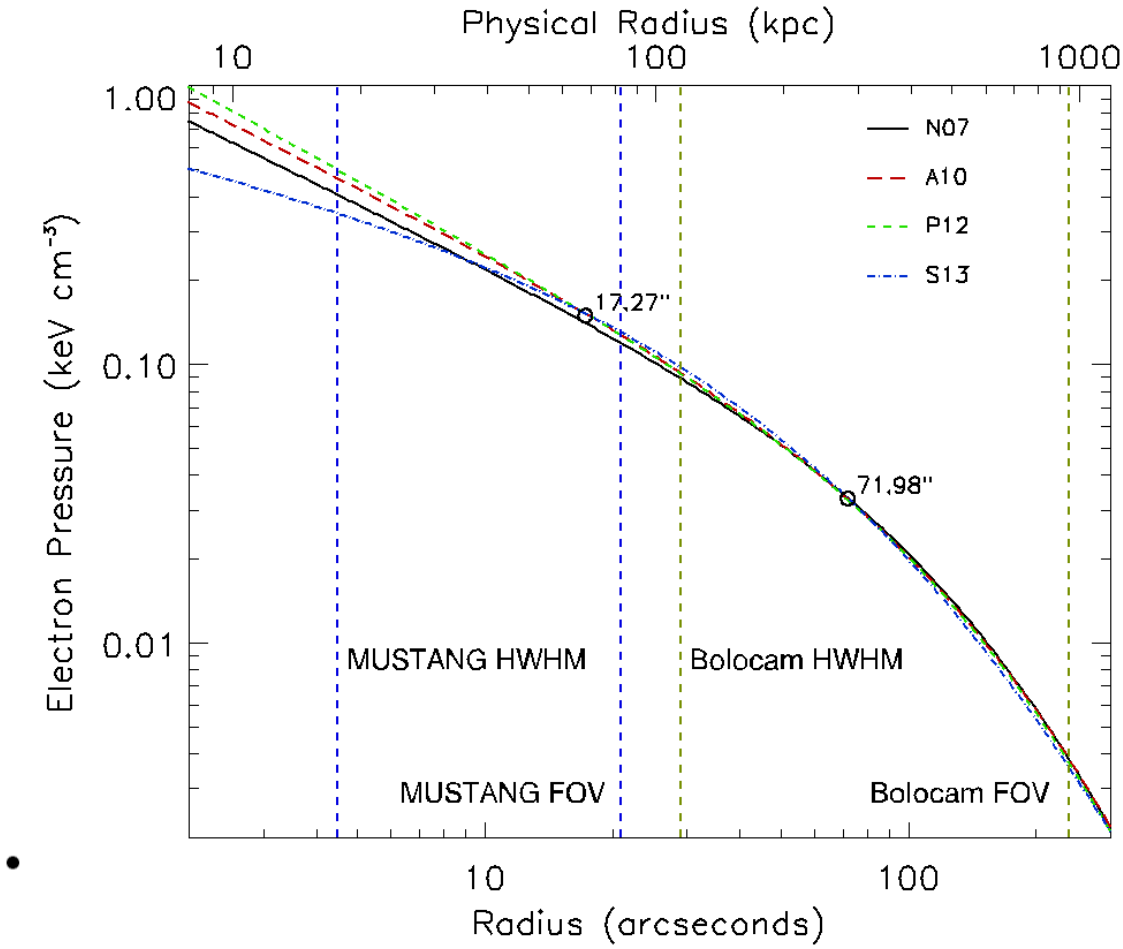

Fig. 4.5.— Best fit pressure profiles for Abell 1835 for the different sets of fixed α and β, denoted by the model from which they are taken. The circles denote radial ranges where the pressure profiles show (local) minimum scatter.

we are confident in our treatment of point sources and allowing only the amplitude to vary.

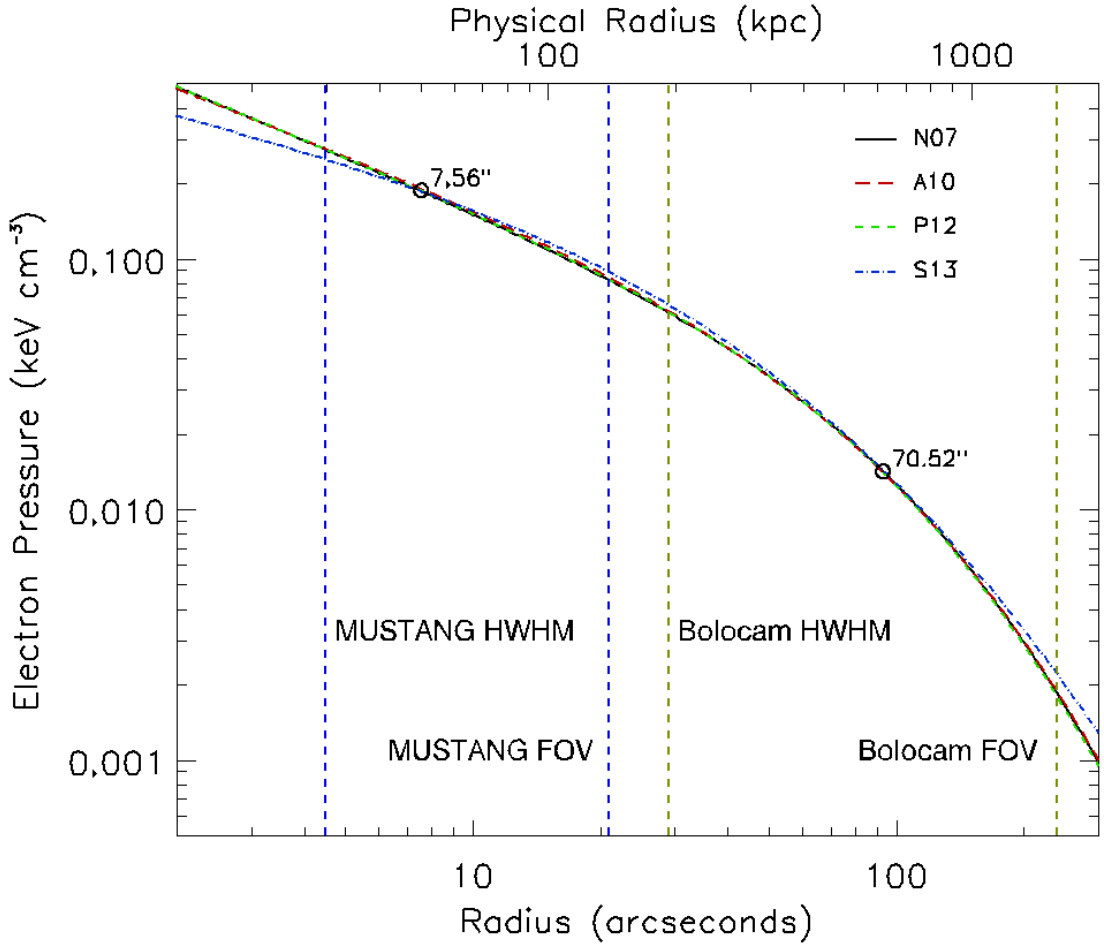

Fig. 4.6.— Best fit pressure profiles for MACS 0647 for the different sets of fixed gNFW α and β, denoted by the model from which the values are taken. The circles denote radial ranges where the pressure profiles show (local) minimum scatter.

4.3 Pressure Profile Constraints

4.3.1 Overview

Here we present some general results from the joint fits. Table 4.8 shows how significantly a previously determined profile shape is fit to the data sets, independently and

jointly.

The joint fit constraints on the pressure profile parameters of individual clusters are shown in Figure 4.8, with the pressure profiles plotted in Figure 4.9. The ensemble constraints for cool-core, clusters, disturbed, "well-behaved" clusters, and all clusters in our sample are shown in Figure 4.7. We defined "well-behaved" in Section 4.3.16; cool-core and disturbed classifications are assigned in Sayers et al. (2013) and are based on concentration of X-ray luminosity and offset in X-ray peak to centroid,.

The azimuthal plots of the data and fitted (and filtered) models are in Appendix D as Figure 8.4.

Cluster	t_M (hrs)	t_B (hrs)	σ_M (μK)	σ_B (μK)	A10$_M$ (σ)	A10$_B$ (σ)	A10$_J$ (σ)	ACCEPT$_M$ (σ)	ACCEPT$_B$	ACCEPT$_J$
Abell 1835	8.6	14.0	87.4	16.2	10.0	28.9	29.9	9.49	28.9	30.08
Abell 611	12.0	18.7	75.6	25.0	1.73	13.9	14.3	1.39	14.4	14.02
MACS1115	10.0	15.7	92.4	22.8	8.66	16.3	18.3	8.22	16.7	18.20
MACS0429	11.6	17.0	77.3	24.1	-0.02	13.2	13.1	-1.41	13.5	12.21
MACS1206	13.3	11.3	70.0	24.9	8.89	28.7	29.8	8.17	28.8	29.36
MACS0329	13.1	10.3	65.3	22.5	8.63	17.4	20.2	7.90	17.8	18.62
RXJ1347	1.9	15.5	452	19.7	8.90	45.3	45.7	11.0	45.8	46.71
MACS1311	10.6	14.2	106	22.5	0.71	11.3	11.6	1.02	11.5	10.97
MACS1423	11.2	21.7	58.5	22.3	6.15	11.8	12.9	5.27	12.0	11.98
MACS1149	13.9	17.7	53.6	24.0	-1.47	22.0	21.4	-0.82	22.3	22.01
MACS0717	14.6	12.5	44.4	29.4	3.05	31.3	31.0	3.40	31.8	31.41
MACS0647	16.4	11.7	33.2	22.0	11.3	24.1	25.9	11.3	23.8	25.02
MACS0744	7.6	16.3	79.4	20.6	7.67	17.8	19.1	7.45	17.7	18.67
CLJ1226	4.9	11.8	140	22.9	9.43	13.7	16.5	9.41	14.4	16.16

Table 4.8: Tabulated cluster observational properties. A10 columns present significances (in σ) of fitted A10 profiles (only P_0 is varied) and ACCEPT columns present significances (in σ) or the fitted ACCEPT gNFW profile. The subscripts $_B$, $_M$, and $_J$ signify fits to Bolocam, MUSTANG, and joint fits respectively.

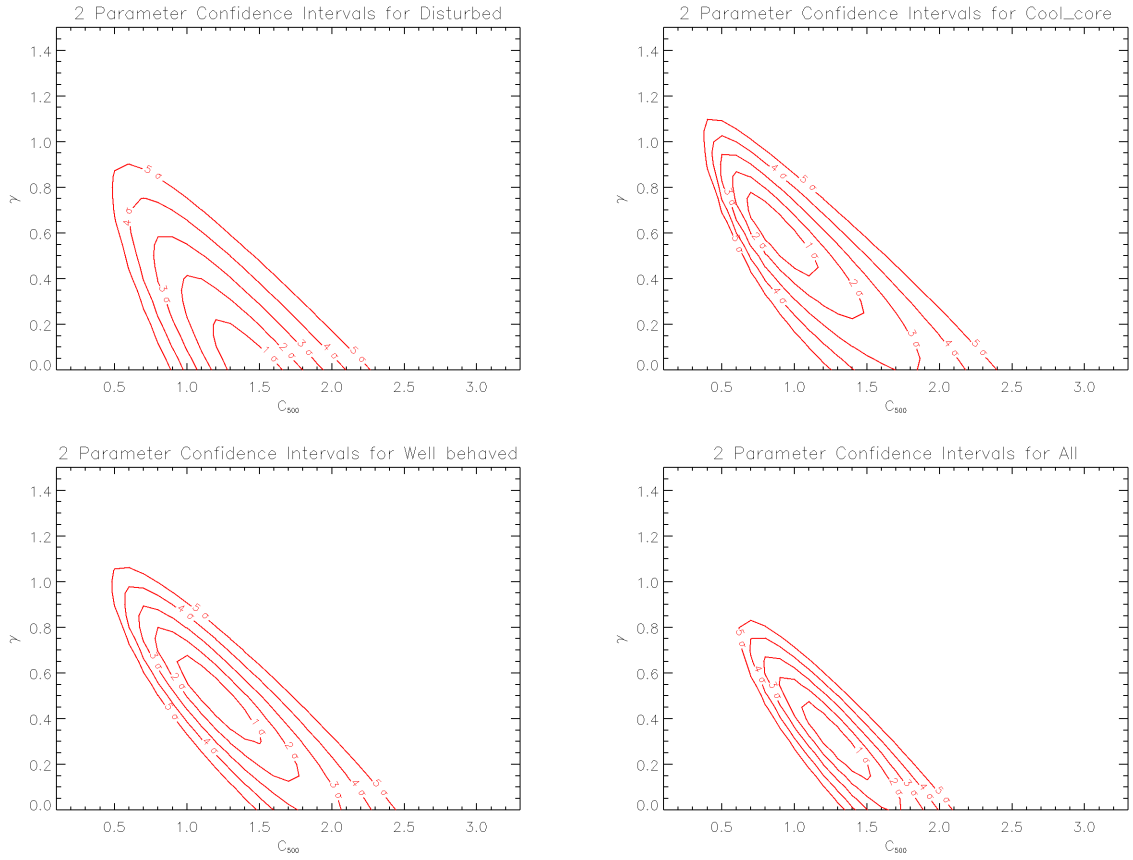

Fig. 4.7.— Confidence intervals over all disturbed clusters, cool-core clusters, and the entire sample. Cool core clusters include: Abell 1835, MACS 1115, MACS 0429, MACS 0329, RXJ 1347, MACS 1311 and MACS 1423. Disturbed clusters include: MACS 0329, MACS 1149, MACS 0717, and MACS 0744. Well behaved clusters include: Abell 1835, MACS 1115, MACS 1206, RXJ 1347, MACS 0647, MACS 0744, and CLJ 1226. Well behaved clusters are identified in Section 4.3.16.

4.3.2 Abell 1835 (z=0.25)

Abell 1835 is a well studied massive cool core cluster. The cool core was noted to have substructure in the central 10″ by Schmidt et al. (2001), and identified as being due the central AGN by McNamara et al. (2006). Abell 1835 has also been extensively studied via the SZ effect (Reese et al. 2002; Benson et al. 2004; Bonamente et al. 2006; Sayers et al. 2011; Mauskopf et al. 2012). The models adopted were either beta models or

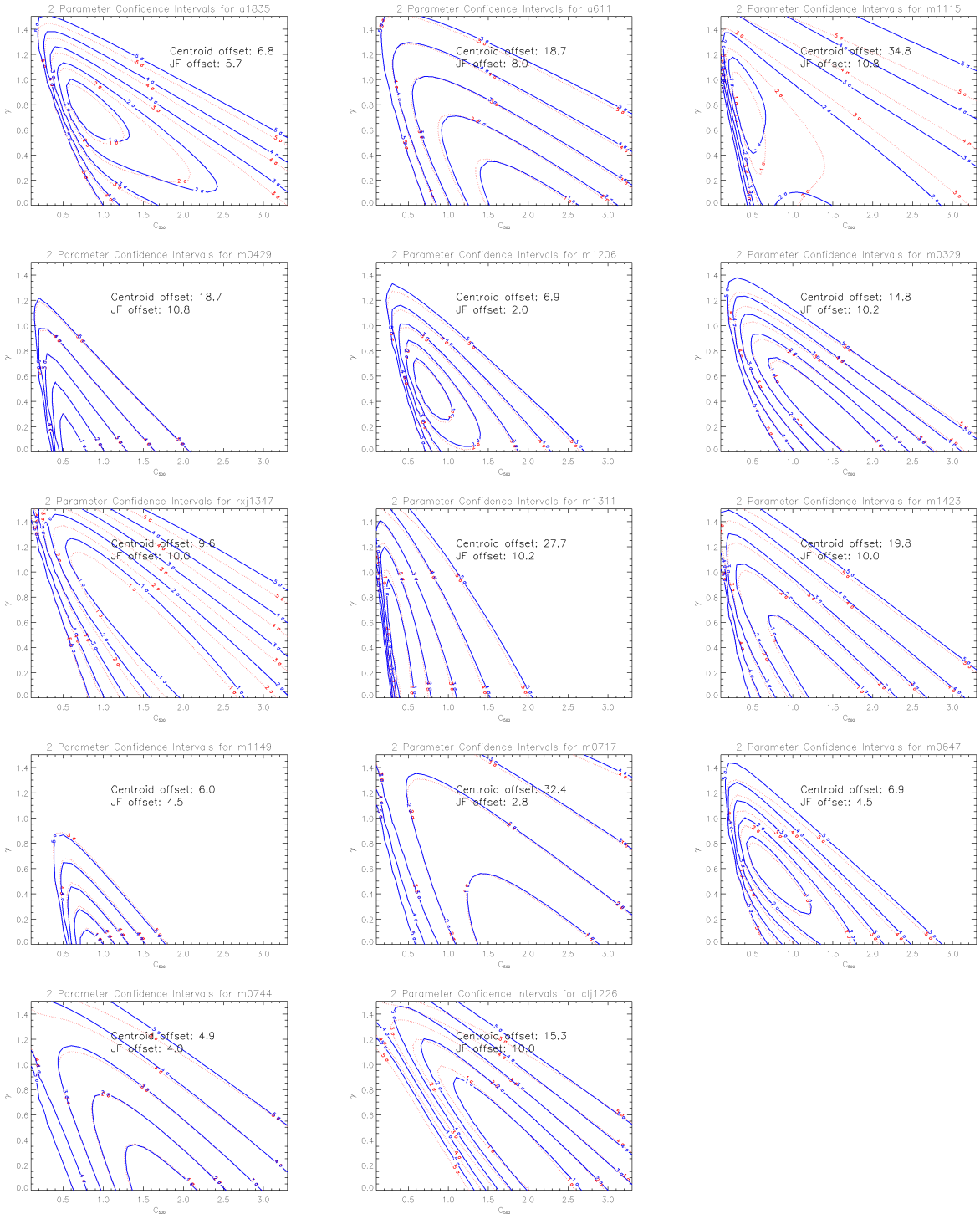

Fig. 4.8.— Confidence intervals for individual clusters. Dotted red contours assume the Bolocam centroid, while solid blue contours assume the ACCEPT centroid. "Centroid Offset" is the offset between the Bolocam centroid and ACCEPT centroid, in arcseconds. "JF offset" is the pointing offset (of Bolocam) in the joint fit assuming the ACCEPT centroid.

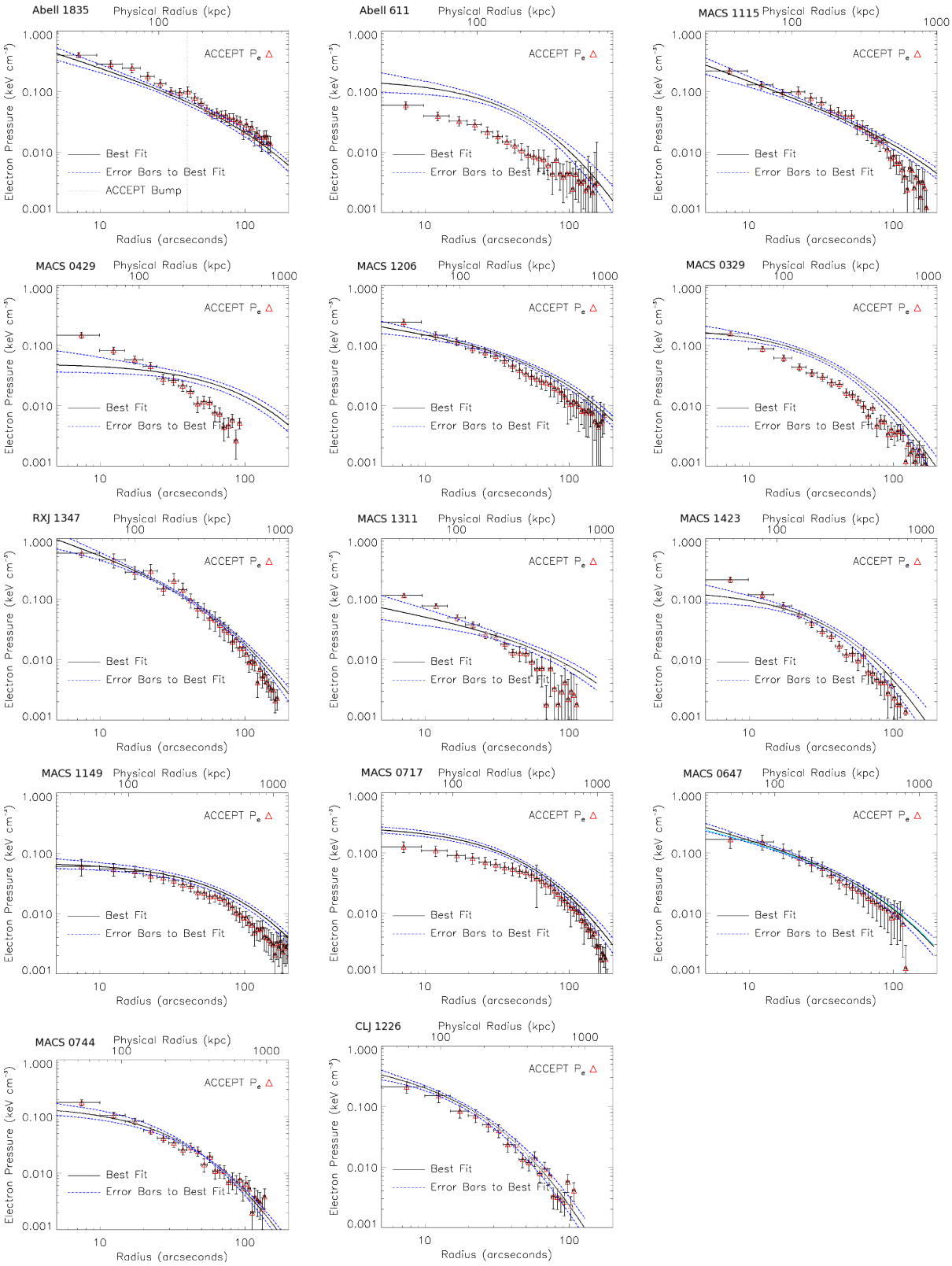

Fig. 4.9.— Preferred pressure profiles of individual clusters (using ACCEPT centroids).

generalized beta models, and tend to suggest a shallow slope for the pressure interior to 10″. Previous analysis of Abell 1835 with MUSTANG data (Korngut et al. 2011) detected the SZ effect decrement, but not at high significance, which is consistent with a featureless, smooth, broad signal. Our updated MUSTANG reduction of Abell 1835 is shown in Figure 4.3, and has the same features as in Korngut et al. (2011).

We find the best fit A10 model (all parameters but P_0 fixed to A10 values) has $\chi^2 = 12861$. To calculate χ^2 for no cluster model, we fix the point source amplitude to that found in the previous fit. We find $\Delta\chi^2 = 892.1$, with ΔDOF$= 2$ corresponds to 29.7σ significance. For Bolocam only, the $\Delta\chi^2$ between a cluster model being fit or not yields a 28.9σ detection, while the for MUSTANG we find a 10.2σ detection of an A10 model from $\Delta\chi^2$, thus indicating that although individual features are weakly detected by MUSTANG, the aggregate bulk SZ is robustly detected by MUSTANG.

Our best joint fit over the four sets of α and β, shown in Table 4.6, comes from the S13 values of α and β: the best fit parameters are: $\gamma = 0.36$, $P_0 = 19.3$, and $C_{500} = 2.28$. Despite variations in the best fit γ values, Figure 4.5 shows the best joint fit pressure profiles of Abell 1835 for each of the four sets of fixed α and β, are in good agreement with each other. Moreover, we find that the four model fits achieve minimum scatter at two separate radii, roughly corresponding to the geometric mean between the resolution and FOV of each instrument.

We find the point source in the MUSTANG map at R.A.=14:01:02.1, Dec=02:52:47 is best fit with a flux density of 1.38 ± 0.10 mJy, and has a correlation coefficient of 0.076 with the cluster amplitude. This minimal degeneracy can also be seen in Figure 4.10. Similarly, changing the assumed beam shape as discussed in Section 4.2.2 has a negligible effect on the flux density. The amplitude of the point source suggests a slight flattening of the spectral index between $\nu = 1.4$ GHz and $\nu = 28.5$ GHz

(Condon et al. 1998; Reese et al. 2002) of $\alpha_\nu = 0.89$, to a spectral index of $\alpha_\nu = 0.59$ between $\nu = 28.5$ GHz and $\nu = 90$ GHz. Such a spectral index is also consistent with McNamara et al. (2014), which find a spectral index of $\alpha_\nu = 0.54$ between $\nu = 92$ GHz and $\nu = 276$ GHz. The assumed flux density of the subtracted point source for Bolocam, 0.77 ± 0.24 mJy at 140 GHz, is consistent with the other measurements.

The point source flux density found with MUSTANG is consistent with that obtained from observations with the Atacama Large Millimeter/Sub-millimeter Array (ALMA) in McNamara et al. (2014), which find the central continuum source has a flux density of 1.26 $\pm$0.03 mJy. We note they also detect a $10^{10} M_\odot$ molecular outflow at 92 GHz, with a total integral flux of 3.6 Jy km s^{-1} for CO (1-0), which would correspond to an equivalent continuum flux density of 6 μJy, and would not contribute much additional flux density to the point source flux density as seen by McNamara et al. (2014). However, this source is reported with a position of R.A.=14:01:02.083, Dec=02:52:42.649, which is 4$''$ offset from the position found in our MUSTANG data. Since we consider our positional uncertainty to be 2$''$, this is a larger than typical pointing offset, but is difficult to rule out. A list of selected point source flux densities is provided in Table 4.9.

Figure 4.2 shows that Bolocam, by itself, can place fairly tight constraints on the gNFW model parameters, primarily on C_{500}. That is, for A10 values of α and β, as in Figure 4.2, Bolocam finds $C_{500} = 0.73^{+0.25}_{-0.17}$, $\gamma = 0.83^{+0.22}_{-0.23}$, and $P_0 = 1.75^{+2.51}_{-1.22}$, whereas the joint fit yields $C_{500} = 0.83^{+0.35}_{-0.15}$, $\gamma = 0.75^{+0.14}_{-0.17}$, and $P_0 = 2.54^{+1.25}_{-1.37}$. Across the model sets, the trend for Abell 1835 is that joint fit tends to loosen the constraint on C_{500}, while improving the constraints on γ and P_0 relative to the fits to solely Bolocam data. It is worth noting that for each value of γ and C_{500}, only P_0 is a free parameter in the Bolocam only fits. In contrast, for the joint fit, the calibration offset and

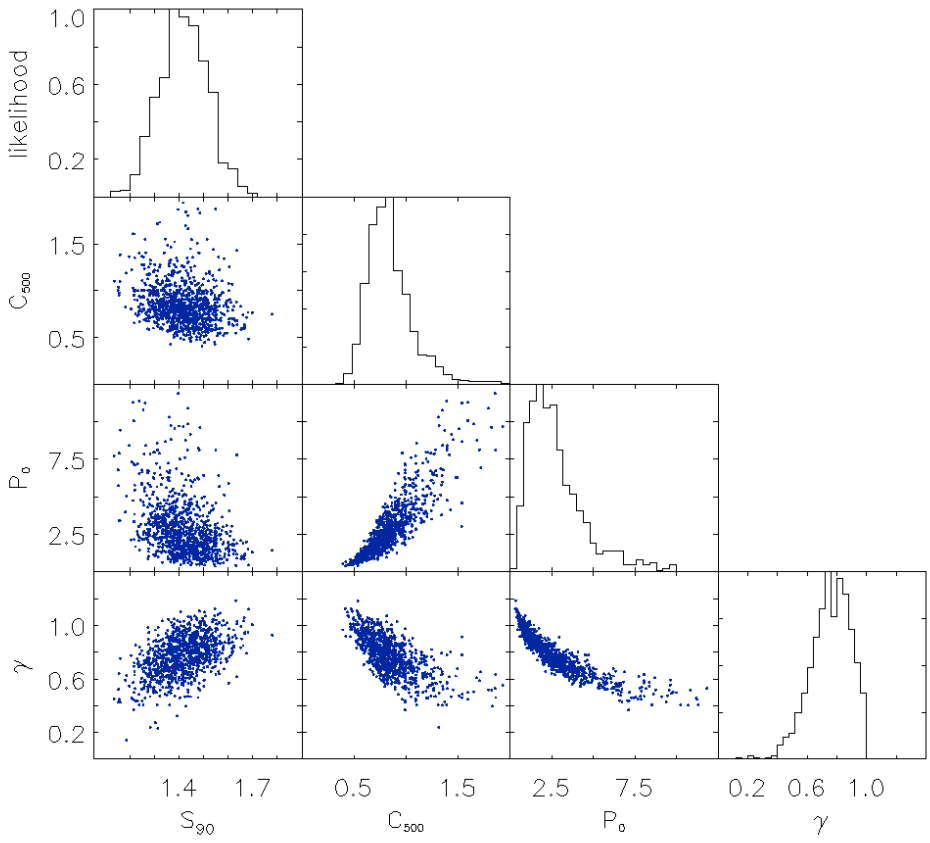

Fig. 4.10.— Distribution and correlation of gNFW parameters for pressure profile fits to Abell 1835.

MUSTANG point source amplitude are additional free parameters. The addition of MUSTANG data slightly reduces the inner slope, γ, relative to the Bolocam-only fit. This is suggestive that Bolocam, with subtraction of its adopted point source model, has not underestimated the SZ effect signal. Moreover, given the peak decrement of -20 mJy in the Bolocam map, an adjustment of ~ 0.2 mJy, which is the uncertainty on the assumed 0.77 mJy, would negligibly alter the constraints. Both the Bolocam and joint constraints indicate a relatively steep slope, which is typical for a cool core cluster (e.g. Arnaud et al. 2010; Sayers et al. 2013).

4.3.3 Abell 611 (z=0.29)

Abell 611 is unique among our clusters for the severity of the discrepancy between our joint SZ fitted pressure profile and that found in the X-rays. The MUSTANG map (Figure 4.3) shows an enhancement south of the X-ray centroid, and the Bolocam map shows elongation towards the south-southwest. Weak lensing maps are suggestive of a southwest-northeast elongation (Newman et al. 2009; Zitrin et al. 2015). Using the density of galaxies, Lemze et al. (2013) find a core and a halo which align with the elongation seen in the SZ (Figure 4.11). We note that AMI (AMI Consortium et al.

Table 4.9. Abell 1835 point source flux densities

$S^a_{1.4}$ (mJy)	$S^b_{28.5}$ (mJy)	S_{90} (mJy)	S^c_{92} (mJy)	S^c_{276} (mJy)
41.4 ± 1.9	2.76 ± 0.14	1.38 ± 0.10	1.26 ± 0.03	0.7 ± 0.1

Note. — S_{90} is from this work.

References. — [a]Condon et al. (1998) [b]Reese et al. (2002) [c]McNamara et al. (2014).

2012) also sees this elongation, while they also note that Abell 611 is the most relaxed cluster in their sample and that the X-ray data presented from LaRoque et al. (2006) is very circular and uniform. Despite being relaxed, Abell 611 is not listed as a cool core cluster (nor disturbed) (Sayers et al. 2013).

In an analysis of the dark matter distribution, Newman et al. (2009) find that the core (logarithmic) slope of the cluster is shallower than an NFW model, with $\beta_{DM} = 0.3$, where the dark matter distribution has been characterized by yet another generalization of the NFW profile:

$$\rho(r) = \frac{\rho_0}{(r/r_s)^{\beta_{tot}}(1 + r/r_s)^{3-\beta_{tot}}} \tag{4.21}$$

They find the distribution of dark matter within Abell 611 to be inconsistent with an NFW model.

4.3.4 MACS 1115 (z=0.36)

MACS 1115 is listed as a cool core cluster (Sayers et al. 2013). It is among seven CLASH clusters that show unambiguous ultraviolet (UV) excesses attributed to unabsorbed star formation rates of 5-80 $M_{\odot}\mathrm{yr}^{-1}$ (Donahue et al. 2015). MACS 1115 has a visible point source in the MUSTANG map. The NVSS, at 1.4 GHz, finds the flux of the point source to be 16.2 mJy. MACS 1115 is fit by a fairly steep inner pressure profile slope to the SZ data (Figure 4.8). Adopting the Bolocam centroid, the inner pressure profile slope is notably reduced, yet the goodness of fit is not significantly changed. In particular, the Bolocam image shows a north-south elongation (particularly to the north of the centroids). In contrast, weak and strong lensing (Zitrin et al. 2015) show a more southeast-northwest elongation.

4.3.5 MACS 0429 (z=0.40)

MACS 0429 has been well studied in the X-ray (Schmidt & Allen 2007; Comerford & Natarajan 2007; Maughan et al. 2008; Allen et al. 2008; Mann & Ebeling 2012) MACS 0429 is indentified as a cool core cluster (cf. Mann & Ebeling 2012; Sayers et al. 2013) and has a very bright point source in the MUSTANG image. At 90 GHz, we find the flux density as 7.67 ± 0.84 mJy. The point source subtracted from the Bolocam data is a 6.0 ± 1.8 mJy source at 140 GHz. At 1.4 GHz, NVSS finds the point source to have a flux density of 138.8 ± 4.2 mJy (Condon et al. 1998). MACS 0429 is noted as having an excesses UV emission (Donahue et al. 2015).

Despite MACS 0429's stature as a cool core cluster, its pressure profile (Figure 4.8) is surprisingly shallow in the core, and shows elevated pressure relative to X-ray derived pressure at moderate radii. The offset between the Bolocam centroid (Sayers et al. 2013) and ACCEPT (Cavagnolo et al. 2009) centroid is 100 kpc, which is notably larger than the X-ray-optical separations of the cluster peaks and centroids reported in Mann & Ebeling (2012) of 12.8 and 19.5 kpc respectively.

4.3.6 MACS 1206 (z=0.44)

MACS 1206 has been observed extensively (e.g. Ebeling et al. 2001, 2009; Gilmour et al. 2009; Umetsu et al. 2012; Zitrin et al. 2012b; Biviano et al. 2013; Sayers et al. 2013). It is not categorized as a cool core or a disturbed cluster (Sayers et al. 2013). Using weak lensing data from Subaru, Umetsu et al. (2012) find that it the major-minor axis ratio of projected mass is $\gtrsim 1.7$ at 1σ. They infer that this high ellipticity and alignment with the BCG, optical, X-ray, and LSS shapes are suggestive that the major axis is aligned close to the plane of the sky. In contrast, this analysis finds that MACS 1206 has a major-minor axis ratio of 1.85 ± 0.45 (Section 5.1), where the

major axis is assumed to be along the line of sight.

The point source was found to have a flux density of 0.77 ± 0.06 mJy with the best fit model in Young et al. (2014). In this analysis, we find it to have a flux density of 0.75 ± 0.08 mJy. In Young et al. (2014), substructure is identified that corresponds to an optically-identified subcluster, which may either be a merging subcluster, or a foreground cluster. A proposal has been accepted for *XMM-Newton* observations of this substructure (PI: Sarazin).

4.3.7 MACS 0329 (z=0.45)

MACS 0329 has a rare distinction of being listed as both a cool core and disturbed cluster. Although it has been classified as relaxed (Schmidt & Allen 2007), subtructure has been noted (Maughan et al. 2008), and it earns its cool core and disturbed classifications based on central weighting of X-ray luminsoity and comparing centroid offsets between optical and X-ray data (Sayers et al. 2013). The elongation of the weak lensing and strong lensing are towards the northwest and southeast of the centroid.

MACS 0329 has two systems with multiple images: one at $z = 6.18$ and the other at $z = 2.17$. The Einstein radii for these two systems are $r_E = 34''$ and $r_E = 28''$, respectively (Zitrin et al. 2012a), which is noted as being typical for relaxed, well-concentrated lensing clusters.

4.3.8 RXJ1347 (z=0.45)

RXJ1347 is one of the most luminous X-ray clusters, and has been well studied in radio, SZ, lensing, optical spectroscopy, and X-rays (e.g. Schindler et al. 1995; Allen et al. 2002; Pointecouteau et al. 1999; Komatsu et al. 2001; Kitayama et al. 2004; Gitti

et al. 2007a; Ota et al. 2008; Bradač et al. 2008; Miranda et al. 2008). X-ray contours have long suggested RXJ1347 is a relaxed system (e.g. Schindler et al. 1997), and it is classified as a cool core cluster (e.g. Mann & Ebeling 2012; Sayers et al. 2013).

Despite the classification of being a cool core cluster, it is also observed that there are hot regions, intially constrained as $kT > 10$ keV (e.g. Allen et al. 2002; Bradač et al. 2008), and more recently constrained to even hotter temperatures ($kT > 20$ keV Johnson et al. 2012), indicative of an unrelaxed cluster. Johnson et al. (2012) also interpret the two cold fronts as being due to sloshing, where a subscluster has returned for a second passage.

Indeed, the first sub-arcminute SZ observations (Komatsu et al. 2001; Kitayama et al. 2004) saw an enhancement to the southeast of the cluster X-ray peak, which was suggested as being due to shock heating. This enhancement was confirmed by MUSTANG (Mason et al. 2010). Further measurements were made with CARMA (Plagge et al. 2013), which find the 9% of the thermal energy in the cluster is in sub-arcminute substructure. At low radio frequencies (Ferrari et al. 2011, 237 MHz and 614 MHz), (Gitti et al. 2007b, 1.4 GHz) find evidence for a radio mini-halo in the core of RXJ1347. The cosmic ray electrons are thought to be reaccelerated because of the shock and sloshing in the cluster (Ferrari et al. 2011).

We observe a point source with flux density of 7.40 ± 0.58 mJy. Previous analysis of the MUSTANG data put the point source flux density at 5 mJy (Mason et al. 2010). The difference in the flux densities is likely accounted in (1) the different modeling of point sources; primarily that we filter the double Gaussian, (2) we simultaneously fit the components, and (3) we almost certainly have a steeper profile in the core than the beta model assumed in Mason et al. (2010). Lower frequency radio observations found the flux density of the source to be 10.81 ± 0.19 mJy at 28.5 GHz (Reese et al.

2002), and 47.6 ± 1.9 mJy at 1.4 GHz (Condon et al. 1998).

RXJ 1347 is observed to have a UV excess in its BCG (Donahue et al. 2014).

4.3.9 MACS 1311 (z=0.49)

MACS 1311 is listed as a cool core cluster (e.g. Sayers et al. 2013), and appears to have quite circular contours in the X-ray and lensing images, yet has evidence for some disturbance, given its classification in Mann & Ebeling (2012). However, the SZ contours from Bolocam show some enhancement to the west, and has a notable centroid shift ($27.7''$) westward from the X-ray centroid. When fitting pressure profiles to this cluster, it appears that the enhanced SZ pressure at moderate radii ($r \sim 100''$) is due to this enhancement, especially when noting that we do use the X-ray centroid. Adopting the Bolocam centroid does not change the pressure profile much, and we still observe a pressure enhancement at moderate radii.

4.3.10 MACS 1423 (z=0.54)

MACS 1423 is a cool core cluster (Mann & Ebeling 2012; Sayers et al. 2013). While the Bolocam (SZ) contours are quite concentric, and suggestive of a relaxed cluster, the centroid is still offset from the X-ray peak by an appreciable angle ($19.8''$). Similarly to MACS 1311, the pressure is slightly less than the ACCEPT X-ray derived pressure in the core, and slightly greater at moderate radii. While this is expected for a centroid offset, we find that adopting the Bolocam centroid again yields no substantial difference in the SZ pressure profile. We observe a point source with flux density of 1.36 ± 0.13 mJy

4.3.11 MACS 1149 (z=0.54)

MACS 1149 is classified as a disturbed cluster (e.g. Mann & Ebeling 2012; Sayers et al. 2013), and lensing studies have found that a single DM halo does not describe the cluster well, but rather at least four large-scale DM hales are used to describe the cluster (Smith et al. 2009). A large radial velocity dispersion (1800 km s^{-1} Ebeling et al. 2007) is observed, indicative of merger activity along the line of sight. X-ray, SZ, and lensing (particularly strong lensing) all show elongation in the northwest-southeast direction. We see a 3σ feature to the east of the centroids, but it is not clear that this is associated with any particular feature.

The SZ derived pressure profile roughly matches the shape of the X-ray derived pressure profile (Figure 4.8), with the SZ pressure consistently greater than the X-ray pressure.We calculate that the axis along the line of sight is 2.08 ± 0.52 (Section 5.1) times greater than the axes in the plane of the sky. Although we do not find previous analysis of the elongation in the plane of the sky, we would certainly expect this given (1) the inferred merger activity along the line of sight, and (2) the lensing strength of the cluster.

4.3.12 MACS 0717 (z=0.55)

Despite MACS 1149's impressive merging activity, MACS 0717 is touted as the most disturbed massive cluster at $z > 0.5$ (Ebeling et al. 2007), which appears to be accreting matter along a 6-Mpc-long filament (Ebeling et al. 2004), and has the largest known Einstein radius ($\theta_e \sim 55''$; Zitrin et al. 2009). Four distinct components are identified from X-ray and optical analyses (Ma et al. 2009), and the lensing analyses (Zitrin et al. 2009; Limousin et al. 2012) find agreement in the location of these four mass peaks with those from the X-ray and optical.

There are four identified subclusters (labeled A through D Mroczkowski et al. 2012). Ma et al. (2009) find that subcluster C is the most massive component, while subcluster A is the least massive, and subclusters B and D are likely remnant cores. The velocities of the components from spectroscopy are found to be $(v_A, v_B, v_C, v_D) = (+278^{+295}_{-339}, +3238^{+252}_{-242}, -733^{+486}_{-478}, +831^{+843}_{-800})$ km s^{-1} (Ma et al. 2009).

MACS 0717 has also been observed at 610 MHz with the Giant Metrewave Radio Telescope (GMRT) which reveals both a radio halo and a radio relic (van Weeren et al. 2009). This is interpreted as likely being due to a diffuse shock acceleration (DSA).

We observe a foreground radio galaxy, modeled as a point source here, with flux density of 2.08±0.25 mJy at 90 GHz. This was previously reported with an integrated flux density of 2.8±0.2 mJy and an extended shape $14.''4 \times 16.''1$ (Mroczkowski et al. 2012). However, an improved beam modeling has allowed us to model the foreground galaxy given a known beam shape. It is also worth noting that the MUSTANG data itself has been processed slightly different from that presented in Mroczkowski et al. (2012); in this work the map is produced with a common calculated as the mean across detectors.

4.3.13 MACS 0647 (z=0.59)

MACS 0647 is at $z = 0.591$ and is classified as neither a cool core nor a disturbed cluster (Sayers et al. 2013). It was included in the CLASH sample due to its strong lensing properties (Postman et al. 2012). Gravitational lensing (Zitrin et al. 2011), X-ray surface brightness (Mann & Ebeling 2012), and SZ effect (MUSTANG, see Figure 4.4, and Bolocam) maps all show elongation in an east-west direction. In the joint analysis presented here, we see that the spherical model provides an adequate

fit to both datasets and we note that the spherical assumption allows for a easier interpretation of the mass profile of the cluster.

To calculate how significantly Bolocam and MUSTANG detect an SZ effect bulk decrement, we calculate a $\Delta\chi^2$ as we did for Abell 1835. $\Delta\chi^2$ is computed as the difference of χ^2 from an A10 profile (all parameters but P_0 fixed to A10 values) fit to our datasets, and χ^2 assuming no model. The joint fit (both data sets) yields a 26.3σ significance, while for Bolocam only, $\Delta\chi^2$ yields a 23.9σ detection, and in the MUSTANG data we find a 10.8σ detection of an A10 model.

Our best fit model comes from the S13 values of α and β, and finds $\gamma = 0.38$, $C_{500} = 1.19$, and $P_0 = 8.18$. The best joint fits, listed in Table 4.10 to the four sets of α and β differ by $\Delta\chi^2 < 3$. With Young et al. (2014) constraining $\gamma = 0.90^{+0.02}_{-0.04}$, it might appear that their result is significantly discrepant with our best fit $\gamma = 0.61^{+0.17}_{-0.11}$ from the A10 set, even though Young et al. (2014) used the identical SZ effect data as we have used in this analysis. A crucial distinction in the fitting procedures is the parameter space searched: in Young et al. (2014), Bolocam is first fit over a grid of fixed γ values, k is fixed at 1.0, and the parameters C_{500} and P_0 are allowed to float. The goodness of fit, χ^2 for each γ are then calculated for the MUSTANG model (all

Table 4.10. Best fit gNFW parameters for MACS 0647

Model	C_{500}	α	β	γ	P_0	k	χ^2
N07	$0.93^{+0.31}_{-0.36}$	1.30	4.30	$0.70^{+0.10}_{-0.17}$	$2.10^{+0.93}_{-1.17}$	1.14	12845
A10	$0.60^{+0.25}_{-0.22}$	1.05	5.49	$0.61^{+0.12}_{-0.15}$	$2.24^{+2.03}_{-1.20}$	1.14	12844
P12	$1.03^{+0.32}_{-0.40}$	1.33	4.13	$0.70^{+0.10}_{-0.17}$	$2.25^{+1.04}_{-1.32}$	1.14	12845
S13	$1.19^{+0.54}_{-0.64}$	0.86	3.67	$0.38^{+0.20}_{-0.25}$	$8.18^{+4.68}_{-1.13}$	1.14	12843

Note. — γ, P_0, and C_{500} were varied. The degrees of freedom were 12914.

parameters fixed) to the MUSTANG map. Thus, the reported error bars reflect a one-parameter search, without the degeneracies between C_{500}, P_0, and γ folded into it, and do not include the χ^2 values from the Bolocam fit.

Given that MUSTANG is only able to constrain the pressure profile on scales $9'' < \theta \lesssim 42''$, and for MACS 0647, $R_{500} = 3.16'$ and $C_{500} = 1.18$ (A10 and S13 value) or $C_{500} = 1.8$ (N07 and P12 value), then β should not relate to the slope within the scales probed by MUSTANG. It is possible for α to relate to the slope within the scales in question. However, as C_{500} decreases, especially below 1.0, as is the case in both this work and Young et al. (2014), then α will relate less to the slope within the scales probed by MUSTANG. Crucially, having the cluster pressure profile steepen with increasing radius gives rise to the degeneracy observed between C_{500} and γ as seen in Figure 4.8.

Figure 4.2 shows that Bolocam does not place strong constraints on γ and C_{500}, especially relative to the joint fit (Table 4.10). Specifically, for the A10 set of α and β, the Bolocam finds $C_{500} = 0.66^{+0.34}_{-0.38}$, $\gamma = 0.39^{+0.49}_{-0.39}$, and $P_0 = 17.7^{+2.76}_{-8.27}$. As in Figure 4.5, we see in Figure 4.6 that the best joint fit pressure profiles from the different gNFW fits of MACS 0647 are in good agreement, and the radii where Bolocam and MUSTANG have the tightest constraints are similar to the radii of tightest constraints found in Abell 1835.

4.3.14 MACS 0744 (z=0.70)

MACS 0744 is neither classified as a cool core cluster nor a disturbed cluster (Mann & Ebeling 2012; Sayers et al. 2013), but qualifies as a relaxed cluster (Mann & Ebeling 2012). There is a dense X-ray core, and a doubly peaked red sequence of galaxies as found by Kartaltepe et al. (2008). The gas is also found to be rather hot: $k_B T_e =$

$17.9^{+10.8}_{-3.4}$ keV, as determined by combining SZ and X-ray data (LaRoque et al. 2003).

The data presented here is the same as in Korngut et al. (2011), but has been processed differently: again, the primary difference is in the treatment of the common mode. Additionally, Korngut et al. (2011) optimize over the low-pass filtering of the common mode and do not implement a correction factor for the SNR map. The surface brightness significance of the shock feature is the same, but is perhaps less bowed than the kidney bean shape seen previously. The excess in Korngut et al. (2011) was an exciting results for MUSTANG, as it marked the first clear detection of a shock in the SZ that had not been previously been known from X-ray observations. Korngut et al. (2011) reanalyze the X-ray data with the knowledge of the shocked region from MUSTANG, and calculate the Mach number of the shock based on (1) the shock density jump, (2) stagnation condition between the pressures at the edge of the cold front and just ahead of the shock, and (3) temperature jump across the shock, and find Mach numbers between 1.2 and 2.1, with a velocity of 1827^{+267}_{-195} km s^{-1}.

4.3.15 CLJ 1226 (z=0.89)

CLJ 1226 is a well studied high redshift cluster (e.g. Mroczkowski et al. 2009; Bulbul et al. 2010; Adam et al. 2015). Adam et al. (2015) find a point source at RA 12:12:00.01 and Dec +33:32:42 with a flux density of 6.8 ± 0.7 (stat.) ± 1.0 (cal.) mJy at 260 GHz and 1.9 ± 0.2 (stat.) at 150 GHz. This is not the same point source seen in Korngut et al. (2011), which is reported as a point source with 4.6σ significance in surface brightness. In our current analysis, we do not clearly observe a point source at either location, but we do model the point source found in Adam et al. (2015) and fit a flux density of 0.36 ± 0.11 mJy.

In the previous analysis of the MUSTANG data, Korngut et al. (2011) find a ridge of significant substructure after subtracting a bulk SZ profile (N07, fitted to SZA data). They find that this ridge, southwest of the cluster center, alongside X-ray profiles, are consistent with a proposed merger scenario.

4.3.16 Discussion

The results of our pressure profile analysis is summarized in Table 4.11. Y_{sph} is calculated using the tabulated value of R_{500}, where Y_{sph} is given by:

$$Y_{sph}(r) = \frac{\sigma_T}{m_e c^2} \int_0^r P_e(r') 4\pi r'^2 dr'. \tag{4.22}$$

The error bars on $Y_{Sph}(R_{500})$ are found by calculating $Y_{Sph}(R_{500})$ to the fits over the 1000 noise realizations, and taking the values encompassing the middle 68%. We compare our values of $Y_{Sph}(R_{500})$ to the scaling relation calculated in Arnaud et al. (2010) in Figure 4.13 and find six clusters which deviate by more than 2σ, in Y_{Sph}, from the scaling relation: MACS 1311, MACS 0429, RXJ 1347, MACS 1149, MACS 0717, and MACS 0744.

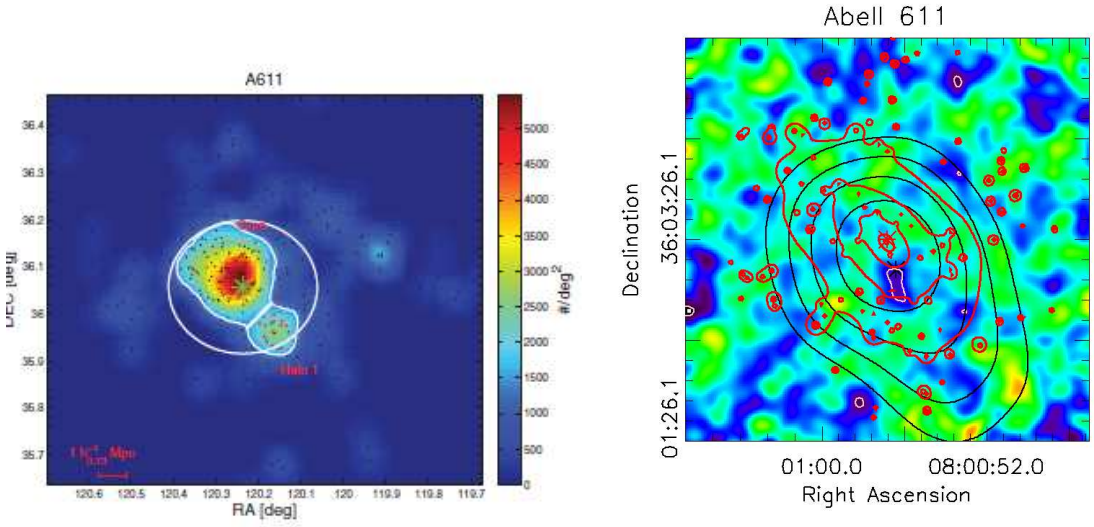

Fig. 4.11.— Left: from Lemze et al. (2013): surface density of bound galaxies and identified halos. Right: MUSTANG map with MUSTANG, Bolocam, and weak lensing surface mass density contours in pale pink, black, and red respectively.

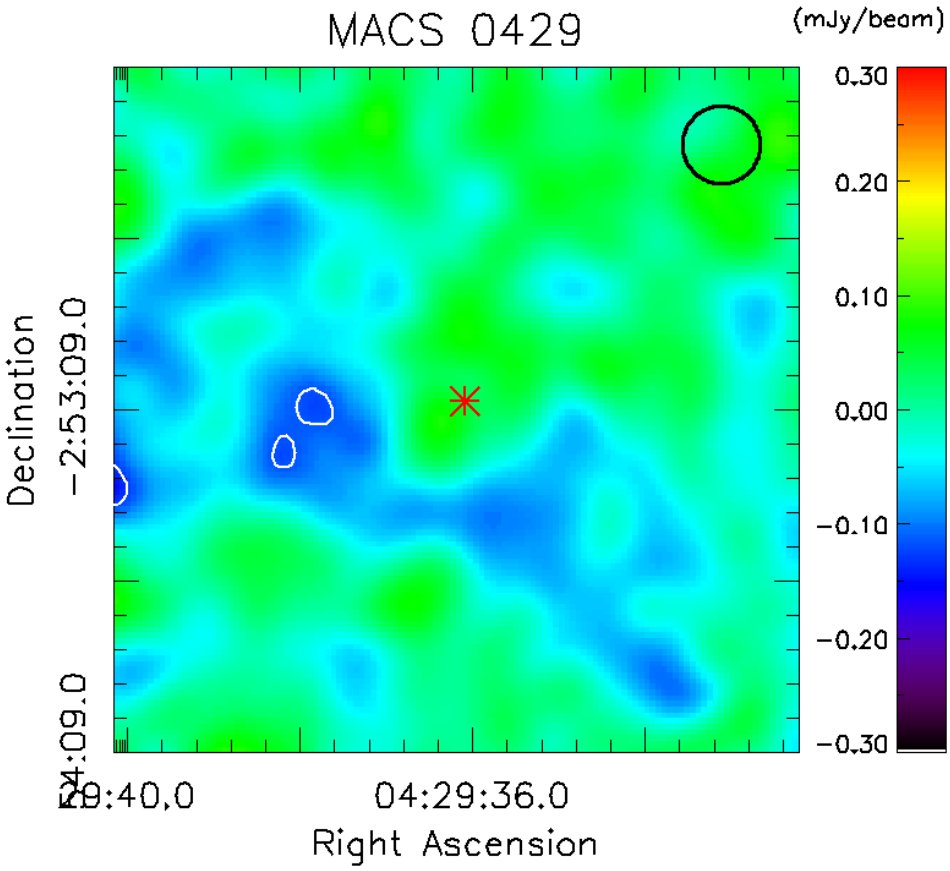
MACS 0429
(mJy/beam)
0.30
0.20
0.10
0.00
−0.10
−0.20
−0.30
Declination
−2:53:09.0
04:09.0
04:29:40.0
04:29:36.0
Right Ascension

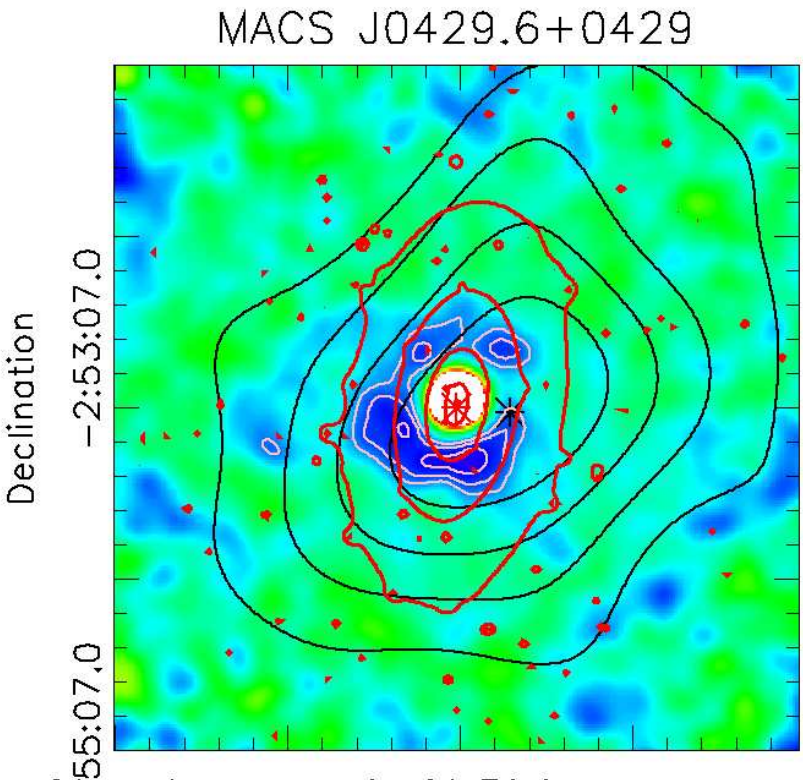
MACS J0429.6+0429
Declination
−2:53:07.0
55:07.0

footnotesize

Table 4.11. Summary of Fitted Pressure Profiles

Cluster	R^a_{500} (Mpc)	$Y_{sph}(R_{500})$ (10^{-5} Mpc^2)	P^a_{500} 10^{-3} keV cm^{-3}	P_0	C_{500}	α
Abell 1835	1.49	$22.50^{+4.12}_{-4.49}$	5.94	2.15 ± 0.07	$0.77^{+0.23}_{-0.17}$	1.05
Abell 611	1.24	$8.14^{+3.68}_{-2.21}$	4.45	35.43 ± 2.46	$2.00^{+0.40}_{-0.30}$	1.05
MACS 1115	1.28	$20.53^{+3.84}_{-3.52}$	5.45	0.67 ± 0.04	$0.35^{+0.15}_{-0.10}$	1.05
MACS 0429	1.10	$19.85^{+4.00}_{-3.74}$	4.48	11.01 ± 0.77	$0.59^{+0.11}_{-0.09}$	1.05
MACS 1206	1.61	$43.24^{+8.19}_{-8.27}$	10.59	2.39 ± 0.10	$0.74^{+0.16}_{-0.14}$	1.05
MACS 0329	1.19	$12.91^{+2.93}_{-2.37}$	5.93	9.30 ± 0.50	$1.18^{+0.72}_{-0.28}$	1.05
RXJ1347	1.67	$37.69^{+5.78}_{-5.11}$	11.71	3.24 ± 0.08	$1.18^{+1.02}_{-0.48}$	1.05
MACS 1311	0.93	$10.16^{+1.79}_{-1.73}$	3.99	2.75 ± 0.22	$0.35^{+0.15}_{-0.05}$	1.05
MACS 1423	1.09	$8.47^{+2.53}_{-2.07}$	6.12	22.39 ± 1.71	$1.58^{+0.22}_{-0.48}$	1.05
MACS 1149	1.53	$42.77^{+4.99}_{-5.67}$	12.28	5.50 ± 0.25	$0.83^{+0.07}_{-0.03}$	1.05
MACS 0717	1.69	$43.44^{+9.28}_{-8.00}$	14.90	21.28 ± 0.68	$1.97^{+0.53}_{-0.37}$	1.05
MACS 0647	1.26	$26.22^{+5.37}_{-4.72}$	9.23	2.78 ± 0.11	$0.70^{+0.30}_{-0.20}$	1.05
MACS 0744	1.26	$12.59^{+3.18}_{-2.29}$	11.99	13.15 ± 0.81	$1.71^{+0.29}_{-0.21}$	1.05
CLJ1226	1.00	$9.03^{+2.03}_{-1.60}$	11.84	19.29 ± 1.25	$1.90^{+0.60}_{-0.50}$	1.05
All	–	–	–	7.94 ± 0.10	$1.3^{+0.1}_{-0.1}$	1.05
Cool Core	–	–	–	3.55 ± 0.06	$0.9^{+0.1}_{-0.1}$	1.05
Disturbed	–	–	–	12.56 ± 0.29	$1.5^{+0.1}_{-0.2}$	1.05

footnotesize

Table 4.11—Continued

footnotesize

Cluster	R^a_{500} (Mpc)	$Y_{sph}(R_{500})$ (10^{-5} Mpc^2)	P^a_{500} 10^{-3} keV cm^{-3}	P_0	C_{500}	α	β	γ	k	$\tilde{\chi}^2$	d.o.f.
Well behaved	–	–	–	5.34 ± 0.08	$1.2^{+0.1}_{-0.1}$	1.05	5.49	$0.5^{+0.1}_{-0.1}$	–	–	–
All (A10)	–	–	–	$8.403h_{70}^{-3/2}$	1.177	1.0510	5.4905	0.3081	–	–	–
Cool core (A10)	–	–	–	$3.249h_{70}^{-3/2}$	1.128	1.2223	5.4905	0.7736	–	–	–
Disturbed (A10)	–	–	–	$3.202h_{70}^{-3/2}$	1.083	1.4063	5.4905	0.3798	–	–	–

Note. — Results from our pressure profile analysis. Y_{sph} is calculated using the tabulated value of R_{500}. [a]Values of R_{500} and P_{500} are taken from Sayers et al. (2013). We have assumed A10 values of α and β. The findings from A10 are reproduced in the last three rows. The h_{70} dependence is included for explicit replication of A10 results; all P_0 values have this dependence (the assumed cosmologies are the same). Well behaved clusters are identified in the next section.

To reiterate, Tables 4.1 and 4.5 have results to fitted point source and residual components. For point sources, while the MUSTANG point sources have been scrutinized substantially, it is worth considering the impact of the assumed point sources in the Bolocam maps of Abell 1835, MACS 0429, RXJ 1347, and MACS 1423. The conversion for S_{140} values from mJy to the equivalent $\mu K_{CMB-amin}$ is ~ 30, which puts the uncertainties of these point sources at 6, 52, 35, and 6 $\mu K_{CMB-amin}$ respectively. From Table 4.3, we see that the noise in the Bolocam maps of these clusters are 16.2, 24.1, 19.7, and 22.3 $\mu K_{CMB-amin}$ respectively. Thus, for MACS 0429 and RXJ 1347, we see that the potential impact of the point sources assumed by Bolocam could be non-trivial.

We note that M_{500}, from Mantz et al. (2010), is calculated by (1) calculating $M_{gas,2500}$, the total gas mass enclosed in R_{2500} from deprojected gas mass (non-parametric) profiles, (2) calculating R_{500} by a ratio of $R_{500}/R2500 \sim 2.3$ assuming an NFW profile with concentration parameter $c = 4$, and (3) calculating to M_{500} as $\frac{4\pi 500 \rho_{cr}(z) r_{500}^3}{3(1+B)}$, where $B = 0.03 \pm 0.06$ is a systematic fractional bias. Mantz et al. (2010) note that the dominant source of systematic uncertainty associated with M_{500} comes from the uncertainty in the assumed $f_{gas}(r_{2500}) = 0.1104$.

4.3.17 Parameter Range

We find that six of our sample of fourteen have a best fit $\gamma = 0$, where we do not allow $\gamma < 0$. We find that our range of C_{500} is sufficient, and that it is generally found to be $0.5 < C_{500} < 2.0$. This is not unprecedented; Arnaud et al. (2010) find six of their 31 analyzed clusters in the REXCESS sample have $\gamma = 0$, where all gNFW parameters except β were fitted for individual clusters. They found a similar range in C_{500}, and $0.3 < \alpha < 2.5$. The sample in Arnaud et al. (2010) is a local ($z < 0.2$), flux limited

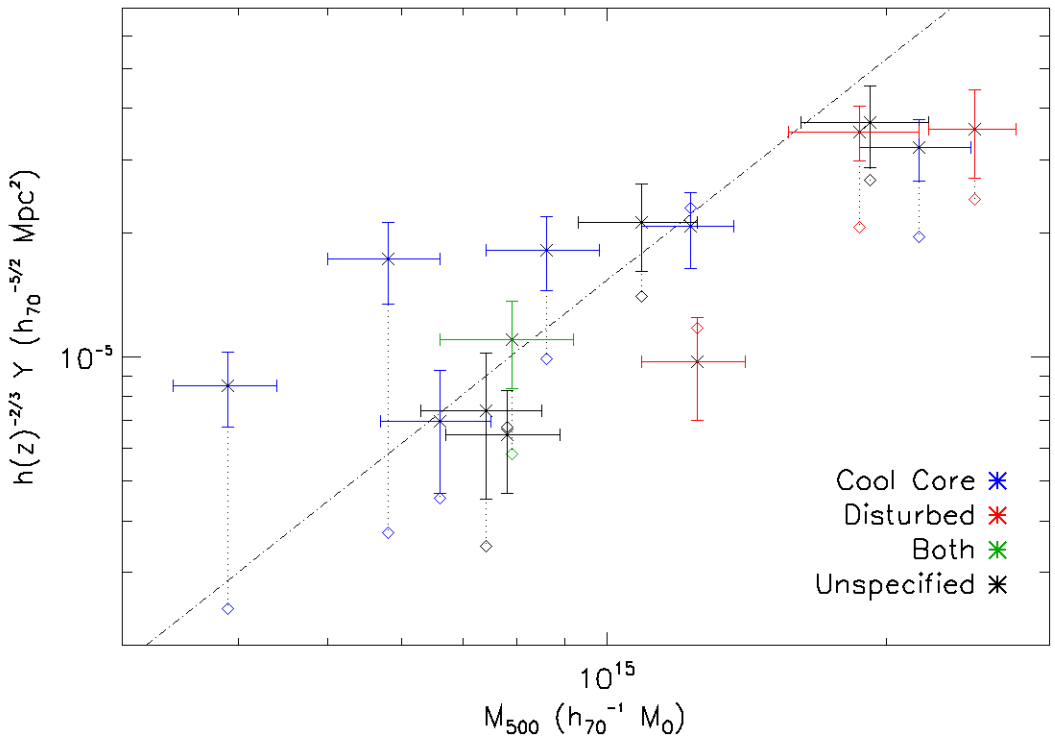

Fig. 4.13.— $Y_{Sph,SZ}(R_{500})$ as calculated in this work (Table 4.11), and M_{500} as calculated from Mantz et al. (2010). The scaling relation (dashed-dotted line) is from Arnaud et al. (2010). The diamonds are $Y_{Sph,X}(R_{500})$ as calculated from the gNFW fits to the ACCEPT pressure profiles. MACS 1311 and MACS 0429 are the notable outliers above the scaling relation.

sample, and for their analysis, they have excluded two clusters (a supercluster, Abell 901/902, and a bimodal cluster, RXC J2157.4-0747) from the full REXCESS sample of 33 clusters. Sayers et al. (2013) determined pressure profile parameters over a sample of 45 clusters with the redshift range $0.15 < z < 0.89$, where most (60%) lie between $0.35 < z < 0.59$. They fit profiles to the stack of deprojected pressure profiles, restricting C_{500} to the A10 value, and fit for the other gNFW parameters. The degeneracies between parameters in Sayers et al. (2013) is shown in Figure 4.14 and the degeneracies in parameters fit in this work are shown in Figure 4.10.

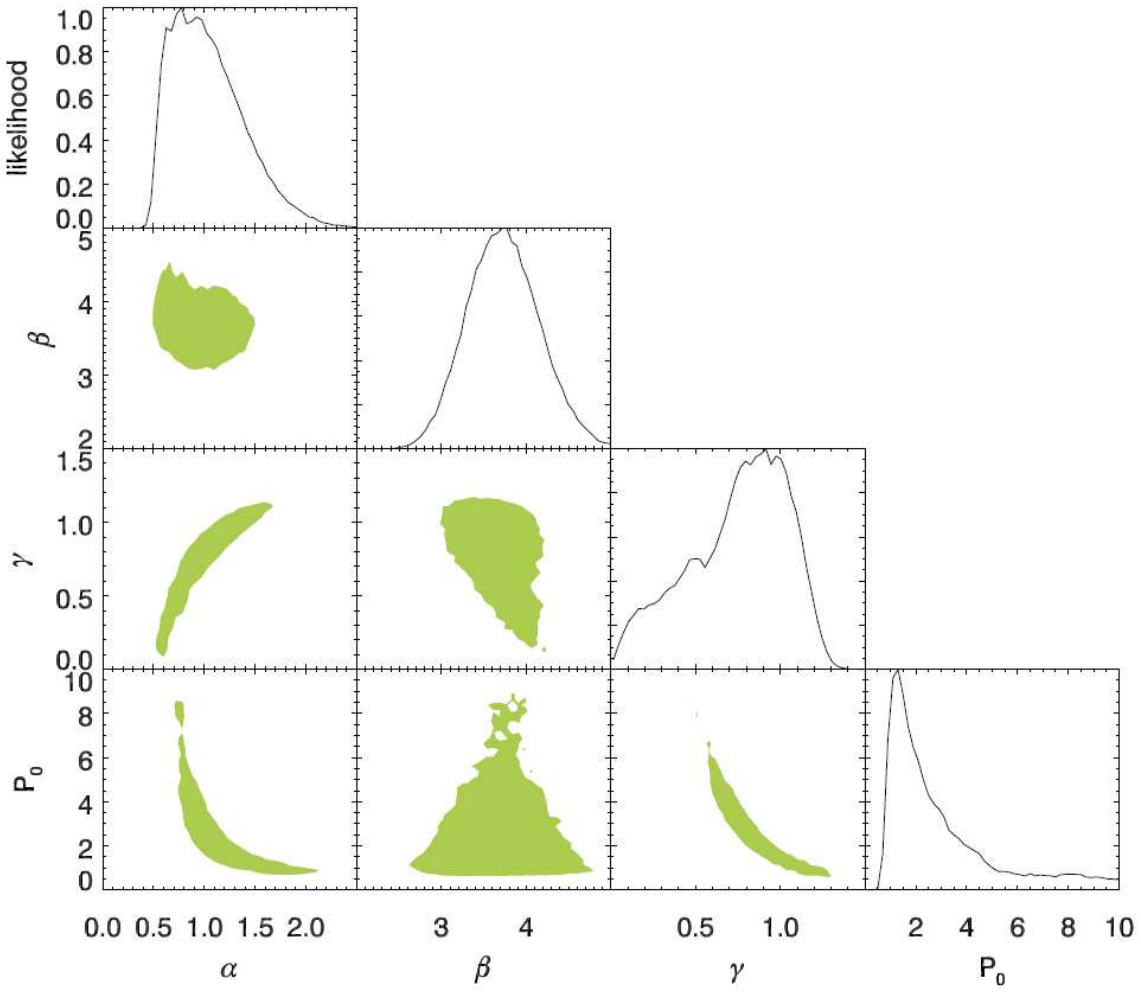

Fig. 4.14.— From Sayers et al. (2013); shaded region denotes 1σ (68%). This figure shows the correlations (degeneracies) between gNFW parameters.

4.3.18 Comparison to other results

Figure 4.9 shows the best joint fit gNFW pressure profiles to MUSTANG and Bolocam, and have deprojected pressure profiles from ACCEPT overplotted. Seven clusters (Abell 611, MACS 0429, MACS 0329, MACS 1311, MACS 1423, MACS 0717, and MACS 1149) have notable discrepancies ($\chi^2_B/d.o.f. = \tilde{\chi}^2 \gtrsim 5$, as in Table 4.12) with the ACCEPT-derived pressures, where χ^2_B is fits the SZ-derived pressure profile

to the ACCEPT pressure profile with only the amplitude being allowed to vary. The remaining seven clusters not listed are considered "well behaved". Most of the clusters with notable discrepancies are fit by $\gamma = 0$, with the exception of MACS 1311, which has a low C_{500}.

However, the parameter space restriction is not to blame. The ACCEPT pressure profiles can be fit by gNFW profiles with the same restrictions on α and β (fixing them to A10 values), and the values of C_{500}, P_0, and γ are well within the parameter space searched and provided qualitatively and quantitatively good fits to the ACCEPT data. The chi^2 values to these fits are reported as χ^2_A, with associated degrees of freedom in Table 4.12. These fitted profiles can then be fit to the SZ data varying just the amplitude, and in all six cases, the SZ pressure is greater than the ACCEPT data, and moreover, fitting the profiles to just the Bolocam data shows that Bolocam fits these clusters at a factor of 1.45 to 3.15. Recall from Section 4.2.5, especially Figures 4.5 and 4.6, Bolocam is able to set strong constraints at radii $\theta \sim 70''$.

footnotesize

Despite the relative discrepancies in pressure profiles, especially as evidenced by χ^2_B in Table 4.12, it is interesting that the pressure profile found over all clusters has very similar parameters to Arnaud et al. (2010). This can also be seen in Figure 4.15, where the A10 pressure profile is consistently close to the line from this work (R15). While all 14 clusters in this work are in Sayers et al. (2013), they find a consistently higher universal pressure profile.

Table 4.12. Derived Cluster Masses

footnotesize

Cluster	$M_{500,SZ}$	$M_{500,X}$	χ^2_A/d.o.f.	χ^2_B/d.o.f.
Abell 1835	11.83	12.30 ± 1.4	22.5/29	39.8/29
Abell 611	6.63	7.40 ± 1.1	4.2/29	1225.3/29
MACS 1115	10.99	8.60 ± 1.2	11.5/32	101.7/32
MACS 0429	10.69	5.80 ± 0.8	8.2/16	572.4/16
MACS 1206	16.41	19.20 ± 3.0	3.4/34	30.0/34
MACS 0329	8.30	7.90 ± 1.3	13.9/32	610.5/32
RXJ 1347	15.16	21.70 ± 3.0	40.7/32	137.8/32
MACS 1311	7.19	3.90 ± 0.5	9.7/21	180.9/21
MACS1423	6.41	6.60 ± 0.9	15.2/22	107.7/21
MACS 1149	15.95	18.70 ± 3.0	4.9/38	209.7/38
MACS 0717	16.06	24.90 ± 2.7	36.1/36	226.1/36
MACS 0647	11.98	10.90 ± 1.6	5.6/22	6.5/22
MACS 0744	7.76	12.50 ± 1.6	10.0/25	24.5/25
CLJ 1226	6.16	7.80 ± 1.1	12.7/19	18.6/19

Note. — $M_{500,sz}$ is the calculated based on the scaling relation with Y_{sph} in Arnaud et al. (2010). Values $M_{500,X}$ are X-ray derived values, taken from Mantz et al. (2010). The column χ^2_A enumerates χ^2 values for gNFW fits to ACCEPT pressure profiles. The column χ^2_B enumerates χ^2 for the SZ-fit gNFW profile to the ACCEPT data, where the inner and outermost bins have been trimmed. In both cases, d.o.f. indicates the degrees of freedom.

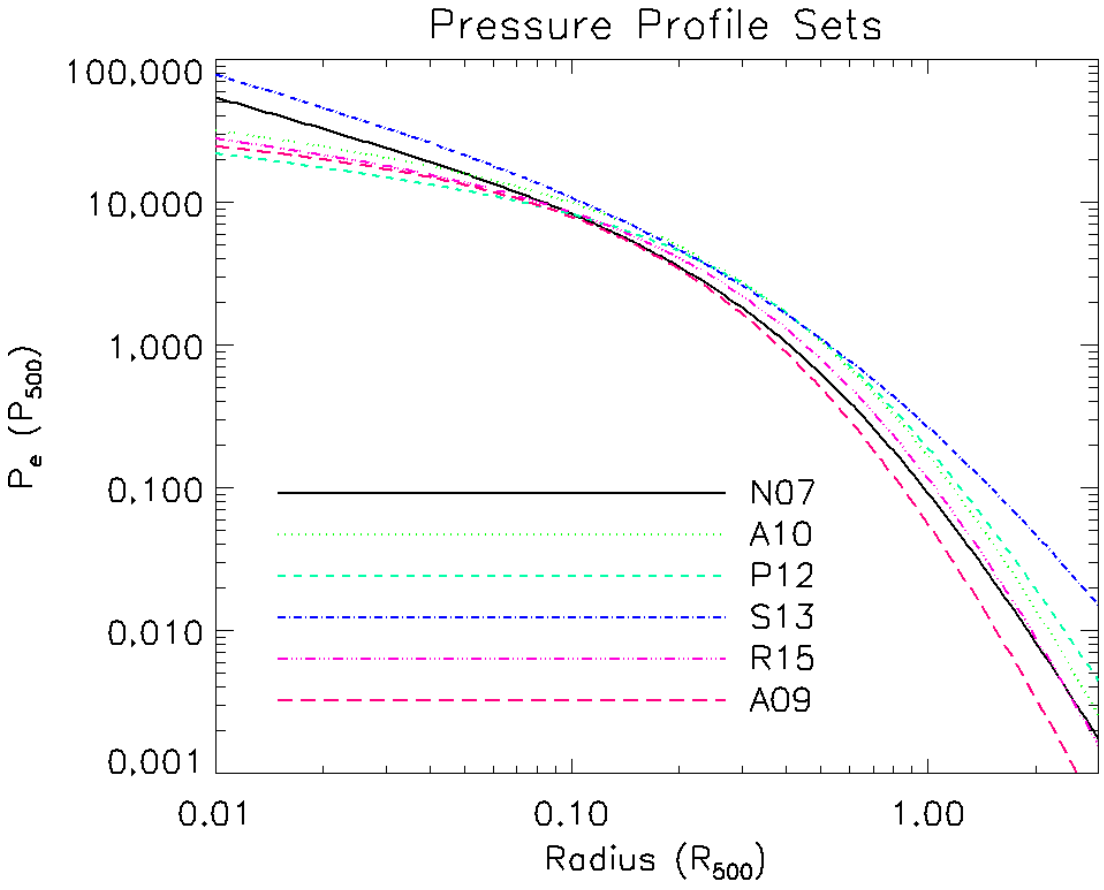

Fig. 4.15.— Pressure Profiles from this (R15) and other works. A09 indicates ACCEPT (Cavagnolo et al. 2009) pressure profile for the 14 clusters in this sample. Note that A09 falls below R15, especially at larger radii. Recall the greatest constraints for this analysis were between $7''$ and $70''$. We thus constrain radii roughly $0.03R_{500} \lesssim r \lesssim R_{500}$.

Chapter 5

Comparison to X-ray Derived Pressure Profiles

Abstract

The primary observables of SZ and X-ray observations of galaxy clusters differ in their proportionality with physical properties in the intracluster medium (ICM). This difference has, in the past, been exploited to make calculations of the Hubble parameter, H_0, assuming spherical geometry of galaxy clusters. However, one relax the spherical assumption and use the differences in SZ and X-ray inferred quantities to calculate cluster elongation along the line of sight, helium sedimentation, or (recalculate) the ICM electron temperature. These are all degenerate (i.e. these can not all be independently constrained). We investigate each constraint individually, and conclude that differences in the SZ and X-ray spherically derived pressure profiles are due to some combination cluster elongation and ICM temperature distribution.

5.1 Ellipsoidal Geometry

The geometry of a cluster, along the line of sight, may be calculated by comparing SZ and X-ray pressure profiles. To show the dependence, we take n_e as the true distribution, and let it be a function of ellipsoidal radius, $E^2 = \frac{x^2}{a^2} + \frac{y^2}{b^2} + \frac{z^2}{c^2}$, where we will define z to be along the line of sight. Additionally, let $\rho = \sqrt{\frac{x^2}{a^2} + \frac{y^2}{b^2}}$ and $s = \frac{z}{c}$ be a "scaled" line of sight variable. Given that our observables are integrals along the line of sight, we can write $O(\rho) = \int Q(\rho, z)dz$, where $O(\rho)$ is our observable as a function of position on the sky, and $Q(\rho, z)$ is our integrable quantity (source function) with ellipsoidal symmetry. We should then recognize that we could alternatively write this as $O(\rho) = \int c \times Q(\rho, s)ds$, as $dz = cds$.

Now, $O(\rho)$ is fixed, and thus $Q(\rho, s) \propto \frac{1}{c}$. Of interest to us is n_e. Here we have $n^2_{e,X}(\rho) \propto c$, and $n_{e,SZ}(\rho) \propto c$. Under the spherical assumption, $a = b = c$, and we may take that these all equal 1. Thus, the ratio of derived (spherical) radial electron densities has the following proportionality: $\frac{n_{e,SZ}(r)}{n_{e,X}(r)} \propto \eta^{-1/2}$. Noting that η is independent of r, we see that it can be ascertained through the normalization of the electron density profiles, or similarly, the electron pressure profiles. Thus, $\frac{P_{e,SZ}}{P_{e,X}}$ will have the same dependence. We can sum this up as saying that a prolate cluster (along the line of sight, $\eta < 1$) will yield greater pressure as derived from SZ than from X-ray, whereas an oblate cluster (along the line of sight) will do the opposite.

To estimate the ellipticity of clusters, we fit the ACCEPT pressure profiles with a gNFW pressure profile, with α and β fixed at their A10 values: 1.05 and 5.49, respectively. These are tabulated in Table 5.1. The resultant gNFW profile is then integrated along the line of sight (LOS) to create a Compton y map, and then filtered as discussed in Romero et al. (2015). The amplitude of the ACCEPT model fitted to Bolocam data, P_{Bolo} in Table 5.1 is used to account for the geometry of the

cluster. The POS-to-LOS ratio given as $\eta = P_{Bolo}^{-2}$, and its associated uncertainty is calculated as $\sigma_\eta^2 = 2P_{Bolo}^{-2}((\sigma_{P_{Bolo}}/P_{Bolo})^2 + (\sigma_{Bolo}/P_{Bolo})^2 + (\sigma_{ACCEPT}/P_{Bolo})^2)$, where $(\sigma_{Bolo}/P_{Bolo}) = 0.05$ and $(\sigma_{ACCEPT}/P_{Bolo}) = 0.10$ are the calibration uncertainties of Bolocam and ACCEPT respectively.

Table 5.1. ACCEPT gNFW Fitted Parameters and Comparison to SZ data

Cluster	P_0	C_{500}	γ	P_{SZ}	k	P_{Bolo}	η	σ_η	Δk (σ)
Abell 1835	12.763	1.366	0.426	0.77	1.21	0.75	1.77	0.41	1.08
Abell 611	3.244	1.180	0.422	3.08	0.94	3.15	0.10	0.03	0.17
MACS1115	18.028	1.687	0.317	0.93	1.17	0.89	1.28	0.32	-0.50
MACS0429	3.763	1.189	0.730	1.79	0.57	2.06	0.24	0.06	3.58
MACS1206	2.821	0.963	0.555	1.36	0.97	1.36	0.54	0.13	1.00
MACS0329	3.486	1.139	0.659	1.90	0.89	1.94	0.26	0.07	1.17
RXJ1347	85.316	3.838	0.028	1.13	1.18	1.12	0.79	0.18	-0.25
MACS1311	35.663	2.105	0.084	1.64	0.81	1.85	0.29	0.08	1.42
MACS1423	14.474	1.859	0.447	1.26	0.82	1.38	0.52	0.15	1.83
MACS1149	6.209	1.117	0.000	1.41	0.82	1.45	0.48	0.12	0.42
MACS0717	12.703	1.864	0.000	1.80	0.51	1.84	0.30	0.07	0.25
MACS0647	24.841	1.741	0.000	1.24	1.09	1.22	0.67	0.16	-0.42
MACS0744	1.532	0.832	0.710	1.14	0.97	1.15	0.76	0.19	0.58
CLJ1226	21.488	1.833	0.118	1.21	1.00	1.22	0.68	0.18	-0.67

Note. — Tabulated gNFW fits to the ACCEPT pressure profiles. P_{SZ} denotes the fitted amplitude (renormalization) of the ACCEPT model to the SZ data. P_{Bolo} denotes the fitted amplitude of the ACCEPT model to just Bolocam data. the gNFW parameters α and β are fixed at A10 values of 1.05 and 5.49. The column Δk (σ) lists the significances of a more spherical core, as compared to the outer regions. Δk was calculated as the difference between the k in this table (column 5), and the values listed in Table 4.11. Negative Δk significances indicate the core is measured to be more ellipsoidal than the outer regions.

5.2 Discussion

It is not too surprising that many of these clusters are elongated along the line of sight ($\eta < 1$). Effectively, any means of observing, and therefore detecting, a cluster is enhanced by elongation along the line of sight. The CLASH sample was X-ray (20 clusters) and lensing (5 clusters) selected; Abell 1835 is not in the CLASH sample, but is a notably well studied cool core cluster, i.e. its the subject of many studies on the basis of its cool core.

This investigation has made the assumption that the geometry of a given cluster is globally consistent. That is, one ellipsoidal geometry applies to all regions of the cluster. However, this need not be the case (Kravtsov & Borgani 2012). The cluster should appear more spherical towards the center, where baryons have condensed (e.g. Kravtsov & Borgani 2012, and references therein). Also, the DM and baryonic distributions need not align (one need only look at the Bullet cluster (Markevitch et al. 2004) for a dramatic example). This is not a particular concern to this analysis as we are comparing quantities based on the baryonic distribution, but would be more of a concern when including lensing.

One way to infer a difference in geometries between the inner and outer regions is to note the calibration offset between Bolocam and MUSTANG in our fits from Table 5.1. In almost all cases, we find that k tends to be inversely related to P_{SZ}, which may suggest that the central pressure distribution is more spherical than the outer pressure distribution. A quick estimate of this significance of this signature is found by comparing to the calibration offset values found in Table 4.11, and finding those clusters that show a preference in Δk towards a more spherical center. Recalling that k has a prior on it of 12%, we can calculate significances shown in Table 5.1.

5.3 Temperature profiles

If we assume a given geometry (known ellipticity), then instead of solving for the ellipticity, we can derive a temperature profile, which may lead to more accurate than that found solely by X-rays, depending on the quality of both data sets. X-rays do not constrain electron temperature as well as electron density because of the scaling in emission, and foremost because of the photon count requirement for X-ray spectra used to derive a temperature from X-rays, which effectively provides lower resolution temperature data, especially at larger radii. Thus, combining the SZ derived pressure and X-ray derived electron density makes use of the strength of each data set.

We find two models (beyond the isothermal model) to describe temperature profiles in the literature: those in Vikhlinin (2006), denoted as (V06) and Bulbul et al. (2010), denoted as (B10). These are given as:

$$T_{e,V06} = \frac{[(r/r_{cool})^{a_{cool}} + T_{min}/T_0]}{(r/r_{cool})^{a_{cool}} + 1} \times \frac{T_0}{(r/r_t)^a[1 + (r/r_t)^b]^{c/b}} \tag{5.1}$$

where r_{cool} is a fitted parameter, indicated the radial scale of the cool core, r_t is a transitional radius, which has been called a scaling radius in other profiles (e.g. NFW). T_{min} is the minimum temperature observed within the cool core. The remaining parameters, a_{cool}, a, b, c, and T_0 are all fit for. The first term in this equation is denoted as the cool core taper:

$$t_{cool} = \frac{[(r/r_{cool})^{a_{cool}} + T_{min}/T_0]}{(r/r_{cool})^{a_{cool}} + 1} \tag{5.2}$$

Thus, the V06 model should be seen as a gNFW temperature profile with a cool core taper, where Greek letters are used for the gNFW profiles used in our pressure profile analysis (Section 4). The letter equivalents are $a = \gamma$, $b = \alpha$, and $c = \beta - \gamma$. Thus,

given that we have fixed α and β from A10 values, we fix b and c in fitting for the V06 temperature model, where we calculate c based on the best fit γ value from our joint fits (Section 4). Thus, we fit for T_0, r_{cool}, and a_{cool}, and a.

The other temperature model (Bulbul et al. 2010) is given as:

$$T_{e,B10} = T_0 \left[\frac{1}{(\beta - 2)} \frac{(1 + r/r_s)^{\beta-2} - 1}{r/r_s(1 + r/r_s)^{\beta-2}} \right] t_{cool} \tag{5.3}$$

where T_0 and parameters in t_{cool} are the only parameters specific to the temperature profile (independent of pressure or density profile). β is a power law term in a generalized NFW profile proposed in Bulbul et al. (2010):

$$\rho_{tot}(r) = \frac{\rho_i}{(r/r_s)(1 + r/r_s)^{\beta}} \tag{5.4}$$

This formulation of density allows for an analytical formulation of $P(r)$ under the assumption of hydrostatic equilibrium. With the assumption of a polytropic equation of state ($P = k\rho_g^{n+1}$, where k is simply a constant, and n is the polytropic index), the temperature profile (Equation 5.3) can be derived. It is worth noting that Equation 5.3 does not diverge at $\beta = 2$ and can be calculated from L'Hopital's rule. As with r_t in the V06 model, we fix $r_s = R_{500}/C_{500}$ based on the fitted value of C_{500}.

We use MPFIT (Markwardt 2009) to solve for the free parameters in the two temperature profiles. For V06 model, we fit for r_{cool}, a_{cool}, T_0, and a, while for the B10 model we fit for r_{cool}, a_{cool}, T_0, and β.

The results of our SZ and X-ray derived temperature profiles are shown in Figure 5.1. We noted that the V06 model typically performs worse than B10 in our fits. This can be attributed to fixing b and c (especially c) as these are fixed at power laws that incorporate the behavior of n_e with radius.

Fig. 5.1.— Temperature Profiles. The green triangles are derived as $T_e = P_{e,SZ}/n_{e,X}$, and the shaded green indicates 1σ uncertainties.The blue plus signs are from ACCEPT. The solid lines are our fitted Vikhlinin temperature models and the dashed lines are our fitted Bulbul temperature models.

5.3.1 Discussion

Given the degeneracy between the geometry of the cluster and temperature, as calculated here, it is most probable that the difference between SZ and X-ray pressure profiles is due to a combination of the cluster geometries and the ICM temperatures. We find it implausible that the temperature is in some cases twice that found by ACCEPT, especially those inferred values of $k_B T_e \gtrsim 15$ keV. However, even accounting for geometry as calculated in Section 5.1, we find that there are some clusters that still appear discrepant with ACCEPT, particularly those whose pressure falls below ACCEPT's pressure towards the center, but above ACCEPT at larger radii. The discrepancy in the core could be suggestive of a centroid offset, but our pointing accuracy is $2''$, and we assume the same (X-ray) centroid. Even more, we can use Bolocam's centroid (Figure 4.8) and find negligible change to the SZ pressure profile. Some cases, especially MACS 0717 and MACS 1149 are likely due to their known merging status. Others, like MACS 1115, a cool core cluster with no documented merger activity, with higher pressure at large radii in the SZ relative to X-rays could likely be explained by the geometry in the plane of the sky. MACS 1115 shows a northern elongation in the Bolocam map that is not present in the X-ray surface brightness maps (Figure 4.3 and 4.4), and MACS 0429 shows a northwest-southeast elongation that is not evident in the X-ray surface brightness maps. Thus, there is a geometric discrepancy between the SZ and X-ray, especially at moderate to large radii. It is interesting to note that this discrepancy appears to bias the SZ inferred pressure high relative to the X-ray inferred pressure. This could be indicative of higher temperature (lower density) regions, as the X-ray measurements would be less sensitive to such a region.

5.4 Helium Sedimentation

5.4.1 Helium Sedimentation Models

It has long been suggested (e.g. Gilfanov & Sunyaev 1984) that the heavier helium nuclei would drift towards the center of the intra cluster medium (ICM). This has implications for the brightest cluster galaxies (BCGs), as the ultraviolet (UV) upturn seen in many of them may be explained by an increased abundance of helium in stars within those galaxies (Peng & Nagai 2009). By combining SZ observations with X-ray data, one can hope to find a helium abundance profile.

Given a specified electron density, a higher helium fraction will increase X-ray emission. Specifically, the X-ray surface brightness has the following proportionality: $S_x \propto \int n_e^2 * (1+4x)/(1+2x)$ (e.g. Markevitch & Vikhlinin 2007). If $x \equiv n_{He}/n_H$, then $n_e = (1 + 2 * x)n_H$ where the contribution from metals is considered insignificant. If the deprojection of X-ray data is done with an assumed helium fraction, x_a, but the true value is $x_{\rm true}$, then we have $n_{e,\rm true} = n_{e,X} * \sqrt{\frac{1+4x_a}{1+2x_a}\frac{1+2x_{\rm true}}{1+4x_{\rm true}}}$.

It is critical to note the helium fraction assumed to obtain the X-ray derived quantities in the ACCEPT collection (Cavagnolo et al. 2009). Their spectral analysis makes use of the MeKaL model (Mewe et al. 1985, 1986) to find the temperature. More specifically, they state that heavy element ratios are taken from Anders & Grevesse (1989), which adopts a fixed value of $x_0 = 0.0977$. The constraints on deprojected electron density profiles are determined from surface brightness profiles. In particular, they adopt the deprojection technique from Kriss et al. (1983), which calculates the electron density as:

$$n_{e,x}(r) = \sqrt{\frac{(n_e/n_H)4\pi[D_A(1+z)]^2 C(r)\eta(r)}{10^-14 f(r)}}, \tag{5.5}$$

where D_A is the angular diameter distance, $\eta(r)$ is a interpolated spectral normalization, $C(r)$ is the radial emission derived from Equation (A1) in Kriss et al. (1983), and $f(r)$ is the interpolated spectral count rate.

By contrast, the signal for SZ measurements is proportional to Compton y, which is defined as: $y = \frac{\sigma_T}{m_e c^2} \int n_e k_B T_e dl$. Thus, we see that $n_{e,SZ}$ does not have a dependence on x, and that $n_{e,SZ}$ must be the true electron density (modulo knowing T_e). Strictly speaking, the SZ signal is directly probing P_e, so rather than introduce further errors to $n_{e,SZ}$ by dividing by T_e, and propagating its errors, we will choose to compare $P_{e,SZ}$ to $P_{e,X}$. This gives us:

$$\left(\frac{P_{e,SZ}}{P_{e,X}}\right)^2 = \left(\frac{1+4x_0}{1+2x_0}\right)\left(\frac{1+2x}{1+4x}\right), \tag{5.6}$$

where $x_0 = 0.0977$ is the value adopted in Anders & Grevesse (1989). Let us define $c = \frac{1+4x_0}{1+2x_0}$, and $q = \frac{P_{e,SZ}}{P_{e,X}}$. Then we can solve for x as:

$$x = \frac{c - q^2}{4q^2 - 2c} \tag{5.7}$$

It is also worth noting here that for $\sigma_c = 0$, the associated uncertainty in x is:

$$\sigma_x = \frac{cq}{(2q^2 - c)^2}\sigma_r \tag{5.8}$$

It is clear that x has some physical and mathematical limits. We know that $x \geq 0$ and that x is finite. This would mean that we should expect, or require, that our pressure ratios have the following values: $\sqrt{c/2} < q < \sqrt{c}$. Given that for an assumed $x = 0.0977$, $c = 1.163$, this leaves little flexibility for q: $0.76 < q < 1.08$. Yet, it is quite conceivable for ratios to fall outside of this range.

Peng & Nagai (2009) solve a set of diffusion equations (Burgers equations; Burgers 1969) assuming an ICM of H-He plasma in HSE with no accretion. They do so using two temperature models: an isothermal model, which had already been calculated in Chuzhoy & Loeb (2004), and a Vikhlinin model based on the temperature profile in Vikhlinin (2006). In either case, T_X, i.e. $T_{spec} = 10$ keV. The clusters are assumed to be static, and a magnetic suppression factor, $f_B \equiv \kappa/\kappa_{Sp} = 1$ relates the thermal conductivity, κ, to the Spitzer thermal conductivity, κ_{Sp}. The results of the two models with the above assumptions is shown in Figure 5.2.

Because the helium sedimentation models (Figure 5.2) have a radial dependence, and especially is not expected to be seen at large radii, we can estimate the cluster elongation and seek to constrain helium sedimentation. To do this, we use P_{Bolo} in Table 5.1, and assume departure of P_{Bolo} from 1 is attributable to the POS-LOS ratio (Section 5.1) globally. Thus, we fit to $P_{e,SZ}/P_{e,X}$, where $P_{e,SZ}$ has been rescaled. Explicitly, let P_e be the joint fit pressure profiles from Chapter 4, so that $P_{e,SZ} = P_e/P_{Bolo}$, and $P_{e,X}$ is the electron pressure from ACCEPT.

Temperature profile check

A reasonable sanity check is to compare the ACCEPT temperature profiles with an approximate ensemble temperature profile found in Vikhlinin (2006):

$$\frac{T(r)}{T_{mg}} = 1.35\frac{(x_r/0.045)^{1.9} + 0.45}{(x_r/0.045)^{1.9} + 1}\frac{1}{(1 + (x_r/0.6)^2)^{0.45}},, \tag{5.9}$$

where $x_r = r/R_{500}$ is the scaled radius and T_{mg} is the gas mass weighted electron temperature. Vikhlinin (2006) fit the temperature profile to a sample of 13 low-redshift clusters and used as a basis for a set of models in Peng & Nagai (2009). Vikhlinin (2006) also find the following relations between derived temperatures over

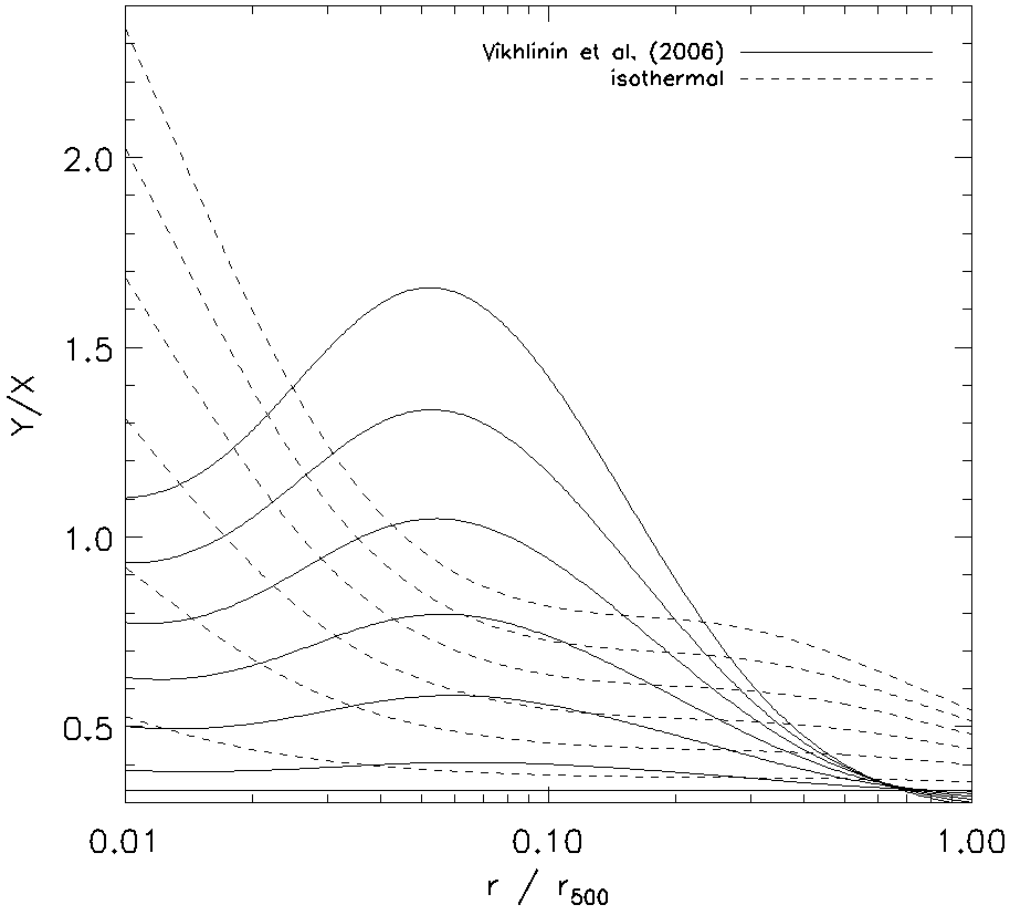

Fig. 5.2.— Models of the He-to-H mass fraction (Y/X) for isothermal and Vikhlinin temperature profiles (Peng & Nagai 2009). The atomic fraction of helium, x, is simply a quarter of Y/X. Ages are 0, 1, 3, 5, 7, 9, and 11 Gyr (Y/X increases with age.)

the range 70 kpc-r_{500} for their sample:

$$T_{peak} : T_{spec} : T_{mg} = 1.21 : 1.11 : 1.0 \tag{5.10}$$

ACCEPT reports an average temperature for each cluster, but does not clarify how it is derived. However, Mantz et al. (2010) states that his values are derived from

spectra over $0.15R_{500} < r < R_{500}$, which according to Vikhlinin (2006), we should expect to be 0.97 of the spectra temperature derived over 70 kpc$-r_{500}$.

To find T_{mg}, we fit the interpolated temperature reported from ACCEPT to Equation 5.9. That is, T_{mg} is simply the amplitude, $\vec{a}_m$, using the same approach that was discussed in Section 4.2. That is, we take $\mathbf{A} = \vec{T}_{Vik}$, and $\vec{d} = \vec{T}(r)$.

5.4.2 Sample for Helium Sedimentation

Given that helium sedimentation (or sedimentation processes generally) is most prominent when the suspending medium is relatively relaxed, we would expect it to be most prominent in cool core clusters. To this end, we select those clusters within our CLASH sample which are listed as cool core by $L_{rat} \geq 0.17$ (Sayers et al. 2013). The clusters are thus: Abell 1835, MACS 1115, MACS 0429, MACS 0329, RXJ1347, MACS 1423, and MACS 1311, giving us seven clusters.

We choose to fit helium sedimentation models to the pressure ratios, $\frac{P_{e,SZ}}{P_{e,X}}$ of each cluster. This ratio is more directly related to the observations than x, allowing a straightforward determination of the uncertainties.

For fitting, we take each of the models calculated in Peng & Nagai (2009) and calculate corresponding pressure ratio models. To do this, we bin the helium fraction and the SZ fitted pressure into the same radial bins as the X-ray data, and fit the models to the data. The pressure ratio models are then used to calculated χ^2. The χ^2 results are reported in Tables 5.2 and 5.3.

5.4.3 Discussion on Helium Sedimentation

The result $\Delta\chi^2 = 165$ in favor of helium sedimentation appears to be a fairly conclusive detection of helium sedimentation. Allowing two degrees of freedom (temperature

Table 5.2. Nominal χ^2 values for helium sedimentation models

Model	0 Gyr	1 Gyr	3 Gyr	5 Gyr	7 Gyr	9 Gyr	11 Gyr
iso	684.3	663.3	628.5	601.7	581.2	565.2	552.6
Vik	684.3	667.5	634.3	603.4	575.9	552.0	531.7

Note. — χ^2 from all seven clusters. The degrees of freedom in each fit are 204.

Table 5.3. Nominal χ^2 values for helium sedimentation models

Model	0 Gyr	1 Gyr	3 Gyr	5 Gyr	7 Gyr	9 Gyr	11 Gyr	Cluster
iso	10.16	10.50	11.32	12.29	13.31	14.36	15.40	Abell 1835
Vik	**10.16**	10.58	11.62	12.92	14.40	15.98	17.62	$\Delta\chi^2 = 0.00$, DOF: 31
iso	34.09	34.32	34.85	35.44	36.06	36.66	37.24	MACS 1115
Vik	34.09	**34.08**	34.14	34.31	34.57	34.89	35.26	$\Delta\chi^2 = 0.01$, DOF: 34
iso	193.14	187.21	177.20	169.26	162.99	157.97	153.87	MACS 0429
Vik	193.14	188.43	178.94	169.89	161.62	154.27	**147.83**	$\Delta\chi^2 = 45.31$, DOF: 18
iso	97.87	92.63	84.42	78.45	74.11	70.89	**68.45**	MACS 0329
Vik	97.87	95.09	89.58	84.39	79.70	75.59	72.07	$\Delta\chi^2 = 29.42$, DOF: 34
iso	22.08	22.24	22.63	23.08	23.55	24.01	24.45	RXJ 1347
Vik	22.08	21.98	21.82	**21.76**	21.77	21.84	21.97	$\Delta\chi^2 = 0.32$, DOF: 34
iso	184.48	179.70	170.91	163.31	156.86	151.37	146.68	MACS 1311
Vik	184.48	178.90	167.81	157.45	148.12	139.94	**132.78**	$\Delta\chi^2 = 51.70$, DOF: 23
iso	142.45	136.70	127.19	119.88	114.29	109.96	106.52	MACS1423
Vik	142.45	138.43	130.37	122.69	115.69	109.50	**104.13**	$\Delta\chi^2 = 38.33$, DOF: 24

Note. — χ^2 for each cluster. We can also find $\Delta\chi^2$ for each cluster is calculated as the difference between the χ^2 for the 0 Gyr model(s) and the minimum χ^2, which is bolded. Using $\sum(min(\chi_i^2))$, we find $\Delta\chi^2 = 165.$ in support of helium sedimentation.

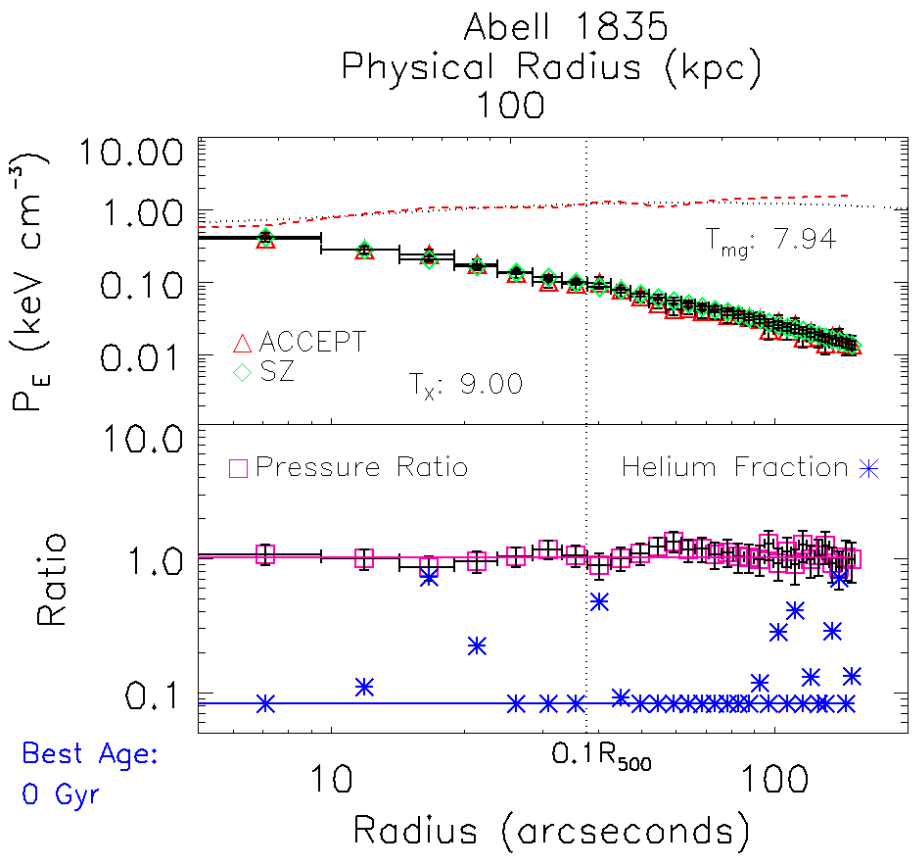

Fig. 5.3.— Electron pressure profiles and SZ-to-X-ray pressure ratios of Abell 1835. The red dashed line shows the normalized temperature from ACCEPT (T_{ACCEPT}/T_{mg}), while the dotted line shows T_{Vik}. In the lower panel, derived helium fraction and pressure ratios ($P_{e,SZ}/P_{e,X}$) are plotted with squares and asterisks, while the solid lines show the best fit of the PN09 models. Plotted helium fractions are limited as previously discussed.

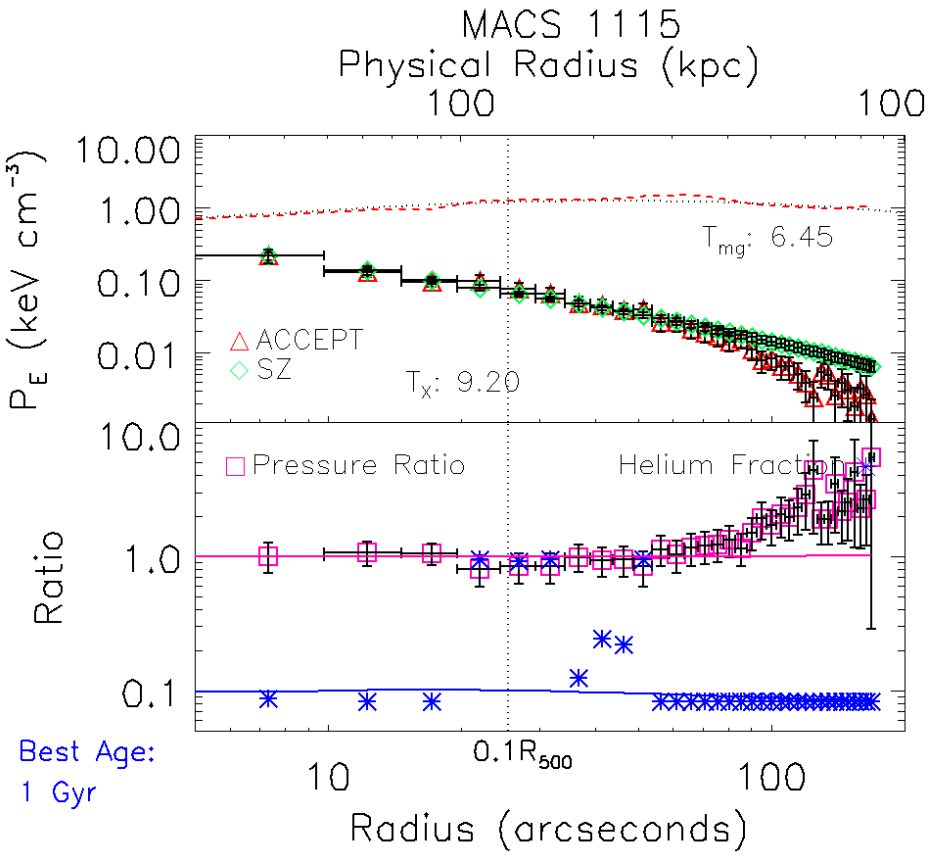

Fig. 5.4.— Notation is identical to Figure 5.3.

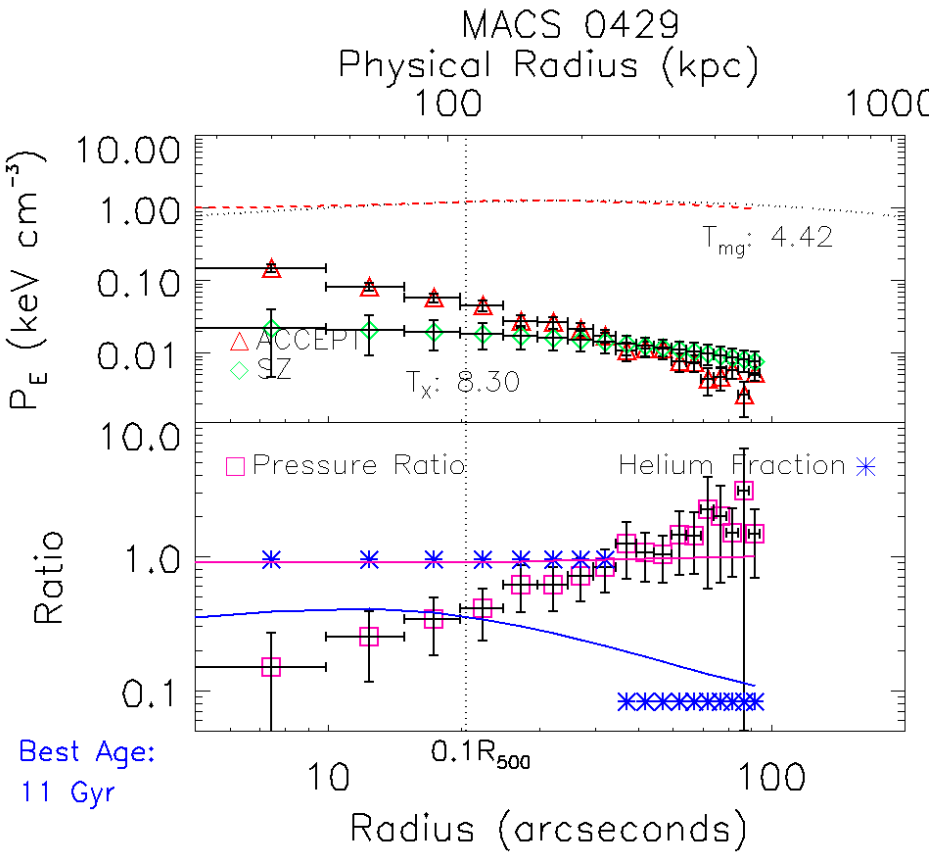

Fig. 5.5.— Notation is identical to Figure 5.3.

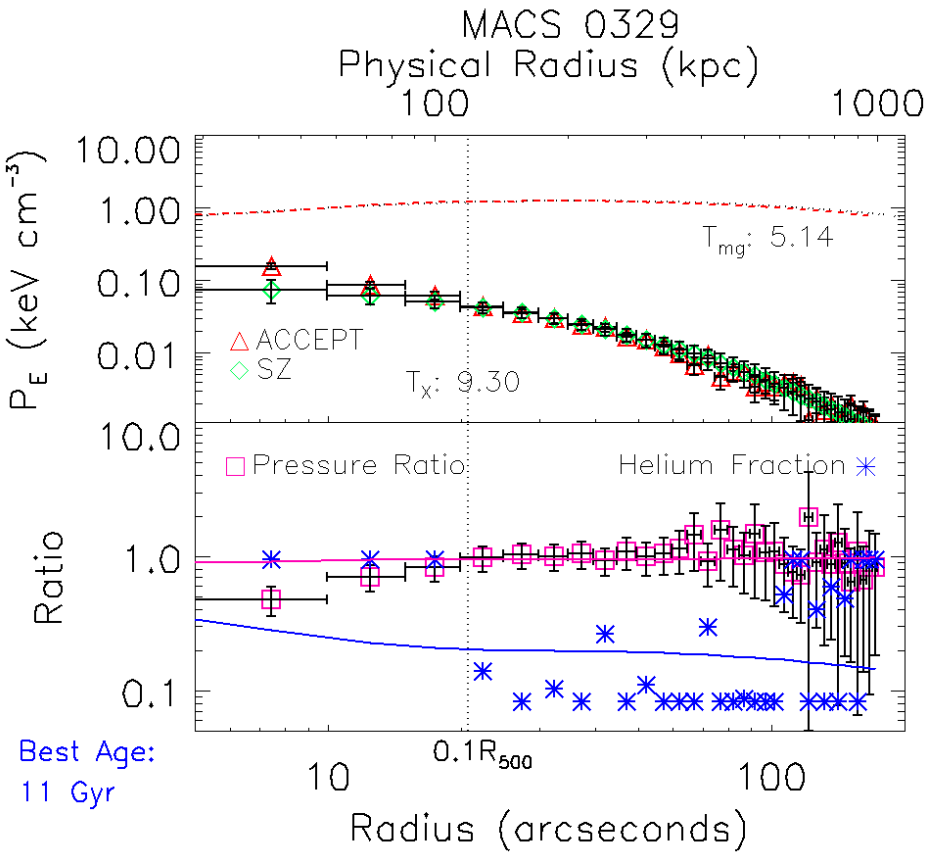

Fig. 5.6.— Notation is identical to Figure 5.3.

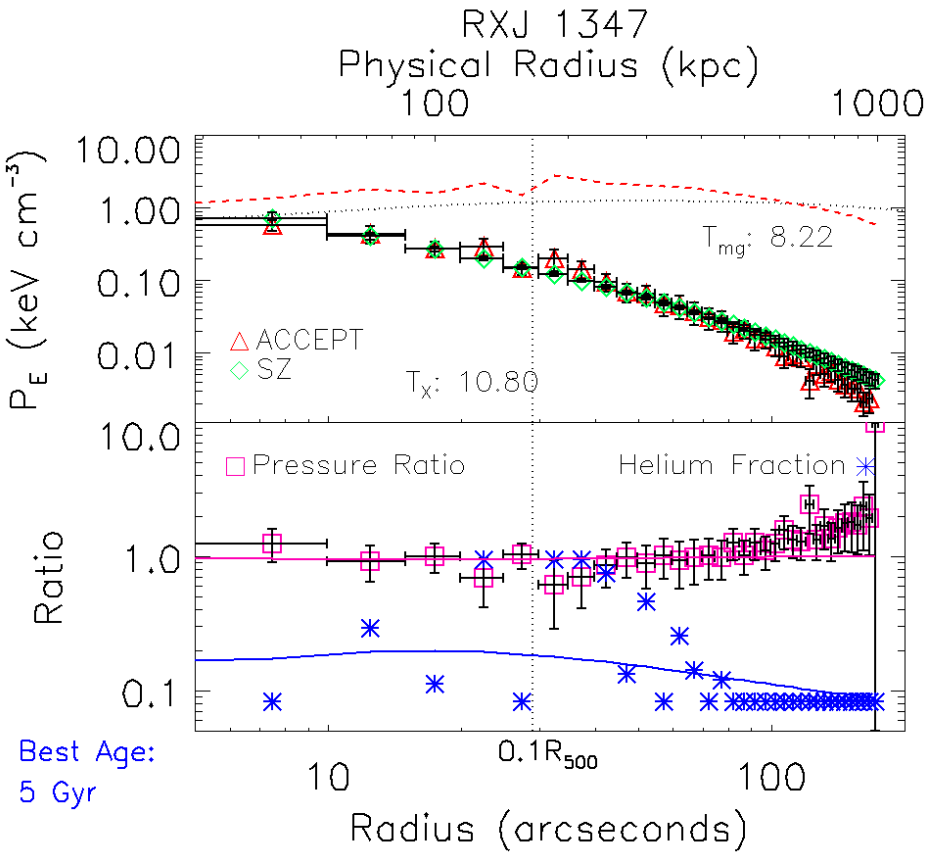

Fig. 5.7.— Notation is identical to Figure 5.3.

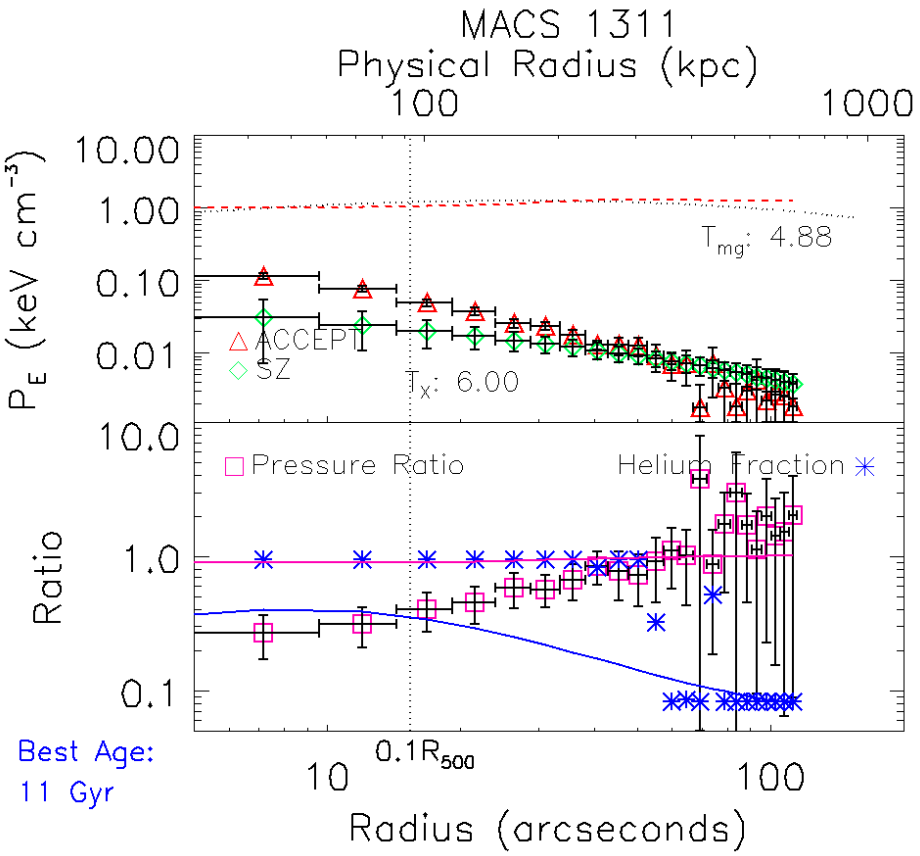

Fig. 5.8.— Notation is identical to Figure 5.3.

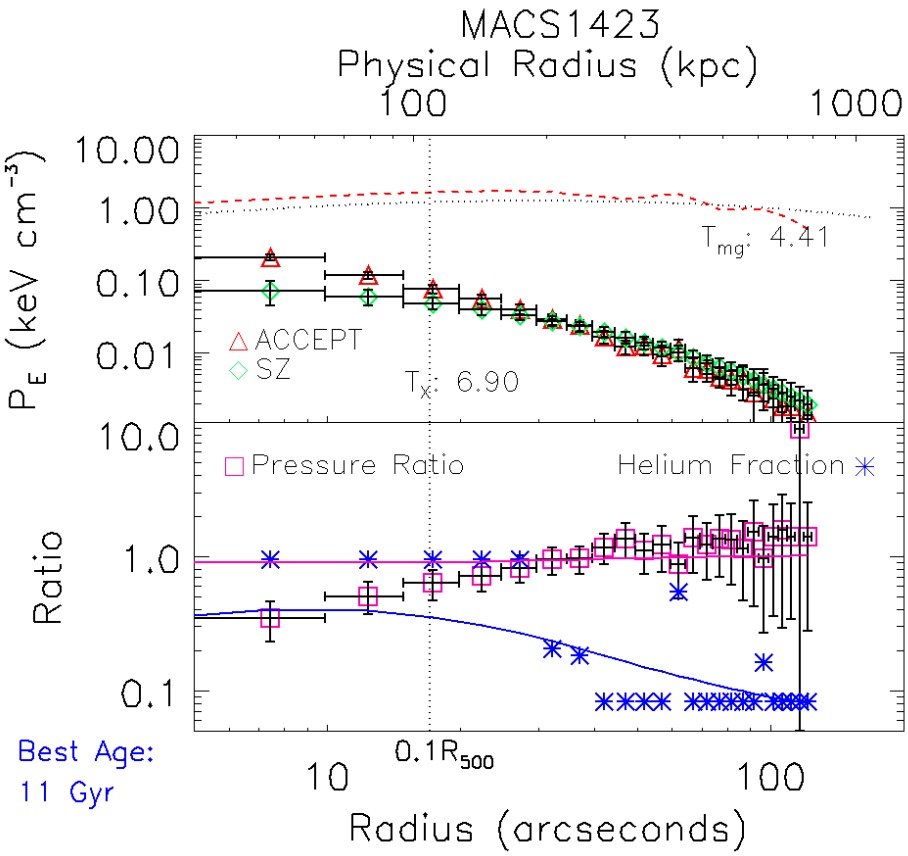

Fig. 5.9.— Notation is identical to Figure 5.3.

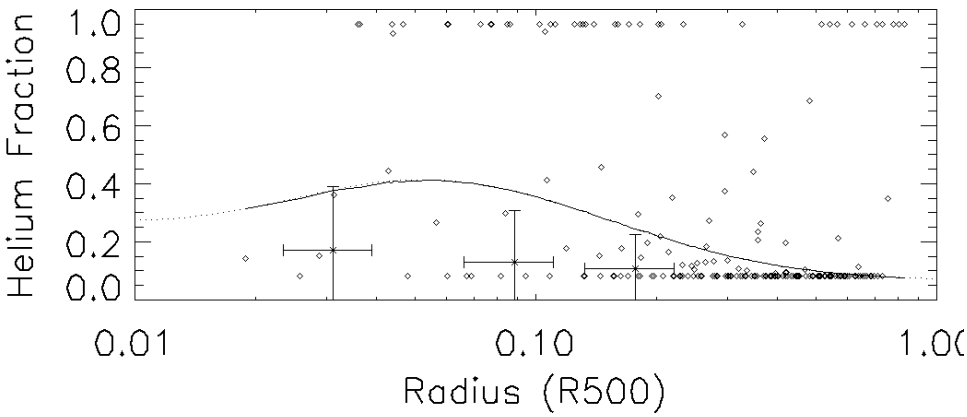

Fig. 5.10.— The helium fraction over all seven cool core clusters within our sample.

model and age), this is equivalent to a 12.6σ detection! However, we do not believe this result due to the relative inconsistencies between X-ray and SZ pressure profiles observed.

We should be wary of the nominal 12.6σ detection also due to the simplistic treatment of the covariance matrix (we adopt a diagonal covariance matrix) used in fitting the data to the models. It is clear that there will be some correlation among bins in the pressure profiles, but it has not been quantified, and thus not implemented. While covariance will degrade the significance, we can expect it still remains (nominally) above 5σ. However, this still relies on the assumption that we have precisely and accurately described the geometry and ongoing physical processes in the cluster (especially the center), which is, at present, not the case. This is highlighted in clusters such as MACS 1311 or MACS 0429, which leave much to be explained given that helium sedimentation would only be able to account for a minor difference in the pressure profiles seen in the SZ and X-rays.

Chapter 6

Detecting Shocks via the SZ Effect

Abstract

Merging shocks have been predicted from numerical simulations since the 1990s, but have only been seen in a handful of systems. Shocks are novel tools to study the intracluster medium (ICM), especially how the ICM is heated and transport processes. As shocks are defined by a pressure jump, they should be revealed via SZ observations. We construct an analytically integrable model of a shock and apply it to a Abell 2146, an cluster with observed shocks in the X-ray. Additionally, we attempt to observe the cluster with MUSTANG, but do not detect the shock.

6.1 Introduction

Shocks within the ICM are thought to arise from three phenomena: (1) AGN outflows, (2) intergalactic medium (IGM) accretion, and (3) cluster mergers. Shocks from AGN outflows are not expected to be strong $M \sim 1$ (Kravtsov & Borgani 2012), and thus would be difficult to detect at any significance. As discussed in Section 1.2.2,

IGM accretion is expected to produce strong shocks, and in turn, produce cosmic rays and gas heating. However, IGM accretion occurs at the outskirts of clusters, where the density is low, making observations, especially with X-rays, more difficult relative to the central regions. Finally, cluster mergers are spectacular events, as to be expected for merger objects that are already touted as the "most massive gravitationally bound" objects. And while shocks from cluster mergers were predicted at least as early as (1993 Schindler & Mueller 1993; Roettiger et al. 1993), it took roughly a decade to have clear detections of shocks in pressure, density, and temperature discontinuities (e.g. Markevitch et al. 2002, 2005; Russell et al. 2010). For a review, see Markevitch & Vikhlinin (2007).

SZ observations may speed up the detection of shocks owing to shocks being defined as a jump in pressure, and SZ directly probing pressure. Observations of RXJ1347 have long suggested the presence of a shock to the southeast of the cluster core, and MUSTANG was able to bolster the evidence for a shock (Mason et al. 2010). More interestingly, in MACS 0744 (Korngut et al. 2011), MUSTANG revealed a shock where none had previously been seen. Upon re-analysis of X-ray data, it was possible to confirm the presence of a shock and constrain the Mach number. A key to observing shocks is the viewing angle: a shock is much more likely to be detectable if it is moving in the plane of the sky, such that the line of sight is along the shock front.

While there are many simulations of cluster mergers (e.g. Wik et al. 2008; Chatzikos 2012; Battaglia et al. 2012; Molnar & Broadhurst 2015, to name just a few), observations can only constrain the physics so well (e.g. Markevitch & Vikhlinin 2007; Russell et al. 2012; van Weeren 2011). Low frequency radio data are able to constrain the cosmic ray population and magnetic field, but cannot constrain the thermal properties of

the gas. X-rays could potentially constrain the cosmic ray population from analysis of inverse Compton scattering, but the primary constraints inferred from X-rays is of the gas density and temperature. SZ observations, of course, directly constrain the pressure. A disadvantage of current X-ray analysis is the limited energy sensitivity of the two commonly used telescopes, Chandra and XMM. Both are limited to energies less than 10 keV, or 10^8 K. With the expectation that shocks will heat the gas, it is critical to be able to probe higher temperatures. Here, the addition of SZ observations is useful, such that temperature may be derived from the pressure SZ observes, and the density that X-ray infers. Such an analysis may lead to better constraints on the degree of Coulomb heating and instantaneous heating, which have already been performed by X-ray observations alone (Markevitch & Vikhlinin 2007; Russell et al. 2012), and are shown in Figure 6.3.

6.2 Modeling Shocks in Systems

While modeling the bulk cluster emission is a challenge in its own right (see Section 4.1), if characterizing the shock takes precedence, then some simplifying assumptions can be made for the bulk component. To model a shock in a cluster, we assume an ellipsoidal model, where the pressure, P, or X-ray emissivity, ϵ is a power law function of ellipsoidal radius, $r = \frac{x^2}{a^2} + \frac{y^2}{b^2} + \frac{z^2}{c^2}$, such that $\epsilon = \epsilon_{0,i} r^{-p_i}$ is the form the quantity takes within region i. The pressure is allowed to be defined on separate regions, each of which hold the same ellipsoidal geometry (axis scalings). The pressure is continuous within a region, but need not be continuous between regions. Finally, we assume two of the axes of the ellipse lie in the plane of the sky, and the other is along our line of sight. Particularly, we adopt z as our line-of-sight axis, and x as the direction of shock propagation. The integrals along the line of sight are then

analytic, and are listed in Appendix E.1.

While fully ellipsoidal regions are appropriate for the bulk ICM, the shocked regions are not ellipsoidally symmetric. In particular, if the shock is propagating in the x direction, then the front should be strongest at $y = z = 0$, and taper as some function of y and z. In the interest of simplifying the calculation, we will assume the shock symmetry about the x axis follows the geometries of the y and z axis with $(\frac{y^2}{b^2} + \frac{z^2}{c^2})$ as a polar radius about the x axis. Next, we observe that $(\frac{\frac{y^2}{b^2}+\frac{z^2}{c^2}}{\frac{x^2}{a^2}})$ is the (trigonometric) tangent of the opening angle, θ. I am not too concerned with the precise shape of the taper I define, but more interested in having the shock be limited in extent, in agreement with observations. Thus, a taper of the form $(\tan(\theta) + 1)^{-\xi}$ is adopted, where ξ is chosen the parameter which effectively controls the extent of the taper (i.e. shock). Note that this formulation is then written as:

$$(\frac{\frac{x^2}{a^2} + \frac{y^2}{b^2} + \frac{z^2}{c^2}}{\frac{x^2}{a^2}})^{-\xi} \tag{6.1}$$

This is wonderfully simple to integrate (in light of Appendix E.1). Because the integral is over z, and not x, $(\frac{x^2}{a^2})^{\xi}$ comes out of the integral, and we have simply added ξ to the power law previously assumed. For clarity, Appendix E.2) lists the integrals for a taper defined on any region.

6.2.1 Modeling Abell 2146

Abell 2146 is a cluster undergoing a merger with a clean geometry allowing for easy modeling. Mergers will alter the thermal and non-thermal intracluster medium (ICM), with relativistic particles being produced in shocks (e.g. Sarazin 2002). Additionally, magnetic field strengths can be augmented during mergers (Feretti & Giovannini 2008). Heating of the thermal ICM electrons may occur in two steps during

cluster mergers. In the first step, the shock heats the electrons directly, while the ions will heat the electrons further via Coulomb equilibration (Wong & Sarazin 2009). Previous observations of Abell 2146 at 330 MHz were unable to detect a radio halo (Russell et al. 2011), placing Abell 2146 below the radio-halo-L_X relation seen for merging systems.

Prior to observations, we investigated the observability of shocks within Abell 2146 and the potential ability to constrain the shock heating mechanisms within the cluster. Using the deprojected physical quantities from Russell et al. (2010), and assuming an ellipsoidal geometry discussed in Section 6.2, we could create models of the cluster and shocks, which we could then simulate observations, as described in Section 2.4.4. Both shocks were investigated at the outset, but focus quickly shifted onto the northwest shock as we expected its detectability to be more favorable than the southeast shock.

Tables 6.1 and 6.2 list the values and errors of the physical quantities derived from Russell et al. (2010). The power laws are obtained by fitting a power law to points within a region. If only one point is present, no power law is assumed (except for the outer region to ensure the signal is bounded, which requires an overall power less than -1). Although -1 is the upper limit in this one-dimensional integral, -3 is the upper limit when integrating pressure spherically. The quantities are specified in the context of the ellipsoidal modeling used. In particular, the electron quantities are defined such that $n_e = n_0 r^{-p_n}$ and $T_e = T_0 r^{-p_T}$ and the value to be integrated over is the electron pressure, $P_e = n_e k_B T_e$. Thus, we have $P_e = n_0 k_B T_o r^{-(p_n+p_T)}$. The integrated quantity of immediate interest is Compton y, $y = \frac{\sigma_T}{m_e c^2} \int P_e dl$, where we assume the line of sight, l, is along the z axis.

In order to simulate observations of the cluster, it will need to be converted from

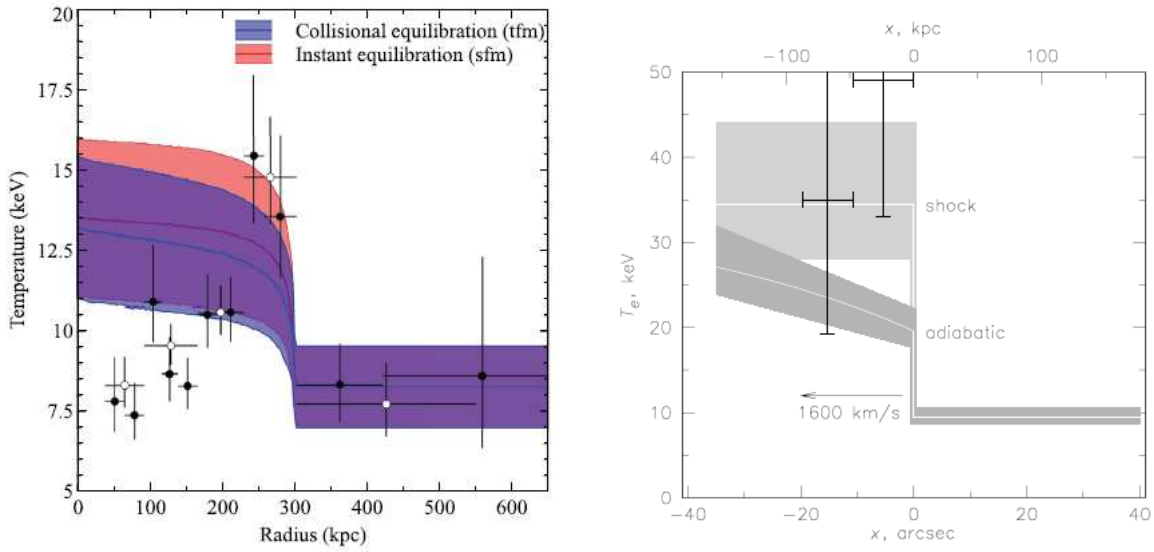

Fig. 6.1.— The panel on the left is from Russell et al. (2012), and the panel on the right is from Markevitch & Vikhlinin (2007). Collisional equilibration is synonymous with Coulomb heating.

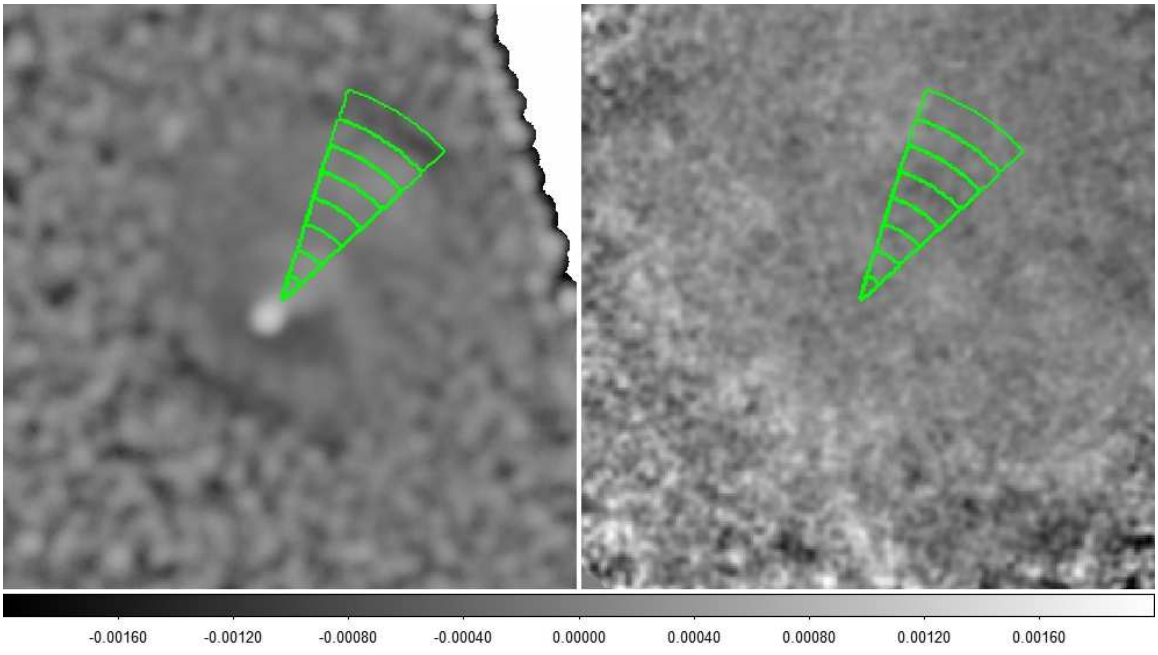

Fig. 6.2.— The left panel shows the unsharp mask image from *Chandra* (Russell et al. 2010). On the right is the MUSTANG map with point sources subtracted; the color bar corresponds to the MUSTANG map and is in Jy/beam. The radial bins are intended to roughly correspond to those used in Russell et al. (2010).

Compton y to Jy/beam. As outlined in Section 2.4.4, the relativistic correction is not accounted for within the integral, but rather, we assume a cluster-averaged temperature and calculate a the correction outside of the integral.

The discrepancy between the heating models (instantaneous and Coulomb) and derived X-ray temperature led me to formulate some resolution between the anticipated temperature and the measured temperature. In particular, I investigate a model which adopts the derived electron temperature, T_e, in Russell et al. (2010), within the shocked region, as the ion temperature, T_i, and solve for Coulomb heating from the pre-shock to post-shock region. The motivation is in part to resolve the lower post-shock electron temperatures seen. If the ion temperature is also cool, then collisional equilibrium will naturally bring the electrons into agreement. The larger issue, beyond the scope of this discussion, is how to accurately deproject temperatures within the ICM.

Electron temperature evolves due to Coulomb heating as (Spitzer 1962; Wong et al. 2010):

$$\frac{d\tau}{dt} = \frac{2\ln\Lambda}{503}\left\langle\frac{Z^2}{A}\right\rangle\frac{n}{\bar{T}^{3/2}}\tau^{-3/2}(1-\tau)s^{-1} \tag{6.2}$$

where n is the total particle density, $\bar{T}$ is the average thermodynamic temperature,

Region	T_0 (keV)	p_T	n_0 (cm^{-3})	p_n
(1) $0''< \theta < 50''$	$6.5^{+0.3}_{-0.2}$	-0.1	7e-3	0.36
(2) $50''< \theta < 120''$	$5.5^{+1.4}_{-1.0}$	-1.16	4e-3	0.35
(3) $120''< \theta$	$4.6^{+1.0}_{-0.7}$	-0	1.1e-4	1.6

Table 6.1: Abell 2146 NW slice. The region is the radial extent in arcseconds. p_T is the power index for electron temperature, and p_n is the power index for the density. Note that the convention is of the form $n = n_0 r^{-p_n}$, such that the negative p_T values indicate that electron temperature is increasing with radius. Value normalizations are given at $50''$, $50''$, and $120''$ respectively. Reported uncertainties correspond to 1σ.

Region	T_0 (keV)	Error	p_T	n_0 (cm^{-3})	p_n
(1) $0'' < \theta < ''18$	$2.4^{+0.1}_{=0.1}$	0.0	1.3e-2	0.0	
(2) $18'' < \theta < 55''$	$5.0^{+1.7}_{-1.0}$	1.28	4e-3	-0.42	
(3) $55'' < \theta$	$4.0^{+2.0}_{-1.0}$	0.0	1.1e-4	-1.09	

Table 6.2: Abell 2146 SE slice. Values are given at 18″, 18″, and 55″ respectively. Quantities are the same as in Table 6.1.

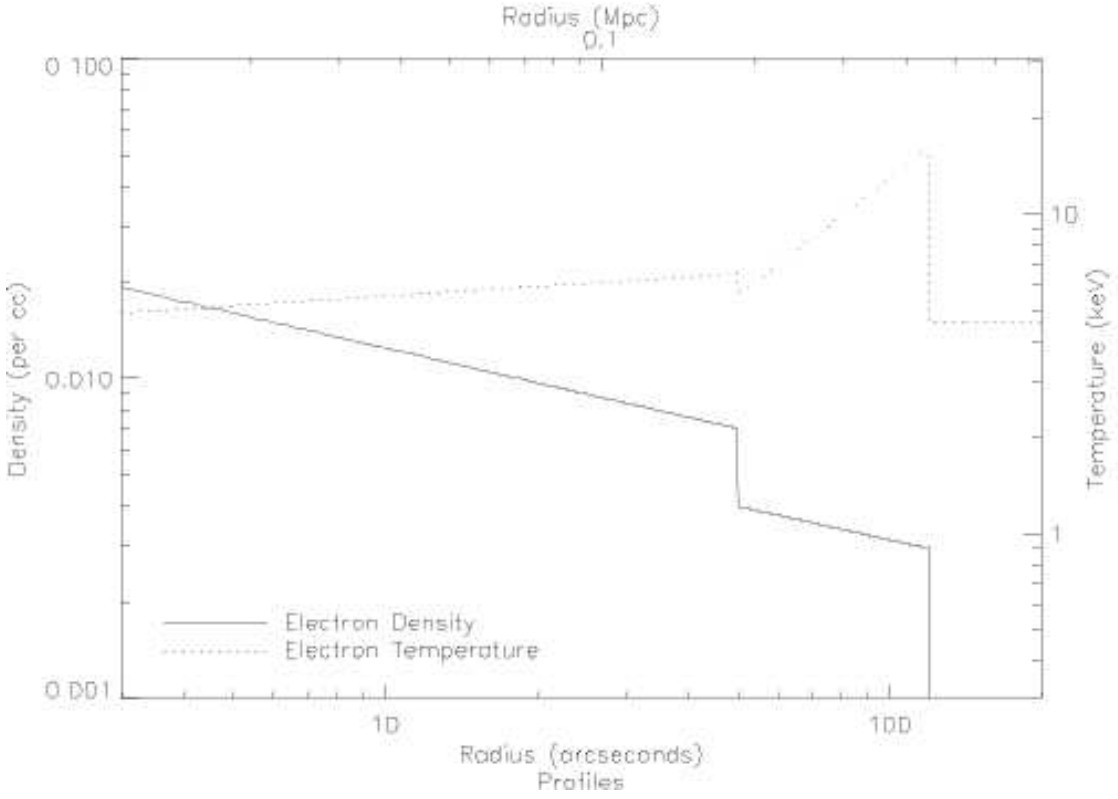

Fig. 6.3.— The density and temperature profiles for the northwest shock in Abell 2146.

given as

$$\bar{T} = \frac{n_e T_e + n_i T_i}{n_e + n_i} \tag{6.3}$$

with n_e and n_i as electron and (all) ion densities respectively, $\ln \Lambda$ is the Coulomb logarithm, which is approximated by $\ln \Lambda \simeq 37.8 + \ln(T_e/10^8\mathrm{K}) - \ln(n_e/10^{-3}\mathrm{cm}^{-3})^{1/2}$ (Wong et al. 2010), Z is the ion charge, A is the atomic number, and $\tau = T_e/\bar{T}$. We assume a solar metallicity, and mean molecular mass μ of 0.59. To relate the transpired since being shocked, we use the shock velocity reported in Russell et al. (2010): $v = 2200$ km/s. The results from this model are shown in Figure 6.4.

The integration of the two models in Figure 6.3 and 6.4 is initially performed assuming a fully ellipsoidal geometry of all regions (including the shocked region), using the integrals in Appendix Appendix E.1. This produces the Compton y profiles for each, shown in Figure 6.5. The two models are subtracted to show the difference, which is otherwise hardly visible.

However, given that the ellipsoidal prescription covers it is evident that the ellipsoidal treatment of the shock is not very realistic. Thus, a taper which could still be analytically integrated was developed (Section 6.2). In the absence of a blue pressure profile, the middle shell was assumed to be a tapered shell, while the inner ellipsoid and outer shell taken as full ellipsoids. The

A better approach to modeling the shock would likely have been to either assume a standard bulk ICM pressure model (see Section 4.1), or to simply interpolate between the inner and outer regions and take that as the bulk ICM pressure in the middle region (using an ellipsoidal geometry, and power law between the edges). The shock component would thus simply be an additional component on top of the bulk model. While such an approach is surely to be implemented for future analyses, it is not to much avail for Abell 2146, as evidenced by Figure 6.7, which compares the simulated

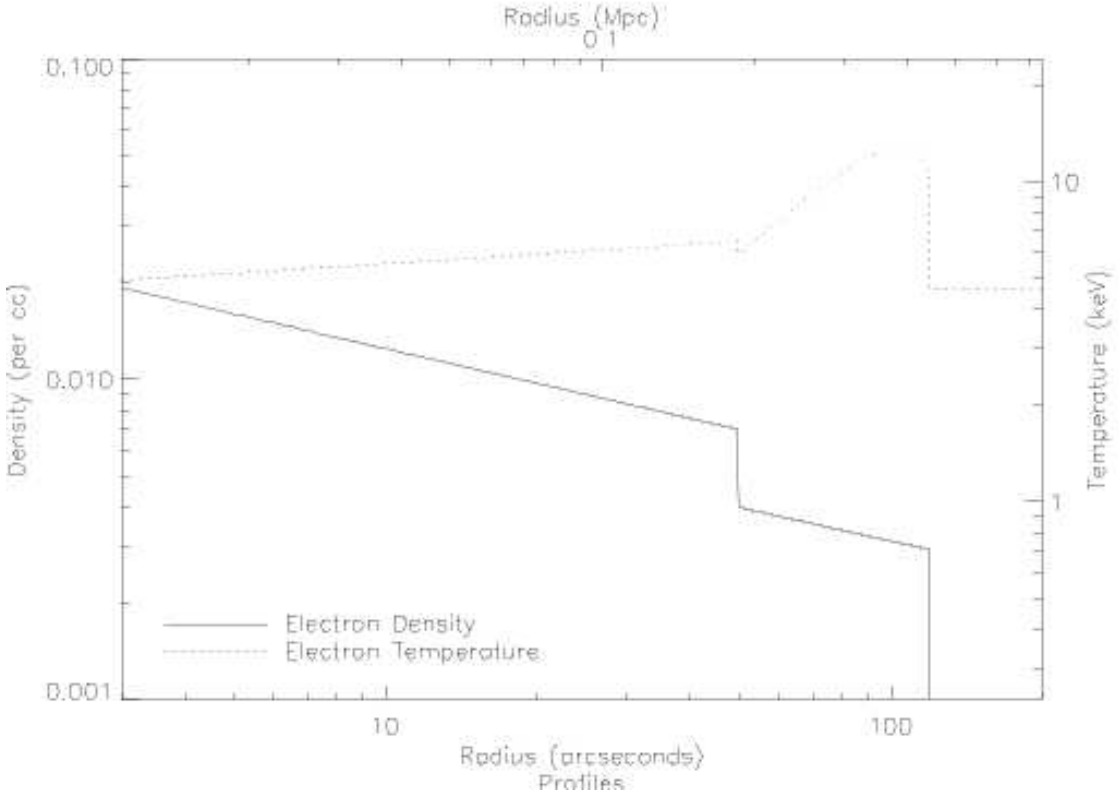

Fig. 6.4.— The density model remains unchanged, but the temperature model adopts a Coulomb heating mechanism post-shock.

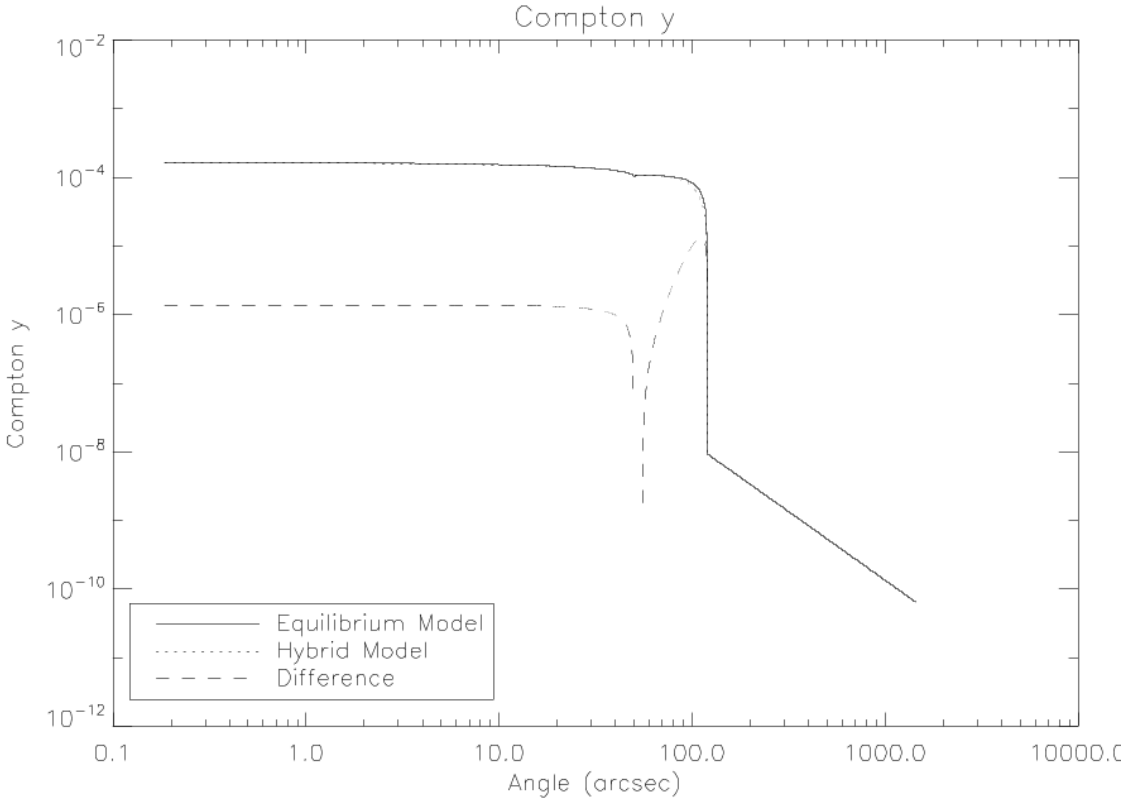

Fig. 6.5.— We compare the derived Compton y values when we use the simple power law, taken to be the (instant) equilibrium model, versus our "hybrid" model, which allows for collisional equilibrium between electrons and ions. As expected, the difference is very slight in Compton y, and would prove very difficult to observe.

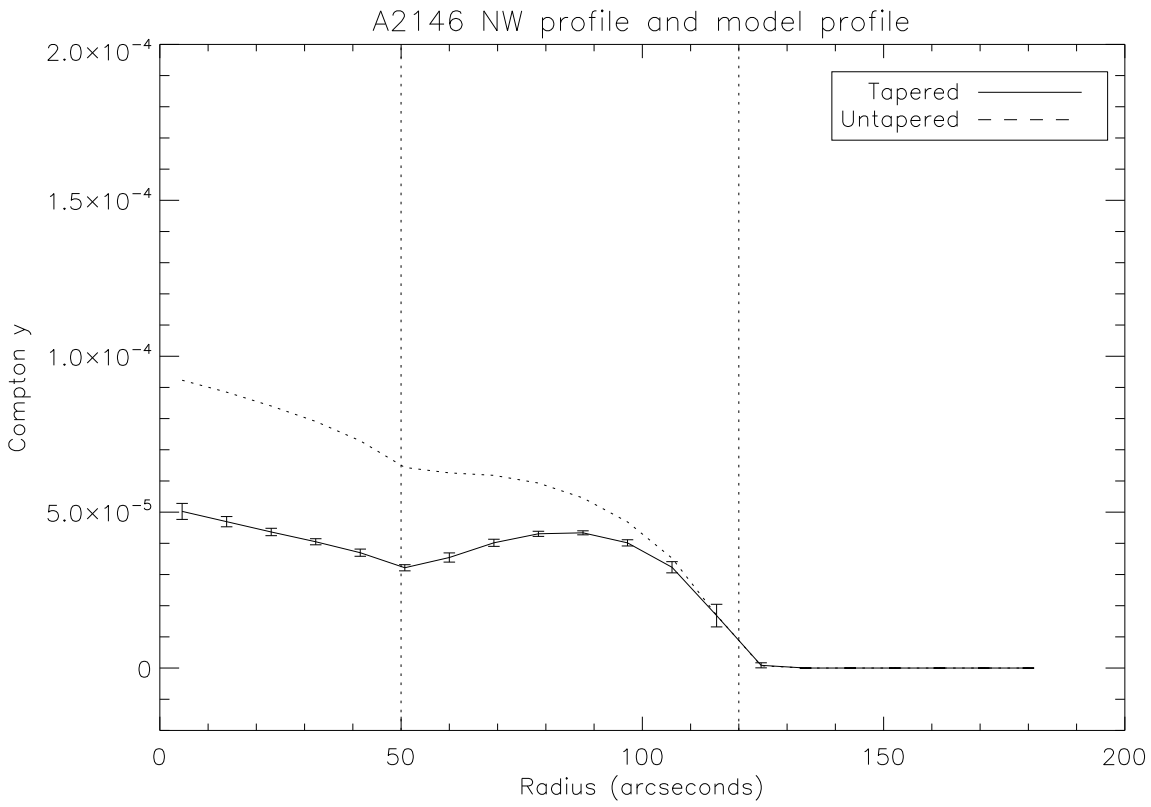

Fig. 6.6.— Here, we compare the tapered model with the untapered model. In both cases, the "hybrid" shock heating is assumed. Note that this plot is linear, as compared to Figure 6.5.

observations of the model and the noise in the data in a number of ways.

6.2.2 Abell 2146

Abell 2146 is a merging cluster with favorable geometry. Its shocks were detected with X-ray observations,and deprojected densities and temperatures derived (Russell et al. 2010). Abell 2146 has two shocks: one in the northwest and one in the southwest. To the northwest, there is also a subcluster tail, while to the southeast there is a cold front in addition to the shock. Russell et al. (2010) assumes a cosmology with $H_0 = 70$ km s^{-1} Mpc^{-1}, $\Omega_m = 0.3$ and $\Omega_\Lambda = 0.7$ with a scale of 3.7 kpc per arcsec at

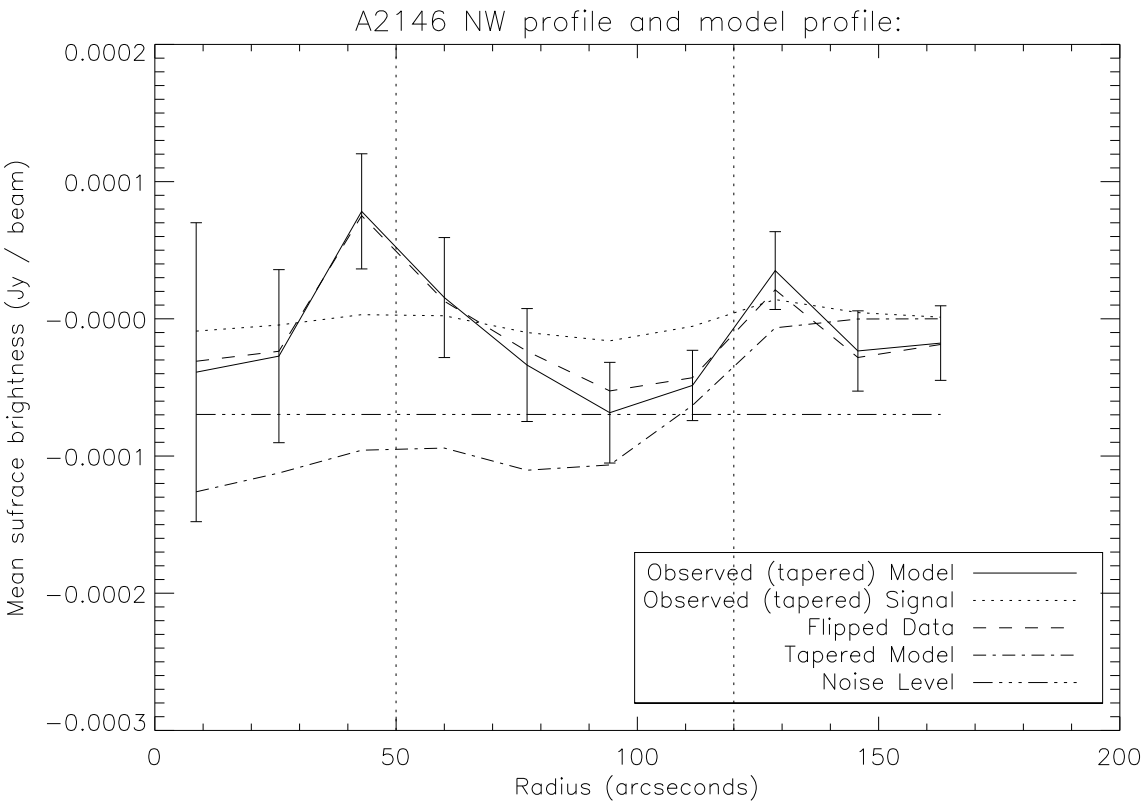

Fig. 6.7.— Comparison between model and simulated observations. Simulated observations make use of flipped data, and thus the filtered signal is the difference between the simulated model and the flipped data. The error bars on the bins are determined as the standard deviation of the mean within a bin, and the noise level (dot-dashed line) is underestimated (in amplitude) on this plot.

$z = 0.234$ (the redshift of A2146). We adopt the same cosmology.

Abell 2146 was observed for 3.4 hours within project AGBT09C_059, and achieved a map noise of 150μJy/beam in the central $3'$ when smoothed by a $5''$ FWHM kernel. (If we smooth by $10''$, the map noise in the same region is 100μJy/beam.) Our pointings were centered on the X-ray cluster center and the northwest shock within Abell 2146. A variety of scan patterns were used. Owing to the differential nature of SZ observations, jumps in signal are best detected, which is to say that rapid change in the signal in the time ordered data (TODs) are desirable. Thus, the goal is to cross

directly over the shock region, such that the scan trajectory is roughly perpendicular to the shock front. To maximize this, we used a "circlescan", which slowly translates circles along the shock front such many circles are completed (there are many passages across the shock front, while the circular pattern progresses along the shock front.

While no bulk emission or shocks are clearly detected, the point source A is very well detected, and point sources C and E are also well detected, as seen in Figure 6.8, and tabulated in Table 6.3

Source	RA (h m s)	Dec (d m s)	S_{610}	$S_{1.4}$	S_{16}	S_{90}
A	15 56 04.23	+66 22 12.94	24.3 ± 0.10	40.6	5.92 ± 0.18	0.96 ± 0.13
C	15 56 14.30	+66 20 53.45	23.6 ± 0.10	–	1.83 ± 0.14	0.47 ± 0.13
E	15 55 57.42	+66 20 03.11	–	–	1.65 ± 0.08	0.77 ± 0.15

Table 6.3: All flux densities and errors are reported in mJy. RA and Dec are in J2000. S_{610} refers to the flux density found with the GMRT at 610 MHz (work from Huib Intema); $S_{1.4}$ refers to the flux density found from NVSS (Condon et al. 1998) at 1.4 GHz; S_{16} refers to the flux density found with AMI (AMI Consortium et al. 2011) at 16 GHz; S_{90} refers to the flux density found with MUSTANG at 90 GHz.

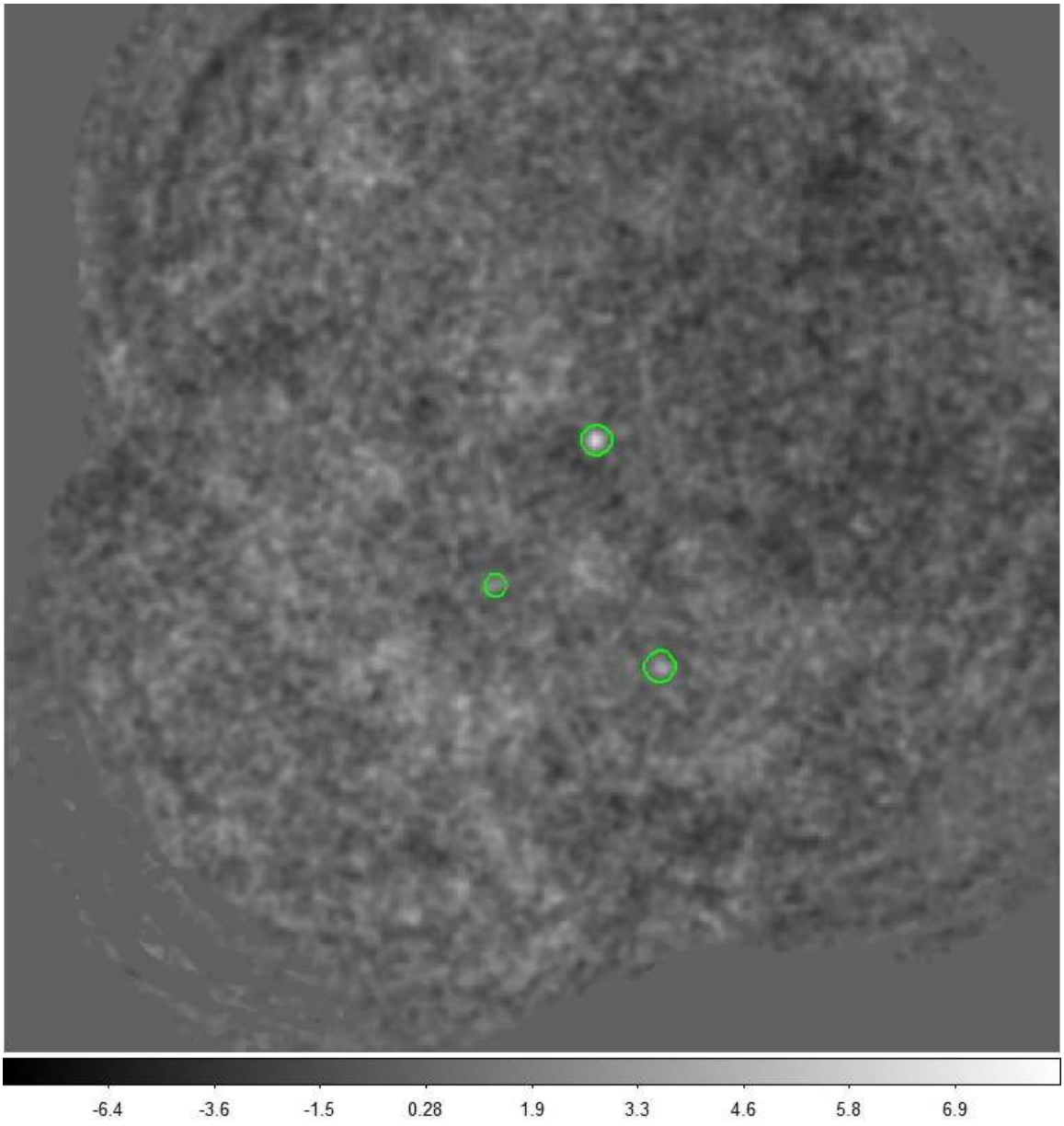

Fig. 6.8.— Highlighted point sources use identifiers from AMI Consortium et al. (2011). The map is smoothed by 5″.

Chapter 7

Conclusions

We developed an algorithm to jointly fit gNFW pressure profiles to clusters observed via the SZ effect with MUSTANG and Bolocam. We apply this algorithm to 14 clusters and find the profiles are consistent with a universal pressure profile found in Arnaud et al. (2010). Specifically, the pressure profile is of the form:

$$\tilde{P}_e = \frac{P_0}{(C_{500}X)^{\gamma}[1+(C_{500}X)^{\alpha}]^{(\beta-\gamma)/\alpha}},$$

where we fixed α and β to values found in Arnaud et al. (2010). A comparison to previous determinations of pressure profiles is shown in Figure 7.1. Within the radii where we have the greatest constraints ($0.03R_{500} \lesssim r \lesssim R_{500}$), the pressure profile from this work is comparable to the other pressure profiles. This is further evidenced in the parameters themselves, as seen in Table 7.1, especially in comparison to A10 parameter values.

Despite agreement for the ensemble constraint, we found discrepancies between the SZ and X-ray derived pressure profiles for individual clusters (Chapter 4). The physical nature of the clusters investigated in Chapter 5, i.e. cluster geometry and

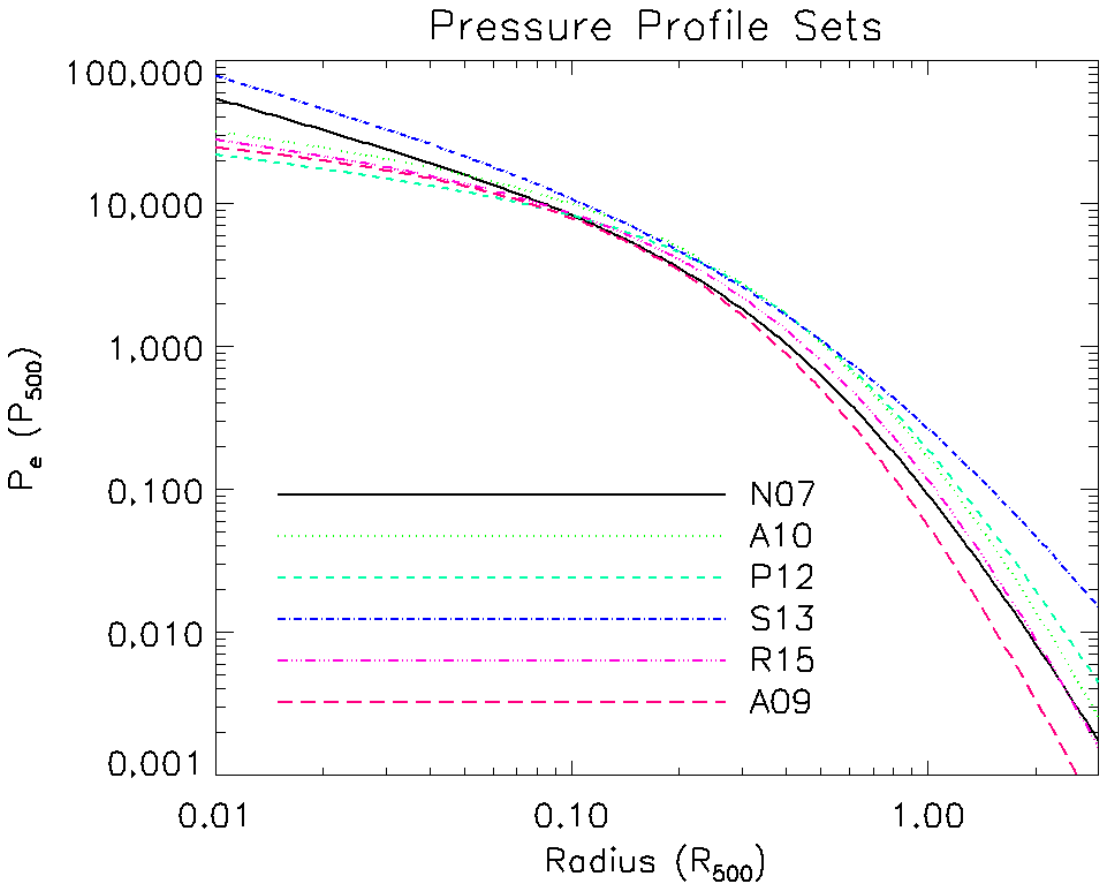

Fig. 7.1.— Pressure Profiles from this (R15) and other works. A09 indicates ACCEPT (Cavagnolo et al. 2009) pressure profile for the 14 clusters in this sample. A09 falls below R15.

Set	$P_0 h_{70}^{-3/2}$	C_{500}	α	β	γ
All	7.94 ± 0.10	$1.3^{+0.1}_{-0.1}$	1.05	5.49	$0.3^{+0.1}_{-0.1}$
Cool Core	3.55 ± 0.06	$0.9^{+0.1}_{-0.1}$	1.05	5.49	$0.6^{+0.1}_{-0.1}$
Disturbed	12.56 ± 0.29	$1.5^{+0.1}_{-0.2}$	1.05	5.49	$0.0^{+0.1}$
Well behaved	5.34 ± 0.08	$1.2^{+0.1}_{-0.1}$	1.05	5.49	$0.5^{+0.1}_{-0.1}$
All (A10)	8.403	1.177	1.0510	5.4905	0.3081
Cool core (A10)	3.249	1.128	1.2223	5.4905	0.7736
Disturbed (A10)	3.202	1.083	1.4063	5.4905	0.3798

Table 7.1: Our best fit gNFW parameters (top), and the best fit gNFW parameters from Arnaud et al. (2010) (A10).

ICM temperature, may be able to account for some discrepancy seen between the pressure profiles we fit and what ACCEPT fits. Specifically, by looking at the ratio between pressure profiles of the same shape as fit to SZ and ACCEPT, we find that the clusters have plane of sky-to-line of sight axis ratios, η, tabulated in Table 7.2, which are generally less than unity, implying that most of these clusters are elongated along the line of sight. This is not too surprising given that both selection methods for the CLASH sample will favor clusters that are elongated along the line of sight. Slightly more interesting is the generally weak signature that the cluster core is more spherical than the cluster itself, which is given in nominal significance (σ) in Table 7.2.

The other property considered is the electron temperature. We tabulate two temperatures derived for the clusters from ACCEPT (Cavagnolo et al. 2009) and Morandi et al. (2015): T_X^1 is calculated from a single spectrum over $0.15R_{500} < r < R_{500}$ for each cluster. T_X^2 is from Morandi et al. (2015) and is calculated over $0.15R_{500} < r < 0.75R_{500}$. Additionally, we calculate T_{mg}, by fitting the ACCEPT temperature profiles to the profile found in Vikhlinin (2006). We then tabulate T_{spec} as $T_{spec} = 1.11 \times T_{mg}$ given the ratio found in Vikhlinin (2006) between T_{spec} and T_{mg}. We may then compare either T_x^1 and T_x^2 to T_{spec}. Thus, we note that generally $T_{spec} < T_X^1 \sim T_X^2$, which may indicate the ACCEPT pressure profiles may be biased low, relative to the SZ pressure profiles by the deprojected (and interpolated) ACCEPT temperature profiles.

These investigations of cluster geometry and electron temperatures may account for the discrepancy between SZ and X-ray pressure profiles. However, these investigations have been simplistic and are indicative of the global geometry and properties of the cluster (at all radii), with the exception that we have also found some indication of a difference in geometry between moderate-to-large radii and core. Yet, the

Cluster	η	σ_η	Δk (σ)	T_x^1	T_x^2	T_{spec}
Abell 1835	1.77	0.41	1.08	9.0	10.0	9.07
Abell 611	0.10	0.03	0.17	6.8	–	7.27
MACS1115	1.28	0.32	-0.50	9.2	9.14	7.18
MACS0429	0.24	0.06	3.58	8.3	8.55	4.80
MACS1206	0.54	0.13	1.00	10.7	11.4	9.78
MACS0329	0.26	0.07	1.17	6.3	5.85	5.61
RXJ1347	0.79	0.18	-0.25	10.8	13.6	8.87
MACS1311	0.29	0.08	1.42	6.0	6.36	5.22
MACS1423	0.52	0.15	1.83	6.9	6.81	4.60
MACS1149	0.48	0.12	0.42	8.5	8.76	8.09
MACS0717	0.30	0.07	0.25	11.8	10.6	8.55
MACS0647	0.67	0.16	-0.42	11.5	12.6	11.1
MACS0744	0.76	0.19	0.58	8.1	8.90	8.15
CLJ1226	0.68	0.18	-0.67	12.0	11.7	9.31

Table 7.2: Table of implied geometries and temperatures. The plane of sky-to-line of sight axis ratio is denoted as η. The column Δk (σ) lists the significances of a more spherical core, as compared to the outer regions. Negative Δk significances indicate the core is measured to be more ellipsoidal than the outer regions. T_X^1 is from Cavagnolo et al. (2009), T_X^2 is from Morandi et al. (2015), and T_{spec} is calculated from T_{mg} given the ratio $T_{spec} : T_{mg} = 1.11 : 1$ cited in Vikhlinin (2006).

discrepancy in pressure profiles is not simply a scalar offset, but that the shapes often differ, especially in that the SZ pressure profile is lower than X-ray in the cluster core, and SZ pressure is generally higher at large radii. Geometry in the plane of the sky may be able to account for this offset, as evidenced by MACS 1115, where an extended decrement to the north of the cluster center is seen by Bolocam, and drives the radial pressure up, whereas this extension does not appear in the X-ray surface brightness image.

Finally, many of these clusters with discrepancies in pressure profiles have weak detections with MUSTANG, and would benefit from additional high resolution observations. While this may not resolve the pressure difference at large radii, it could bring the pressure profile shape into greater alignment.

7.1 Future Work

Further work with CLASH

There were a total of 21 clusters out of the 25 CLASH clusters which are observable from Green Bank with MUSTANG. However, MUSTANG-2 (and MUSTANG-1.5) will be able to observe 24 of the 25 CLASH clusters due as the new instrument was designed to allow observations below 30° elevation, with the new elevation limit being $\sim 20°$. Further observations with MUSTANG-1.5 will produce broader coverage, and with relative ease should achieve similar sensitivity as obtained with MUSTANG.

Revisiting several of the CLASH clusters will allow us to address more definitively the discrepancies seen relative to X-ray data. Expanding our (MUSTANG) sample closer towards the full CLASH sample will provide further insights into the scaling relation dependencies on substructure and the inner pressure profile.

Improving our joint fitting algorithm

An aspect where the joint analysis could see significant improvement is in the parameter space searched, and the speed of doing so. While the parameter space searched in this work was well matched to the data quality, with additional high resolution data, it should be very feasible to allow α and β in the gNFW profiles to vary as well, as well as allow for ellipticity in the plane of the sky. To explore this broader parameter space efficiently, we would employ a Markov-chain Monte Carlo (MCMC) technique.

ICM Physics

We've already seen that MUSTANG does well at detecting shocks, and MUSTANG-1.5 will certainly detect more shocks. There are additional features in the ICM that may well be observable with the SZ effect, such as X-ray cavities. In either case, deep SZ observations can be used to determine the pressure in shocks or X-ray cavities, and combined with X-ray analysis, should produce excellent constraints on ICM temperature, and subsequently ICM heating mechanisms.

Chapter 8

Appendices

Appendix A

Useful Equations

Compton y $y = (\sigma_T / m_e c^2) \int P_e dl$

SZE intensity $\frac{\Delta I_{SZE}}{I_{CMB}} = [\frac{x^4 e^x}{(e^x-1)^2}(x\frac{e^x+1}{e^x-1} - 4)(1 + \delta_{SZE}(x, T_e))] \times y$

SZE intensity factor $g(x) = [\frac{x^4 e^x}{(e^x-1)^2}(x\frac{e^x+1}{e^x-1} - 4)(1 + \delta_{SZE}(x, T_e))]$

HSE $\frac{dP_{gas}}{dr} = -\rho_{gas}(r)\frac{GM_{tot}}{r^2}$

Continuity Equation $\frac{dM_{tot}}{dr} = 4\pi r^2 \rho_{tot}$

Ideal Gas Law $P_{gas} = n_{gas} k T_{gas} = \frac{\rho_{gas} k T_{gas}}{\mu m_p}$

Propogation of Independent Errors $\sigma_f = \sqrt{(\frac{\partial f}{\partial x})^2 \sigma_x^2 + (\frac{\partial f}{\partial y})^2 \sigma_y^2 + (\frac{\partial f}{\partial z})^2 \sigma_z^2 + \ldots}$

$$Y_{SZ} \equiv \int y d\Omega \tag{A.1}$$

$$Y_X \equiv \int y_x d\Omega \tag{A.2}$$

$$Y_{sph}(r) = \frac{\sigma_T}{m_e c^2} \int_0^r P_e(r') 4\pi r'^2 dr' \tag{A.3}$$

$$Y_{cyl} = \frac{\sigma_T}{m_e c^2} \int_0^R P_e(r) 2\pi r dr \int_r^{R_b} \frac{2P(r')r'dr'}{\sqrt{r'^2 - r^2}} \tag{A.4}$$

$$Y_{cyl} = Y_{SZ} D_A^2 \tag{A.5}$$

$$Y_{500} = \frac{\omega_T}{m_e c^2} \frac{4\pi}{3} R_{500}^3 P_{500} \tag{A.6}$$

Appendix B

Fundamentals of Radio Astronomy

Brightness Temperature $T_b(\nu) \equiv \frac{I_\nu c^2}{2k\nu^2}$

Appendix B.1

Opacity

The principle concern for opacity at radio, especially millimeter and submillimeter wavelengths, is the amount of water in the sky, or precipitable water vapor (PWV). The best sites like the Atacama Plateau or Mauna Kea may see nights with 1 mm PWV or less. In fact, ALMA's technical handbook (Cycle 3 Staff 2015) lists a PWV of 0.913 mm as the 3rd octile, i.e. 37.5% of the time, the PWV is 0.913 mm or less (the first quartile is 0.472 mm PWV). By contrast, a PWV of ~ 10 mm is a fiducial estimate for observing conditions at Green Bank, WV (Mason 2012).

For a fixed frequency, opacity scales quite linearly with PWV (e.g. Holdaway & Pardo 1997; Pardo et al. 2001). However, molecular transitions impose atmospheric

windows, and as a general trend, opacity at lower frequencies (longer wavelengths) is less than at higher frequencies, for a given PWV, as showing in Figure 8.1

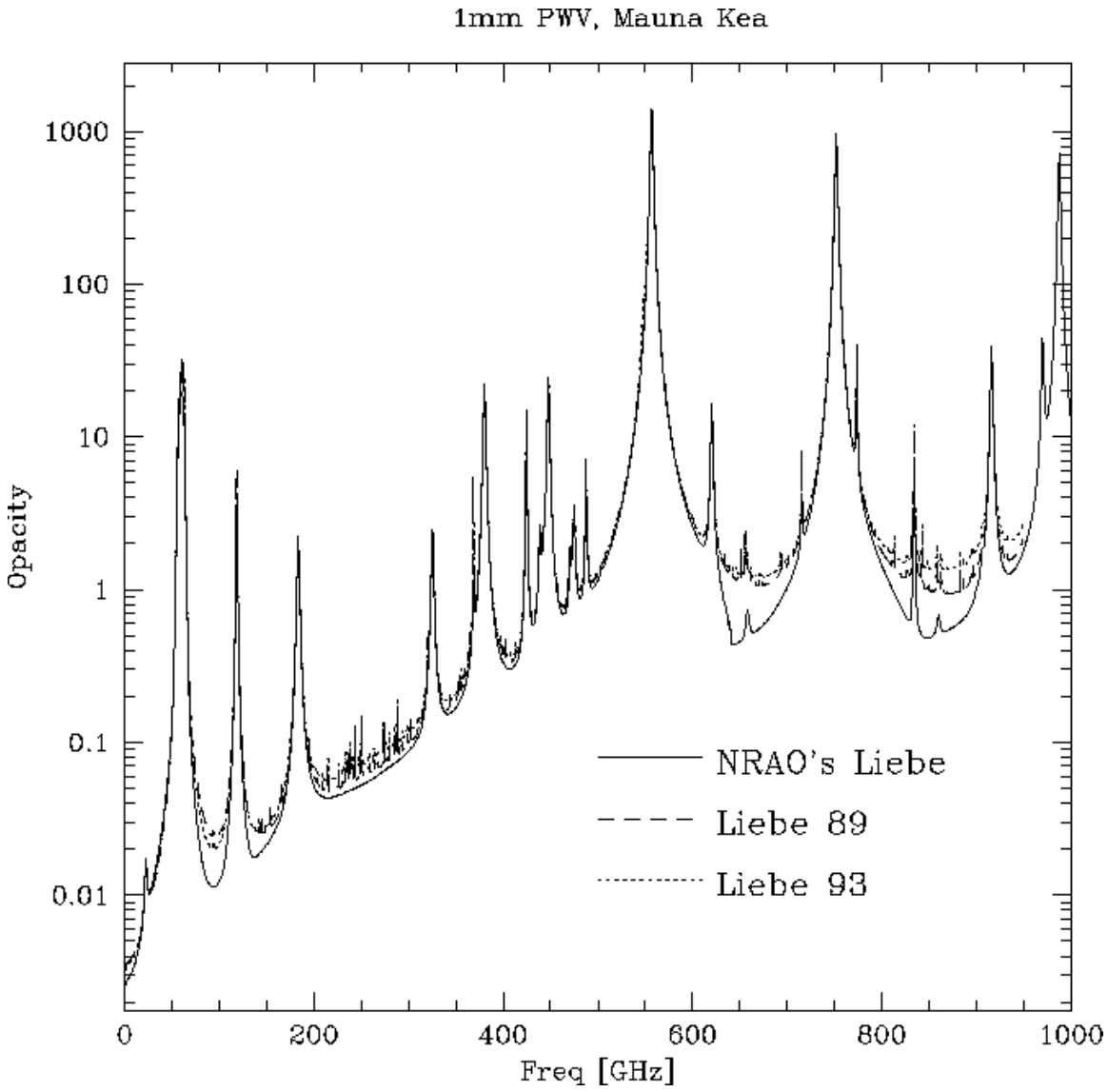

Fig. 8.1.— Figure 1 from Holdaway & Pardo (1997). Assuming 1 mm PWV, the following opacities are calculated.

Appendix C

MUSTANG Maps

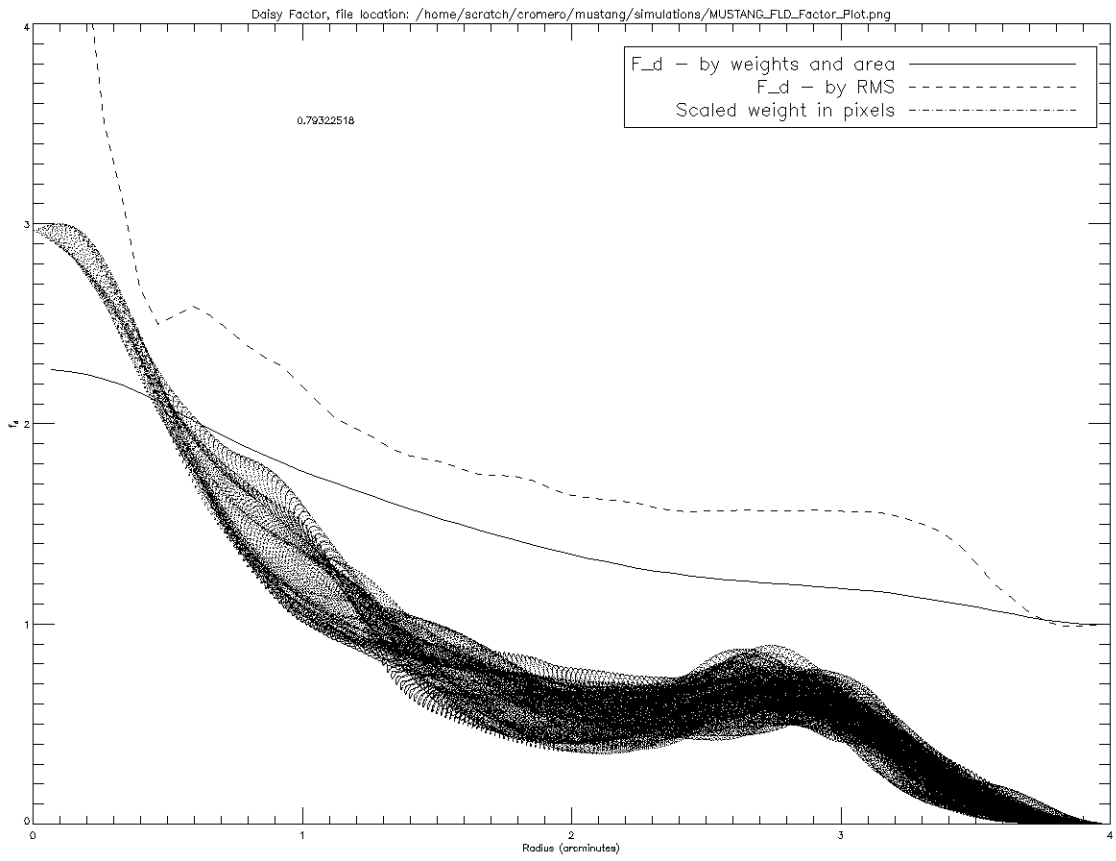

Fig. 8.2.— The plotted points are scaled pixel weight values.

Appendix D

Filtered, Azimuthal Profiles

An extra check on the joint fitting process is to compare the azimuthal profiles of the filtered maps (data and cluster models) and see how the fits are doing in this

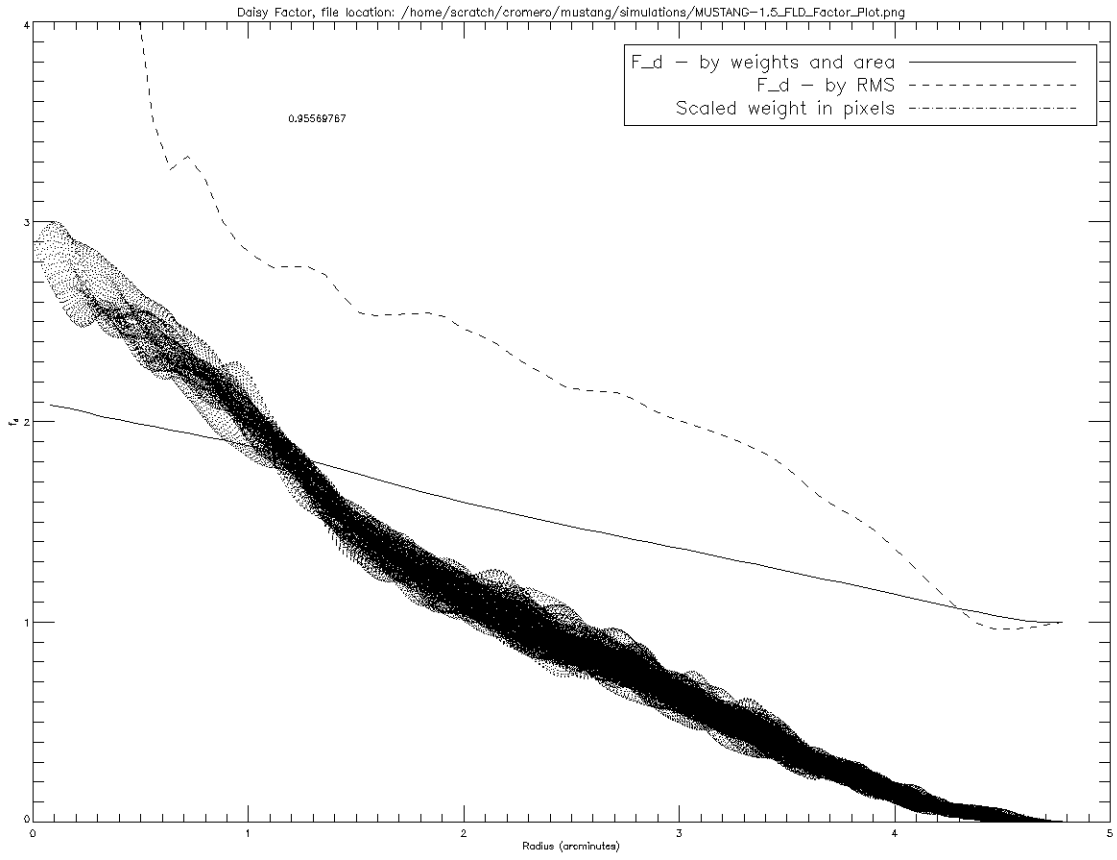

Fig. 8.3.— The plotted points are scaled pixel weight values.

manner. Of course, it is important to account for other components (point sources and residuals) as well. To do so, we subtract these fitted components from the data.

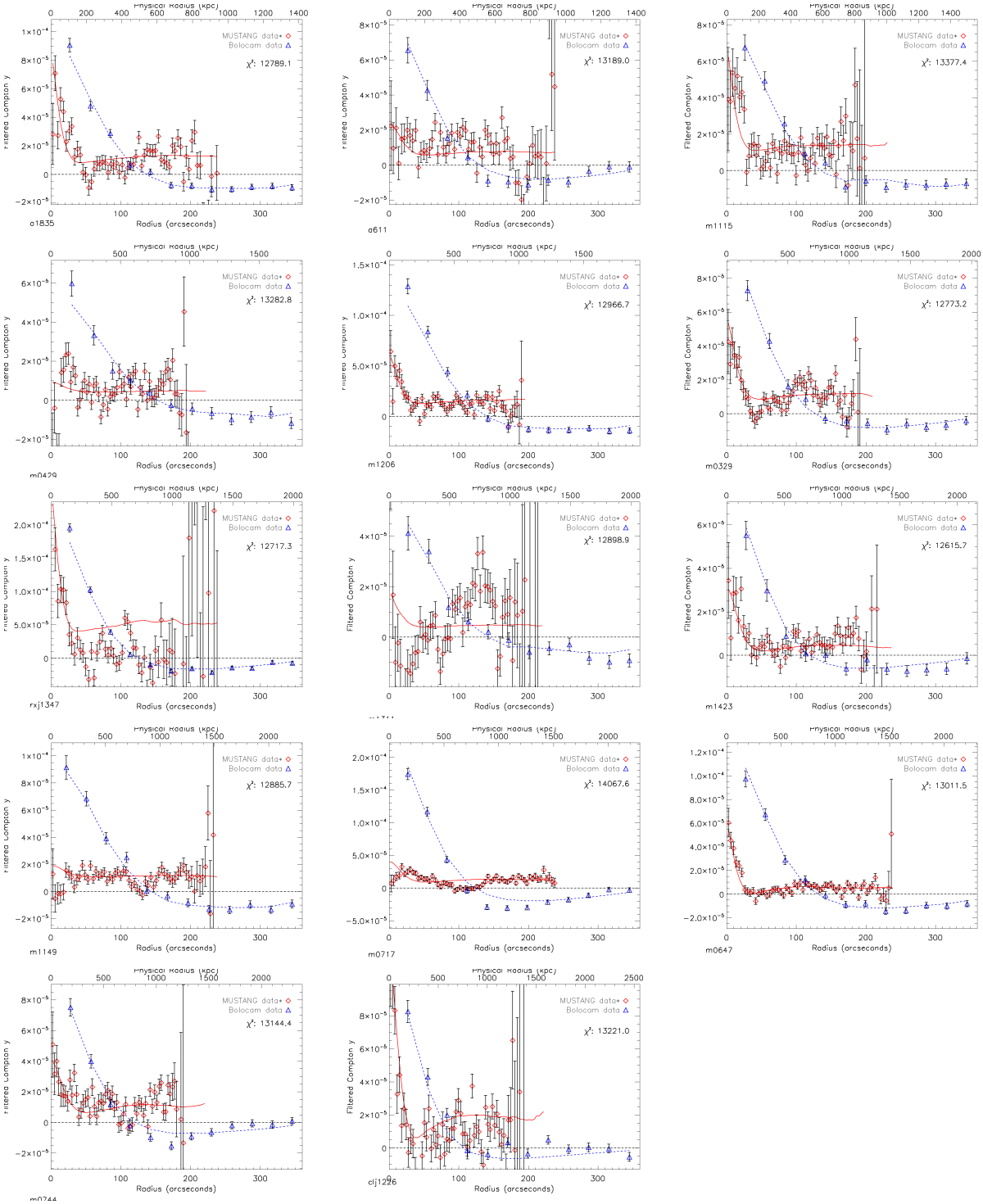

Fig. 8.4.— Azimuthal profiles showing the fits (lines) to the data (points). MUSTANG data points have an asterisk in the legend because they have been point source- and residual component- subtracted (if there was a point source or residual component). The model for MUSTANG includes a mean level, which is determined from a dataflip map. The cluster is identified in the lower left of each panel. The χ^2 value is for the best joint fit.

Appendix E

Galaxy cluster models

NFW profile $\rho = \frac{\rho_0}{(r/R_s)(1+r/R_s)^2}$

Generalised NFW profile $\mathbb{P}(x) = \frac{P_0}{(c_{500}x)^\gamma[1+(c_{500}x)^\alpha]^{(\beta-\gamma)/\alpha}}$

Appendix E.1

Integrals of power law ellipsoids

Quantities with power law distributions and ellipsoidal geometries can be integrated analytically along an axis. Moreover, this holds for any ellipsoidal range (0 to ∞ or any range in between). For a general-purpose approach to analyzing shocks, it's useful to have three regions defined. Geometrically, this corresponds to an inner ellipsoid, a middle ellipsoidal shell, and an outer ellipsoidal shell (which goes to infinity). The quantity of interest may either be emmisivity, as is the case for X-ray emmision, or pressure, as is the case for SZ signal. We choose ϵ for its use as emmisivity, and this avoids confusion between power law, p and pressure P,

Define the ellipsoidal radius, r, by $r^2 = (\frac{x^2}{a^2} + \frac{y^2}{b^2} + \frac{z^2}{c^2})$. We then divide the radial range into three regions: $r^2 < 1$, $1 \leq r^2 \leq R^2$, and $R^2 < r^2$, which we label with subscripts 1, 2, and 3 respectively. We define our quantity to integrate over with as ϵ_i, where i corresponds to the regions; $\epsilon_{0,i}$ should be understood as the normalization to the quantity within region i. If one wishes to impose continuity of emmisivities, they are related as: $\epsilon_{0,1} = \epsilon_{0,2} = \epsilon_{0,3}(R^2)^{-P}$, Our integrated quantity (especially for the outer shells) must still be integrated over the inner regions (on the sky. Therefore, we also define the projected radius, A, as $A^2 = (\frac{x^2}{a^2} + \frac{y^2}{b^2})$ (z is the line of sight), and subscript the on the sky region j, in the same manner as the physical region: $A^2 < 1$,

$1 \leq A^2 \leq R^2$, and $R^2 < A^2$ as 1,2, and 3 respectively. In this manner, we have $\phi_{i,j}(x,y)$. Below, I is the incomplete Beta Function, and B is the (complete) Beta function.

Inner Ellipsoid

$$\epsilon_1(x,y,z) = \epsilon_{0,1}(\frac{x^2}{a^2} + \frac{y^2}{b^2} + \frac{z^2}{c^2})^{-p_1}$$
$$\epsilon_2(x,y,z) = 0$$
$$\epsilon_3(x,y,z) = 0$$

$$\phi_{1,1}(x,y) = \sqrt{\pi}\epsilon_0 c \frac{\Gamma(p_1 - 0.5)}{\Gamma(0.5)} A^{1-2p_1} * (1 - I_{A^2}(p_1 - 0.5, 0.5))$$
$$\phi_{1,2}(x,y) = 0$$
$$\phi_{1,3}(x,y) = 0$$

Middle Ellipsoid

$$\epsilon_1(x,y,z) = 0$$
$$\epsilon_2(x,y,z) = \epsilon_{0,2}(\frac{x^2}{a^2} + \frac{y^2}{b^2} + \frac{z^2}{c^2})^{-p_2}$$
$$\epsilon_3(x,y,z) = 0$$

$$\phi_{2,1}(x,y) = \sqrt{\pi}\epsilon_{0,2}c\frac{\Gamma(p_2-0.5)}{\Gamma(0.5)}A^{1-2p_2} * (I_{A^2}(p_2-0.5,0.5) - I_{A^2/R^2}(p_2-0.5,0.5))$$
$$\phi_{2,2}(x,y) = \sqrt{\pi}\epsilon_{0,2}c\frac{\Gamma(p_2-0.5)}{\Gamma(0.5)}A^{1-2p_2} * (1 - I_{A^2/R^2}(p_2-0.5,0.5))$$
$$\phi_{2,3}(x,y) = 0$$

Outer Ellipsoid

$$\epsilon_1(x,y,z) = 0$$
$$\epsilon_2(x,y,z) = 0$$
$$\epsilon_3(x,y,z) = \epsilon_{0,3}(\frac{x^2}{a^2} + \frac{y^2}{b^2} + \frac{z^2}{c^2})^{-p_3}$$

$$\phi_{3,1}(x,y) = \sqrt{\pi}\epsilon_{0,3}c\frac{\Gamma(p_3-0.5)}{\Gamma(0.5)}A^{1-2p_3} * (I_{A^2}(p_3-0.5,0.5))$$
$$\phi_{3,2}(x,y) = \sqrt{\pi}\epsilon_{0,3}c\frac{\Gamma(p_3-0.5)}{\Gamma(0.5)}A^{1-2p_3} * (I_{A^2}(p_3-0.5,0.5))$$
$$\phi_{3,3}(x,y) = \sqrt{\pi}\epsilon_{0,3}c\frac{\Gamma(p_3-0.5)}{\Gamma(0.5)}A^{1-2p_3}$$

Appendix E.2

Integrals of tapered power law ellipsoids

We can think of $(\frac{y^2}{b^2} + \frac{z^2}{c^2})$ as a polar radius about the x-axis. Furthermore, $(\frac{\frac{y^2}{b^2}+\frac{z^2}{c^2}}{\frac{x^2}{a^2}})$ is thus the tangent of the opening angle, θ. For simplicity, a taper of the form

$(\tan(\theta)+C)^{-\xi}$ is adopted. In particular, if we choose $C=1$, then we have our taper, τ,:

$$\tau = (\frac{\frac{x^2}{a^2}+\frac{y^2}{b^2}+\frac{z^2}{c^2}}{\frac{x^2}{a^2}})^{-\xi} \tag{E.7}$$

Our taper is thus restricted such that $0 < \tau \leq 1$.

Inner Ellipsoid

$$\epsilon_1(x,y,z) = \epsilon_{0,1}(\frac{x^2}{a^2}+\frac{y^2}{b^2}+\frac{z^2}{c^2})^{-p_1}(\frac{\frac{x^2}{a^2}+\frac{y^2}{b^2}+\frac{z^2}{c^2}}{\frac{x^2}{a^2}})^{-\xi}$$

$$\epsilon_2(x,y,z) = 0$$

$$\epsilon_3(x,y,z) = 0$$

$$phi_{1,1}(x,y) = \sqrt{\pi}\epsilon_{0,1}c(\frac{x^2}{a^2})^{\xi}\frac{\Gamma(p_1+\xi-0.5)}{\Gamma(0.5)}A^{1-2(p_1+\xi)}(1-I_{A^2}(P+\xi-0.5,0.5))$$

$$phi_{1,2}(x,y) = 0$$

$$phi_{1,3}(x,y) = 0$$

It should be clear that $\epsilon_1(x,y,z)$ can also be written as $\epsilon_{0,1}(\frac{x^2}{a^2}+\frac{y^2}{b^2}+\frac{z^2}{c^2})^{-p_1-\xi}(\frac{x^2}{a^2})^{\xi}$

Middle Ellipsoid

$$\epsilon_2(x,y,z) = 0$$

$$\epsilon_2(x,y,z) = \epsilon_{0,2}(\frac{x^2}{a^2}+\frac{y^2}{b^2}+\frac{z^2}{c^2})^{-p_2}(\frac{\frac{x^2}{a^2}+\frac{y^2}{b^2}+\frac{z^2}{c^2}}{\frac{x^2}{a^2}})^{\xi}$$

$$\epsilon_2(x,y,z) = 0$$

$$\phi_{2,1}(x,y) = \sqrt{\pi}\epsilon_{0,2}c(\frac{x^2}{a^2})^{\xi}\frac{\Gamma(p_2+\xi-0.5)}{\Gamma(0.5)}A^{1-2(p_2+\xi)}(I_{A^2}(p_2+\xi-0.5,0.5)-I_{A^2/R^2}(p_2+\xi-0.5,0.5))$$

$$\phi_{2,2}(x,y) = \sqrt{\pi}\epsilon_{0,2}c(\frac{x^2}{a^2})^{\xi}\frac{\Gamma(p_2+\xi-0.5)}{\Gamma(0.5)}A^{1-2(p_2+\xi)}(1-I_{A^2/R^2}(p_2+\xi-0.5,0.5))$$

$$\phi_{2,3}(x,y) = 0$$

Outer Ellipsoid

$$\epsilon_1(x,y,z) = 0$$

$$\epsilon_2(x,y,z) = \epsilon_0(\frac{x^2}{a^2}+\frac{y^2}{b^2}+\frac{z^2}{c^2})^{-p_3}(\frac{\frac{x^2}{a^2}+\frac{y^2}{b^2}+\frac{z^2}{c^2}}{\frac{x^2}{a^2}})^{-\xi}$$

$$\epsilon_3(x,y,z) = 0$$

$$\phi_{3,1}(x,y) = \sqrt{\pi}\epsilon_{0,3}c(\frac{x^2}{a^2})^{\xi}\frac{\Gamma(p_3+\xi-0.5)}{\Gamma(0.5)}A^{1-2(p_3+\xi)}(I_{A^2}(p_3+\xi-0.5,0.5))$$

$$\phi_{3,2}(x,y) = \sqrt{\pi}\epsilon_{0,3}c(\frac{x^2}{a^2})^{\xi}\frac{\Gamma(p_3+\xi-0.5)}{\Gamma(0.5)}A^{1-2(p_3+\xi)}(I_{A^2}(p_3+\xi-0.5,0.5))$$

$$\phi_{3,3}(x,y) = \sqrt{\pi}\epsilon_{0,3}c(\frac{x^2}{a^2})^{\xi}\frac{\Gamma(p_3+\xi-0.5)}{\Gamma(0.5)}A^{1-2(p_3+\xi)}$$

Appendix F

Other Maps of CLASH Clusters

The following maps are based on work from Zitrin et al. (2015), and are available at `https://archive.stsci.edu/prepds/clash/`.

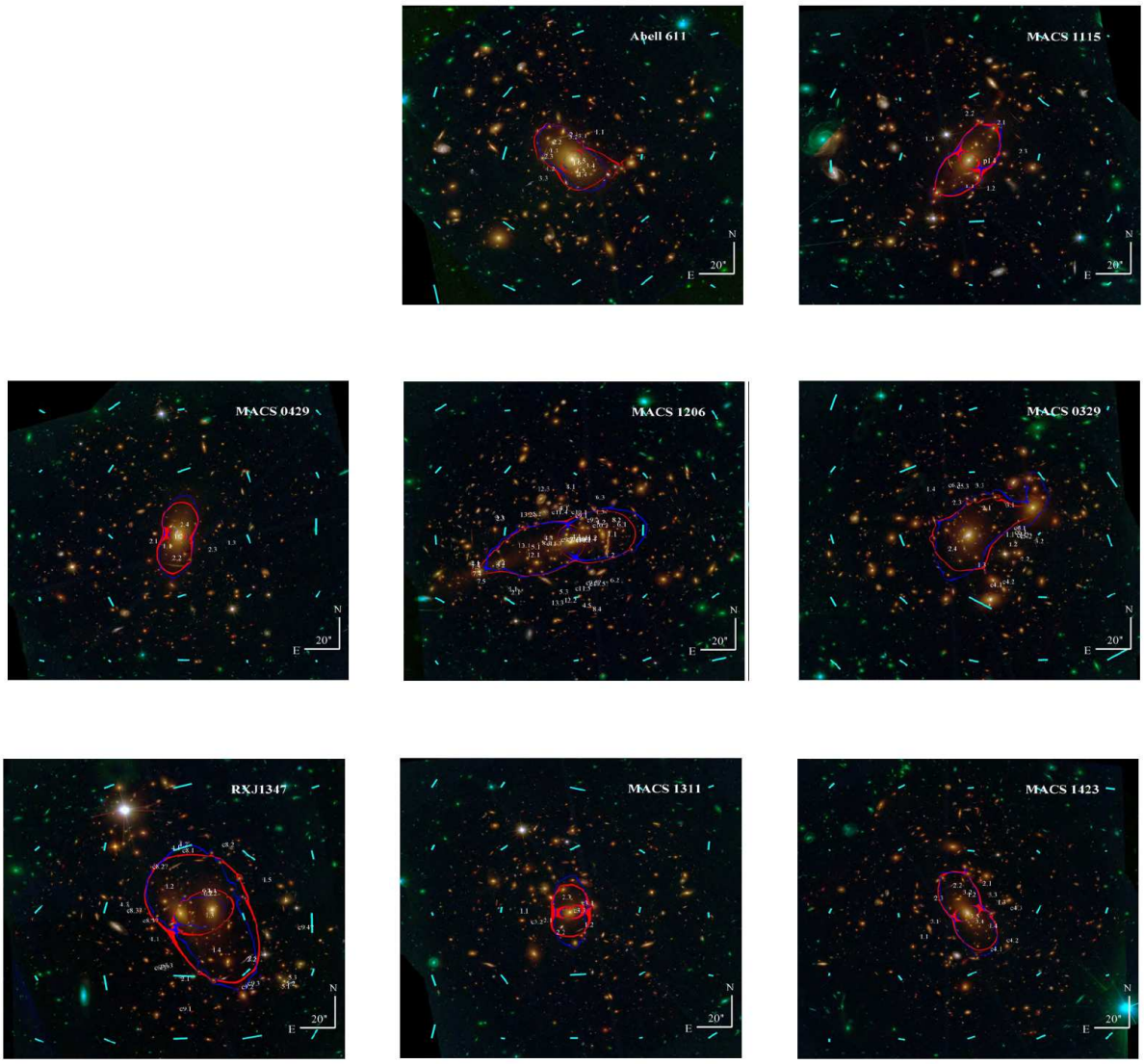

Fig. 8.5.— Cluster optical image with strong lensing magnification contours

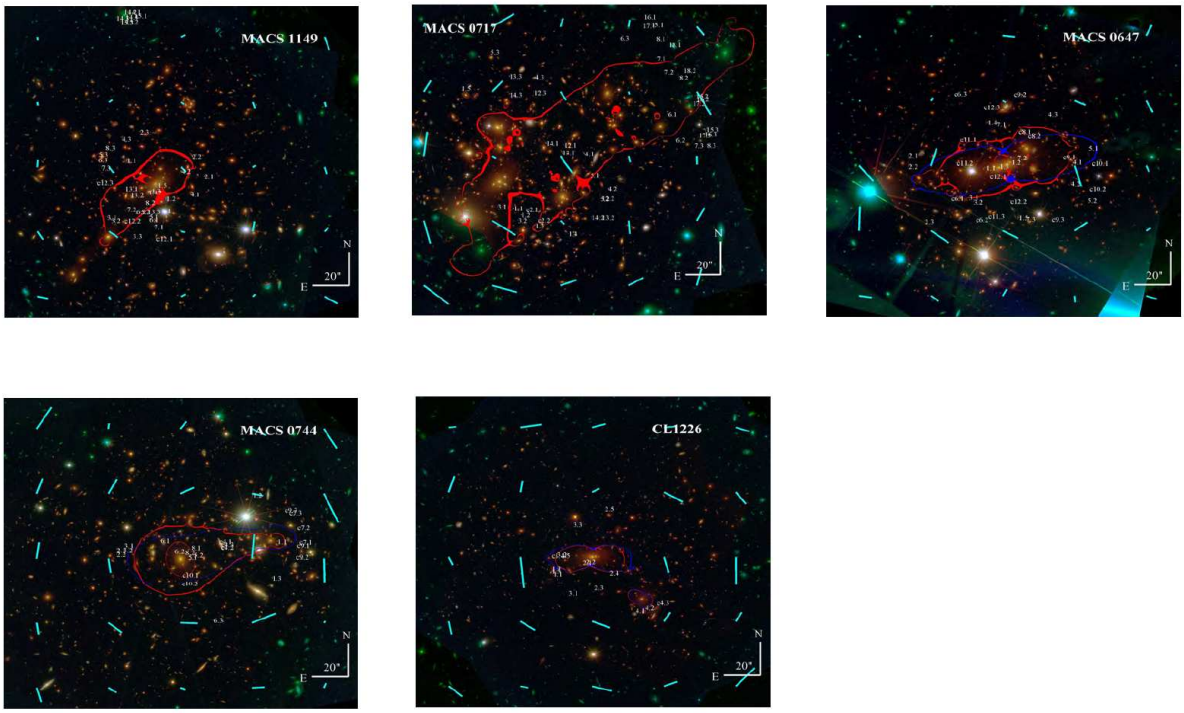

Fig. 8.6.— Cluster optical image with strong lensing magnification contours

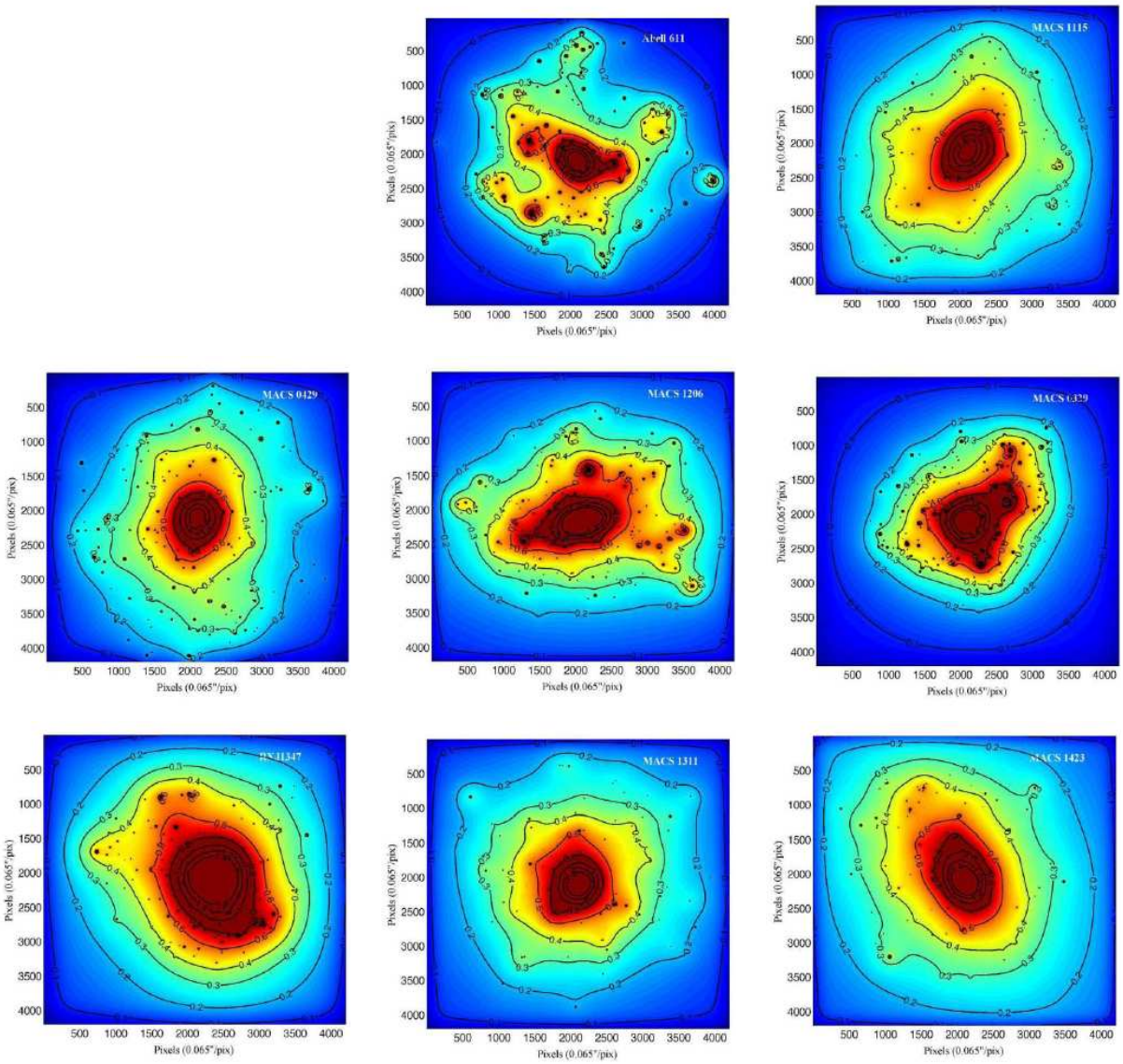

Fig. 8.7.— Cluster weak lensing (surface mass density) maps.

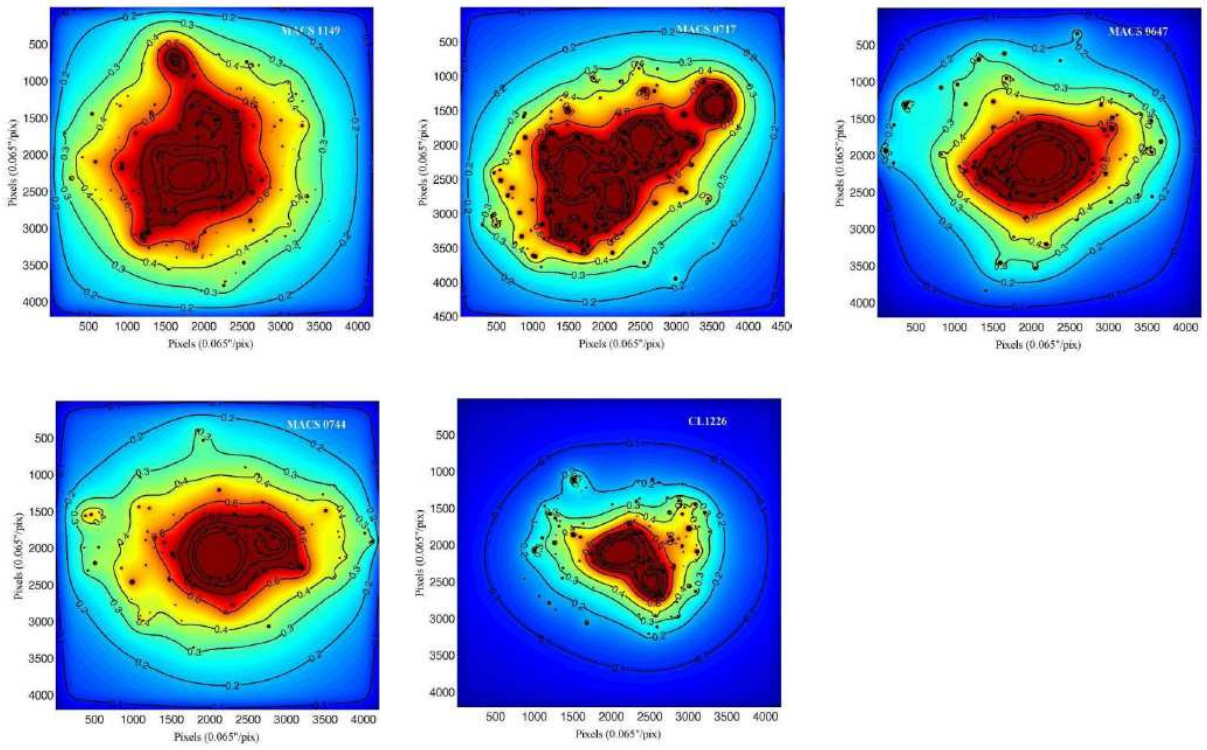

Fig. 8.8.— Cluster weak lensing (surface mass density) maps.

Appendix G

Timestream fitting

Appendix G.1

Introduction

MUSTANG data is recorded as a stream of integrations for each detector, known as timestreams, or alternatively called time-ordered-data (TOD). While gridding (calibrated) data will produce maps of the galaxy cluster, important for visualizing the SZE, the noise, specifically the covariance matrix, is not well known in the map domain, while we expect to be able to better characterize it in the time domain. Still, the primary reason to pursue timestream fitting is that we can attempt to recover signal in the common mode that is subtracted out in the production of our maps. Crucially, this signal could extend beyond the FOV of MUSTANG, so that timestream fitting would not just yield stronger results generally, but actually be able to constrain the pressure profile (Section 4) beyond what can be done in the map domain ($r \sim 21''$).

This approach of fitting models in the time domain was our initial pursuit to model fitting. While the method provided plausible results with real data, upon checking performance with simulated data, we found that the simulated data did not provide consistent results in certain cases of simulated common mode noise (realistic to what is seen with MUSTANG data). While improvements were made, and this approach is still of interest to the MUSTANG collaboration, the means to fit models in the map domain was developed and shown to be consistent. Thus, we further developed the map domain fits to allow for the principle analysis of this thesis (Chapter 4).

Appendix G.2

Formalism

Timestream fitting follows the formalism presented in Section 4.2, and is altered and expanded upon here. We write the timestream data as a vector $\overrightarrow{d}$, where it is the concatenation of the detectors that have acceptable timestreams for a scan. For a model timestream, $\overrightarrow{d}_{mod}$, we can calculate the χ^2 value as:

$$\chi^2 = (\overrightarrow{d} - \overrightarrow{d}_{mod})^T \mathbf{N}^{-1} (\overrightarrow{d} - \overrightarrow{d}_{mod}) \tag{G.8}$$

provided that the noise is Gaussian (it does not have to be independent):

$$N_{ij} = \langle d_i d_j \rangle - \langle d_i \rangle \langle d_j \rangle \tag{G.9}$$

If one were to solve for the noise matrix as written above, the computational expense would be prohibitively large for an entire observation of a cluster, even with the reasonable assumption that noise is independent between scans (i.e. one can solve for a noise matrix for each scan individually). We use the circulant approximation for the common-mode subtracted data (taken as $\overrightarrow{d}$ above) which reduces the noise matrix to a diagonal matrix, N_F, in fourier space. Our common mode noise is well described by $1/f$ power spectrum with a cutoff, where it becomes white noise), $N_{F,CM}$. The total noise matrix is then

$$N_{F,tot} = N_F + N_{F,CM} \tag{G.10}$$

We assume that a model timestream is some linearizable model: $\overrightarrow{d}_{mod} = \mathbf{A}\overrightarrow{x}_{mod}$, where $\overrightarrow{x}_{mod}$ is the model parameter vector, and will be $N_{parameters}$ in length. This allows our model timestream to come from more than one model parameter (or com-

ponent). In other words, this allows us to fit for a point source, as well as the cluster decrement, and pootentially additional sources of signal. In practice, the creation of **A** comes from taking a model sky map (for each parameter) and using the scan trajectory to create a model timestream. With these variable in place, we would like to solve for the amplitudes of the model parameters $\overrightarrow{x}_{mod}$. The least squares solution to the above setup is given by:

$$\overrightarrow{x}_m = (\mathbf{A}^T\mathbf{N}^{-1}\mathbf{A})^{-1}\mathbf{A}^T\mathbf{N}^{-1}\overrightarrow{d} \tag{G.11}$$

As presented, this is valid for data (d) and models (x_{mod}) which have had the filtering applied to it. However, we wish to work from gain-calibrated data, with poor data already excised or flagged, and apply the filtering within our fitting framework. These must be linear operators to work in this framework. The operators we then care about are: (1) a pulse tube subtraction, and (2) a polynomial-subtraction

Appendix G.3

Initial inconsistencies

Real Data

The following plots show that there is an inconsistency between reported error bars, and propogation of errors.

Fake Data

Rather than flipping data (either in the time domain, or flipping the sign of the gain), I have replaced the data with white noise (hereafter, "WN") and in another case, with random values that have the same power spectrum as the real data (hereafter, "PS").

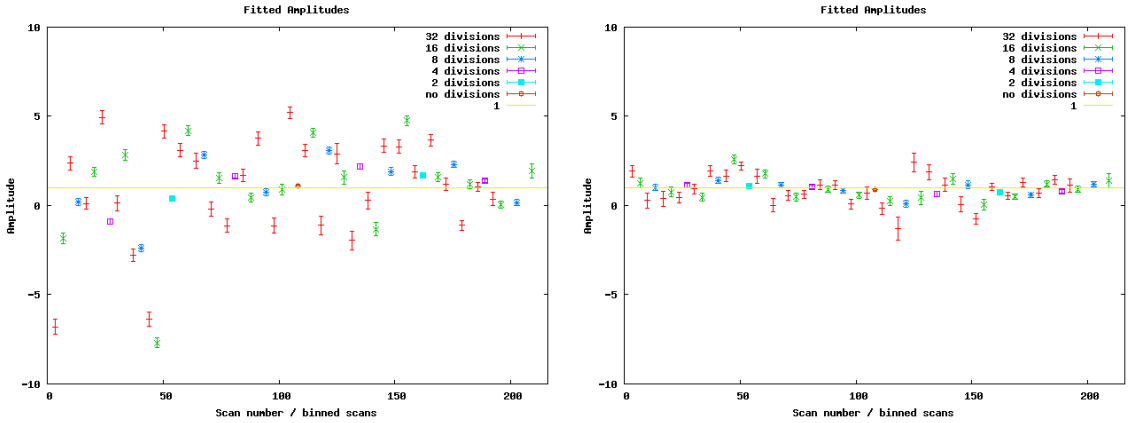

Fig. 8.9.— The left plot shows the amplitude fits to the cluster model, while the right plot shows the amplitude fits to the point source model. This simulated observation was done with dataflip.

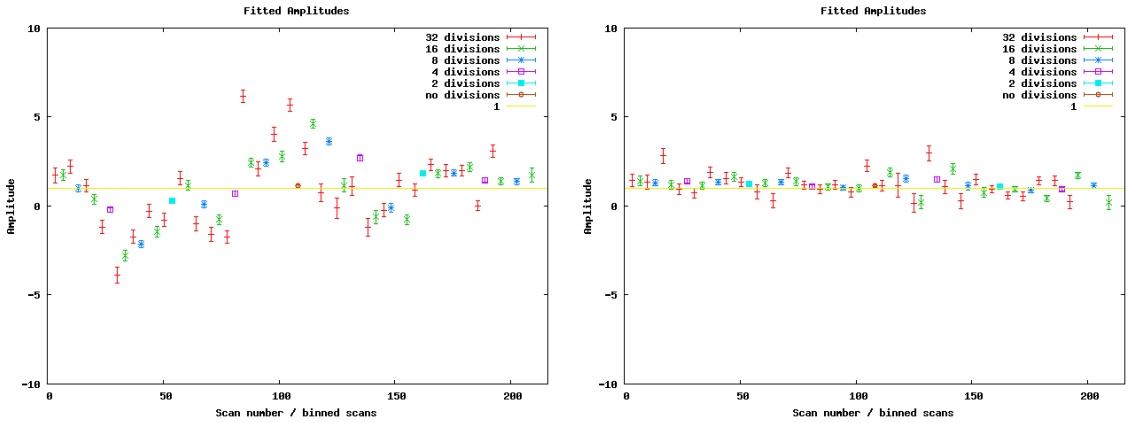

Fig. 8.10.— Same as figure 1, but this simulated observation was done with gainflip.

Using a point source as a handle on error bars

With a point source (not slightly extended as the "compact" source in the real MACS0717 observations is), it is fairly trivial to have a comparison between the error in the fit (reported by Ninkasi) and the error per pixel in an unsmoothed map. For further simplification, I set the flux of the point source to 1 mJy.

In the PS case, for the entire data set, the fit to the amplitude of the input model point source was 0.98 (where 1 is a perfect match to the input model). The error

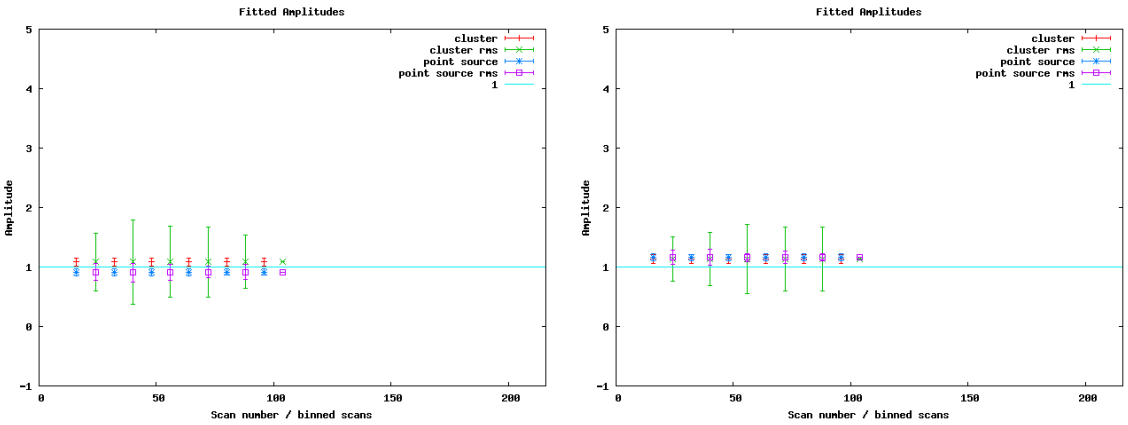

Fig. 8.11.— The weighted averages for both models. The left plot uses the dataflipped simulation, while the right plot uses the gainflipped simulation. "rms" in the legend indicates that the error bars are determined by the rms of the divisions (not valid for far right points.) From left to right, points indicate 32,16,8,4,2, and 1 bin(s) of data that have been averaged by weight; x-values are irrelevant.

on this fit is 0.061. (Also, of note, this error is consistent to 1% for the propogated errors of any of the different cases of division of data.) We can describe our fit to the point source as:

$$\overrightarrow{d}_{mod} = \mathbf{A} * \overrightarrow{x}_{mod} \text{ or:} \tag{G.12}$$

$$\mathbf{d_{mod}} = \mathbf{A} * x_{mod} \tag{G.13}$$

I've switched to calling $\mathbf{d_{mod}}$ and $\mathbf{A}$ matricies since I'm considering them in the map domain. $\mathbf{A}$ is the value of each pixel for 1 mJy point source (at the correct position) smoothed by a MUSTANG beam. Here I'm just concerned about the point source, so x_{mod} is just a scalar. In this case, we have:

$$\sigma_{x_{mod}} = \frac{\sigma_{d_{mod}}}{\sqrt{\sum A^2}} \tag{G.14}$$

Where $\sigma_{x_{mod}}$ is the uncertainty reported by Ninkasi, σd_{mod} is the uncertainty per pixel

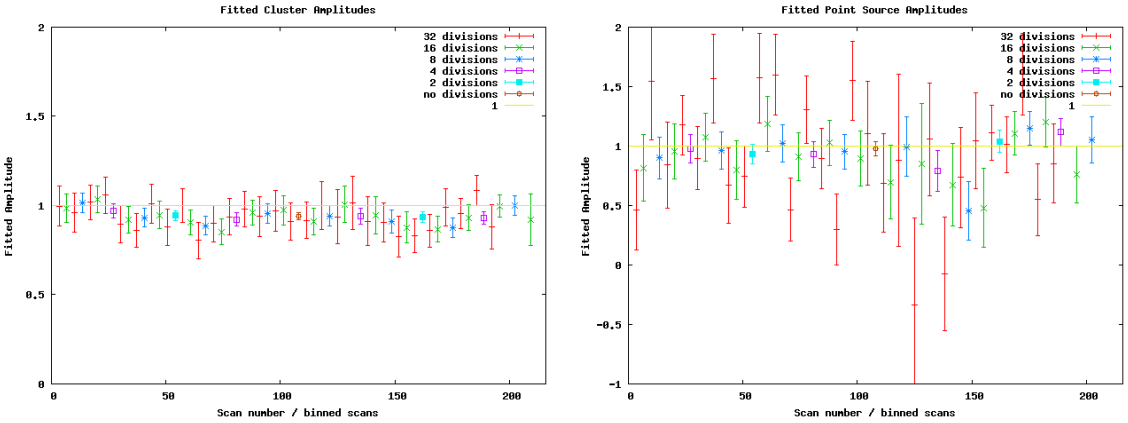

Fig. 8.12.— Fits from fake data with the same power spectrum as the real data.

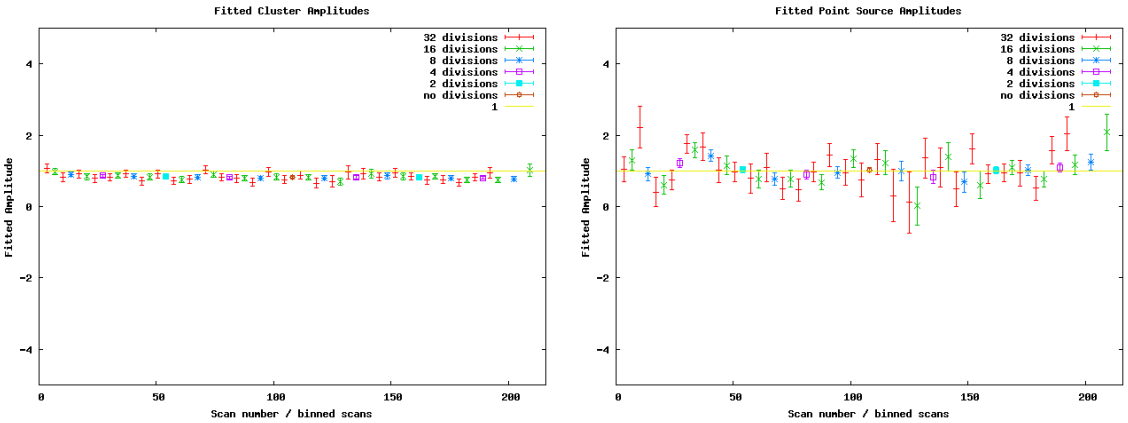

Fig. 8.13.— Fits from fake data with white noise.

in our unsmoothed maps. For simplicity, it is assumed to be a scalar, with the value found at the location of the point source. For clarity, a pixel size of 1.25" (on a side) were used for all maps in this analysis.

The values of each of these are:

Arguably, this is suggestive that Ninkasi could be overestimating the error. However, this analysis did not take into account any covariance with the cluster fit. (On this note, σ_{12} is an order of magnitude less than either σ_{11} or σ_{22}.)

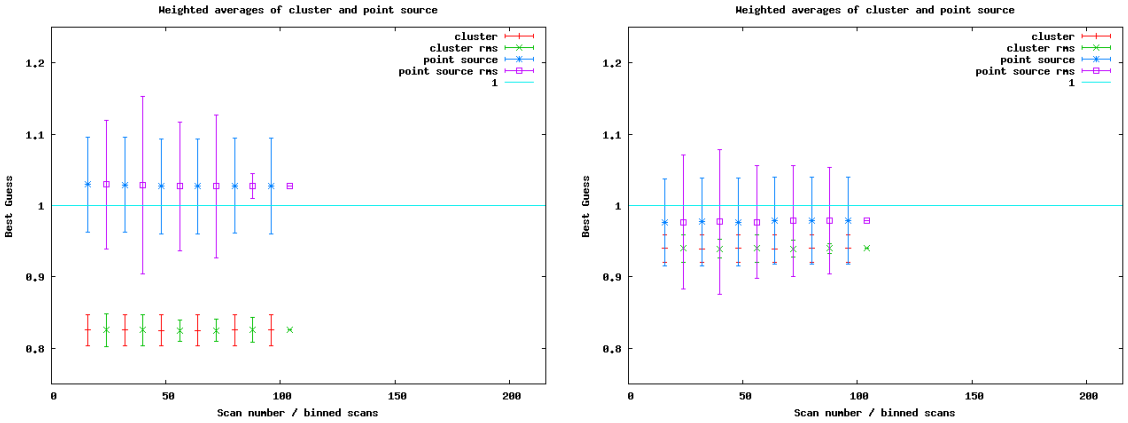

Fig. 8.14.— Weighted averages for the white noise case (left) and power spectrum case (right).

Case	DOF	$\chi^2_{cluster}$	PTE$_{cluster}$	χ^2_{ptsrc}	PTE$_{ptsrc}$
WN	29	90.1	3.58e-08	42.4	5.20e-02
WN	16	77.5	4.61e-10	29.5	2.06e-02
WN	8	69.7	5.67e-12	11.1	1.97e-01
WN	4	67.9	6.21e-14	4.68	3.23e-01
PS	29	23.2	7.68e-01	52.2	5.23e-03
PS	16	16.5	4.18e-01	16.5	4.16e-01
PS	8	15.4	5.22e-02	6.59	5.81e-01
PS	4	10.3	3.52e-02	3.02	5.55e-01
PS	2	9.50	8.67e-03	0.85	6.56e-01
PS	1	9.45	2.12e-03	0.12	7.36e-01

Table 8.1: WN ‾"white noise" and PS ‾"power spectrum". χ^2 values are *not* reduced χ^2 values. PTE ‾"probability to exceed" (χ^2 values).

Appendix G.4

Further investigations

After the summer of 2012, the NINKASI code has experienced a significant overhaul. Although the initial discrepancy between weighted averages and the fit for a whole data set seems to be dwindling, there are a variety of other checks that must be vetted before we proceed to using this code on real data. Currently, our principle test is looking at the average χ^2 values on fits for two models: a cluster model and point

Variable	Value (mJy)	Determined by:
$\sigma_{x_{mod}}$	0.061	Ninkasi
$\sigma_{d_{mod}}$	0.275	IDL
$\frac{1}{\sqrt{\sum A^2}}$	0.185	IDL
$\sigma_{x_{mod}} = \frac{\sigma_{d_{mod}}}{\sqrt{\sum A^2}}$	0.051	IDL

Table 8.2: These values are for the PS case.

source model. The χ^2 values should be close to 1. Secondly, since our data is noise dominated, d/σ should be 1, or put another way: $dN^{-1}d$ should be 1, where N is the covariance matrix. If we were to include pulse tube subtraction (since the pulse tube contribution is significant in real data), we would use $dPN^{-1}Pd$. While that comes out to be one number, we could also look at a plot of $N^{-1/2}Pd$ (in either fourier or time domain, although fourier domain will likely be more revealing), and see that it looks flat - like white noise.

The updated code has performed well with white noise on all tests. However, real data has not done so well. Because real data is not understood to utter detail, we have employed a noise generation that approximates real data (the same functional form as what is used to fit for a noise model). That is, we create $1/f$ noise that has a knee in it.

Avenues

A key part of calculating our covariance matrix is the assumption that our data is circulant. To this end, Jon has ensured that the noise generation script can indeed produce circulant data (but it can also produce non-circulant data). Outside of this, a few other tools are at our disposal in attempts to produce better results:

Windowing The idea is to keep as much data as possible, but throw out (possibly) bad data at the ends. This can be done as a straight step function, or it can

be tapered. Curently, a taper with 1% scan length is used on each end of a timestream.

- Windowing improved χ^2 values dramatically for synthetic data with steep 1/f slopes.

Detrending If employed (currently the default is to use detrending), this occurs before windowing. Detrending takes out any linear slope from the start to finish of a timestream, as well as setting the ends of the timestream to 0.

- One might think that well-generated noise would not need detrending, and this is fairly true - circulant data did not see much, if any improvement from just detrending. However, Non-circulant data did see improvement, and real data definitely has trends in the data, so it is a necessary part for real data.

References

Adam, R., Comis, B., Macías-Pérez, J.-F., Adane, A., Ade, P., André, P., Beelen, A., Belier, B., Benoît, A., Bideaud, A., Billot, N., Blanquer, G., Bourrion, O., Calvo, M., Catalano, A., Coiffard, G., Cruciani, A., D'Addabbo, A., Désert, F.-X., Doyle, S., Goupy, J., Kramer, C., Leclercq, S., Martino, J., Mauskopf, P., Mayet, F., Monfardini, A., Pajot, F., Pascale, E., Perotto, L., Pointecouteau, E., Ponthieu, N., Revéret, V., Ritacco, A., Rodriguez, L., Savini, G., Schuster, K., Sievers, A., Tucker, C., & Zylka, R. 2015, A&A, 576, A12

Allen, S. W., Rapetti, D. A., Schmidt, R. W., Ebeling, H., Morris, R. G., & Fabian, A. C. 2008, MNRAS, 383, 879

Allen, S. W., Schmidt, R. W., Ebeling, H., Fabian, A. C., & van Speybroeck, L. 2004, MNRAS, 353, 457

Allen, S. W., Schmidt, R. W., & Fabian, A. C. 2002, MNRAS, 335, 256

AMI Consortium, Hurley-Walker, N., Bridle, S., Cypriano, E. S., Davies, M. L., Erben, T., Feroz, F., Franzen, T. M. O., Grainge, K., Hobson, M. P., Lasenby, A., Marshall, P. J., Olamaie, M., Pooley, G., Rodríguez-Gonzálvez, C., Saunders, R. D. E., Scaife, A. M. M., Schammel, M. P., Scott, P. F., Shimwell, T., Titterington, D., Waldram, E., & Zwart, J. T. L. 2012, MNRAS, 419, 2921

AMI Consortium, Rodríguez-Gonzálvez, C., Olamaie, M., Davies, M. L., Fabian, A. C., Feroz, F., Franzen, T. M. O., Grainge, K. J. B., Hobson, M. P., Hurley-Walker, N., Lasenby, A. N., Pooley, G. G., Russell, H. R., Sanders, J. S., Saunders, R. D. E., Scaife, A. M. M., Schammel, M. P., Scott, P. F., Shimwell, T. W., Titterington, D. J., Waldram, E. M., & Zwart, J. T. L. 2011, MNRAS, 414, 3751

Anders, E. & Grevesse, N. 1989, Geochim. Cosmochim. Acta, 53, 197

Andersson, K., Benson, B. A., Ade, P. A. R., Aird, K. A., Armstrong, B., Bautz, M., Bleem, L. E., Brodwin, M., Carlstrom, J. E., Chang, C. L., Crawford, T. M., Crites, A. T., de Haan, T., Desai, S., Dobbs, M. A., Dudley, J. P., Foley, R. J., Forman, W. R., Garmire, G., George, E. M., Gladders, M. D., Halverson, N. W., High, F. W., Holder, G. P., Holzapfel, W. L., Hrubes, J. D., Jones, C., Joy, M., Keisler, R., Knox, L., Lee, A. T., Leitch, E. M., Lueker, M., Marrone, D. P., McMahon, J. J., Mehl, J., Meyer, S. S., Mohr, J. J., Montroy, T. E., Murray, S. S., Padin, S., Plagge, T., Pryke, C., Reichardt, C. L., Rest, A., Ruel, J., Ruhl, J. E., Schaffer, K. K., Shaw, L., Shirokoff, E., Song, J., Spieler, H. G., Stalder, B., Staniszewski, Z., Stark, A. A., Stubbs, C. W., Vanderlinde, K., Vieira, J. D., Vikhlinin, A., Williamson, R., Yang, Y., Zahn, O., & Zenteno, A. 2011, ApJ, 738, 48

Arnaud, M., Pratt, G. W., Piffaretti, R., Böhringer, H., Croston, J. H., & Pointecouteau, E. 2010, A&A, 517, A92

Austermann, J. E., Aird, K. A., Beall, J. A., Becker, D., Bender, A., Benson, B. A., Bleem, L. E., Britton, J., Carlstrom, J. E., Chang, C. L., Chiang, H. C., Cho, H.-M., Crawford, T. M., Crites, A. T., Datesman, A., de Haan, T., Dobbs, M. A., George, E. M., Halverson, N. W., Harrington, N., Henning, J. W., Hilton, G. C., Holder, G. P., Holzapfel, W. L., Hoover, S., Huang, N., Hubmayr, J., Irwin, K. D.,

Keisler, R., Kennedy, J., Knox, L., Lee, A. T., Leitch, E., Li, D., Lueker, M., Marrone, D. P., McMahon, J. J., Mehl, J., Meyer, S. S., Montroy, T. E., Natoli, T., Nibarger, J. P., Niemack, M. D., Novosad, V., Padin, S., Pryke, C., Reichardt, C. L., Ruhl, J. E., Saliwanchik, B. R., Sayre, J. T., Schaffer, K. K., Shirokoff, E., Stark, A. A., Story, K., Vanderlinde, K., Vieira, J. D., Wang, G., Williamson, R., Yefremenko, V., Yoon, K. W., & Zahn, O. 2012, in Society of Photo-Optical Instrumentation Engineers (SPIE) Conference Series, Vol. 8452, Society of Photo-Optical Instrumentation Engineers (SPIE) Conference Series, 1

Bahcall, N. A. & Fan, X. 1998, ApJ, 504, 1

Balbus, S. A. 2000, ApJ, 534, 420

Battaglia, N., Bond, J. R., Pfrommer, C., & Sievers, J. L. 2012, ApJ, 758, 75

Benson, B. A., Ade, P. A. R., Ahmed, Z., Allen, S. W., Arnold, K., Austermann, J. E., Bender, A. N., Bleem, L. E., Carlstrom, J. E., Chang, C. L., Cho, H. M., Cliche, J. F., Crawford, T. M., Cukierman, A., de Haan, T., Dobbs, M. A., Dutcher, D., Everett, W., Gilbert, A., Halverson, N. W., Hanson, D., Harrington, N. L., Hattori, K., Henning, J. W., Hilton, G. C., Holder, G. P., Holzapfel, W. L., Irwin, K. D., Keisler, R., Knox, L., Kubik, D., Kuo, C. L., Lee, A. T., Leitch, E. M., Li, D., McDonald, M., Meyer, S. S., Montgomery, J., Myers, M., Natoli, T., Nguyen, H., Novosad, V., Padin, S., Pan, Z., Pearson, J., Reichardt, C., Ruhl, J. E., Saliwanchik, B. R., Simard, G., Smecher, G., Sayre, J. T., Shirokoff, E., Stark, A. A., Story, K., Suzuki, A., Thompson, K. L., Tucker, C., Vanderlinde, K., Vieira, J. D., Vikhlinin, A., Wang, G., Yefremenko, V., & Yoon, K. W. 2014, in Society of Photo-Optical Instrumentation Engineers (SPIE) Conference Series, Vol. 9153, Society of Photo-Optical Instrumentation Engineers (SPIE) Conference Series, 1

Benson, B. A., Church, S. E., Ade, P. A. R., Bock, J. J., Ganga, K. M., Henson, C. N., & Thompson, K. L. 2004, ApJ, 617, 829

Benson, B. A., Church, S. E., Ade, P. A. R., Bock, J. J., Ganga, K. M., Hinderks, J. R., Mauskopf, P. D., Philhour, B., Runyan, M. C., & Thompson, K. L. 2003, ApJ, 592, 674

Birkinshaw, M. 1979, MNRAS, 187, 847

—. 1999, Phys. Rep., 310, 97

Birkinshaw, M. & Lancaster, K. 2008, in Lecture Notes in Physics, Berlin Springer Verlag, Vol. 740, A Pan-Chromatic View of Clusters of Galaxies and the Large-Scale Structure, ed. M. Plionis, O. López-Cruz, & D. Hughes, 255

Biviano, A., Rosati, P., Balestra, I., Mercurio, A., Girardi, M., Nonino, M., Grillo, C., Scodeggio, M., Lemze, D., Kelson, D., Umetsu, K., Postman, M., Zitrin, A., Czoske, O., Ettori, S., Fritz, A., Lombardi, M., Maier, C., Medezinski, E., Mei, S., Presotto, V., Strazzullo, V., Tozzi, P., Ziegler, B., Annunziatella, M., Bartelmann, M., Benitez, N., Bradley, L., Brescia, M., Broadhurst, T., Coe, D., Demarco, R., Donahue, M., Ford, H., Gobat, R., Graves, G., Koekemoer, A., Kuchner, U., Melchior, P., Meneghetti, M., Merten, J., Moustakas, L., Munari, E., Regős, E., Sartoris, B., Seitz, S., & Zheng, W. 2013, A&A, 558, A1

Bleem, L. E., Stalder, B., de Haan, T., Aird, K. A., Allen, S. W., Applegate, D. E., Ashby, M. L. N., Bautz, M., Bayliss, M., Benson, B. A., Bocquet, S., Brodwin, M., Carlstrom, J. E., Chang, C. L., Chiu, I., Cho, H. M., Clocchiatti, A., Crawford, T. M., Crites, A. T., Desai, S., Dietrich, J. P., Dobbs, M. A., Foley, R. J., Forman, W. R., George, E. M., Gladders, M. D., Gonzalez, A. H., Halverson, N. W., Hennig,

C., Hoekstra, H., Holder, G. P., Holzapfel, W. L., Hrubes, J. D., Jones, C., Keisler, R., Knox, L., Lee, A. T., Leitch, E. M., Liu, J., Lueker, M., Luong-Van, D., Mantz, A., Marrone, D. P., McDonald, M., McMahon, J. J., Meyer, S. S., Mocanu, L., Mohr, J. J., Murray, S. S., Padin, S., Pryke, C., Reichardt, C. L., Rest, A., Ruel, J., Ruhl, J. E., Saliwanchik, B. R., Saro, A., Sayre, J. T., Schaffer, K. K., Schrabback, T., Shirokoff, E., Song, J., Spieler, H. G., Stanford, S. A., Staniszewski, Z., Stark, A. A., Story, K. T., Stubbs, C. W., Vanderlinde, K., Vieira, J. D., Vikhlinin, A., Williamson, R., Zahn, O., & Zenteno, A. 2015, ApJS, 216, 27

Böhringer, H., Chon, G., & Collins, C. A. 2014, A&A, 570, A31

Bonamente, M., Carlstrom, J., Leitch, E., Joy, M., Marrone, D., Mantz, A., Muchovej, S., Plagge, T., & Reese, E. 2013, in IAU Symposium, Vol. 289, IAU Symposium, ed. R. de Grijs, 339–343

Bonamente, M., Joy, M. K., LaRoque, S. J., Carlstrom, J. E., Reese, E. D., & Dawson, K. S. 2006, ApJ, 647, 25

Borgani, S. & Kravtsov, A. 2011, Advanced Science Letters, 4, 204

Bradač, M., Schrabback, T., Erben, T., McCourt, M., Million, E., Mantz, A., Allen, S., Blandford, R., Halkola, A., Hildebrandt, H., Lombardi, M., Marshall, P., Schneider, P., Treu, T., & Kneib, J.-P. 2008, ApJ, 681, 187

Bulbul, G. E., Hasler, N., Bonamente, M., & Joy, M. 2010, ApJ, 720, 1038

Burenin, R. A., Vikhlinin, A., Hornstrup, A., Ebeling, H., Quintana, H., & Meshcheryakov, A. 2007, ApJS, 172, 561

Burgers, J. M. 1969, Flow Equations for Composite Gases

Carlstrom, J. E., Ade, P. A. R., Aird, K. A., Benson, B. A., Bleem, L. E., Busetti, S., Chang, C. L., Chauvin, E., Cho, H., Crawford, T. M., Crites, A. T., Dobbs, M. A., Halverson, N. W., Heimsath, S., Holzapfel, W. L., Hrubes, J. D., Joy, M., Keisler, R., Lanting, T. M., Lee, A. T., Leitch, E. M., Leong, J., Lu, W., Lueker, M., McMahon, J. J., Mehl, J., Meyer, S. S., Mohr, J. J., Montroy, T. E., Padin, S., Plagge, T., Pryke, C., Ruhl, J. E., Schaffer, K. K., Schwan, D., Shirokoff, E., Spieler, H. G., Staniszewski, Z., Stark, A. A., & Vieira, K. V. J. D. 2009, ArXiv e-prints

Carlstrom, J. E., Holder, G. P., & Reese, E. D. 2002, ARA&A, 40, 643

Cavagnolo, K. W., Donahue, M., Voit, G. M., & Sun, M. 2009, ApJS, 182, 12

Cavaliere, A., Danese, L., & de Zotti, G. 1979, A&A, 75, 322

Cavaliere, A. & Fusco-Femiano, R. 1978, A&A, 70, 677

Chatzikos, M. 2012, PhD thesis, University of Virginia

Chuzhoy, L. & Loeb, A. 2004, MNRAS, 349, L13

Comerford, J. M. & Natarajan, P. 2007, MNRAS, 379, 190

Condon, J. J., Cotton, W. D., Greisen, E. W., Yin, Q. F., Perley, R. A., Taylor, G. B., & Broderick, J. J. 1998, AJ, 115, 1693

Croston, J. H., Pratt, G. W., Böhringer, H., Arnaud, M., Pointecouteau, E., Ponman, T. J., Sanderson, A. J. R., Temple, R. F., Bower, R. G., & Donahue, M. 2008, A&A, 487, 431

Czakon, N. G., Sayers, J., Mantz, A., Golwala, S. R., Downes, T. P., Koch, P. M., Lin, K.-Y., Molnar, S. M., Moustakas, L. A., Mroczkowski, T., Pierpaoli, E., Shitanishi, J. A., Siegel, S., & Umetsu, K. 2014, ArXiv e-prints 1406.2800

da Silva, A. J. C. 2004, Ap&SS, 290, 167

Dicker, S. R., Abrahams, J. A., Ade, P. A. R., Ames, T. J., Benford, D. J., Chen, T. C., Chervenak, J. A., Devlin, M. J., Irwin, K. D., Korngut, P. M., Maher, S., Mason, B. S., Mello, M., Moseley, S. H., Norrod, R. D., Shafer, R. A., Staguhn, J. G., Talley, D. J., Tucker, C., Werner, B. A., & White, S. D. 2006, in Society of Photo-Optical Instrumentation Engineers (SPIE) Conference Series, Vol. 6275, Society of Photo-Optical Instrumentation Engineers (SPIE) Conference Series, 1

Dicker, S. R., Ade, P. A. R., Aguirre, J., Brevik, J. A., Cho, H. M., Datta, R., Devlin, M. J., Dober, B., Egan, D., Ford, J., Ford, P., Hilton, G., Hubmayr, J., Irwin, K. D., Mason, B. S., Marganian, P., Mello, M., McMahon, J. J., Mroczkowski, T., Romero, C., Stanchfield, S., Tucker, C., Vale, L., White, S., Whitehead, M., & Young, A. H. 2014a, in Society of Photo-Optical Instrumentation Engineers (SPIE) Conference Series, Vol. 9153, Society of Photo-Optical Instrumentation Engineers (SPIE) Conference Series, 0

Dicker, S. R., Ade, P. A. R., Aguirre, J., Brevik, J. A., Cho, H. M., Datta, R., Devlin, M. J., Dober, B., Egan, D., Ford, J., Ford, P., Hilton, G., Irwin, K. D., Mason, B. S., Marganian, P., Mello, M., McMahon, J. J., Mroczkowski, T., Rosenman, M., Tucker, C., Vale, L., White, S., Whitehead, M., & Young, A. H. 2014b, in , 808–814

Dicker, S. R., Korngut, P. M., Mason, B. S., Ade, P. A. R., Aguirre, J., Ames, T. J., Benford, D. J., Chen, T. C., Chervenak, J. A., Cotton, W. D., Devlin, M. J., Figueroa-Feliciano, E., Irwin, K. D., Maher, S., Mello, M., Moseley, S. H., Tally,

D. J., Tucker, C., & White, S. D. 2008, in Society of Photo-Optical Instrumentation Engineers (SPIE) Conference Series, Vol. 7020, Society of Photo-Optical Instrumentation Engineers (SPIE) Conference Series

Donahue, M., Connor, T., Fogarty, K., Li, Y., Voit, G. M., Postman, M., Koekemoer, A., Moustakas, J., Bradley, L., & Ford, H. 2015, ArXiv e-prints

Donahue, M., Voit, G. M., Mahdavi, A., Umetsu, K., Ettori, S., Merten, J., Postman, M., Hoffer, A., Baldi, A., Coe, D., Czakon, N., Bartelmann, M., Benitez, N., Bouwens, R., Bradley, L., Broadhurst, T., Ford, H., Gastaldello, F., Grillo, C., Infante, L., Jouvel, S., Koekemoer, A., Kelson, D., Lahav, O., Lemze, D., Medezinski, E., Melchior, P., Meneghetti, M., Molino, A., Moustakas, J., Moustakas, L. A., Nonino, M., Rosati, P., Sayers, J., Seitz, S., Van der Wel, A., Zheng, W., & Zitrin, A. 2014, ApJ, 794, 136

Ebeling, H., Barrett, E., & Donovan, D. 2004, ApJ, 609, L49

Ebeling, H., Barrett, E., Donovan, D., Ma, C.-J., Edge, A. C., & van Speybroeck, L. 2007, ApJ, 661, L33

Ebeling, H., Edge, A. C., & Henry, J. P. 2001, ApJ, 553, 668

Ebeling, H., Ma, C. J., Kneib, J.-P., Jullo, E., Courtney, N. J. D., Barrett, E., Edge, A. C., & Le Borgne, J.-F. 2009, MNRAS, 395, 1213

Eckert, D., Vazza, F., Ettori, S., Molendi, S., Nagai, D., Lau, E. T., Roncarelli, M., Rossetti, M., Snowden, S. L., & Gastaldello, F. 2012, A&A, 541, A57

Ettori, S., Morandi, A., Tozzi, P., Balestra, I., Borgani, S., Rosati, P., Lovisari, L., & F., T. 2009, astro-ph/0904.2740

Fabian, A. C. 1994, ARA&A, 32, 277

Fabian, A. C. & Pringle, J. E. 1977, MNRAS, 181, 5P

Fabian, A. C., Sanders, J. S., Taylor, G. B., Allen, S. W., Crawford, C. S., Johnstone, R. M., & Iwasawa, K. 2006, MNRAS, 366, 417

Fagaly, R. L. 2006, Review of Scientific Instruments, 77, 101101

Feretti, L. & Giovannini, G. 2008, in Lecture Notes in Physics, Berlin Springer Verlag, Vol. 740, A Pan-Chromatic View of Clusters of Galaxies and the Large-Scale Structure, ed. M. Plionis, O. López-Cruz, & D. Hughes, 143

Ferrari, C., Intema, H. T., Orrù, E., Govoni, F., Murgia, M., Mason, B., Bourdin, H., Asad, K. M., Mazzotta, P., Wise, M. W., Mroczkowski, T., & Croston, J. H. 2011, A&A, 534, L12

Freedman, W. L., Madore, B. F., Gibson, B. K., Ferrarese, L., Kelson, D. D., Sakai, S., Mould, J. R., Kennicutt, R. C., Ford, H. C., Graham, J. A., Huchra, J. P., Hughes, S. M. G., Illingworth, G. D., Macri, L. M., & Stetson, P. B. 2001, ApJ, 553, 47

Friedman, S. H., Heinz, S., & Churazov, E. 2012, ApJ, 746, 112

Fritz, G., Davidsen, A., Meekins, J. F., & Friedman, H. 1971, ApJ, 164, L81

George, E. M., Reichardt, C. L., Aird, K. A., Benson, B. A., Bleem, L. E., Carlstrom, J. E., Chang, C. L., Cho, H.-M., Crawford, T. M., Crites, A. T., de Haan, T., Dobbs, M. A., Dudley, J., Halverson, N. W., Harrington, N. L., Holder, G. P., Holzapfel, W. L., Hou, Z., Hrubes, J. D., Keisler, R., Knox, L., Lee, A. T., Leitch, E. M., Lueker, M., Luong-Van, D., McMahon, J. J., Mehl, J., Meyer, S. S., Millea,

M., Mocanu, L. M., Mohr, J. J., Montroy, T. E., Padin, S., Plagge, T., Pryke, C., Ruhl, J. E., Schaffer, K. K., Shaw, L., Shirokoff, E., Spieler, H. G., Staniszewski, Z., Stark, A. A., Story, K. T., van Engelen, A., Vanderlinde, K., Vieira, J. D., Williamson, R., & Zahn, O. 2015, ApJ, 799, 177

Giacconi, R., Murray, S., Gursky, H., Kellogg, E., Schreier, E., & Tananbaum, H. 1972, ApJ, 178, 281

Gilfanov, M. R. & Syunyaev, R. A. 1984, Soviet Astronomy Letters, 10, 137

Gilmour, R., Best, P., & Almaini, O. 2009, MNRAS, 392, 1509

Gitti, M., Ferrari, C., Domainko, W., Feretti, L., & Schindler, S. 2007a, A&A, 470, L25

Gitti, M., Piffaretti, R., & Schindler, S. 2007b, A&A, 475, 441

Glenn, J., Bock, J. J., Chattopadhyay, G., Edgington, S. F., Lange, A. E., Zmuidzinas, J., Mauskopf, P. D., Rownd, B., Yuen, L., & Ade, P. A. 1998, Proc. SPIE, 3357, 326

Glenn, J., Knowles, B., Rownd, B. K., Edgington, S. F., Golwala, S., Lange, A. E., Bock, J. J., Goldin, A., Nguyen, H., Ade, P. A. R., Haig, D., & Mauskopf, P. D. 2002, in Astronomical Society of the Pacific Conference Series, Vol. 283, A New Era in Cosmology, ed. N. Metcalfe & T. Shanks, 398

Gull, S. F. & Northover, K. J. E. 1976, Nature, 263, 572

Gunn, J. E. 1978, in Saas-Fee Advanced Course 8: Observational Cosmology Advanced Course, ed. A. Maeder, L. Martinet, & G. Tammann, 1

Gursky, H., Kellogg, E., Murray, S., Leong, C., Tananbaum, H., & Giacconi, R. 1971, ApJ, 167, L81

Haig, D. J., Ade, P. A. R., Aguirre, J. E., Bock, J. J., Edgington, S. F., Enoch, M. L., Glenn, J., Goldin, A., Golwala, S., Heng, K., Laurent, G., Maloney, P. R., Mauskopf, P. D., Rossinot, P., Sayers, J., Stover, P., & Tucker, C. 2004, in Society of Photo-Optical Instrumentation Engineers (SPIE) Conference Series, Vol. 5498, Society of Photo-Optical Instrumentation Engineers (SPIE) Conference Series, ed. C. M. Bradford, P. A. R. Ade, J. E. Aguirre, J. J. Bock, M. Dragovan, L. Duband, L. Earle, J. Glenn, H. Matsuhara, B. J. Naylor, H. T. Nguyen, M. Yun, & J. Zmuidzinas, 78–94

Hand, N., Addison, G. E., Aubourg, E., Battaglia, N., Battistelli, E. S., Bizyaev, D., Bond, J. R., Brewington, H., Brinkmann, J., Brown, B. R., Das, S., Dawson, K. S., Devlin, M. J., Dunkley, J., Dunner, R., Eisenstein, D. J., Fowler, J. W., Gralla, M. B., Hajian, A., Halpern, M., Hilton, M., Hincks, A. D., Hlozek, R., Hughes, J. P., Infante, L., Irwin, K. D., Kosowsky, A., Lin, Y.-T., Malanushenko, E., Malanushenko, V., Marriage, T. A., Marsden, D., Menanteau, F., Moodley, K., Niemack, M. D., Nolta, M. R., Oravetz, D., Page, L. A., Palanque-Delabrouille, N., Pan, K., Reese, E. D., Schlegel, D. J., Schneider, D. P., Sehgal, N., Shelden, A., Sievers, J., Sifón, C., Simmons, A., Snedden, S., Spergel, D. N., Staggs, S. T., Swetz, D. S., Switzer, E. R., Trac, H., Weaver, B. A., Wollack, E. J., Yeche, C., & Zunckel, C. 2012, Physical Review Letters, 109, 041101

Hills, R. E. & Beasley, A. J. 2008, in Society of Photo-Optical Instrumentation Engineers (SPIE) Conference Series, Vol. 7012, Society of Photo-Optical Instrumentation Engineers (SPIE) Conference Series, 0

Ho, P. T. P., Altamirano, P., Chang, C.-H., Chang, S.-H., Chang, S.-W., Chen, C.-C., Chen, K.-J., Chen, M.-T., Han, C.-C., Ho, W. M., Huang, Y.-D., Hwang, Y.-J., Ibañez-Romano, F., Jiang, H., Koch, P. M., Kubo, D. Y., Li, C.-T., Lim, J., Lin, K.-Y., Liu, G.-C., Lo, K.-Y., Ma, C.-J., Martin, R. N., Martin-Cocher, P., Molnar, S. M., Ng, K.-W., Nishioka, H., O'Connell, K. E., Oshiro, P., Patt, F., Raffin, P., Umetsu, K., Wei, T., Wu, J.-H. P., Chiueh, T.-D., Chiueh, T., Chu, T.-H., Huang, C.-W. L., Hwang, W. Y. P., Liao, Y.-W., Lien, C.-H., Wang, F.-C., Wang, H., Wei, R.-M., Yang, C.-H., Kesteven, M., Kingsley, J., Sinclair, M. M., Wilson, W., Birkinshaw, M., Liang, H., Lancaster, K., Park, C.-G., Pen, U.-L., & Peterson, J. B. 2009, ApJ, 694, 1610

Holdaway, M. & Pardo, J. R. 1997, MMA Memo

Holland, W. S., Bintley, D., Chapin, E. L., Chrysostomou, A., Davis, G. R., Dempsey, J. T., Duncan, W. D., Fich, M., Friberg, P., Halpern, M., Irwin, K. D., Jenness, T., Kelly, B. D., MacIntosh, M. J., Robson, E. I., Scott, D., Ade, P. A. R., Atad-Ettedgui, E., Berry, D. S., Craig, S. C., Gao, X., Gibb, A. G., Hilton, G. C., Hollister, M. I., Kycia, J. B., Lunney, D. W., McGregor, H., Montgomery, D., Parkes, W., Tilanus, R. P. J., Ullom, J. N., Walther, C. A., Walton, A. J., Woodcraft, A. L., Amiri, M., Atkinson, D., Burger, B., Chuter, T., Coulson, I. M., Doriese, W. B., Dunare, C., Economou, F., Niemack, M. D., Parsons, H. A. L., Reintsema, C. D., Sibthorpe, B., Smail, I., Sudiwala, R., & Thomas, H. S. 2013, MNRAS, 430, 2513

Holland, W. S., Robson, E. I., Gear, W. K., Cunningham, C. R., Lightfoot, J. F., Jenness, T., Ivison, R. J., Stevens, J. A., Ade, P. A. R., Griffin, M. J., Duncan, W. D., Murphy, J. A., & Naylor, D. A. 1999, MNRAS, 303, 659

Holzapfel, W. L., Arnaud, M., Ade, P. A. R., Church, S. E., Fischer, M. L., Mauskopf, P. D., Rephaeli, Y., Wilbanks, T. M., & Lange, A. E. 1997, ApJ, 480, 449

Hu, W. & White, M. 1997, ApJ, 479, 568

Hunter, T. R., Schwab, F. R., White, S. D., Ford, J. M., Ghigo, F. D., Maddalena, R. J., Mason, B. S., Nelson, J. D., Prestage, R. M., Ray, J., Ries, P., Simon, R., Srikanth, S., & Whiteis, P. 2011, PASP, 123, 1087

Irwin, K. D. & Hilton, G. C. Transition-Edge Sensors, ed. C. Enss, 63

Itoh, N., Kohyama, Y., & Nozawa, S. 1998, ApJ, 502, 7

Jewell, P. R. & Prestage, R. M. 2004, in Society of Photo-Optical Instrumentation Engineers (SPIE) Conference Series, Vol. 5489, Ground-based Telescopes, ed. J. M. Oschmann, Jr., 312–323

Johnson, R. E., Zuhone, J., Jones, C., Forman, W. R., & Markevitch, M. 2012, ApJ, 751, 95

Jones, C. & Forman, W. 1984, ApJ, 276, 38

Kaiser, N. 1986, MNRAS, 222, 323

Kartaltepe, J. S., Ebeling, H., Ma, C. J., & Donovan, D. 2008, MNRAS, 389, 1240

King, I. R. 1966, AJ, 71, 276

Kitayama, T., Komatsu, E., Ota, N., Kuwabara, T., Suto, Y., Yoshikawa, K., Hattori, M., & Matsuo, H. 2004, PASJ, 56, 17

Kneissl, R., Jones, M. E., Saunders, R., Eke, V. R., Lasenby, A. N., Grainge, K., & Cotter, G. 2001, MNRAS, 328, 783

Koester, B. P., McKay, T. A., Annis, J., Wechsler, R. H., Evrard, A., Bleem, L., Becker, M., Johnston, D., Sheldon, E., Nichol, R., Miller, C., Scranton, R., Bahcall, N., Barentine, J., Brewington, H., Brinkmann, J., Harvanek, M., Kleinman, S., Krzesinski, J., Long, D., Nitta, A., Schneider, D. P., Sneddin, S., Voges, W., & York, D. 2007, ApJ, 660, 239

Komatsu, E., Matsuo, H., Kitayama, T., Kawabe, R., Kuno, N., Schindler, S., & Yoshikawa, K. 2001, PASJ, 53, 57

Korngut, P. M., Dicker, S. R., Reese, E. D., Mason, B. S., Devlin, M. J., Mroczkowski, T., Sarazin, C. L., Sun, M., & Sievers, J. 2011, ApJ, 734, 10

Korolev, V. A., Syunyaev, R. A., & Yakubsev, L. A. 1986, Pisma v Astronomicheskii Zhurnal, 12, 339

Kravtsov, A. V. & Borgani, S. 2012, ARA&A, 50, 353

Kriss, G. A., Cioffi, D. F., & Canizares, C. R. 1983, ApJ, 272, 439

Kuno, N., Matsuo, H., Mizumoto, Y., Lange, A. E., Beeman, J. W., & Haller, E. E. 1993, International Journal of Infrared and Millimeter Waves, 14, 749

Landau, L. D. & Lifshitz, E. M. 1959, Fluid mechanics

Langley, S. P. 1881, Nature, 25, 14

LaRoque, S. J., Bonamente, M., Carlstrom, J. E., Joy, M. K., Nagai, D., Reese, E. D., & Dawson, K. S. 2006, ApJ, 652, 917

LaRoque, S. J., Joy, M., Carlstrom, J. E., Ebeling, H., Bonamente, M., Dawson, K. S., Edge, A., Holzapfel, W. L., Miller, A. D., Nagai, D., Patel, S. K., & Reese, E. D. 2003, ApJ, 583, 559

Leccardi, A. & Molendi, S. 2008, A&A, 486, 359

Lemze, D., Postman, M., Genel, S., Ford, H. C., Balestra, I., Donahue, M., Kelson, D., Nonino, M., Mercurio, A., Biviano, A., Rosati, P., Umetsu, K., Sand, D., Koekemoer, A., Meneghetti, M., Melchior, P., Newman, A. B., Bhatti, W. A., Voit, G. M., Medezinski, E., Zitrin, A., Zheng, W., Broadhurst, T., Bartelmann, M., Benitez, N., Bouwens, R., Bradley, L., Coe, D., Graves, G., Grillo, C., Infante, L., Jimenez-Teja, Y., Jouvel, S., Lahav, O., Maoz, D., Merten, J., Molino, A., Moustakas, J., Moustakas, L., Ogaz, S., Scodeggio, M., & Seitz, S. 2013, ApJ, 776, 91

Limousin, M., Ebeling, H., Richard, J., Swinbank, A. M., Smith, G. P., Jauzac, M., Rodionov, S., Ma, C.-J., Smail, I., Edge, A. C., Jullo, E., & Kneib, J.-P. 2012, A&A, 544, A71

Lueker, M., Reichardt, C. L., Schaffer, K. K., Zahn, O., Ade, P. A. R., Aird, K. A., Benson, B. A., Bleem, L. E., Carlstrom, J. E., Chang, C. L., Cho, H., Crawford, T. M., Crites, A. T., de Haan, T., Dobbs, M. A., George, E. M., Hall, N. R., Halverson, N. W., Holder, G. P., Holzapfel, W. L., Hrubes, J. D., Joy, M., Keisler, R., Knox, L., Lee, A. T., Leitch, E. M., McMahon, J. J., Mehl, J., Meyer, S. S., Mohr, J. J., Montroy, T. E., Padin, S., Plagge, T., Pryke, C., Ruhl, J. E., Shaw, L., Shirokoff, E., Spieler, H. G., Stalder, B., Staniszewski, Z., Stark, A. A., Vanderlinde, K., Vieira, J. D., & Williamson, R. 2010, ApJ, 719, 1045

Ma, C.-J., Ebeling, H., & Barrett, E. 2009, ApJ, 693, L56

Madore, B. F., Freedman, W. L., Silbermann, N., Harding, P., Huchra, J., Mould, J. R., Graham, J. A., Ferrarese, L., Gibson, B. K., Han, M., Hoessel, J. G., Hughes, S. M., Illingworth, G. D., Phelps, R., Sakai, S., & Stetson, P. 1999, ApJ, 515, 29

Mann, A. W. & Ebeling, H. 2012, MNRAS, 420, 2120

Mantz, A., Allen, S. W., Rapetti, D., & Ebeling, H. 2010, MNRAS, 406, 1759

Markevitch, M., Gonzalez, A. H., Clowe, D., Vikhlinin, A., Forman, W., Jones, C., Murray, S., & Tucker, W. 2004, ApJ, 606, 819

Markevitch, M., Gonzalez, A. H., David, L., Vikhlinin, A., Murray, S., Forman, W., Jones, C., & Tucker, W. 2002, ApJ, 567, L27

Markevitch, M., Govoni, F., Brunetti, G., & Jerius, D. 2005, ApJ, 627, 733

Markevitch, M. & Vikhlinin, A. 2007, Phys. Rep., 443, 1

Markwardt, C. B. 2009, in Astronomical Society of the Pacific Conference Series, Vol. 411, Astronomical Data Analysis Software and Systems XVIII, ed. D. A. Bohlender, D. Durand, & P. Dowler, 251

Marriage, T. A., Baptiste Juin, J., Lin, Y.-T., Marsden, D., Nolta, M. R., Partridge, B., Ade, P. A. R., Aguirre, P., Amiri, M., Appel, J. W., Barrientos, L. F., Battistelli, E. S., Bond, J. R., Brown, B., Burger, B., Chervenak, J., Das, S., Devlin, M. J., Dicker, S. R., Bertrand Doriese, W., Dunkley, J., Dünner, R., Essinger-Hileman, T., Fisher, R. P., Fowler, J. W., Hajian, A., Halpern, M., Hasselfield, M., Hernández-Monteagudo, C., Hilton, G. C., Hilton, M., Hincks, A. D., Hlozek, R., Huffenberger, K. M., Handel Hughes, D., Hughes, J. P., Infante, L., Irwin, K. D., Kaul, M., Klein, J., Kosowsky, A., Lau, J. M., Limon, M., Lupton, R. H., Martocci, K., Mauskopf, P., Menanteau, F., Moodley, K., Moseley, H., Netterfield, C. B., Niemack, M. D., Page, L. A., Parker, L., Quintana, H., Reid, B., Sehgal, N., Sherwin, B. D., Sievers, J., Spergel, D. N., Staggs, S. T., Swetz, D. S., Switzer, E. R., Thornton, R., Trac,

H., Tucker, C., Warne, R., Wilson, G., Wollack, E., & Zhao, Y. 2011, ApJ, 731, 100

Mason, B. S. 2012, GBT Memo

Mason, B. S., Dicker, S. R., Korngut, P. M., Devlin, M. J., Cotton, W. D., Koch, P. M., Molnar, S. M., Sievers, J., Aguirre, J. E., Benford, D., Staguhn, J. G., Moseley, H., Irwin, K. D., & Ade, P. 2010, ApJ, 716, 739

Maughan, B. J., Giles, P. A., Randall, S. W., Jones, C., & Forman, W. R. 2012, MNRAS, 421, 1583

Maughan, B. J., Jones, C., Forman, W., & Van Speybroeck, L. 2008, ApJS, 174, 117

Mauskopf, P. D., Horner, P. F., Aguirre, J., Bock, J. J., Egami, E., Glenn, J., Golwala, S. R., Laurent, G., Nguyen, H. T., & Sayers, J. 2012, MNRAS, 421, 224

McNamara, B. R. & Nulsen, P. E. J. 2007, ARA&A, 45, 117

McNamara, B. R., Rafferty, D. A., Bîrzan, L., Steiner, J., Wise, M. W., Nulsen, P. E. J., Carilli, C. L., Ryan, R., & Sharma, M. 2006, ApJ, 648, 164

McNamara, B. R., Russell, H. R., Nulsen, P. E. J., Edge, A. C., Murray, N. W., Main, R. A., Vantyghem, A. N., Combes, F., Fabian, A. C., Salome, P., Kirkpatrick, C. C., Baum, S. A., Bregman, J. N., Donahue, M., Egami, E., Hamer, S., O'Dea, C. P., Oonk, J. B. R., Tremblay, G., & Voit, G. M. 2014, ApJ, 785, 44

Mewe, R., Gronenschild, E. H. B. M., & van den Oord, G. H. J. 1985, A&AS, 62, 197

Mewe, R., Lemen, J. R., & van den Oord, G. H. J. 1986, A&AS, 65, 511

Meyer, S. S., Jeffries, A. D., & Weiss, R. 1983, ApJ, 271, L1

Miranda, M., Sereno, M., de Filippis, E., & Paolillo, M. 2008, MNRAS, 385, 511

Molnar, S. M. & Broadhurst, T. 2015, ApJ, 800, 37

Monfardini, A., Adam, R., Adane, A., Ade, P., André, P., Beelen, A., Belier, B., Benoit, A., Bideaud, A., Billot, N., Bourrion, O., Calvo, M., Catalano, A., Coiffard, G., Comis, B., D'Addabbo, A., Désert, F.-X., Doyle, S., Goupy, J., Kramer, C., Leclercq, S., Macias-Perez, J., Martino, J., Mauskopf, P., Mayet, F., Pajot, F., Pascale, E., Ponthieu, N., Revéret, V., Rodriguez, L., Savini, G., Schuster, K., Sievers, A., Tucker, C., & Zylka, R. 2014, Journal of Low Temperature Physics, 176, 787

Monfardini, A., Swenson, L. J., Bideaud, A., Désert, F. X., Yates, S. J. C., Benoit, A., Baryshev, A. M., Baselmans, J. J. A., Doyle, S., Klein, B., Roesch, M., Tucker, C., Ade, P., Calvo, M., Camus, P., Giordano, C., Guesten, R., Hoffmann, C., Leclercq, S., Mauskopf, P., & Schuster, K. F. 2010, A&A, 521, A29

Morandi, A., Sun, M., Forman, W., & Jones, C. 2015, ArXiv e-prints

Mroczkowski, T. 2011, ApJ, 728, L35

—. 2012, ApJ, 746, L29

Mroczkowski, T., Bonamente, M., Carlstrom, J. E., Culverhouse, T. L., Greer, C., Hawkins, D., Hennessy, R., Joy, M., Lamb, J. W., Leitch, E. M., Loh, M., Maughan, B., Marrone, D. P., Miller, A., Muchovej, S., Nagai, D., Pryke, C., Sharp, M., & Woody, D. 2009, ApJ, 694, 1034

Mroczkowski, T., Dicker, S., Sayers, J., Reese, E. D., Mason, B., Czakon, N., Romero, C., Young, A., Devlin, M., Golwala, S., Korngut, P., Sarazin, C., Bock, J., Koch,

P. M., Lin, K.-Y., Molnar, S. M., Pierpaoli, E., Umetsu, K., & Zemcov, M. 2012, ApJ, 761, 47

Muchovej, S., Mroczkowski, T., Carlstrom, J. E., Cartwright, J., Greer, C., Hennessy, R., Loh, M., Pryke, C., Reddall, B., Runyan, M., Sharp, M., Hawkins, D., Lamb, J. W., Woody, D., Joy, M., Leitch, E. M., & Miller, A. D. 2007, ApJ, 663, 708

Nagai, D. 2006, ApJ, 650, 538

Nagai, D., Kravtsov, A. V., & Vikhlinin, A. 2007, ApJ, 668, 1

Navarro, J. F., Frenk, C. S., & White, S. D. M. 1996, ApJ, 462, 563

—. 1997, ApJ, 490, 493

Newman, A. B., Treu, T., Ellis, R. S., Sand, D. J., Richard, J., Marshall, P. J., Capak, P., & Miyazaki, S. 2009, ApJ, 706, 1078

Niemack, M. D., Ade, P. A. R., Aguirre, J., Barrientos, F., Beall, J. A., Bond, J. R., Britton, J., Cho, H. M., Das, S., Devlin, M. J., Dicker, S., Dunkley, J., Dünner, R., Fowler, J. W., Hajian, A., Halpern, M., Hasselfield, M., Hilton, G. C., Hilton, M., Hubmayr, J., Hughes, J. P., Infante, L., Irwin, K. D., Jarosik, N., Klein, J., Kosowsky, A., Marriage, T. A., McMahon, J., Menanteau, F., Moodley, K., Nibarger, J. P., Nolta, M. R., Page, L. A., Partridge, B., Reese, E. D., Sievers, J., Spergel, D. N., Staggs, S. T., Thornton, R., Tucker, C., Wollack, E., & Yoon, K. W. 2010, in Society of Photo-Optical Instrumentation Engineers (SPIE) Conference Series, Vol. 7741, Society of Photo-Optical Instrumentation Engineers (SPIE) Conference Series, 1

Nikolic, B., Prestage, R. M., Balser, D. S., Chandler, C. J., & Hills, R. E. 2007, A&A, 465, 685

Ota, N., Murase, K., Kitayama, T., Komatsu, E., Hattori, M., Matsuo, H., Oshima, T., Suto, Y., & Yoshikawa, K. 2008, A&A, 491, 363

Padin, S., Scott, S. L., Woody, D. P., Scoville, N. Z., Seling, T. V., Finch, R. P., Giovanine, C. J., & Lawrence, R. P. 1991, PASP, 103, 461

Pardo, J. R., Cernicharo, J., & Serabyn, E. 2001, IEEE Transactions on Antennas and Propagation, 49, 1683

Peng, F. & Nagai, D. 2009, ApJ, 693, 839

Penzias, A. A. & Wilson, R. W. 1965, ApJ, 142, 419

Pfrommer, C., Springel, V., Enßlin, T. A., & Jubelgas, M. 2006, MNRAS, 367, 113

Plagge, T. J., Marrone, D. P., Abdulla, Z., Bonamente, M., Carlstrom, J. E., Gralla, M., Greer, C. H., Joy, M., Lamb, J. W., Leitch, E. M., Mantz, A., Muchovej, S., & Woody, D. 2013, ApJ, 770, 112

Planck Collaboration, Ade, P. A. R., Aghanim, N., Arnaud, M., Ashdown, M., Atrio-Barandela, F., Aumont, J., Baccigalupi, C., Balbi, A., Banday, A. J., & et al. 2013, A&A, 558, C2

Planck Collaboration, Ade, P. A. R., Aghanim, N., Arnaud, M., Ashdown, M., Aumont, J., Baccigalupi, C., Baker, M., Balbi, A., Banday, A. J., & et al. 2011, A&A, 536, A1

Planck Collaboration, Ade, P. A. R., Aghanim, N., Arnaud, M., Ashdown, M., Aumont, J., Baccigalupi, C., Banday, A. J., Barreiro, R. B., Barrena, R., & et al. 2015, ArXiv e-prints

Plionis, M., López-Cruz, O., & Hughes, D., eds. 2008, Lecture Notes in Physics, Berlin Springer Verlag, Vol. 740, A Pan-Chromatic View of Clusters of Galaxies and the Large-Scale Structure

Pointecouteau, E., Giard, M., Benoit, A., Désert, F. X., Aghanim, N., Coron, N., Lamarre, J. M., & Delabrouille, J. 1999, ApJ, 519, L115

Postman, M., Coe, D., Benítez, N., Bradley, L., Broadhurst, T., Donahue, M., Ford, H., Graur, O., Graves, G., Jouvel, S., Koekemoer, A., Lemze, D., Medezinski, E., Molino, A., Moustakas, L., Ogaz, S., Riess, A., Rodney, S., Rosati, P., Umetsu, K., Zheng, W., Zitrin, A., Bartelmann, M., Bouwens, R., Czakon, N., Golwala, S., Host, O., Infante, L., Jha, S., Jimenez-Teja, Y., Kelson, D., Lahav, O., Lazkoz, R., Maoz, D., McCully, C., Melchior, P., Meneghetti, M., Merten, J., Moustakas, J., Nonino, M., Patel, B., Regös, E., Sayers, J., Seitz, S., & Van der Wel, A. 2012, ApJS, 199, 25

Pratt, G. W., Böhringer, H., Croston, J. H., Arnaud, M., Borgani, S., Finoguenov, A., & Temple, R. F. 2007, A&A, 461, 71

Press, W. H. & Schechter, P. 1974, ApJ, 187, 425

Quataert, E. 2008, ApJ, 673, 758

Reese, E. D., Carlstrom, J. E., Joy, M., Mohr, J. J., Grego, L., & Holzapfel, W. L. 2002, ApJ, 581, 53

Reichardt, C. L., Stalder, B., Bleem, L. E., Montroy, T. E., Aird, K. A., Andersson, K., Armstrong, R., Ashby, M. L. N., Bautz, M., Bayliss, M., Bazin, G., Benson, B. A., Brodwin, M., Carlstrom, J. E., Chang, C. L., Cho, H. M., Clocchiatti, A., Crawford, T. M., Crites, A. T., de Haan, T., Desai, S., Dobbs, M. A., Dudley,

J. P., Foley, R. J., Forman, W. R., George, E. M., Gladders, M. D., Gonzalez, A. H., Halverson, N. W., Harrington, N. L., High, F. W., Holder, G. P., Holzapfel, W. L., Hoover, S., Hrubes, J. D., Jones, C., Joy, M., Keisler, R., Knox, L., Lee, A. T., Leitch, E. M., Liu, J., Lueker, M., Luong-Van, D., Mantz, A., Marrone, D. P., McDonald, M., McMahon, J. J., Mehl, J., Meyer, S. S., Mocanu, L., Mohr, J. J., Murray, S. S., Natoli, T., Padin, S., Plagge, T., Pryke, C., Rest, A., Ruel, J., Ruhl, J. E., Saliwanchik, B. R., Saro, A., Sayre, J. T., Schaffer, K. K., Shaw, L., Shirokoff, E., Song, J., Spieler, H. G., Staniszewski, Z., Stark, A. A., Story, K., Stubbs, C. W., Šuhada, R., van Engelen, A., Vanderlinde, K., Vieira, J. D., Vikhlinin, A., Williamson, R., Zahn, O., & Zenteno, A. 2013, ApJ, 763, 127

Reid, B. A. & Spergel, D. N. 2006, ApJ, 651, 643

Reiprich, T. H. & Böhringer, H. 2002, ApJ, 567, 716

Richards, P. L. 1994, Journal of Applied Physics, 76, 1

Roettiger, K., Burns, J., & Loken, C. 1993, ApJ, 407, L53

Romero, C., Mason, B. S., Sayers, J., Young, A. H., Mroczkowski, T., Clarke, T. E., Sarazin, C., Sievers, J., Dicker, S. R., Reese, E. D., Czakon, N., Devlin, M., Korngut, P. M., & Golwala, S. 2015, ArXiv e-prints

Russell, H. R., McNamara, B. R., Sanders, J. S., Fabian, A. C., Nulsen, P. E. J., Canning, R. E. A., Baum, S. A., Donahue, M., Edge, A. C., King, L. J., & O'Dea, C. P. 2012, MNRAS, 423, 236

Russell, H. R., Sanders, J. S., Fabian, A. C., Baum, S. A., Donahue, M., Edge, A. C., McNamara, B. R., & O'Dea, C. P. 2010, MNRAS, 406, 1721

Russell, H. R., van Weeren, R. J., Edge, A. C., McNamara, B. R., Sanders, J. S., Fabian, A. C., Baum, S. A., Canning, R. E. A., Donahue, M., & O'Dea, C. P. 2011, Monthly Notices of the Royal Astronomical Society: Letters, L297

Sarazin, C. L. 1988, X-ray emission from clusters of galaxies (Cambridge Astrophysics Series, Cambridge: Cambridge University Press, 1988)

Sarazin, C. L. 2002, in Astrophysics and Space Science Library, Vol. 272, Merging Processes in Galaxy Clusters, ed. L. Feretti, I. M. Gioia, & G. Giovannini, 1

Sayers, J., Bockstiegel, C., Brugger, S., Czakon, N. G., Day, P. K., Downes, T. P., Duan, R. P., Gao, J., Gill, A. K., Glenn, J., Golwala, S. R., Hollister, M. I., Lam, A., LeDuc, H. G., Maloney, P. R., Mazin, B. A., McHugh, S. G., Miller, D. A., Mroczkowski, A. K., Noroozian, O., Nguyen, H. T., Schlaerth, J. A., Siegel, S. R., Vayonakis, A., Wilson, P. R., & Zmuidzinas, J. 2014, in Society of Photo-Optical Instrumentation Engineers (SPIE) Conference Series, Vol. 9153, Society of Photo-Optical Instrumentation Engineers (SPIE) Conference Series, 4

Sayers, J., Czakon, N. G., Bridge, C., Golwala, S. R., Koch, P. M., Lin, K.-Y., Molnar, S. M., & Umetsu, K. 2012, ApJ, 749, L15

Sayers, J., Czakon, N. G., Mantz, A., Golwala, S. R., Ameglio, S., Downes, T. P., Koch, P. M., Lin, K.-Y., Maughan, B. J., Molnar, S. M., Moustakas, L., Mroczkowski, T., Pierpaoli, E., Shitanishi, J. A., Siegel, S., Umetsu, K., & Van der Pyl, N. 2013, ApJ, 768, 177

Sayers, J., Golwala, S. R., Ameglio, S., & Pierpaoli, E. 2011, ApJ, 728, 39

Schindler, S., Guzzo, L., Ebeling, H., Boehringer, H., Chincarini, G., Collins, C. A.,

de Grandi, S., Neumann, D. M., Briel, U. G., Shaver, P., & Vettolani, G. 1995, A&A, 299, L9

Schindler, S., Hattori, M., Neumann, D. M., & Boehringer, H. 1997, A&A, 317, 646

Schindler, S. & Mueller, E. 1993, A&A, 272, 137

Schmidt, R. W. & Allen, S. W. 2007, MNRAS, 379, 209

Schmidt, R. W., Allen, S. W., & Fabian, A. C. 2001, MNRAS, 327, 1057

Schwan, D., Ade, P. A. R., Basu, K., Bender, A. N., Bertoldi, F., Cho, H.-M., Chon, G., Clarke, J., Dobbs, M., Ferrusca, D., Güsten, R., Halverson, N. W., Holzapfel, W. L., Horellou, C., Johansson, D., Johnson, B. R., Kennedy, J., Kermish, Z., Kneissl, R., Lanting, T., Lee, A. T., Lueker, M., Mehl, J., Menten, K. M., Muders, D., Pacaud, F., Plagge, T., Reichardt, C. L., Richards, P. L., Schaaf, R., Schilke, P., Sommer, M. W., Spieler, H., Tucker, C., Weiss, A., Westbrook, B., & Zahn, O. 2011, Review of Scientific Instruments, 82, 091301

Schwan, D., Kneissl, R., Ade, P., Basu, K., Bender, A., Bertoldi, F., Böhringer, H., Cho, H.-M., Chon, G., Clarke, J., Dobbs, M., Ferrusca, D., Flanigan, D., Halverson, N., Holzapfel, W., Horellou, C., Johansson, D., Johnson, B., Kennedy, J., Kermish, Z., Klein, M., Lanting, T., Lee, A., Lueker, M., Mehl, J., Menten, K., Muders, D., Pacaud, F., Plagge, T., Reichardt, C., Richards, P., Schaaf, R., Schilke, P., Sommer, M., Spieler, H., Tucker, C., Weiss, A., Westbrook, B., & Zahn, O. 2012, The Messenger, 147, 7

Sehgal, N., Addison, G., Battaglia, N., Battistelli, E. S., Bond, J. R., Das, S., Devlin, M. J., Dunkley, J., Dünner, R., Gralla, M., Hajian, A., Halpern, M., Hasselfield, M., Hilton, M., Hincks, A. D., Hlozek, R., Hughes, J. P., Kosowsky, A., Lin, Y.-T.,

Louis, T., Marriage, T. A., Marsden, D., Menanteau, F., Moodley, K., Niemack, M. D., Page, L. A., Partridge, B., Reese, E. D., Sherwin, B. D., Sievers, J., Sifón, C., Spergel, D. N., Staggs, S. T., Swetz, D. S., Switzer, E. R., & Wollack, E. 2013, ApJ, 767, 38

Sehgal, N., Trac, H., Acquaviva, V., Ade, P. A. R., Aguirre, P., Amiri, M., Appel, J. W., Barrientos, L. F., Battistelli, E. S., Bond, J. R., Brown, B., Burger, B., Chervenak, J., Das, S., Devlin, M. J., Dicker, S. R., Bertrand Doriese, W., Dunkley, J., Dünner, R., Essinger-Hileman, T., Fisher, R. P., Fowler, J. W., Hajian, A., Halpern, M., Hasselfield, M., Hernández-Monteagudo, C., Hilton, G. C., Hilton, M., Hincks, A. D., Hlozek, R., Holtz, D., Huffenberger, K. M., Hughes, D. H., Hughes, J. P., Infante, L., Irwin, K. D., Jones, A., Baptiste Juin, J., Klein, J., Kosowsky, A., Lau, J. M., Limon, M., Lin, Y., Lupton, R. H., Marriage, T. A., Marsden, D., Martocci, K., Mauskopf, P., Menanteau, F., Moodley, K., Moseley, H., Netterfield, C. B., Niemack, M. D., Nolta, M. R., Page, L. A., Parker, L., Partridge, B., Reid, B., Sherwin, B. D., Sievers, J., Spergel, D. N., Staggs, S. T., Swetz, D. S., Switzer, E. R., Thornton, R., Tucker, C., Warne, R., Wollack, E., & Zhao, Y. 2011, ApJ, 732, 44

Silk, J. & White, S. D. M. 1978, ApJ, 226, L103

Sinclair, M. W., Gough, R. G., Graves, G. R., Carrad, G. J., Leach, M. R., Bolton, R. J., Sykes, P. B., & Reilly, L. J. 2001, in 2001 Asia-Pacific Radio Science Conference AP-RASC '01, 386

Siringo, G., Kreysa, E., Kovács, A., Schuller, F., Weiß, A., Esch, W., Gemünd, H.-P., Jethava, N., Lundershausen, G., Colin, A., Güsten, R., Menten, K. M., Beelen, A., Bertoldi, F., Beeman, J. W., & Haller, E. E. 2009, A&A, 497, 945

Skillman, S. W., O'Shea, B. W., Hallman, E. J., Burns, J. O., & Norman, M. L. 2008, ApJ, 689, 1063

Smith, G. P., Ebeling, H., Limousin, M., Kneib, J.-P., Swinbank, A. M., Ma, C.-J., Jauzac, M., Richard, J., Jullo, E., Sand, D. J., Edge, A. C., & Smail, I. 2009, ApJ, 707, L163

Spitzer, L. 1962, Physics of Fully Ionized Gases

Staff, A. 2015, ALMA Documents

Staguhn, J. G., Benford, D. J., Allen, C. A., Moseley, S. H., Sharp, E. H., Ames, T. J., Brunswig, W., Chuss, D. T., Dwek, E., Maher, S. F., Marx, C. T., Miller, T. M., Navarro, S., & Wollack, E. J. 2006, in Society of Photo-Optical Instrumentation Engineers (SPIE) Conference Series, Vol. 6275, Society of Photo-Optical Instrumentation Engineers (SPIE) Conference Series, 1

Staguhn, J. G., Benford, D. J., Fixsen, D. J., Hilton, G., Irwin, K. D., Jhabvala, C. A., Kovacs, A., Leclercq, S., Maher, S. F., Miller, T. M., Moseley, S. H., Sharp, E. H., & Wollack, E. J. 2012, in Society of Photo-Optical Instrumentation Engineers (SPIE) Conference Series, Vol. 8452, Society of Photo-Optical Instrumentation Engineers (SPIE) Conference Series, 0

Sun, M., Sehgal, N., Voit, G. M., Donahue, M., Jones, C., Forman, W., Vikhlinin, A., & Sarazin, C. 2011, ApJ, 727, L49

Sunyaev, R. A. & Zel'dovich, Y. B. 1970, Comments Astrophys. Space Phys., 2, 66

Swetz, D. S., Ade, P. A. R., Amiri, M., Appel, J. W., Battistelli, E. S., Burger, B., Chervenak, J., Devlin, M. J., Dicker, S. R., Doriese, W. B., Dünner, R., Essinger-Hileman, T., Fisher, R. P., Fowler, J. W., Halpern, M., Hasselfield, M., Hilton,

G. C., Hincks, A. D., Irwin, K. D., Jarosik, N., Kaul, M., Klein, J., Lau, J. M., Limon, M., Marriage, T. A., Marsden, D., Martocci, K., Mauskopf, P., Moseley, H., Netterfield, C. B., Niemack, M. D., Nolta, M. R., Page, L. A., Parker, L., Staggs, S. T., Stryzak, O., Switzer, E. R., Thornton, R., Tucker, C., Wollack, E., & Zhao, Y. 2011, ApJS, 194, 41

Udomprasert, P. S., Mason, B. S., Readhead, A. C. S., & Pearson, T. J. 2004, ApJ, 615, 63

Umetsu, K., Medezinski, E., Nonino, M., Merten, J., Zitrin, A., Molino, A., Grillo, C., Carrasco, M., Donahue, M., Mahdavi, A., Coe, D., Postman, M., Koekemoer, A., Czakon, N., Sayers, J., Mroczkowski, T., Golwala, S., Koch, P. M., Lin, K.-Y., Molnar, S. M., Rosati, P., Balestra, I., Mercurio, A., Scodeggio, M., Biviano, A., Anguita, T., Infante, L., Seidel, G., Sendra, I., Jouvel, S., Host, O., Lemze, D., Broadhurst, T., Meneghetti, M., Moustakas, L., Bartelmann, M., Benítez, N., Bouwens, R., Bradley, L., Ford, H., Jiménez-Teja, Y., Kelson, D., Lahav, O., Melchior, P., Moustakas, J., Ogaz, S., Seitz, S., & Zheng, W. 2012, ApJ, 755, 56

van Weeren, R. J. 2011, PhD thesis, Leiden Observatory, The Netherlands

van Weeren, R. J., Röttgering, H. J. A., Brüggen, M., & Cohen, A. 2009, A&A, 505, 991

Vazza, F., Brunetti, G., Kritsuk, A., Wagner, R., Gheller, C., & Norman, M. 2009, A&A, 504, 33

Vikhlinin, A. 2006, ApJ, 640, 710

Vikhlinin, A., Kravtsov, A. V., Burenin, R. A., Ebeling, H., Forman, W. R., Horn-

strup, A., Jones, C., Murray, S. S., Nagai, D., Quintana, H., & Voevodkin, A. 2009, ApJ, 692, 1060

Voit, G. M. 2005, Reviews of Modern Physics, 77, 207

Weiland, J. L., Odegard, N., Hill, R. S., Wollack, E., Hinshaw, G., Greason, M. R., Jarosik, N., Page, L., Bennett, C. L., Dunkley, J., Gold, B., Halpern, M., Kogut, A., Komatsu, E., Larson, D., Limon, M., Meyer, S. S., Nolta, M. R., Smith, K. M., Spergel, D. N., Tucker, G. S., & Wright, E. L. 2011, ApJS, 192, 19

Welch, W. J., Thornton, D. D., Plambeck, R. L., Wright, M. C. H., Lugten, J., Urry, L., Fleming, M., Hoffman, W., Hudson, J., Lum, W. T., Forster, J. . R., Thatte, N., Zhang, X., Zivanovic, S., Snyder, L., Crutcher, R., Lo, K. Y., Wakker, B., Stupar, M., Sault, R., Miao, Y., Rao, R., Wan, K., Dickel, H., Blitz, L., Vogel, S. N., Mundy, L., Erickson, W., Teuben, P. J., Morgan, J., Helfer, T., Looney, L., de Gues, E., Grossman, A., Howe, J. E., Pound, M., & Regan, R. 1996, PASP, 108, 93

Wik, D. R., Sarazin, C. L., Ricker, P. M., & Randall, S. W. 2008, ApJ, 680, 17

Wilson, G. W., Austermann, J. E., Perera, T. A., Scott, K. S., Ade, P. A. R., Bock, J. J., Glenn, J., Golwala, S. R., Kim, S., Kang, Y., Lydon, D., Mauskopf, P. D., Predmore, C. R., Roberts, C. M., Souccar, K., & Yun, M. S. 2008, MNRAS, 386, 807

Wong, K.-W. & Sarazin, C. L. 2009, ApJ, 707, 1141

Wong, K.-W., Sarazin, C. L., & Wik, D. R. 2010, ApJ, 719, 1

Woody, D. P., Beasley, A. J., Bolatto, A. D., Carlstrom, J. E., Harris, A., Hawkins, D. W., Lamb, J., Looney, L., Mundy, L. G., Plambeck, R. L., Scott, S., & Wright,

M. 2004, in Society of Photo-Optical Instrumentation Engineers (SPIE) Conference Series, Vol. 5498, Z-Spec: a broadband millimeter-wave grating spectrometer: design, construction, and first cryogenic measurements, ed. C. M. Bradford, P. A. R. Ade, J. E. Aguirre, J. J. Bock, M. Dragovan, L. Duband, L. Earle, J. Glenn, H. Matsuhara, B. J. Naylor, H. T. Nguyen, M. Yun, & J. Zmuidzinas, 30–41

Wright, E. L. 2007, ArXiv Astrophysics e-prints

Young, A. H., Mroczkowski, T., Romero, C., Sayers, J., Balestra, I., Clarke, T. E., Czakon, N., Devlin, M., Dicker, S. R., Ferrari, C., Girardi, M., Golwala, S., Intema, H., Korngut, P. M., Mason, B. S., Mercurio, A., Nonino, M., Reese, E. D., Rosati, P., Sarazin, C., & Umetsu, K. 2014, ArXiv e-prints 1411.0317

Zitrin, A., Broadhurst, T., Barkana, R., Rephaeli, Y., & Benítez, N. 2011, MNRAS, 410, 1939

Zitrin, A., Broadhurst, T., Rephaeli, Y., & Sadeh, S. 2009, ApJ, 707, L102

Zitrin, A., Fabris, A., Merten, J., Melchior, P., Meneghetti, M., Koekemoer, A., Coe, D., Maturi, M., Bartelmann, M., Postman, M., Umetsu, K., Seidel, G., Sendra, I., Broadhurst, T., Balestra, I., Biviano, A., Grillo, C., Mercurio, A., Nonino, M., Rosati, P., Bradley, L., Carrasco, M., Donahue, M., Ford, H., Frye, B. L., & Moustakas, J. 2015, ApJ, 801, 44

Zitrin, A., Moustakas, J., Bradley, L., Coe, D., Moustakas, L. A., Postman, M., Shu, X., Zheng, W., Benítez, N., Bouwens, R., Broadhurst, T., Ford, H., Host, O., Jouvel, S., Koekemoer, A., Meneghetti, M., Rosati, P., Donahue, M., Grillo, C., Kelson, D., Lemze, D., Medezinski, E., Molino, A., Nonino, M., & Ogaz, S. 2012a, ApJ, 747, L9

Zitrin, A., Rosati, P., Nonino, M., Grillo, C., Postman, M., Coe, D., Seitz, S., Eichner, T., Broadhurst, T., Jouvel, S., Balestra, I., Mercurio, A., Scodeggio, M., Benítez, N., Bradley, L., Ford, H., Host, O., Jimenez-Teja, Y., Koekemoer, A., Zheng, W., Bartelmann, M., Bouwens, R., Czoske, O., Donahue, M., Graur, O., Graves, G., Infante, L., Jha, S., Kelson, D., Lahav, O., Lazkoz, R., Lemze, D., Lombardi, M., Maoz, D., McCully, C., Medezinski, E., Melchior, P., Meneghetti, M., Merten, J., Molino, A., Moustakas, L. A., Ogaz, S., Patel, B., Regoes, E., Riess, A., Rodney, S., Umetsu, K., & Van der Wel, A. 2012b, ApJ, 749, 97

ZuHone, J. A., Markevitch, M., & Johnson, R. E. 2010, ApJ, 717, 908